

MEASUREMENTS OF FRESNEL-DRAG USING
A PASSIVE RING RESONATOR TECHNIQUE

by

GLEN AARON SANDERS

B.S., University of Colorado, Boulder
(1977)

Submitted to the Department of Physics
in Partial Fulfillment of the
Requirements of the
Degree of

DOCTOR OF PHILOSOPHY

at the

MASSACHUSETTS INSTITUTE OF TECHNOLOGY

June 1983

© Massachusetts Institute of Technology, 1983

Signature of Author.....
Department of Physics
May 13, 1983

Certified by.. ..
Shaoul Ezekiel,
Thesis Supervisor

Accepted by.....
George F. Koster
Head, Ph.D. Committee

Archives
MASSACHUSETTS INSTITUTE
OF TECHNOLOGY

JUN 14 1983

LIBRARIES

MEASUREMENTS OF FRESNEL-DRAG USING
A PASSIVE RING RESONATOR TECHNIQUE

by

GLEN AARON SANDERS

Submitted to the Department of Physics
on May 13, 1983 in partial fulfillment of the requirements
for the Degree of Doctor of Philosophy in Physics

ABSTRACT

Measurements of Fresnel-drag in moving glass samples were performed using a passive ring resonator technique. The glass samples were moved with sinusoidal velocity inside the resonator and the resultant oscillatory difference in the resonance frequencies of the cavity due to the "drag" was detected.

Measurements were taken with glass materials fused silica, BK-7, SF-1 and SF-57 giving a range in index of 1.46 to 1.84 and a variation in dispersion from $-0.029 \mu\text{m}^{-1}$ to $-0.138 \mu\text{m}^{-1}$. The lengths of the samples were varied from 0.2 cm to 1.5 cm. In addition, the dependence of the "drag" on velocity and angle of incidence was measured. The measured drag coefficient α_e was compared to the theoretical value α_{th} . Using an unweighted average of the measurements, the spread in $(\alpha_e - \alpha_{th})/\alpha_{th}$ was -5×10^{-4} with a mean of -5×10^{-5} . Weighting the measurements according to each error bar gave a spread in $(\alpha_e - \alpha_{th})/\alpha_{th}$ of -2.4×10^{-4} with a mean of -4×10^{-5} . In the case of SF-57, the contribution of the dispersion term was $\sim 10\%$ of the drag coefficient. By varying n and $\partial n/\partial \lambda$ it was possible to determine α with greater precision, a factor of at least 30 better than previous reported measurements using ring lasers.

In order to obtain greater precision using the present technique a vacuum system should be used as well as more homogeneous glass samples and better readout procedures.

Thesis Supervisor: Dr. Shaoul Ezekiel
Title: Professor of Aeronautics and Astronautics and
Electrical Engineering and Computer Science

ACKNOWLEDGEMENTS

I would first like to thank my advisor, Prof. Shaoul Ezekiel, for his interest and enthusiastic support of this research. Through him, I was exposed to many valuable experimental research methods. In addition, I would like to thank him for his many hours of guidance, advice and helpful suggestions.

I would also like to thank Professors Weiss and King for reading the thesis and making helpful suggestions.

I would also like to thank my fellow graduate students, particularly B. Peuse, R. Tench, M. Prentiss, R. Meyer and J. Davis for helpful discussions as well as their contributions to this research. I also wish to thank J. Kierstead for his assistance and helpful suggestions, particularly those pertinent to the mechanical apparatus used in this experiment. In addition, I would like to thank Debi Lauricella for her heroic and immaculate typing job.

I would also like to thank the Research Laboratory of Electronics for the use of its facilities and the Air Force Office of Scientific Research, the Air Force Geophysics Laboratory and the Joint Services Electronics Program for their support of this research.

Last, but not least, I would like to thank my parents and my wife, Leslie for their support, and encouragement throughout my stay at MIT.

Dedicated:

to my wife, Leslie

TABLE OF CONTENTS

	<u>Page</u>
CHAPTER 1. INTRODUCTION.....	8
1.1. Motivation.....	8
1.2. Contents of Thesis.....	10
CHAPTER 2. HISTORICAL BACKGROUND.....	12
2.1. Introduction and Fresnel's Contribution.....	12
2.2. Fizeau's Measurement.....	14
2.3. Special Relativistic Explanation of Drag.....	16
2.4a. Zeeman's Measurements and Dispersion Correction..	17
2.4b. Analysis of Drag in Shuttling Rod Configuration..	21
2.5. Ring Laser Experiments.....	25
CHAPTER 3. TECHNIQUES FOR DRAG MEASUREMENT.....	31
3.1. Introduction.....	31
3.2. Interferometric Techniques.....	32
3.3. Ring Laser Technique.....	32
3.4. Passive Ring Resonator Technique.....	36
3.5. Comparison of Sensing Techniques for Fresnel Drag Measurements.....	44
CHAPTER 4. PASSIVE RING RESONATOR TECHNIQUE.....	48
4.1. Introduction.....	48
4.2. Application of Passive Ring Resonator Technique to Inertial Rotation Sensing and Fresnel-Drag Measurement.....	48
4.3. Technique Employed for Measurement of Cavity Resonance Frequencies.....	53
4.4. Passive Ring Resonator Setup for Measurement of Non-Reciprocal Phase Shift.....	60
4.5. Sensor Performance and Fundamental Limits.....	63
4.6. Sources of Error in Passive Ring Resonator Technique.....	70
4.6a. Mode Pulling Effects.....	70
4.6b. Electronic Error Sources.....	83

	<u>Page</u>
4.6c. Effects of Air Currents.....	89
4.6d. Scattering Effects.....	90
4.6e. Polarization Effects.....	97
CHAPTER 5. MEASUREMENT OF FRESNEL-DRAG IN THE PASSIVE RING RESONATOR.....	108
5.1. Introduction and Overview of Experimental Arrangement.....	108
5.2. Considerations and Apparatus for Moving Glass in Cavity.....	111
5.3. Details of Alignment, Measurement and Stabilization of the Velocity.....	122
5.4. Details of the Measurement of Resonance Frequency Shift Due to Light Drag.....	141
5.5. Calibration: System Checks and Parameter Measurements.....	148
5.5.1. System Checks.....	148
5.5.2. Parameter Measurements.....	153
5.5.2a. Measurement of $\Delta f(f_f)$: Data Readout and Scale Factor Calibration.....	153
5.5.2b. Measurement of $v(f_f)$: Data Readout and Calibration.....	161
5.5.2c. Determination of Index of Refraction and Dispersion.....	163
5.5.2d. Determination of the Length of Glass Windows.....	165
5.5.2e. Index of Air.....	167
5.5.2f. Determination of Optical Perimeter of Cavity.....	168
5.5.2g. Determination of Angle of Incidence.....	171
5.5.2h. Determination of Wavelength of Laser.....	174
5.6. Correction for Angular Dependence in Drag Calculation.....	175

	<u>Page</u>
CHAPTER 6. DATA ANALYSIS, SUMMARY AND CONCLUSION.....	187
6.1. Introduction.....	187
6.2. Data Analysis.....	187
6.3. Determination of the Drag Coefficient.....	205
6.4. Conclusion.....	212
CHAPTER 7. SUMMARY AND SUGGESTIONS FOR FUTURE WORK.....	213
7.1. Summary.....	213
7.2. Suggestions for Future Work.....	219
REFERENCES.....	222

CHAPTER 1

INTRODUCTION

1.1. Motivation

There is no doubt that the advent of the laser, in 1960, has opened many technological avenues, but this is also true of its contributions to fundamental physics. After all, physics as an experimental science, relies upon continually increasing the accuracies of its basic experimental methods. The laser, in conjunction with improved experimental techniques, such as laser frequency stabilization techniques, has provided the impetus for the many precision optical experiments now under consideration. Laser optical methods offer much promise for experimental checks of very sensitive, but fundamental, effects that have thus far been difficult to measure. Among these, is of course, the many proposed tests of general relativity, ranging from gravity wave detection to the tests of, metric gravitation theories.¹ In the latter case, laser rotation sensors, based on the Sagnac effect,² have been proposed as a possible experimental technique.³ In addition, these optical inertial rotation sensors are under consideration for sensitive geophysical applications, such as measurements of the precession and nutation of the earth's axis, and earth "wobble."⁴

It was the possibility of sensitive inertial rotation applications, that originally motivated this experimental research. Certainly, the ring laser "gyroscope" has received considerable

attention in this area, and is now being employed, very successfully, for navigation. This application requires a rotation measurement sensitivity of approximately $10^{-3} \Omega_{\epsilon}$ (Ω_{ϵ} = earth rate). The sensitivity required for measurements relevant to geophysics and relativity is on the order of 10^{-7} to $10^{-10} \Omega_{\epsilon}$.^{3,6} It is therefore clear that much research is needed in order to extend the sensitivity of the optical rotation sensing techniques for these applications. It follows that further examination of the various experimental approaches to optical inertial rotation sensing is warranted. Many Sagnac rotation sensors are under investigation today, including the ring laser "gyroscope,"⁵ fiber-optic interferometers⁸ and the passive ring resonator method.⁹ The technique employed in this research is the passive ring resonator method.

Although the interest in the passive cavity technique was generated by its rotation sensing applications,⁹ this is certainly not the only application for this sensor. The Sagnac effect is only one effect in the general category of non-reciprocal optical phase shifts (NRPS) experienced in the propagation of light. Another such non-reciprocal phase shift is the Fresnel drag effect. While special relativity has been verified to 5 parts in 10^9 by various methods,¹⁰ no such precision tests can be claimed regarding the predictions of special relativity for light propagation in moving media. The explanation of the original Fizeau experiment was, of course, one of the key requirements for Einstein's theory of special relativity; that is, not only was it necessary for the theory to explain light propagation in a vacuum,

but in a medium as well.¹¹ Further investigation of the Fresnel drag effect, with greater experimental accuracy provides for an improved test of special relativistic predictions for light propagation in a moving medium and this was the motivation of the thesis.

The passive ring resonator setup used in this research was by no means optimized for precision studies of the Fresnel-drag. The very fact that the passive cavity technique was being developed and studied in the lab as a result of its rotation sensor applications, suggested a convenient method for measuring the Fresnel-drag.

1.2. Contents of the Thesis

The Fresnel-drag in moving glass was studied and measured using an experimental setup basically consisting of a passive ring resonator and an external HeNe laser. In Chapter 2, the basic physics of the Fresnel-drag is presented as well as the history associated with previous measurements. The various possible modern approaches to the measurement are surveyed in Chapter 3. Chapter 4 focuses on the passive ring resonator method. This includes the general concept for measurement of NRPS, with specific extensions to the Sagnac effect and the drag effect, as well as a detailed description of how the setup works. In addition, the performance of the sensor is presented and compared to the fundamental measurement sensitivity. Sources of error, drift and noise are discussed.

Measurement of the Fresnel-drag required moving a glass window at a precisely known velocity inside the cavity. The additional

apparatus involved with providing and measuring this velocity is discussed in Chapter 5. The method used for data readout is discussed in this chapter, as well as the calibration of the system and the measurement of all relevant parameters. A calculation of the drag experienced in the specific configuration employed is also included in this chapter. The measurement results are discussed in Chapter 6, which also includes a discussion of the data reduction and analysis. Chapter 7 concludes the thesis with a summary and suggestions for future work.

CHAPTER 2

HISTORICAL BACKGROUND

2.1. Introduction and Fresnel's Contribution

A considerable portion of nineteenth century physics was devoted to the development of the wave theory of light. In the early 1800's, T. Young's measurements of interference phenomena were explained by J. Fresnel's application of the wave theory of light. In addition, Fresnel's calculations showed how polarization, diffraction, reflection and refraction could be accounted for by means of the wave theory. The problem, however, was that waves, like vibrations on a string, require a medium.¹¹ It was therefore hypothesized that light waves propagate through a medium known as the "luminiferous ether."

In order to explain various observations pertaining to stellar aberration experiments, Fresnel postulated, in 1818, a partial dragging of the light by moving media. He assumed that a moving medium does not impart any of its motion to both the ether that permeates the medium and to the ether that surrounds the medium. The propagation of light was supposed to be supported partly by the material and partly by the ether.¹¹ Since the material was moving and not the ether, only part of the velocity v of the medium was imparted to the light, given by, (see Fig. 2.1)

$$u = \frac{c}{n} + \alpha v \quad (2.1)$$

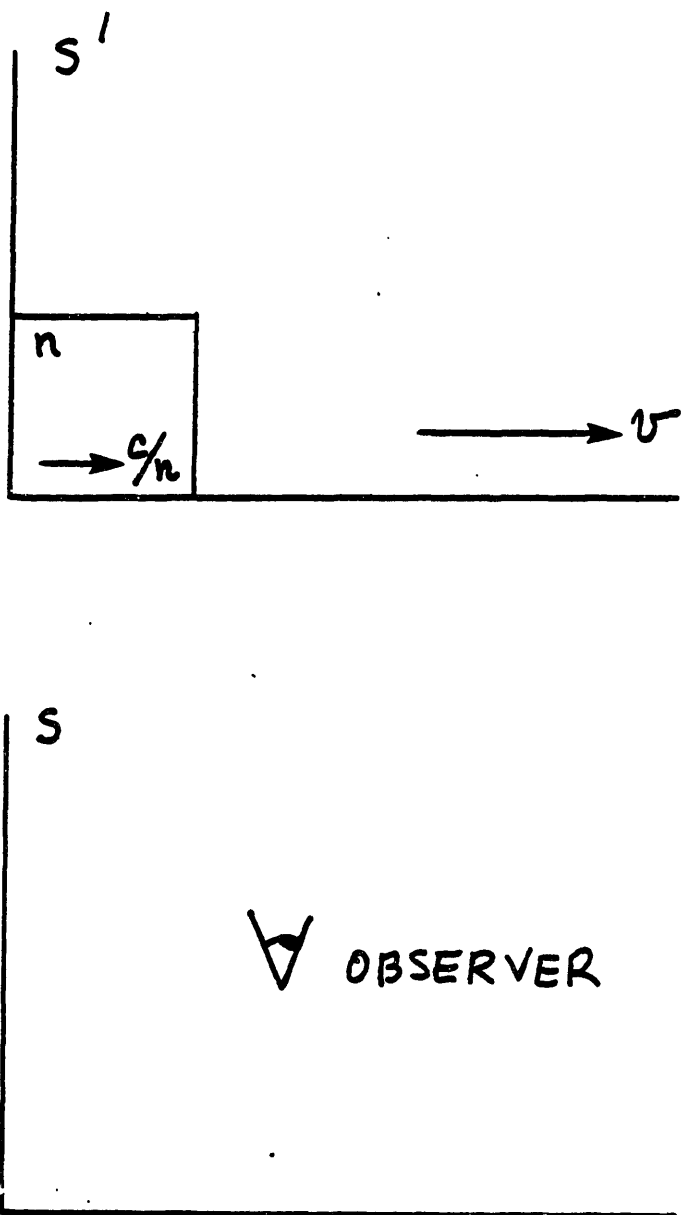


Figure 2.1

where u is the velocity of light observed in a frame moving at $-v$ with respect to the medium, and $\alpha = 1 - 1/n^2$ is known as the Fresnel-drag coefficient. In Newtonian theory, the velocities add such that

$$u = \frac{c}{n} + v \quad (2.2)$$

Thus, the parameter α signifies the value of the "partial drag" proposed by Fresnel.

2.2. Fizeau's Measurement

In 1851, H. Fizeau conducted the first direct experimental measurement of the Fresnel-drag coefficient.¹² In his apparatus, depicted in Figure 2.2, a sunlight source of average wavelength $\lambda = .53 \mu\text{m}$, was split into two equal intensities by a beam splitter, M_s . One beam propagated clockwise (cw) around the path enclosed by M_s and the mirrors M_1 , M_2 and M_3 and was then reflected off M_s into a telescope. The other beam propagated counter clockwise (ccw) around the same path and its transmission through the beam splitter was interfered with the cw beam in the telescope, where fringes were observed.

To produce drag, water was made to flow with velocity, \vec{v} , through two transparent tubes, of length ℓ , connected as shown in the figure. The velocity, and thus the drag, was oppositely directed for the two beams, therefore doubling the expected fringe shift. The time difference for the arrival of the two beams at the telescope in this configuration is given by,

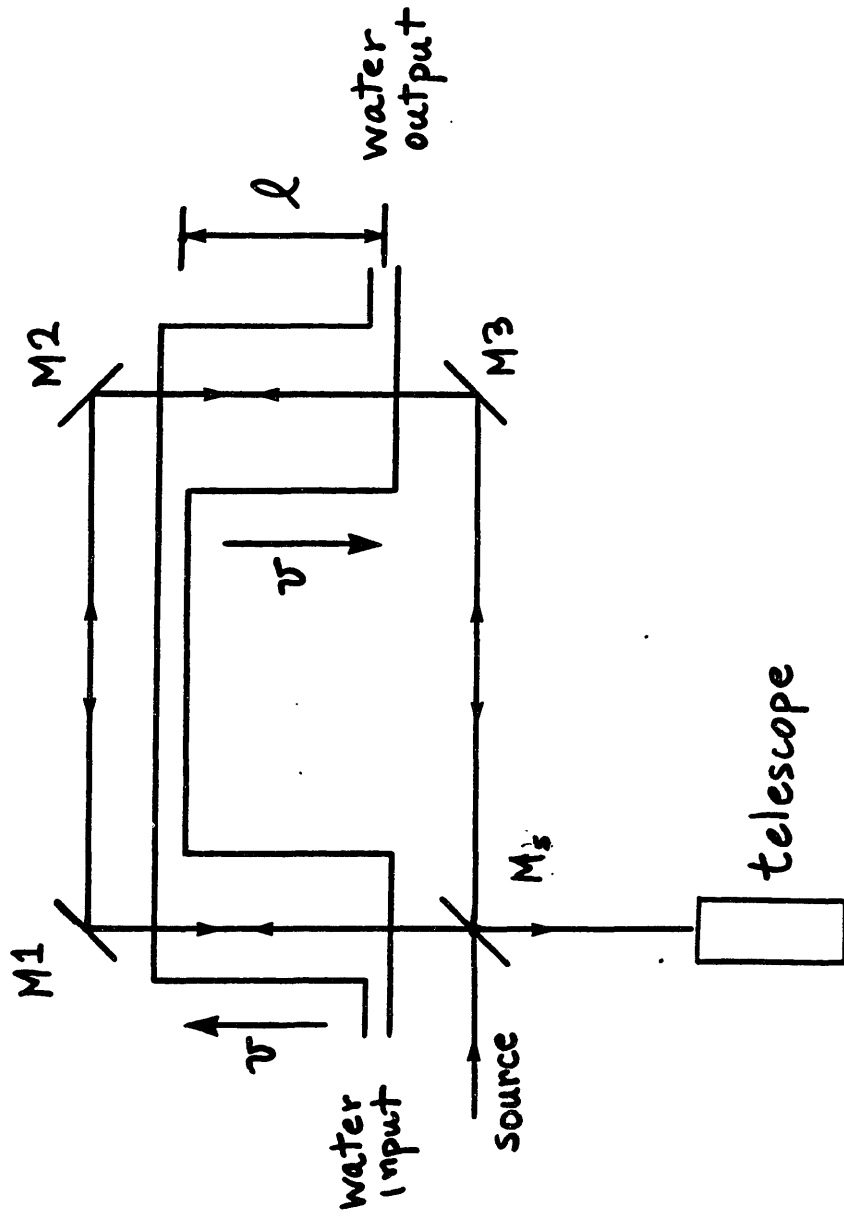


Figure 2.2

$$\Delta t = \frac{2l}{\frac{c}{n} - \alpha v} - \frac{2l}{\frac{c}{n} + \alpha v} = 4ln^2\alpha \frac{v}{c^2} \quad (2.3)$$

where n is the index of water, and α is the drag coefficient. The fringe shift ΔW is then given by,

$$\Delta W = \frac{c}{\lambda} \Delta t = \frac{4ln^2\alpha v}{\lambda c} \quad (2.4)$$

The observed fringe shift was $\Delta W = .23$ fringes leading to a measured value of $\alpha_m = .48$, while the calculated value was $\alpha_c = .43$.¹¹

In 1886, A. Michelson and E. Morley repeated Fizeau's experiment with greater precision, with the result that,¹³

$$\frac{\alpha_m - \alpha_c}{\alpha_c} = .007 \pm .05 \quad (2.5)$$

2.3. Special Relativistic Explanation of Drag

The measurements of Fizeau and Michelson and Morley were taken to be confirmation of the Fresnel's "partial dragging" hypothesis. However, when Michelson and Morley,¹⁴ in 1887, failed to detect the expected motion of the earth through the ether, serious discrepancies arose with the ether theory. This gave rise to Einstein's theory of special relativity. In order to explain the results of the Fizeau experiment, no ether was needed: Einstein's theory showed that the Fresnel-drag was a result of observing the speed of light in a moving medium in a different inertial frame of reference than that of the medium itself. Using the relativistic addition of velocities it is

easy to derive the Fresnel-drag coefficient, and hence, explain Fizeau's result. Suppose light travels through the medium with speed c/n in a coordinate system S' attached to the medium, as shown in Figure 2.1. If the medium moves with velocity v with respect to an observer in another inertial frame, S , the velocity in the unprimed coordinate system is given by,

$$u = \frac{c/n + v}{1 + \frac{vc}{nc^2}} \quad (2.6)$$

assuming \vec{v} and the light velocity to be parallel. To first order in v/c ,

$$u \approx \frac{c}{n} + v(1 - 1/n^2) \quad (2.7)$$

where $1 - 1/n^2$ is the familiar Fresnel-drag coefficient observed by Fizeau.

2.4a. Zeeman's Measurements and Dispersion Correction

After the advent of special relativity, P. Zeeman, from 1914-1922, performed a host of measurements of the drag coefficient. In his earlier measurements, he also used flowing water.¹⁵ However, in his later experiments he used "shuttling" glass rods made of both quartz and flint glass.¹⁶ Today, the "shuttling rod" experiments are recognized as the more accurate of the two types of measurements made by Zeeman. The basic optical configuration is shown in Figure 2.3.

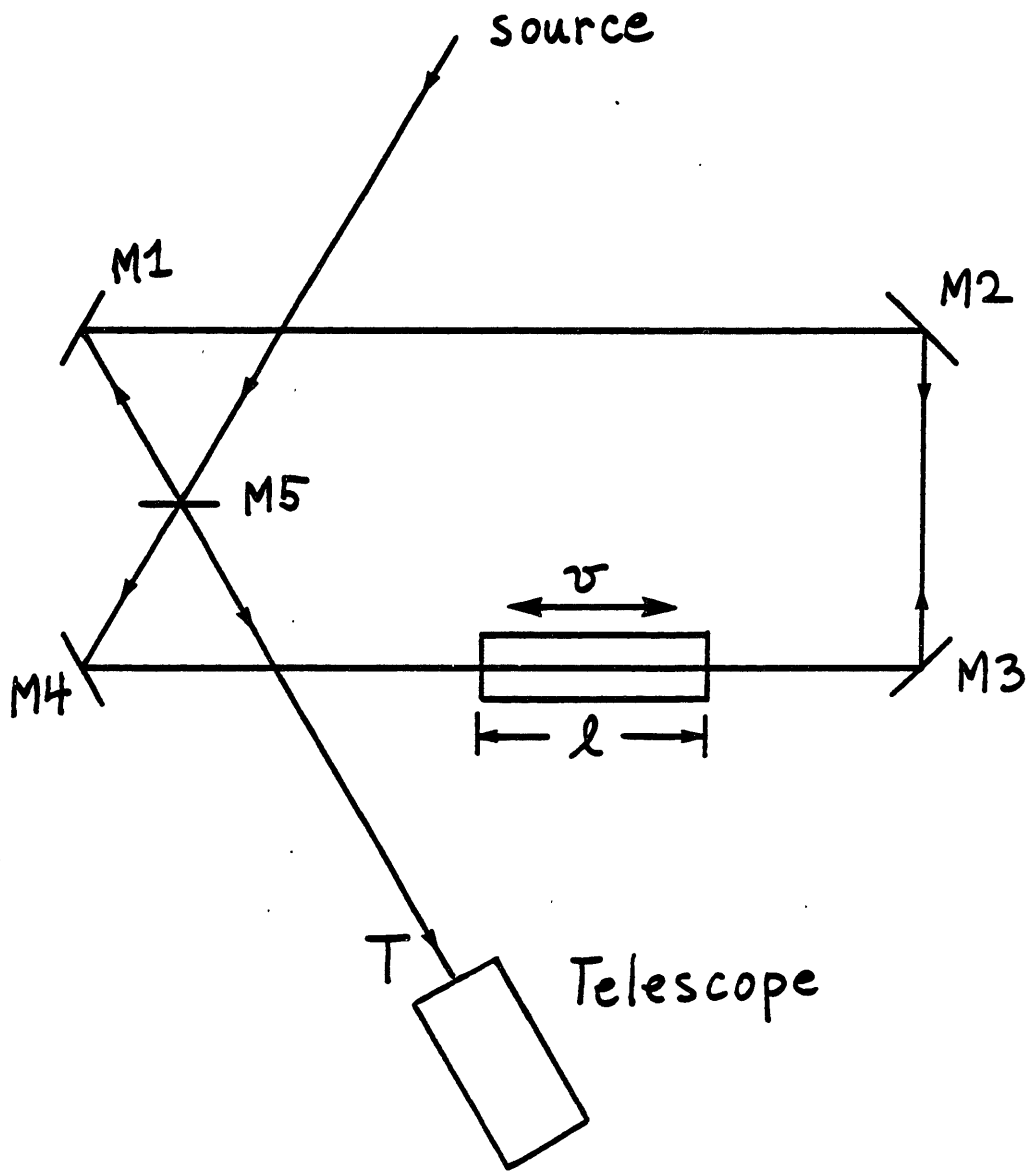


Figure 2.3

A light source, incident on a beam splitter, M_5 , was split into two beams, one encircling the cw path $M_5 M_1 M_2 M_3 M_4 M_5$ and the other encircling the ccw path $M_5 M_4 M_3 M_2 M_1 M_5$. The two beams were then interfered at the telescope where fringes were observed. A glass of length l , in one arm of the interferometer, is moved back and forth at velocity v parallel to the light propagation. When the rod reached its maximum speed a photograph of the fringe pattern was taken by means of an automatic shutter. The fringe shift was recorded both for when the rod was moving forward and for when it was moving backward.

Zeeman used an arc lamp as his light source, followed by a series of filters in order to select various wavelengths of nearly monochromatic light. He was particularly motivated to use monochromatic light because of the suggestion by H. Lorentz¹⁷ that an additional term should be included in the drag coefficient. Lorentz demonstrated that due to a doppler shift, the wavelength in the moving medium, for the case depicted in Figure 2.3, is given by

$$\lambda_m \approx \lambda_o + \Delta\lambda = \lambda_o + \lambda_o v/c \quad (2.8)$$

where λ_o is the vacuum wavelength observed at rest with respect to the source. Since the index of the medium is a function of λ , the index n , in equation 1 must be replaced by

$$n \rightarrow n(\lambda_o) + \Delta n = n(\lambda_o) + \Delta\lambda \frac{\partial n}{\partial \lambda} = n(\lambda_o) + \lambda_o \frac{v}{c} \frac{\partial n}{\partial \lambda} \quad (2.9)$$

where $\frac{\partial n}{\partial \lambda}$ is evaluated at $\lambda = \lambda_0$. Substituting into Eq. (2.7), the velocity of light in the moving medium, as observed in the lab frame, is given by

$$u' \approx \frac{c}{(n(\lambda_0) + \lambda_0 \frac{v}{c} \frac{\partial n}{\partial \lambda})} + v \left[1 - \frac{1}{(n(\lambda_0) + \lambda_0 \frac{v}{c} \frac{\partial n}{\partial \lambda})^2} \right] \quad (2.10)$$

Expanding this expression and neglecting higher order terms in v ,

$$u' \approx \frac{c}{n(\lambda_0)} + v \left[1 - \frac{1}{n^2(\lambda_0)} - \frac{\lambda_0}{n^2(\lambda_0)} \frac{\partial n}{\partial \lambda} \right] \quad (2.11)$$

Redefining $n \equiv n(\lambda_0)$ and $\alpha \equiv \alpha(\lambda_0)$,

$$u' \approx \frac{c}{n} + v\alpha \quad (2.12)$$

where

$$\alpha = 1 - \frac{1}{n^2} - \frac{\lambda_0}{n^2} \frac{\partial n}{\partial \lambda} \quad (2.13)$$

It must be noted that the extra dispersion term only would have changed the drag coefficient by ~2% in the original Fizeau Experiment and would have been very difficult to observe with white light.

2.4b. Analysis of Drag in "Shuttling Rod" Configuration

Because the "shuttling rod" configuration was also employed in this experiment, it is convenient here to discuss in greater detail the Fresnel drag as applied to this configuration.

There was a major difference, however, in the form of the fringe shift, predicted for the Zeeman experimental configuration than that used by Fizeau. In the Fizeau experiment, the boundaries of the moving water were stationary. In the "shuttling rod" configuration of Zeeman, the boundaries moved with the medium. The transit time through the medium was then increased or decreased for a beam travelling parallel or antiparallel to \vec{v} , respectively. To calculate the expected fringe shift for the parallel case, as shown in Figure 2.4, the time inside the medium t_m , as observed in the lab frame, is given by

$$t_m = \frac{l + vt_m}{u'} \quad (2.14)$$

solving for t_m and substituting the expression (Eq. (2.12)) for u' ,

$$t_m = \frac{l}{\frac{c}{n} + v(\alpha-1)} \approx \frac{ln}{c} \left[1 - \frac{nv}{c} (\alpha-1) \right] \quad (2.15)$$

However, the time spent in propagation through air is decreased by Δt_a for the case of parallel propagation (and increased by Δt_a for the antiparallel case) and must be subtracted from t_m :

$$\Delta t \approx \frac{vt_m}{c} \quad (2.16)$$

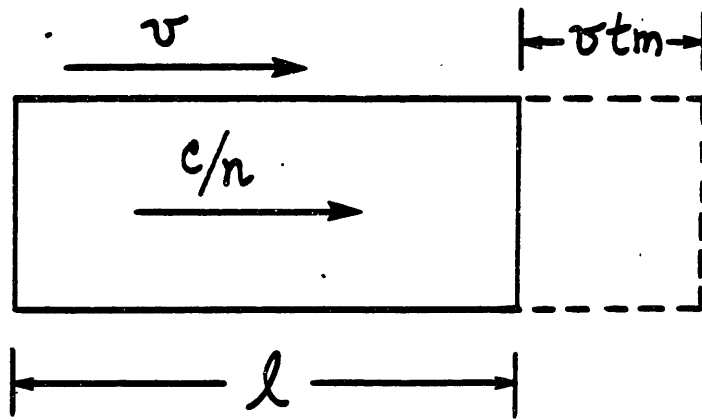


Figure 2.4

and

$$t_m - \Delta t_a \approx (1 - v/c) t_m \quad (2.17)$$

where the index of refraction of air has been neglected in Eq. (2.16).

Substituting from Eq. (2.15) for t_m and dropping $(v/c)^2$ terms gives,

$$t_m - \Delta t_a \approx \frac{\ell n}{c} \left[1 - \frac{vn}{c} (\alpha - 1 + 1/n) \right] \quad (2.18)$$

Likewise, for a beam propagating in the opposite direction,

$$t_m - \Delta t_a = \frac{\ell n}{c} \left[1 + \frac{vn}{c} (\alpha - 1 + 1/n) \right] \quad (2.19)$$

The time difference between the two interfered beams, Δt , in the "shuttling rod" configuration is thus obtained by subtracting Eq. (2.18) from Eq. (2.19),

$$\Delta t = \frac{2\ell n^2}{c} \left(\frac{v}{c} \right) [\alpha - 1 + 1/n] \quad (2.20)$$

The fringe shift ΔW is obtained by multiplying by c/λ_o , giving

$$\Delta W = \frac{2\ell n^2}{\lambda_o} \left(\frac{v}{c} \right) [\alpha - 1 + 1/n] \quad (2.21)$$

Substituting for α we get,

$$\Delta W = \frac{2\ell}{\lambda_0} \left(\frac{v}{c} \right) \left(n - 1 - \lambda_0 \frac{\partial n}{\partial \lambda} \right) \quad (2.22)$$

By connecting several glass pieces together, the total length of the glass rods in the Zeeman experiments were approximately 100 cm. The various measurements for $v \approx 1000$ cm/s are compared to the theoretical values in Table I, where ΔW_1 and ΔW_2 were the fringe shifts obtained by

Table I
Zeeman's Results

<u>Material</u>	<u>λ</u>	<u>ΔW_1</u>	<u>ΔW_{th}</u>	<u>ΔW_2</u>
quartz	4750	.156 ± .007	.166	.156 ± .008
quartz	5380	.148 ± .006	.143	.148 ± .012
quartz	6510	.125 ± .007	.115	.123 ± .014
flint	4750 ± 25 ^o A	.242 ± .004	.242 ± .003*	.243 ± .006

using two separate averaging techniques.¹⁶ ΔW_{th} was the expected fringe shift. Because he made experimental improvements in the flint glass experiment, Zeeman considered this his best measurement. Here, the contribution from the dispersion term was approximately .028 fringes. From this, and the error bars in Table I, the confidence in the inclusion of the dispersion term was about 1 part in 5 or 6. Zeeman's work was regarded by many as having established the validity of the dispersion term in the drag coefficient.¹⁸

2.5. Ring Laser Experiments

Until the development of the ring laser in the 1960's, there were few significant attempts to measure the Fresnel-drag. Because of its increased sensitivity over simple interferometric methods (see Chapter 3), the ring laser was employed by a number of researchers including Macek et al,¹⁹ Massey and Siegman,²⁰ and Bilger and coworkers.^{13,21} The most precise determination of the drag coefficient was reported by Bilger and Zavodny¹³ and later by Bilger and Stowell.²¹ In the first of these experiments, they attempted to study the drag in nitrogen gas.¹³ Since the gas flow could not be determined to better than 1%, they decided that an accurate measurement was not feasible. Bilger and Zavodny then used the arrangement shown in Figure 2.5 to measure the drag in a rotating disc of fused silica. Here, the cavity of the triangular ring laser is formed by mirrors M_1 , M_2 and M_3 . The laser supports the oppositely directed beams oscillating at frequencies of f_{cw} and f_{ccw} . The beams are interfered at the laser output (M_3) and the beat frequency, as shown in Section 3.3, is given by

$$\Delta f = -f \frac{\Delta L}{L} \quad (2.23)$$

where ΔL is the difference in optical path length for clockwise propagation versus counter-clockwise propagation. In the arrangement used by Bilger, a fused silica disk was inserted in the cavity at Brewsters angle to avoid reflection losses in the laser amplifier. By means of a motor and a drive belt the disc was rotated at angular speed ω . In

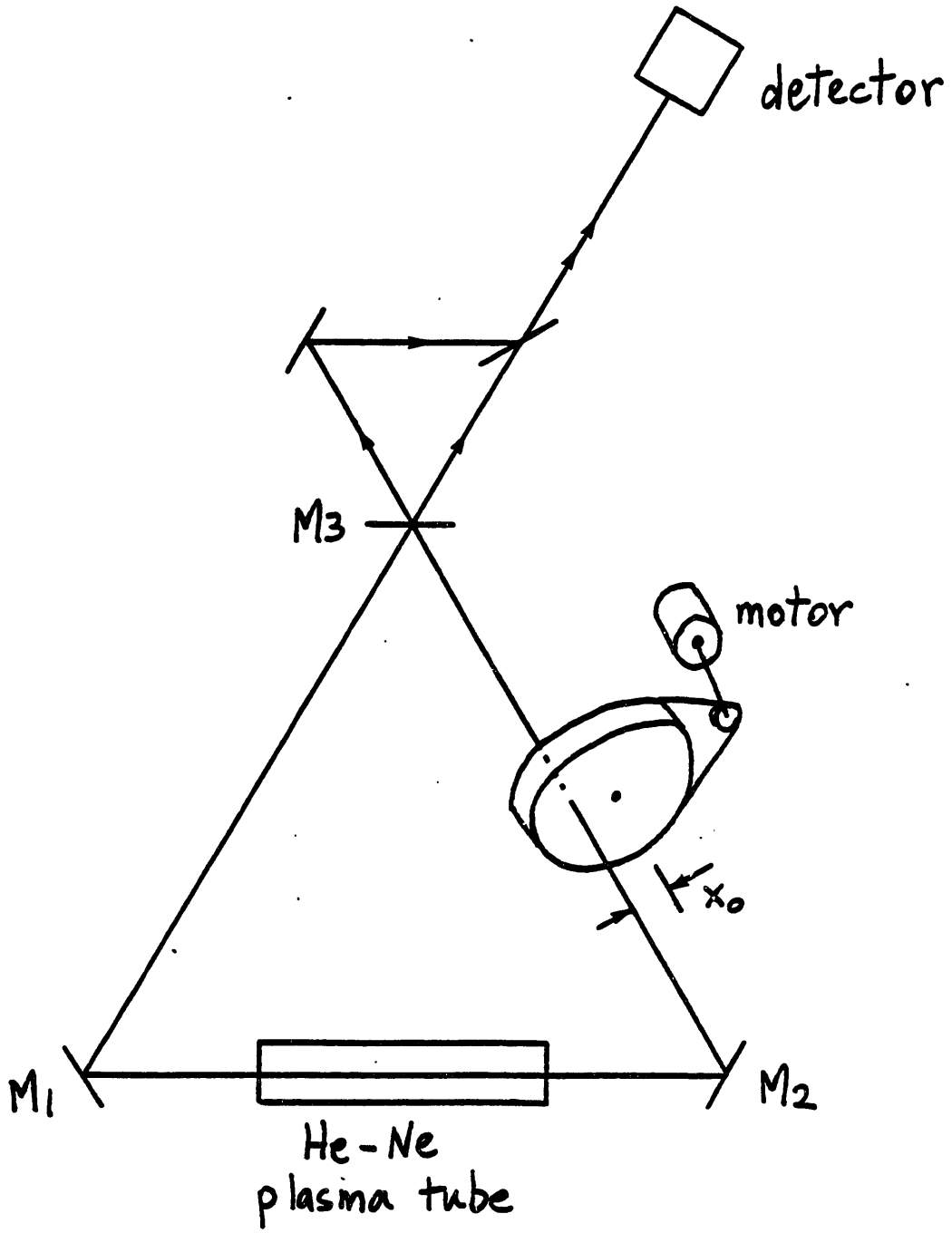


Figure 2.5

order to have a velocity component v_m in the direction of the light, the rotation axis was displaced from the beam by a distance x_o . The geometry in the case of drag in a rotating disc is treated in Bilger's paper,¹³ with the result that

$$\Delta L = \frac{2n^2 \ell v_m}{c} \alpha \quad (2.24)$$

Here, v_m is the medium velocity along the direction of refracted light given by,

$$v_m = \omega dx_o / n \ell \quad (2.25)$$

where ℓ is the light path length inside the glass and d is the disc thickness. The observed beat frequency is then given by,¹³

$$\Delta f = \frac{2n^2 \alpha \ell v_m}{\lambda L} \quad (2.26)$$

Bilger and Zavodny measured Δf in a range of values from 1 to 50 KHz, corresponding to rotation rates of 100 to 2500 rpm. They used a single disc thickness of approximately 1.3 cm throughout their measurements, and they used four different displacements x_o , ranging from .5 cm to 2 cm. The perimeter of the ring was approximately 3 m. By plotting Δf vs. ω , they were able to account for the offset at $\omega = 0$ caused the Sagnac Effect due to the earth's rotation (here about 43 Hz). In addition, the range for ω was selected to be sufficiently high such

that Δf was not influenced by the "Lockin-In"²² effect in the ring laser. By measuring the slope of Δf vs. ω , they obtained α from Eq. (2.13),

$$\alpha = .541 \pm .003 \quad (2.27)$$

as compared to the theoretical value of

$$\alpha_{th} = .5423 \quad (2.28)$$

The agreement with theory was thus given by

$$\frac{\alpha - \alpha_{th}}{\alpha_{th}} = -.003 \pm .005 \quad (2.29)$$

The major contribution to the error, reported by Bilger and Zavodny, was due to the difficulty in measuring the displacement of the beam from the rotation axis, x_0 . This depends on precise knowledge of the spot size of the Gaussian beam at the drag site. The agreement with theory for the inclusion of the dispersion term was

$$\frac{\left. \frac{\lambda}{n} \frac{\partial n}{\partial \lambda} - \frac{\lambda}{n} \frac{\partial n}{\partial \lambda} \right|_{theory}}{\left. \frac{\lambda}{n} \frac{\partial n}{\partial \lambda} \right|_{theory}} = .87 \pm .22 \quad (2.30)$$

While there was no significant quantitative improvement in the measurement of α (or its dispersion term) over Zeeman's flint glass measurement. Bilger and Zavodny demonstrated the potential for using a ring laser for precise studies of the drag effect. A second and more carefully optimized attempt, using the same arrangement, was made by Bilger and Stowell²¹ in 1977. Varying ω and x_0 over a range comparable to the earlier experiment, they reported a result

$$\alpha = 0.5424 \pm 0.0002 \quad (2.31)$$

where the error bar included one standard deviation of their measurements and all known error sources. The theoretical value was

$$\alpha_{th} = .5418 \quad (2.32)$$

giving an agreement with theory of

$$\frac{\alpha - \alpha_{th}}{\alpha_{th}} = .0011 \pm .0004 \quad (2.33)$$

While the theoretical value actually fell almost three standard deviations outside their stated error bars, Bilger and Stowell remarked that the disagreement was too small to claim a serious discrepancy with theory. Using the results for α and propagating the error bars into the dispersion term gives a similar comparison with theory,

$$\frac{\left. \frac{\lambda}{n} \frac{\partial n}{\partial \lambda} - \frac{\lambda}{n} \frac{\partial n}{\partial \lambda} \right|_{th}}{\left. \frac{\lambda}{n} \frac{\partial n}{\partial \lambda} \right|_{th}} = .048 \pm .012 \quad (2.34)$$

CHAPTER 3

TECHNIQUES FOR DRAG MEASUREMENT

3.1. Introduction

There are a few modern techniques that are both convenient and have the sensitivity required to measure light drag in a moving medium. Among these methods are the interferometer, the ring laser and the passive ring cavity technique. The first two of these methods were briefly discussed in Chapter 2 in conjunction with previous drag measurements. All of these techniques rely on differential sensing, using two counter propagating beams such that the absolute or reciprocal pathlengths subtract, thus measuring only the non-reciprocal pathlength. For instance, in the ring laser experiment of Bilger^{13,21} the extra pathlength of the light is $\approx 5 \times 10^{-11}$ m, which would be very difficult to observe in an arrangement where only one beam was sensitive to this pathlength change.

In this chapter, the concepts of these techniques are briefly discussed, with greater emphasis on the passive resonator technique because of its relevance to this research. In addition, a brief comparison of these methods and their applicability to the Fresnel-drag measurement is also included in this chapter.

3.2. Interferometric Technique

As was demonstrated by Fizeau and Zeeman, an interferometer may be used as a sensor for non-reciprocal phase shifts and may be conveniently applied to Fresnel-drag measurements. As its basic principle, the interferometer employs two beam interference and for every non-reciprocal pathlength shift of λ , one fringe is observed as is shown in Figure 3.1. In the earlier experiments mentioned previously, the fringe shifts were measured by eye. With modern modulation techniques and the advantage of the monochromaticity of lasers, it is possible to measure fringe shifts of 10^{-6} to 10^{-7} fringes and below.

3.3. Ring Laser Technique

Another sensor of non-reciprocal phase shift that may be employed for Fresnel drag measurements is the ring laser. This was demonstrated by the researchers referenced in Chapter 2. In principle, the ring laser supports two oppositely directed traveling wave laser oscillations.⁵ If the optical pathlength of the ring is P , the oscillation condition necessary for constructive multiple beam interference is given by,

$$P = q\lambda \quad (q \text{ is an integer}) \quad (3.1)$$

Thus, the oscillation frequency is given by,

$$f = q c/P \quad (3.2)$$

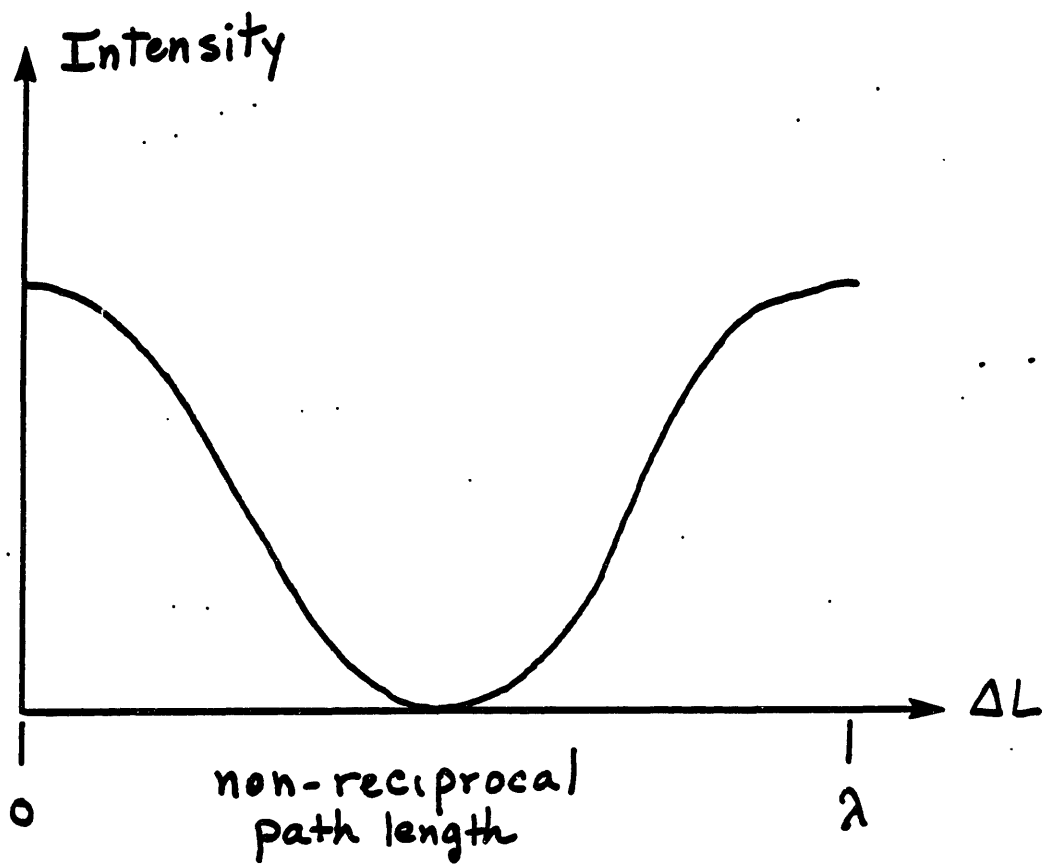


Figure 3.1

In the presence of a non-reciprocal phase shift the clockwise (cw) and counter-clockwise (ccw) optical pathlengths are different, thus resulting in different oscillation frequencies. Hence, for the same axial mode q ,

$$f_{cw} = q c/P_{cw} \quad \text{and} \quad f_{ccw} = q c/P_{ccw} \quad (3.3)$$

Denoting the pathlength common to both beams as P and the difference as $\Delta P = P_{cw} - P_{ccw}$ ($\ll P$),

$$\Delta f \equiv f_{cw} - f_{ccw} \approx -f \Delta P/P \quad (3.4)$$

where f is the frequency component common in both beams. For a given P , the oscillation frequency splitting is depicted in Figure 3.2. Any fluctuations in P are reciprocal to both beams, thus preserving Δf provided that the fluctuations in P are sufficiently small to ignore changes in the scale factor of Eq. (3.4). The frequency difference Δf is easily obtained by beating f_{cw} and f_{ccw} at the ring laser output as shown in Figure 2.5. (The application of this technique to measurements of Fresnel-drag is discussed in Section 2.5.)

In practice, because of laser amplifier coupling induced by backscattering from one beam into the other, the oscillation frequencies are not independent for very small Δf ($\lesssim 1$ KHz) and tend to lock

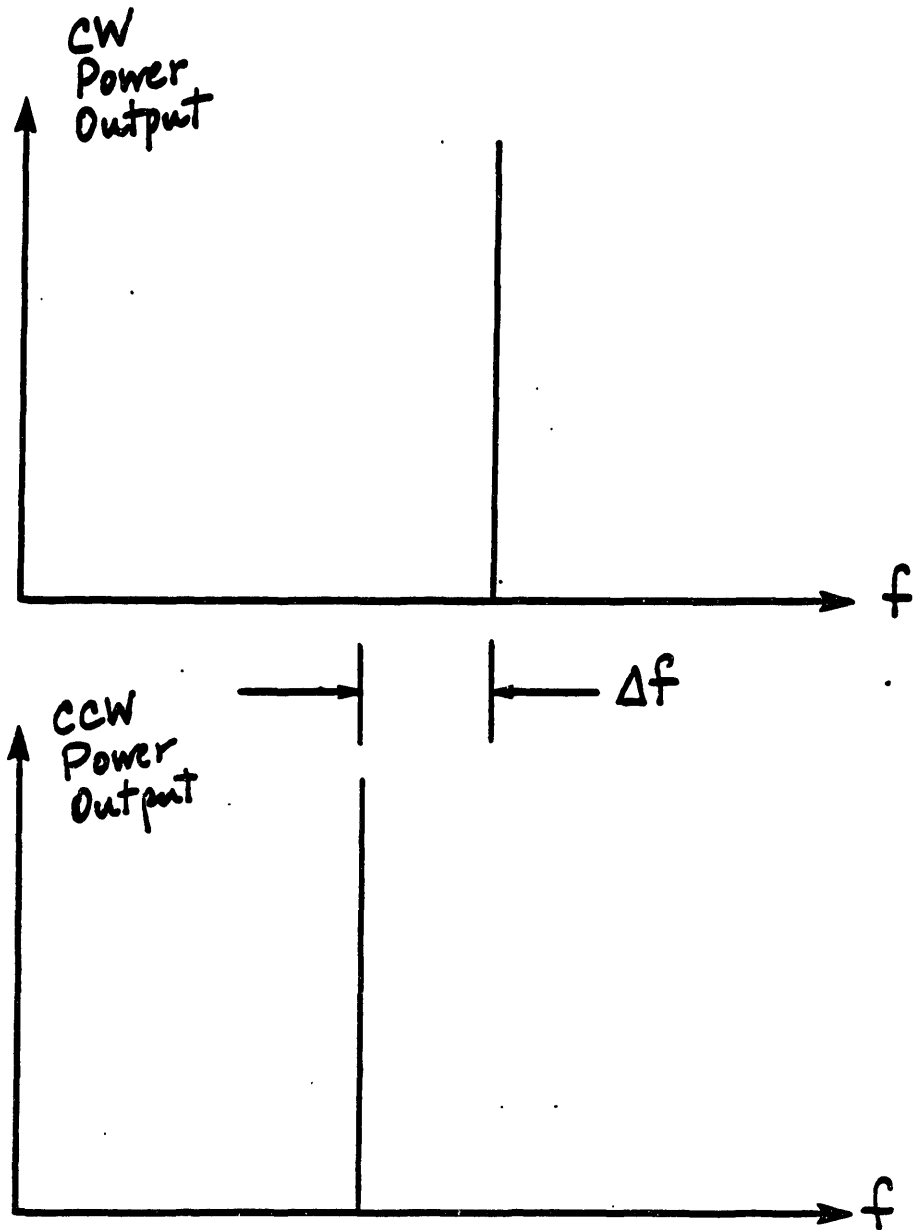


Figure 3.2

together. This effect, called the "Lockin effect"²² causes a dead zone near $\Delta f = 0$, as shown by the solid line in Figure 3.3. The dotted line represents the functional dependence from Eq. (3.4), for a change in optical pathlength ΔP due to rotation or Fresnel-drag.

3.4. Passive Ring Resonator Technique

The passive ring resonator technique⁹ for measuring non-reciprocal phase shift was, in part, motivated by efforts to eliminate the problems encountered in the ring laser sensor; particularly those problems caused by the presence of the gain medium located inside the ring cavity such as the "Lockin effect" (see Section 3.3). In the passive resonator technique, the laser is mounted external to the ring cavity, as shown in Figure 3.4. A laser light source at f_{cw} measures the cw resonance frequency of the cavity and a source at f_{ccw} measures the ccw resonance of the cavity. In practice, it is desirable to derive both f_{cw} and f_{ccw} from the same laser source as discussed in Section 4.3. Because the resonance frequencies f_{cw} and f_{ccw} , of the cavity are determined by the corresponding optical lengths of the cavity, P_{cw} and P_{ccw} , any non-reciprocal phase shifts in the cavity are related to the difference $f_{cw} - f_{ccw}$. In this way, placement of a moving medium inside the cavity provides for a measurement of the Fresnel drag.

The resonance frequencies and lineshapes of the ring cavity are given by the criteria necessary for constructive multiple beam interference, similar to the condition for the case of a two mirror Fabry-Perot etalon. A brief, simplified treatment of the resonance condition, observed in transmission, is presented here. More

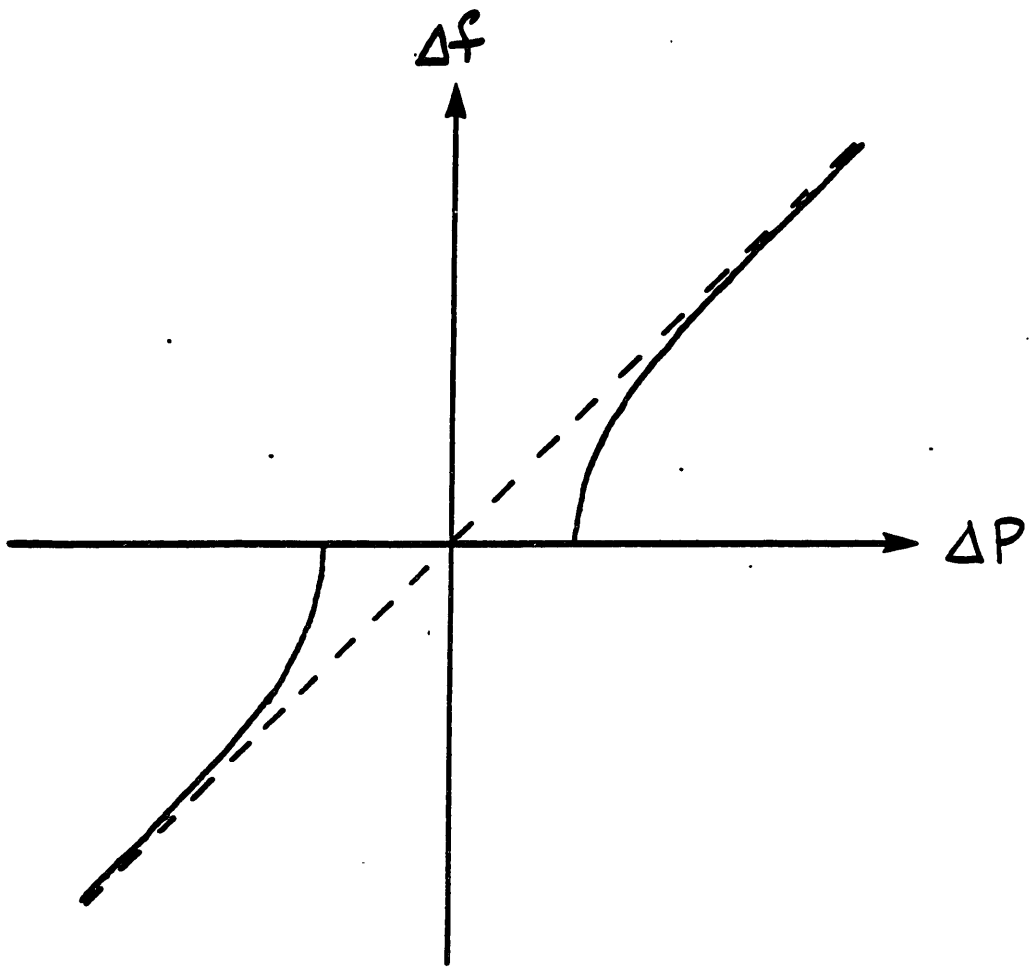


Figure 3.3

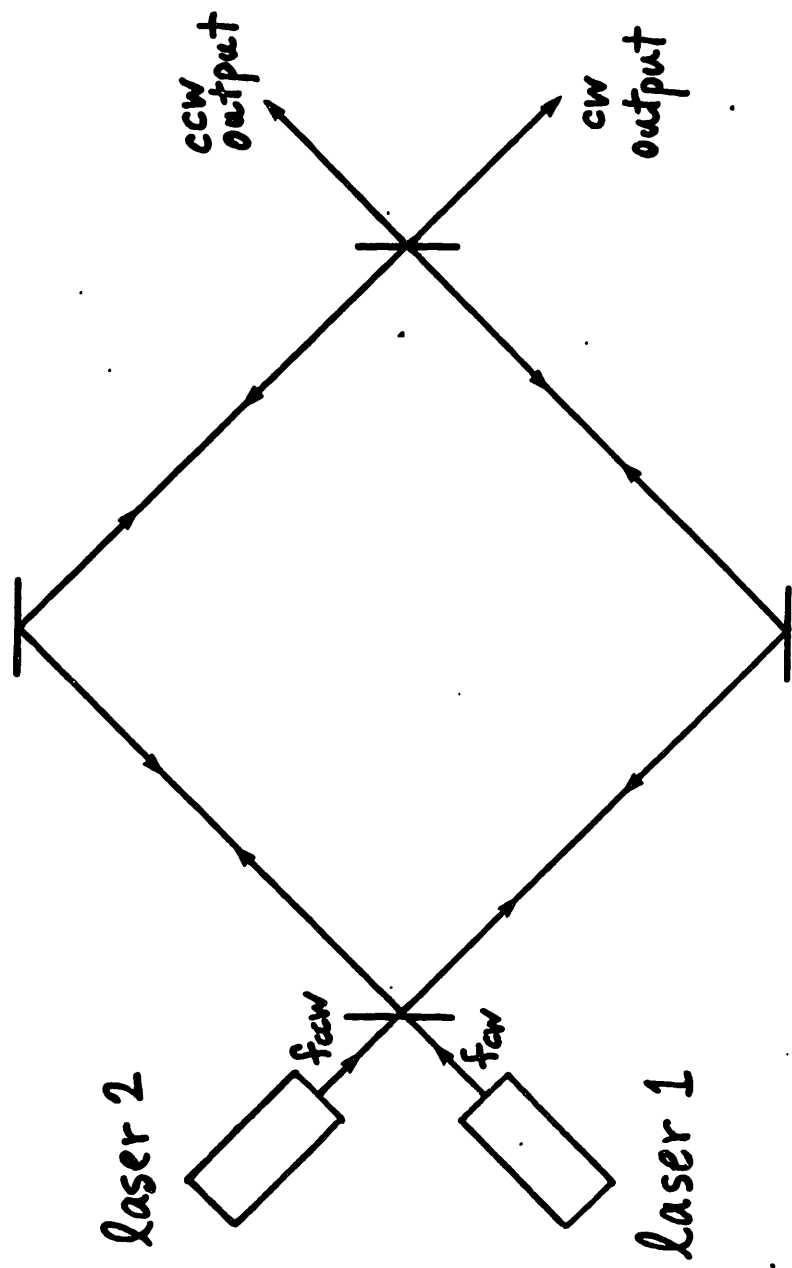


Figure 3.4

detailed treatments may be found elsewhere.²⁴ Suppose an input field of amplitude E_i is incident on the ring cavity, formed by mirrors M_1 , M_2 , M_3 and M_4 , as shown in Figure 3.5. Here, for simplicity, a square cavity of perimeter P is assumed and that the complex electric field transmission and reflection coefficients for each mirror (assumed to be lossless) are given by,

$$\begin{aligned}
 t_1, r_1 & \quad \text{for } M_1 \\
 t_2, r_2 & \quad \text{for } M_2 \\
 t_3 = 0, r_3 = 1 & \quad \text{for } M_3 \\
 t_4 = 0, r_4 = 1 & \quad \text{for } M_4
 \end{aligned} \tag{3.5}$$

The field E_i is split at M_1 into the reflected field E_{r_1} and $t_1 E_i$ which propagates cw in the cavity. At M_2 the transmitted component E_{T_1} is $t_1 t_2 E_i$ and the reflected component $E_i t_1 r_2$, propagates around the cavity and is partially reflected at M_1 , and so on. Hence, for a continuous input source, E_i , the fields reflected from the cavity, inside the cavity, and transmitted through the cavity are superpositions of multiple traveling waves. The round-trip phase shift inside the cavity is given by

$$\delta = Kz = \frac{2\pi}{\lambda} P \tag{3.6}$$

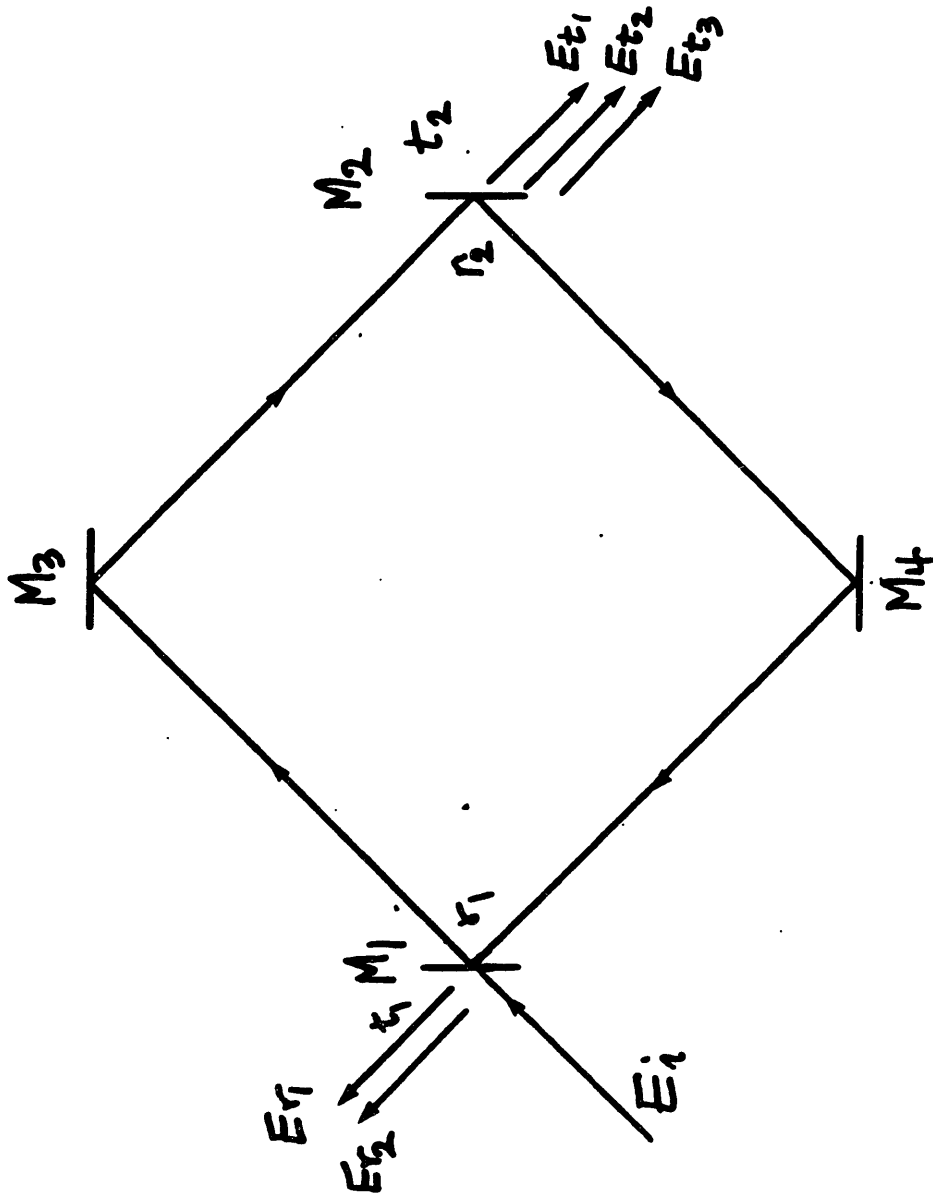


Figure 3.5

and hence the transmitted field is given by

$$\begin{aligned}
 E_T &= E_1 + E_2 + E_3 \dots \\
 &= E_1 e^{i\delta/2} t_1 t_2 (1 + r_1 r_2 e^{i\delta} + r_1^2 r_2^2 e^{2i\delta} + \dots) \quad (3.7)
 \end{aligned}$$

Summing the geometric series in Eq. (3.7),

$$E_T = E_i e^{i\delta/2} \frac{t_1 t_2}{1 - r_1 r_2 e^{i\delta}} \quad (3.8)$$

Assuming a configuration where $r_1 = r_2 \equiv r$, $t_1 = t_2 \equiv t$ the transmitted intensity I_T is given by

$$I_T = E_T E_T^* = \frac{I_i T^2}{(1 - r^2 e^{i\delta})(1 - r^2 e^{i\delta})^*} \quad (3.9)$$

where $tt^* = T$. Setting $rr^* = R$, $T = 1 - R$, and simplifying,

$$\frac{I_T}{I_i} = \frac{(1 - R)^2}{(1 - R)^2 + 4R \sin^2 \delta/2} \quad (3.10)$$

The transmitted intensity is maximized by setting $\sin^2 \delta/2 = 0$ giving the resonance condition,

$$P = q\lambda \quad q = \text{integer} \quad (3.11)$$

Thus, the resonance frequencies of the cavity are given by

$$f = q c/P \quad q = \text{integer} \quad (3.12)$$

For a given q , or longitudinal mode of the cavity, it can be shown that for a change in frequency of $\Delta f_{1/2}$ results in half the output transmission intensity, where

$$\Delta f_{1/2} = \frac{c}{2P} \frac{1 - R}{\pi\sqrt{R}} \quad (3.13)$$

The full resonance width at half power, defined as Γ , is given by

$$\Gamma = 2\Delta f_{1/2} = \frac{c}{P} \frac{1 - R}{\pi\sqrt{R}} \quad (3.14)$$

$$= \frac{c}{P} \frac{1}{F} \quad (3.15)$$

where F is the finesse of the cavity. For a given input frequency, the output intensity versus the perimeter is shown for one free spectral range ($\Delta q = 1$, $\Delta P = \lambda$) in Figure 3.6.

In the presence of a non-reciprocal phase shift, the effective optical pathlengths of the cw beam and ccw beams are unequal and so are the corresponding resonance frequencies, given by

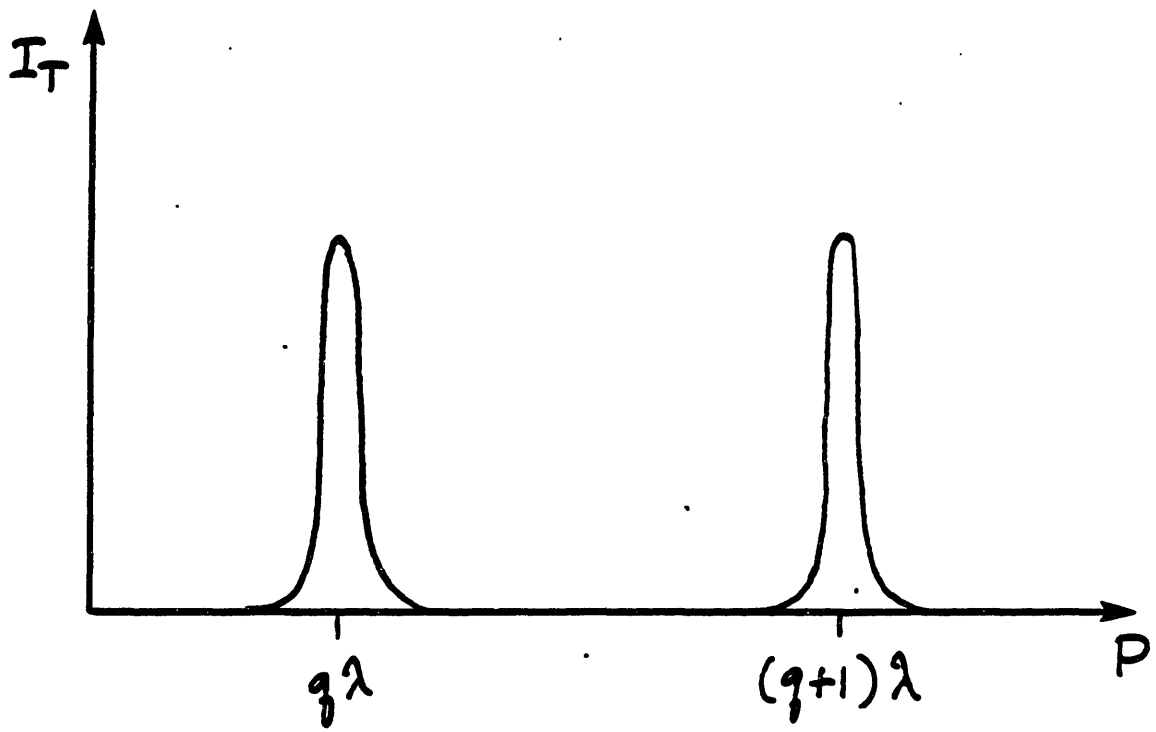


Figure 3.6

$$f_{cw} = q \frac{c}{P_{cw}} \quad (3.16)$$

$$f_{ccw} = q \frac{c}{P_{ccw}} \quad (3.17)$$

An illustration of this case is shown in Figure 3.7, where the output intensity is plotted as a function of input frequency for both beams. Using the same definitions as in the last section, the frequency difference is related to the difference in optical pathlength, ΔP , by

$$\Delta f = -f \left(\frac{\Delta P}{P} \right) \quad (3.18)$$

As in the ring laser case, since the perimeter P is reciprocal to both beams Δf is insensitive to changes in P provided changes in the scale factor are sufficiently small.

3.5. Comparison of Sensing Techniques For Fresnel-Drag Measurement

Each of the previously mentioned techniques have certain advantages when applied to sensing non-reciprocal phase shifts, and in this case, the Fresnel-drag. As a rule of thumb, however, the techniques employing multiple beam interference are inherently more sensitive than those employing two beam interference. For instance, with a finesse of F the output intensity of the passive cavity is halved by a change of $|\Delta P| = \lambda/2F$, whereas a pathlength change $|\Delta P| = \lambda/4$ is required for the corresponding intensity change in the

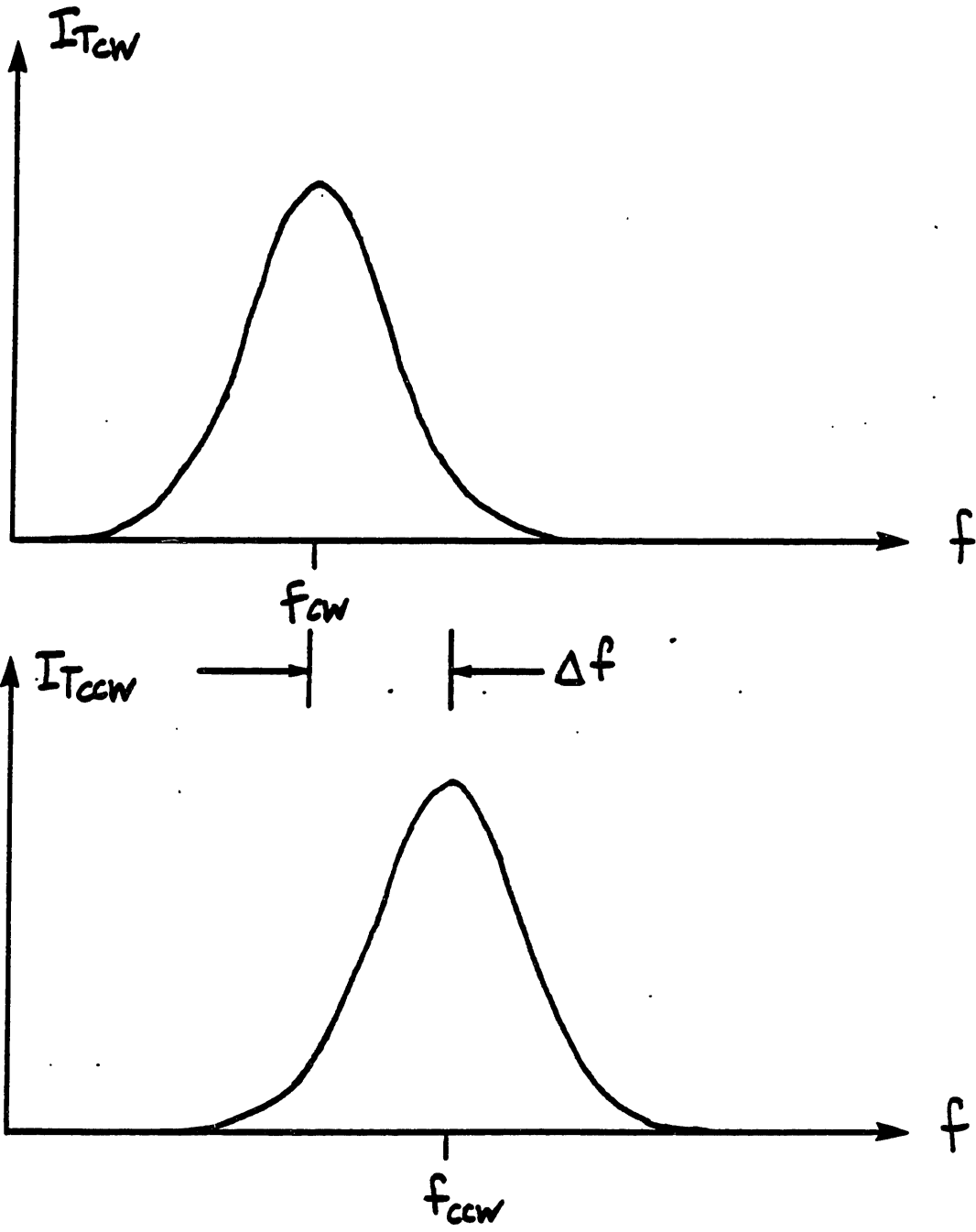


Figure 3.7

interferometer. With high reflectivity mirrors, $F > 100$ may easily be achieved.

For the two multiple beam interference techniques, the ring laser and the passive ring resonator, the fundamental measurement sensitivity to a non-reciprocal phase shift is nearly identical for setups of equal light intensity, perimeter and mirror reflectivity.^{4,25} This fundamental limit is discussed for the passive ring resonator technique in Chapter 4. In practice, the measurement of the resonance frequency splitting Δf due to a non-reciprocal phase shift is conveniently done automatically in the ring laser case, resulting in the output beat frequency. In the passive cavity technique, however, Δf has to be measured by external means.

The passive resonator technique used in this experiment, already existed in the laboratory and was being studied for its applications as a rotation sensor. Certainly we hoped to benefit from these advantages pertinent to rotation sensing for which the passive resonator technique was originally being developed as an alternative to the ring laser. For instance, in order to distinguish between the Fresnel-drag and other sources of non-reciprocal phase shift, it was desirable to apply a sinusoidal velocity to the medium and use AC detection techniques. In the ring laser case, that would require a stable bias source in order to bias Δf out of the "Lock in" region and thus avoid modulating Δf through this region. This was not necessary using the passive technique. In summary, we were able to benefit from these advantages of the passive technique, but the setup was not greatly modified or optimized

for the Fresnel-drag measurements.

CHAPTER 4

PASSIVE RING RESONATOR TECHNIQUE

4.1. Introduction

In this chapter, a brief conceptual treatment is presented of how the passive ring resonator may be applied to measurement of non-reciprocal phase shifts, such as those due to Fresnel-drag and the Sagnac effect. This is followed by an introduction to the technique for measuring the cavity resonance frequencies, and then by a description of the passive ring resonator setup. A discussion of the fundamental measurement limits is included and compared to the observed performance of the system. The chapter concludes with a discussion of the sources of error and drift pertinent to the passive ring resonator technique.

4.2. Application of the Passive Ring Resonator Technique to Inertial Rotation Sensing and Fresnel Drag Measurement

As discussed in Chapter 3, the basic method for measuring non-reciprocal phase shifts using the passive ring resonator technique, is to detect the difference between cw and ccw cavity resonance frequencies resulting from the non-reciprocal phase shift. This frequency shift is then related to the difference in optical pathlengths of the cavity by Eq. (3.18). Two of the important non-reciprocal phase shifts to

which this measurement technique may be applied are those caused by inertial rotation and by the Fresnel-drag in a moving medium.

As in all optical inertial rotation sensors, the passive ring technique is based on the Sagnac Effect. This effect relates the optical pathlength difference for two beams, counter-propagating around a closed path, to the inertial rotation rate of the closed path. Consider two beams constrained to travel around a closed path of area \vec{A} as shown in Figure 4.1. If the closed path is rotating at angular velocity $\vec{\Omega}$ relative to an inertial frame of reference, then the pathlength difference between the two beams after completion of the optical circuit² is given by,

$$\Delta P = P_{\text{cw}} - P_{\text{ccw}} = \frac{4\vec{\Omega} \cdot \vec{A}}{c} \quad (4.1)$$

where c is the free-space speed of light.

The passive ring resonator technique may be employed as a rotation sensor, where the ring cavity of area \vec{A} and optical perimeter P is employed as the light path, as shown in Fig. 4.2. Using Eqs. (3.18) and (4.1), the rotation rate $\vec{\Omega}$ results in a difference in cavity resonance frequencies given by

$$\Delta f = \frac{-4\vec{A} \cdot \vec{\Omega}}{\lambda_0 P} \quad (4.2)$$

where λ_0 is the free-space wavelength of the light utilized. As an illustration, for the 0.7 m square cavity used in this research and $\lambda_0 = 0.6328 \mu\text{m}$, the earth's rotation rate results in $\Delta f \approx 53 \text{ Hz}$ at this

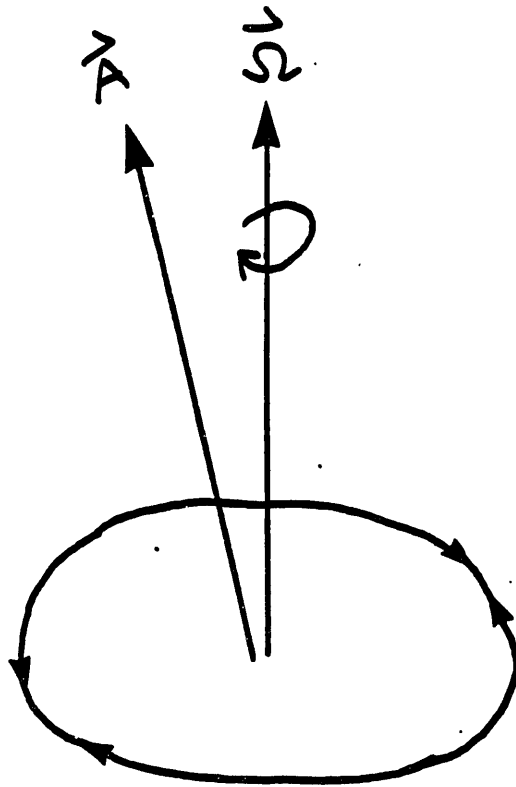


Figure 4.1

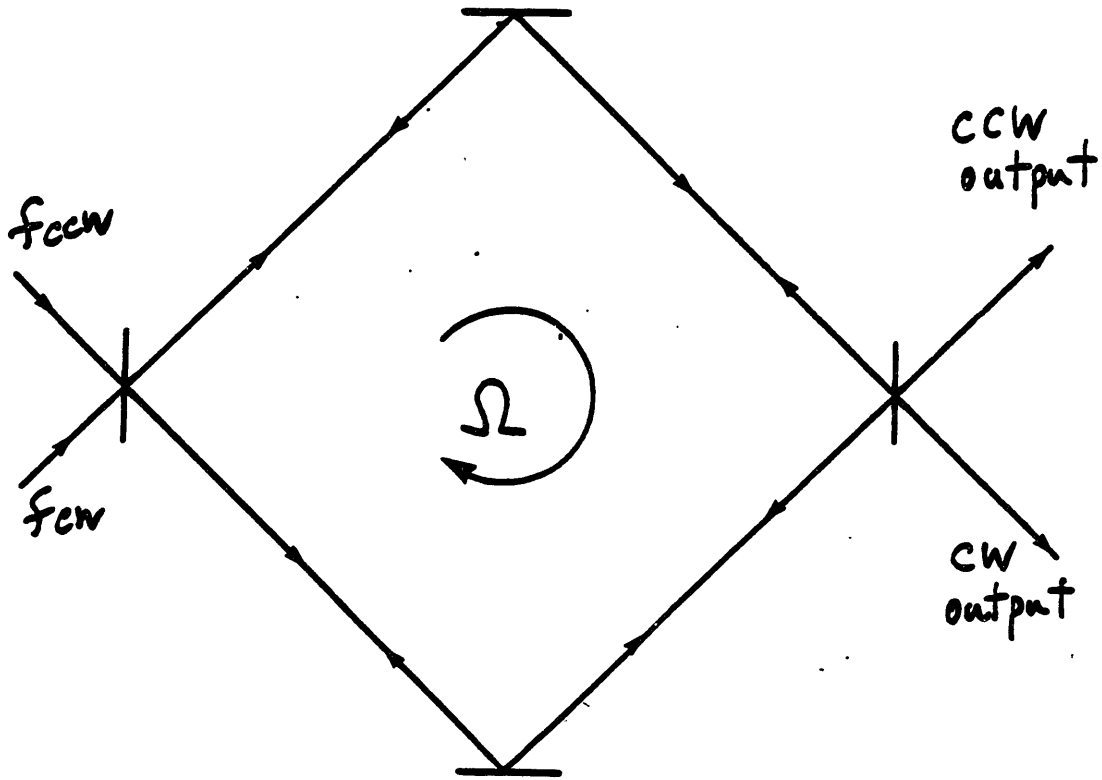


Figure 4.2

latitude. This corresponds to an optical pathlength difference of $\Delta P \approx 3 \times 10^{-13}$ m.

In contrast to passive ring technique as a rotation sensor in which an evacuated cavity may be used, the measurement of Fresnel drag requires the placement of a medium inside the cavity as shown in Figure 4.3. As motion is applied to the medium the drag produces a difference, ΔP , between the cw and ccw optical pathlengths of the cavity. This difference in pathlengths is then observed as a resonance frequency shift given by Eq. (3.18).

In this experiment, there were two primary considerations associated with a precision measurement of the Fresnel drag. The first of these considerations simply involved the choice of a medium. Since it is difficult to accurately measure the velocity of fluid flow, as was the problem mentioned in many of the previous measurements,¹³ a moving solid was desirable. The second consideration, mentioned in Chapter 3, was whether to move the medium with a constant velocity and thus detect a constant output frequency shift, or to apply a sinusoidal velocity and use an AC detection scheme for measuring the output frequency difference. Modulating the drag effect provided a means for distinguishing this effect from all the other possible sources of non-reciprocal phase shift. These other sources of error, as discussed in Section 4.6, generally affect the DC output and the DC stability of the sensor system. Hence, since it was considered very feasible to move a solid with a well known sinusoidal velocity, we decided to use this technique in our experiment, which was essentially an AC form of

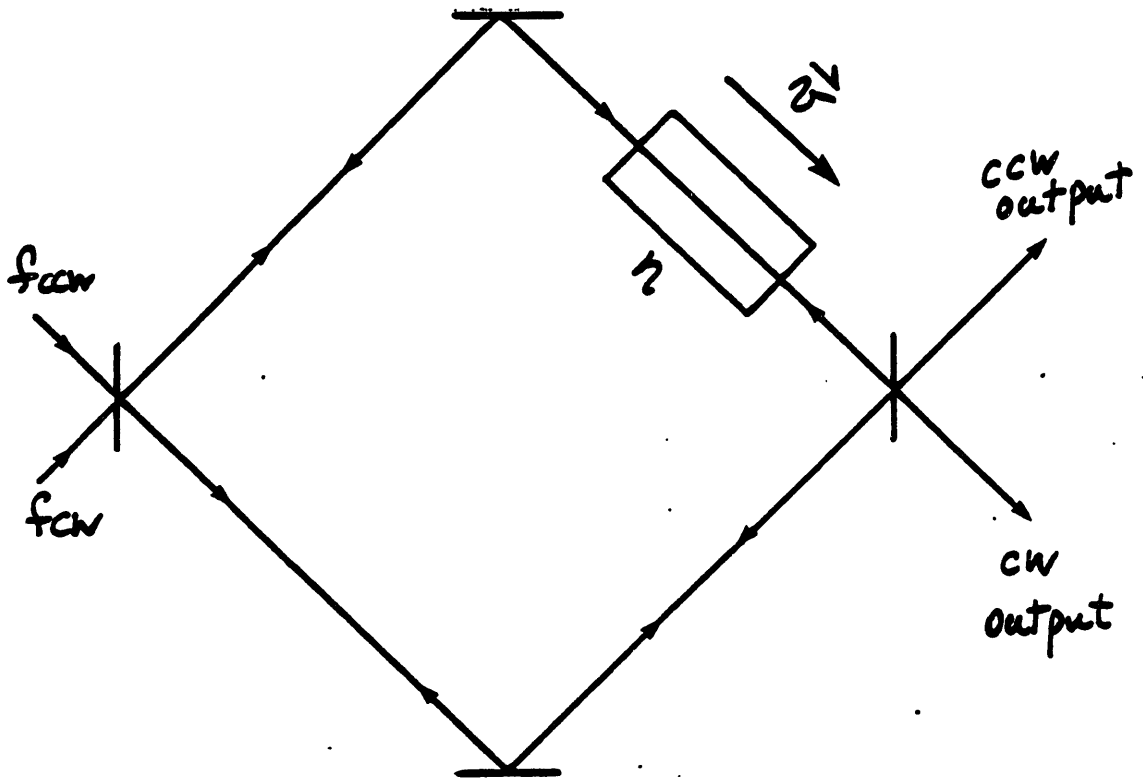


Figure 5.3

Zeeman's "shuttling rod" experiment. Thus, for glass at normal incidence the non-reciprocal pathlength ΔP is given by the product of λ_0 and the fringe shift ΔW obtained for the Zeeman experiment in equation (2.22). Combining this with Eq. (3.18) gives

$$\Delta f = - \frac{2\ell}{\lambda_0} \frac{v}{P} \left(n - 1 - \lambda_0 \frac{\partial n}{\partial \lambda} \right) \quad (4.3)$$

The "shuttling rods" used in this experiment were glass windows.

As an illustration, for a window of index $n \approx 1.5$ and length $\ell \approx 6$ mm, a peak to peak velocity of $v_{pp} \approx 25$ cm/sec results in a peak to peak pathlength difference of $\Delta P_{pp} \approx 6 \times 10^{-12}$ m. For the cavity used in this experiment, the resultant frequency splitting was $\Delta f_{pp} \approx 1$ KHz. The details of producing and measuring the velocity, as well as detection and measurement of the drag are presented in Chapter 5.

4.3. Technique Employed for Measurement of Cavity Resonance Frequencies

As discussed in Chapter 2, the passive resonator method consists of measuring and comparing the cw and ccw resonance frequencies of the cavity. As was also previously mentioned, the measurement of the cavity resonance frequencies requires two light sources at frequencies f_{cw} and f_{ccw} . If f_{cw} and f_{ccw} are generated by two separate laser sources, however, the measurement of $\Delta f = f_{ccw} - f_{cw}$ will be dependent on the relative frequency fluctuations between the two lasers. To measure Δf to better than $\sim 10^{-2}$ Hz, as many applications require, the relative

frequency between the two laser sources would have to be stabilized to that accuracy. Because of the difficulty in achieving this relative stability at optical frequencies it is necessary to derive f_{cw} and f_{ccw} from a common laser source.

In this arrangement, as shown in Figure 4.4, a common laser at f_0 is split into two beams, each of which is frequency shifted by an acousto-optic modulator (A/O). The cw beam is shifted to $f_0 + f_1$ prior to entering the cavity. The cavity length is then adjusted (represented by the switch in the open position), via a mirror mounted on a piezoelectric transducer (PZT), such that the cw cavity resonance frequency is $f_0 + f_1$. In practice, because of laser frequency and cavity length fluctuations, the cw resonance frequency must be stabilized (represented by the switch in the closed position), via servo electronics to $f_0 + f_1$. The frequency of the ccw beam, $f_0 + f_2$, is then adjusted via a voltage controlled oscillator (VCO), to be equal to the ccw cavity resonance frequency, as shown in Figure 4.5. In the case where the oscillator at f_2 is jittering or drifting with respect to f_1 , it is necessary to employ a second feedback loop (represented by the closed position of the switch to the VCO), to stabilize $f_0 + f_2$ to the ccw cavity resonance. In the absence of any non-reciprocal phase shifts the two cavity resonance frequencies are, in principle, equal and f_{ccw} is adjusted such that $f_0 + f_2 = f_0 + f_1$. In the presence of a non-reciprocal phase shift, $\Delta f = f_{cw} - f_{ccw} = f_1 - f_2$ is measured and then related to the difference in optical pathlengths of the cavity

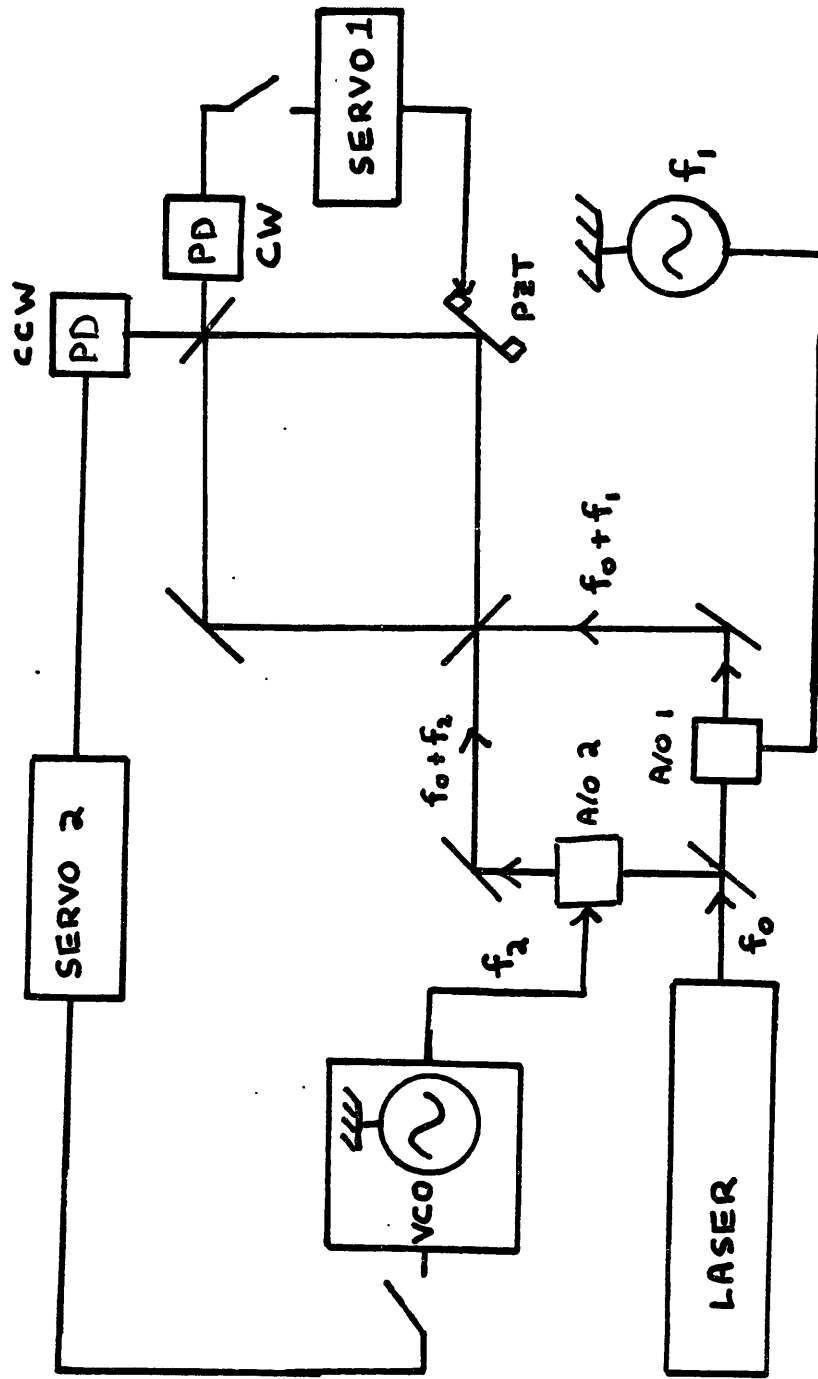


Figure 4.4

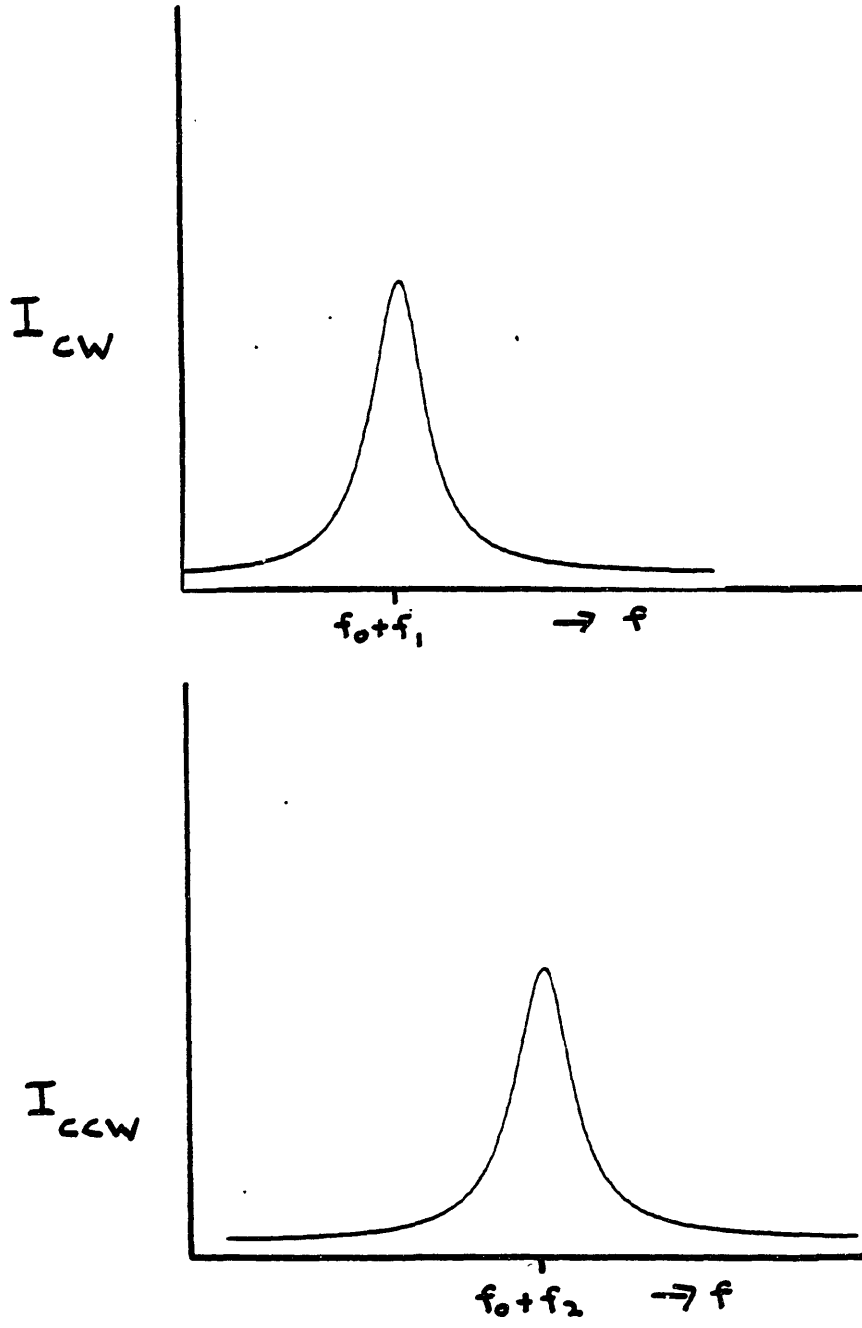


Figure 4.4

via Eq. (3.18). In this way, the measurement of ΔP is insensitive to fluctuations in the laser frequency f_o , which only appears in the scale factor of Eq. (3.18).

The measurement of Δf relies on the precise determination of each of the two resonance frequencies of the cavity. In order to do this we use an AC modulation technique to produce a discriminant that uniquely defines the resonance frequency of the cavity. In this technique, depicted in Figure 4.6, the cavity length is modulated by applying a sinusoidal signal v_m , at frequency f_m , to the PZT. To get the discriminant shown here for the cw case, the resultant intensity output of the cavity is observed with a photodetector (PD#1) and phase sensitive demodulated in PSD#1. As shown in Figure 4.7, if the input frequency f_{cw} is at a point x on the side of the resonance, the output intensity will fluctuate at the fundamental frequency f_m , with an amplitude proportional to the slope at x . Hence, the demodulated output is a measure of the slope of the resonance at x . The output of PSD#1 is shown in Figure 4.8, as f_{cw} is scanned slowly compared to f_m . (This is equivalent to scanning the cavity length relative to f_{cw} .) The zero of this derivative-like function corresponds to the top of the resonance and uniquely defines the cavity resonance frequency, independent of output intensity. In addition, the sign of this function changes about the center of the cavity resonance. In this way, the output of PSD#1 serves as the discriminant for a servo loop that stabilizes the cavity resonance frequency (via the cavity length) to f_{cw} as shown in Figure 4.4. A similar technique employing another

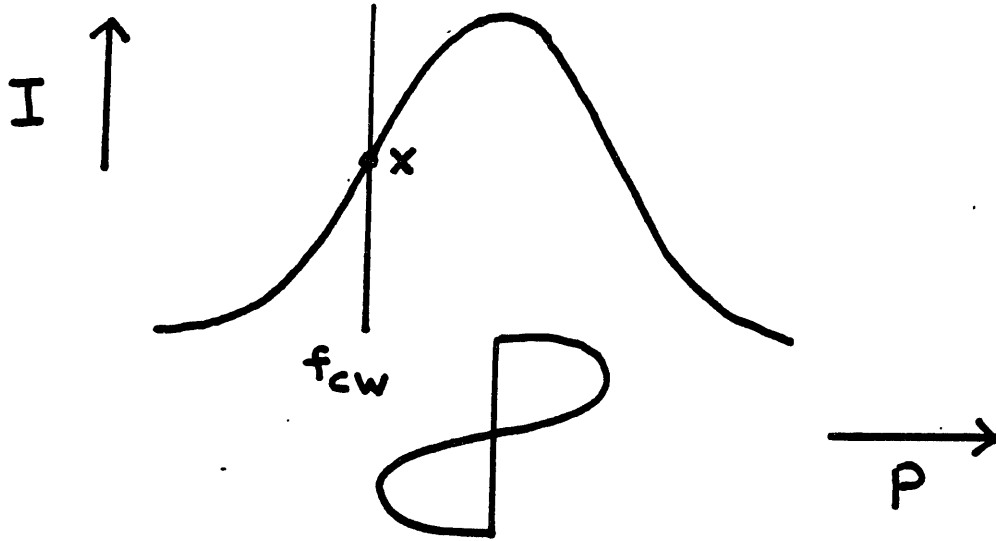


Figure 4.7

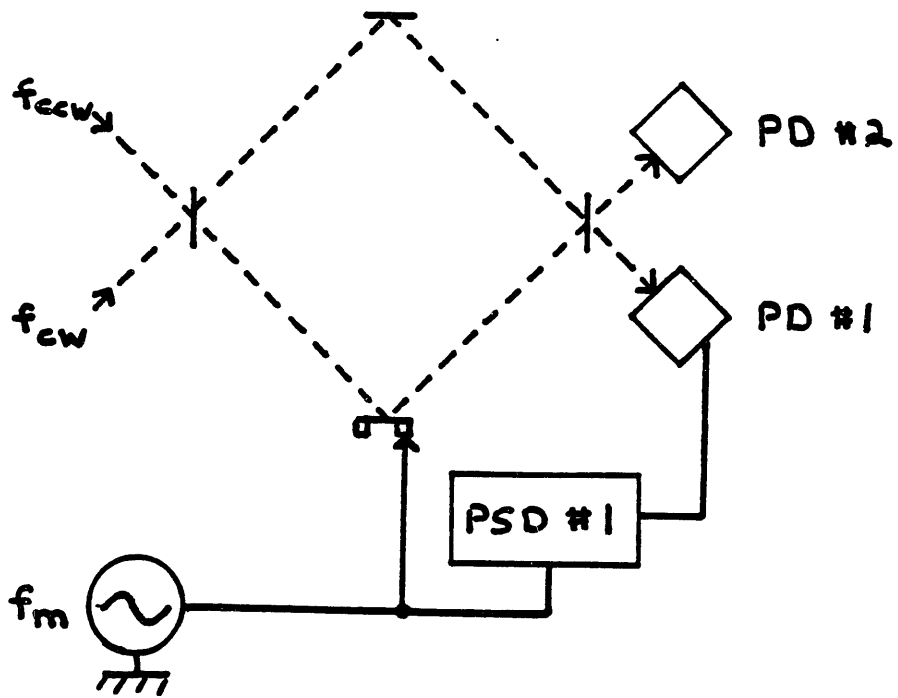


Figure 4.6

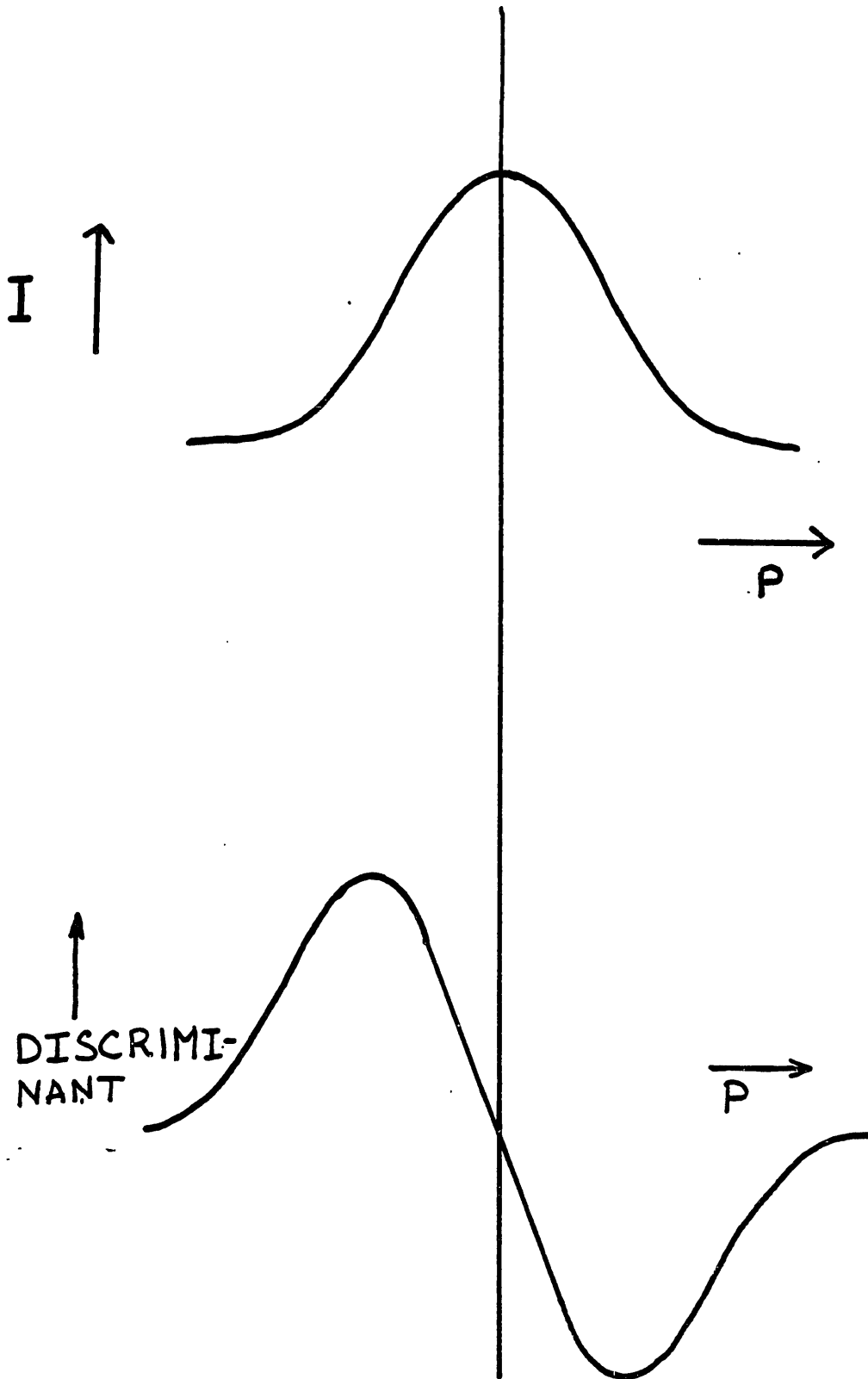


Figure 4.8

phase sensitive demodulator (PSD#2) is used to determine the cw resonance frequency as shown in Figure 4.9 of the next section.

4.4. Passive Resonator Setup for Measurement of Non-Reciprocal Phase Shift

As discussed earlier, the passive ring resonator technique, in general, may be applied to measurements of various non-reciprocal phase shifts. For some applications, such as the Fresnel-drag measurement, discussed in Chapter 5, the system requires extra hardware and slight modifications. However, the setup described here was the basic sensor employed for the measurement of non-reciprocal phase shifts.

Figure 4.9 shows the experimental system. A square resonator 0.7 m on a side was formed by two flat mirrors and two spherical mirrors, each having a radius of curvature of 1.2 m. The spherical mirrors were coated for maximum reflectivity while the flat mirrors, used for coupling into and out of the cavity, were coated for 99% reflectivity. The cavity mirror mounts were fastened to a super invar table and the paths between the mirrors were sealed to minimize airflow.

Light from a single frequency 0.7 mW He-Ne laser was split into two beams, each of which was shifted in frequency by an acousto-optic (A/O) modulator before entering the resonator. The polarization of the light was aligned with one of the polarization axes of the cavity. The beam propagating in the cw direction of the cavity was shifted by a fixed frequency of $f_1 \approx 40$ MHz. The beam propagating in the ccw direction of the cavity was shifted by a variable frequency f_2 of

approximately 40 MHz.

As discussed in Section 4.3, the cw resonance of the cavity is automatically locked to $f_0 + f_1$ by means of a primary feedback loop driving a piezoelectrically controlled cavity mirror. The operation of the feedback loop was based on a 32 KHz cavity modulation rate f_m with an equivalent peak to peak frequency excursion of about 150 KHz to achieve optimum discriminant sensitivity (see Section 4.5) with respect to the 450 KHz cavity linewidth. The output of the cw photodetector (PD#1) was passed through a notch filter at $2f_m$ to eliminate errors caused by the presence of the second harmonic in the signal (see Section 4.6b). As described in Section 4.3, the signal was then phase-sensitive demodulated in PSD#1. The output of PSD#1 was then used to drive the PZT through servo electronics (for more on the servo electronics, see Section 4.6b).

The output of the ccw detector (PD#2) was also notch filtered and phase sensitive demodulated in PSD#2. To reduce residual noise that is common to both cw and ccw beams, the output of PD#1 was subtracted from that of PD#2 (see Section 4.6b). In open loop operation, f_2 was adjusted to null the output of PSD#2. In closed loop operation, the output of PSD#2 automatically adjusted f_2 through a voltage-controlled oscillator (VCO#2) to lock $f_0 + f_2$ to the ccw cavity resonance. The resonance frequency difference $\Delta f = f_2 - f_1$ was then related to the difference in pathlengths via Eq. (3.18).

As discussed in Section 4.6d, the cw beam was phase modulated at 4 KHz, with amplitude sufficient to suppress the carrier frequency. In this way, effects due to backscattering of light from one beam to the other, are attenuated, as discussed in Section 4.6b.

4.5. Sensor Performance and Fundamental Limits

In order to determine the feasibility of the passive resonator technique for precise measurements of non-reciprocal phase shifts, we studied the noise and drift performance of the setup described in the previous section. While the setup was by no means optimized to alleviate all of the measurement problems mentioned in the next section, care was taken to evaluate the system under reasonably stable conditions. In addition, it was well known that the earth's rotation rate is constant to orders of magnitude beyond the fundamental measurement sensitivity for this setup.

The random drift of the experimental setup is shown in Figure 4.10, where the uncertainty in $\Delta f = f_2 - f_1$, given by δf , is plotted against the integration time, τ . For $\tau = 4s$, the data point was obtained in open loop operation by observing the output of PSD#2 for fixed frequencies of f_1 and f_2 . The output drift of PSD#2 was calibrated in terms of the equivalent uncertainty in Δf . In this case, many data runs were taken with a 1s, 12 db filter time constant, which is equivalent to a 4s integration time. The random drift measurements obtained from these data runs for $\tau = 4s$ were averaged

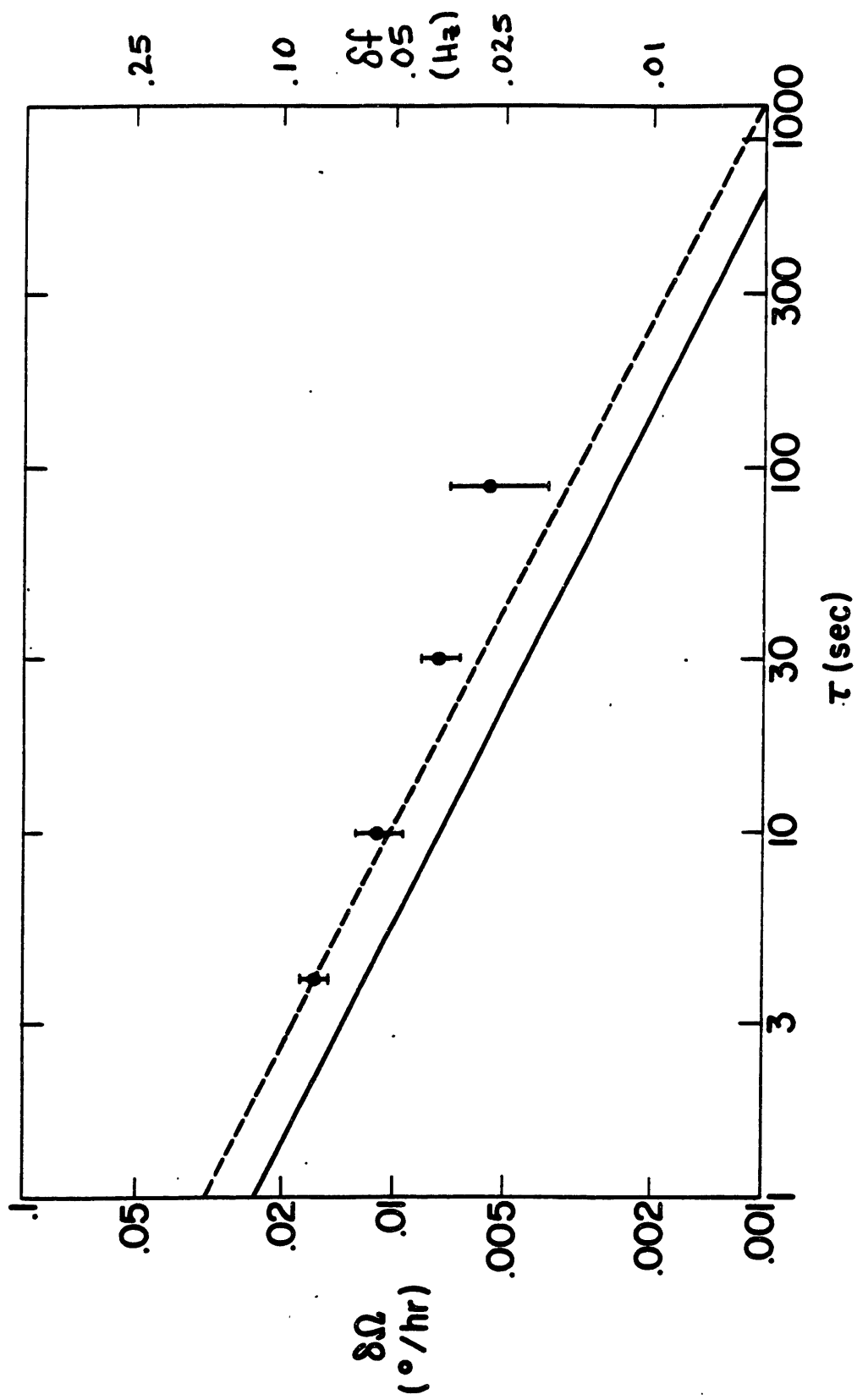


Figure 4.10

to obtain the mean of this drift as well as the standard deviation of this drift as depicted in the plot. The other points on the graph were taken in closed loop operation, where the frequency $\Delta f = f_2 - f_1$ was directly measured by a stable frequency counter. The output Δf was read and recorded every 10s. For the $\tau = 10s$ point, the standard deviation was computed for each run. By comparing several runs the mean standard deviation and the error was computed. In the case of the 30s and 90s points, blocks of 3 or 9 of the 10s observations were combined to form each time constant. In a similar way, the rms drift was computed and averaged for many runs to form the data points and standard deviations shown in the plot.

For applications to rotation sensing, the uncertainty δf can be translated into the uncertainty in measuring the rotation rate $\delta\Omega$ by the relation,

$$\delta\Omega = \frac{\lambda P}{4A} \delta f \quad (4.4)$$

Using the above expression the plot in Figure 4.10 is also labelled in terms $\delta\Omega$.

The fundamental measurement uncertainty in the determination of Δf is given by shot noise statistics. To illustrate this measurement uncertainty, consider the simplified case of square wave cavity length modulation at frequency f_m and amplitude V_m in Figures 4.10a and 4.10b for the case of the cw resonance. The line in the center represents

the light frequency $f_0 + f_1$. The transmission output intensity I_T at any time is given by this line and the point on the resonance cavity resonance function that it intercepts. The resonance frequency is modulated here to the points $e + e'$. The quiescent value of $f_0 + f_1$ is at the center of the cavity resonance. The demodulated output is obtained by mixing V_m and I_T , i.e. $V_m \times I_T$, and then by taking the DC average. In the absence of noise at the fundamental frequency f_m , I_T has no fluctuations at f_m and the demodulated output is zero indicating the "on resonance" condition (Figure 4.10a). In the presence of intensity noise of amplitude I_n at frequency f_m , as shown in Figure 4.10b, I_T varies at the fundamental frequency. This gives a non-zero demodulated output, erroneously indicating an "off resonance" condition. As the noise varies in phase and amplitude, the servo loop will respond by moving the cavity resonance back and forth off center to seek a zero demodulated output. The size of frequency excursion necessary to achieve this correction is approximately given by the noise amplitude, I_n divided by the slope of the resonance at e and e' . Thus if the modulation excursion extends to the point of maximum slope, the resonance frequency error δf is minimized. For this case, the maximum slope is approximately I_0/Γ , where Γ is the resonance linewidth. The uncertainty in the resonance frequency (in this case, the cw resonance frequency) is thus given by,

$$\delta f_{cw} \approx \frac{I_n}{I_0/\Gamma} = \frac{\Gamma}{I_0/I_n} \quad (4.5)$$

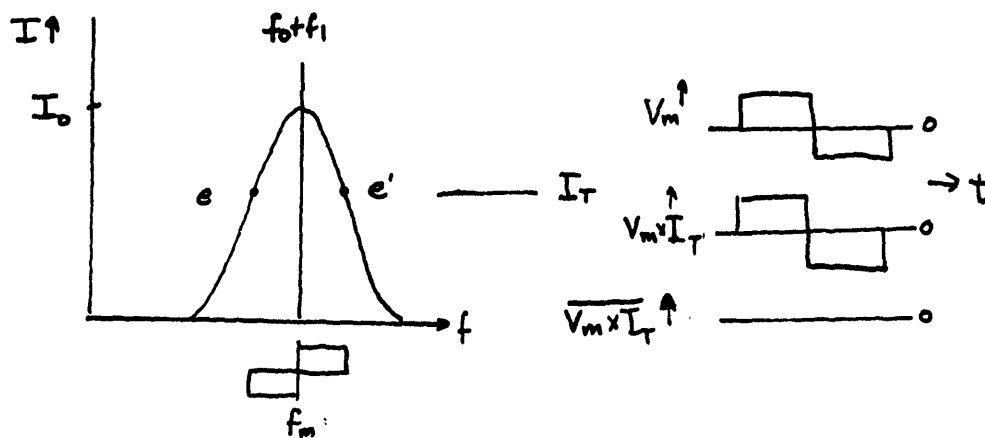


Figure 4.10a

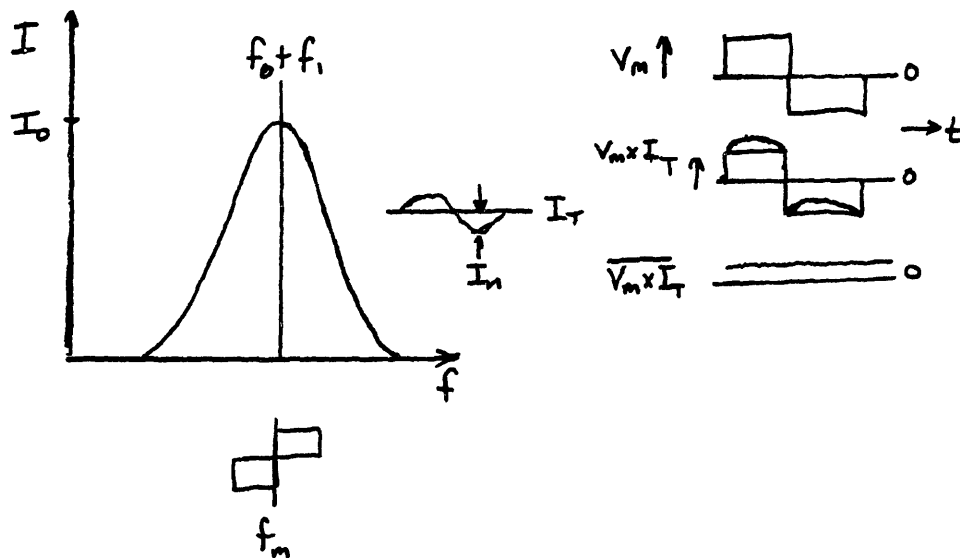


Figure 4.10b

where I_o/I_n is the signal to noise ratio.

In general, the error in measuring the resonance frequency splitting Δf , is given by,

$$\delta f = \delta f_{cw} - \delta f_{ccw} \quad (4.6)$$

where δf_{ccw} is the error in measuring the ccw resonance frequency which is of the same form as Eq. (4.5). In principle, if Γ and I_o are equal for the two beams, then any noise I_n that is common to both beams does not contribute to δf . In practice, because of imperfect matching of I_o and Γ it is necessary to modulate the cavity resonance (and thus detect the output intensity) at a rate f_m such that the dominant source of noise I_n at f_m is that due to shot noise. For shot noise limited detection, the signal to noise ratio²⁶ is given by,

$$I_n/I_o = \left(\frac{1}{N\eta_o\tau} \right)^{1/2} \quad (4.7)$$

where N is the average number of photons arriving at the detector per unit time, η_o is the detector quantum efficiency, and τ is the observation time. Hence, substituting Eq. (4.7) in Eq. (4.5), the uncertainty in the determination of the resonance frequency (in this case f_{cw}) is given by,

$$\delta f_{cw} \sim \frac{\Gamma}{(N\eta_o\tau)^{1/2}} \quad (4.8)$$

Assuming a similar expression for δf_{CCW} and equal parameters as those appearing in Eq. (4.8), the fundamental uncertainty in the determination of the difference frequency Δf is given by,

$$\delta f \approx \frac{\sqrt{2} \Gamma}{(N \eta_o \tau)^{1/2}} \quad (4.9)$$

where the factor $\sqrt{2}$ is due to the incoherent addition of the uncertainties in δf_{CW} and δf_{CCW} .

The fundamental limit* δf , for the setup used in this research is represented by the solid line in Figure 4.10. This uncertainty δf was computed from Eq. (4.9) for $N \approx 10^{14}$ photons/s, $\eta_D \approx 0.3$ and $\Gamma \approx 450$ KHz. The dotted line represents the effective limit for our setup taking into consideration the additional white noise in the detector-preamplifier. As can be seen in Figure 4.10, the data points are consistent with the fundamental measurement uncertainty (for this setup) for $\tau \lesssim 10$ s but depart slightly from the predicted $\tau^{-1/2}$ dependence for $\tau \gtrsim 10$ s.

Several sources of error were investigated as possible causes for the long-term drift of the setup. These sources of error are discussed in the next section.

*The equivalent fundamental limit $\delta\Omega$, for measurement of rotation, may be obtained by combining Eqs. (4.9) and (4.4).

4.6. Sources of Error in Passive Ring Resonator Technique

As mentioned in the previous section, many sources of error, namely those effects which cause "apparent" non-reciprocal phase shifts, were investigated. In Sections 4.6a through 4.6e, those errors due to mode pulling effects, polarization-related effects, light backscattering effects, air currents and electronic effects are discussed.

4.6a. Mode Pulling Effects

The presence of higher order transverse modes in a cavity can introduce errors in the determination of the resonance frequency of the TEM₀₀ mode that is used as a reference. These mode pulling effects result from the higher order modes contributing to the observed output intensity in the region close to the resonance frequency of the TEM₀₀ mode. This intensity contribution then introduces an asymmetry in the TEM₀₀ mode lineshape that pulls the TEM₀₀ resonance frequency to a different apparent resonance frequency. Consider the simple case of only one higher order mode, in this case the TEM₁₀ mode (in cartesian coordinates) shown in Figure 4.11. The influence of the TEM₁₀ mode on the transmitted intensity in the region of the TEM₀₀ mode is given by

$$I_T = |E_{00}|^2 + |E_{10}|^2 + 2 E_{00} E_{10} \cos(\phi_{00} - \phi_{10}) \quad (4.10)$$

where E_{10} and ϕ_{10} are the TEM₁₀ electric field amplitude and phase near the TEM₀₀ resonance frequency and E_{00} and ϕ_{00} are the field

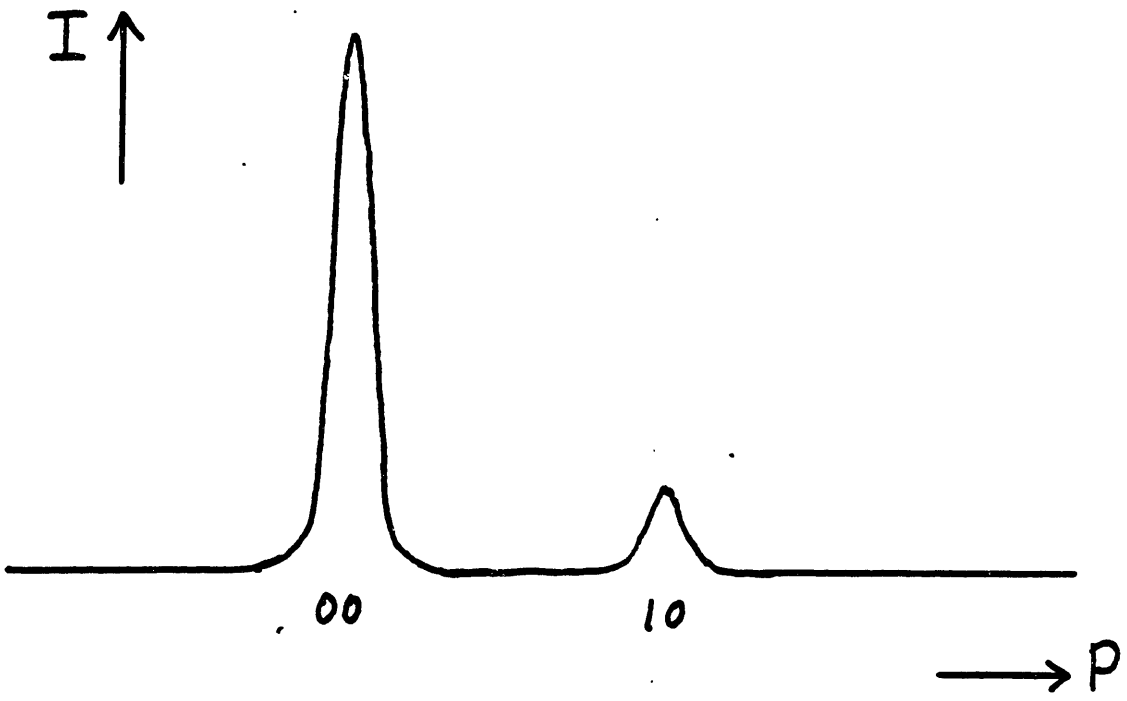


Figure 4.11

amplitude and phase of the TEM_{00} mode. These quantities all depend on the cavity perimeter P . As shown in Eq. (4.10), the TEM_{10} mode affects the output intensity by means of both an intensity term and an interference term.

In principle, the interference term is zero if this term is averaged over all space because the two Gaussian cavity modes are spatially orthogonal. If, however, the output intensity of the cavity is detected with a finite aperture or if the detector is spatially inhomogeneous, the orthogonality condition is no longer valid. Under these non-ideal conditions the interference term will in fact pull the TEM_{00} resonance frequency. If this pulling effect is different for the cw and ccw resonances, an apparent non-reciprocal phase shift is observed.

This effect was studied under controlled conditions in a separate experiment in our laboratory.²⁷ It was found that because of inhomogeneities in the detector surface and aperturing of the beam, the apparent resonance frequency of the cavity was a function of the transverse position of the detector with respect to the output beam. In this setup, the maximum variation of the observed resonance frequency as the detector was scanned across the output beam was ~75 Hz. While this effect represents a large error in the measurement of dc, non-reciprocal phase shifts such as rotation sensing, it does not vary rapidly (as evidenced by the performance data in Section 4.5) and wasn't considered crucial to an AC measurement such as that used in the Fresnel drag. Hence, no effort was made to optimize the setup to greatly reduce this effect.

The other contribution to the total mode pulling effect, as shown in Eq. (4.10), is that due to the intensity $|E_{10}|^2$ of the higher order mode. To illustrate this, it is instructive to look at the effect of the 1-0 mode on the discriminant of the 0-0 mode. The zero of this discriminant, described in Section 4.3, defines the 0-0 cavity resonance frequency. Hence, if another mode is nearby, its discriminant is summed with that of the 0-0. In the case shown in Figure 4.12, the resultant zero of the sum is shifted toward the 1-0 mode, thus pulling the effective resonance frequency of the 0-0 mode.

To estimate this effect, it is possible to approximate the discriminant as the derivative of the lineshape function given by Eq. (3.10). The discriminant as a function of cavity length, P , is thus given by,

$$\frac{\partial I_T}{\partial P} = - \frac{(1-R)^2 I_i}{\left[(1-R)^2 + 4R \sin^2 \left(\frac{\pi}{\lambda} P \right) \right]^2} \left(\frac{8\pi R}{\lambda} \right) \sin \left(\frac{\pi}{\lambda} P \right) \cos \left(\frac{\pi}{\lambda} P \right) \quad (4.11)$$

where the parameters are defined in Section 3.4. When the argument $\frac{\pi}{\lambda} P$ is an integer multiple of π the derivative is zero, corresponding to the "on resonance" case. For a given axial mode number, q , the argument may be replaced by, $\frac{\pi}{\lambda} \Delta P$, where ΔP is the detuning in the cavity length with respect to the "on resonance" cavity length. Defining the detuning from resonance as ΔP_{00} and ΔP_{10} for the 0-0 mode and the 1-0 mode, respectively, the corresponding derivatives are given by

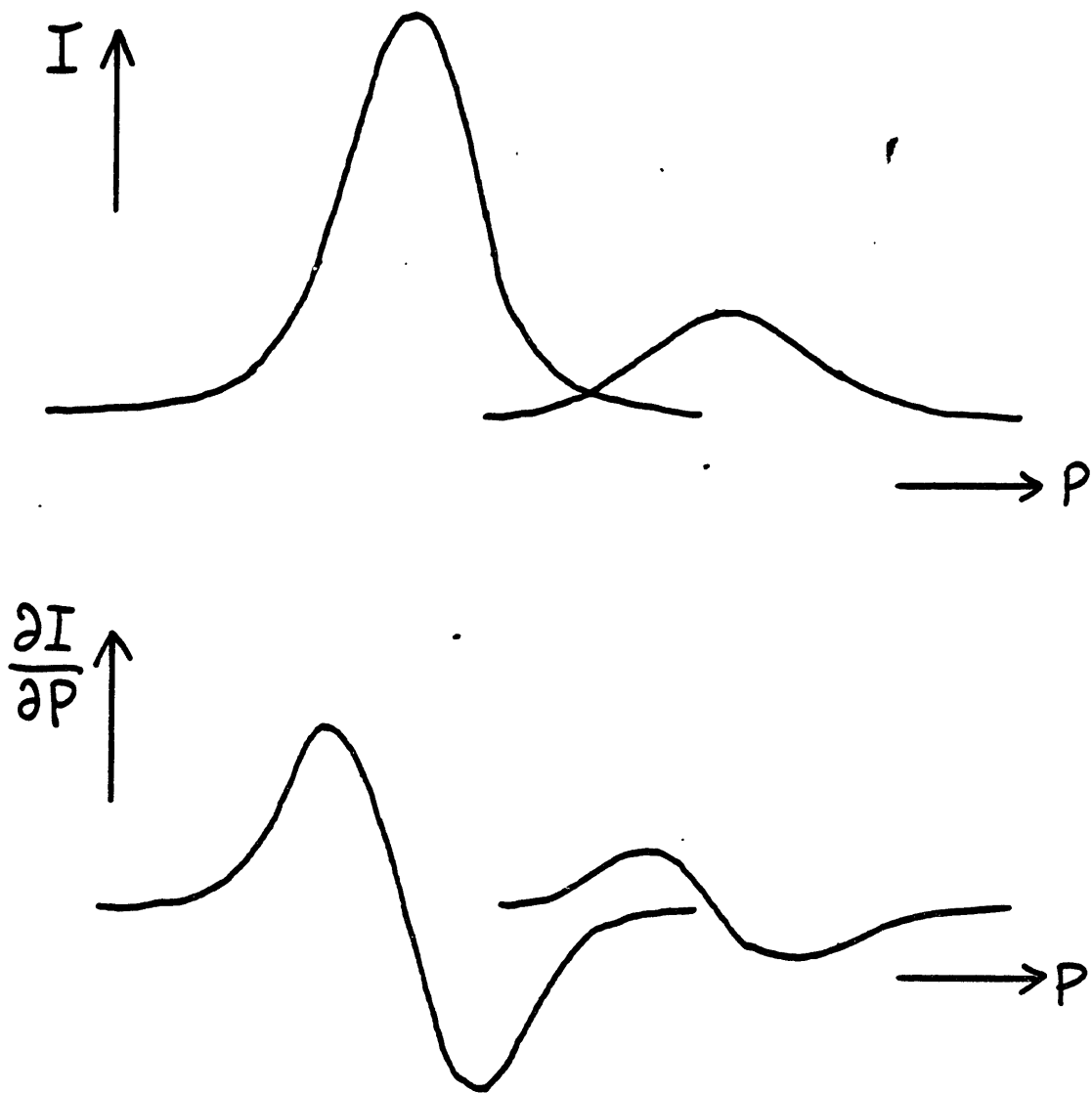


Figure 4.12

$$\frac{\partial I_{T_{00}}}{\partial P} = - \frac{(1 - R)^2 I_{i_{00}}}{\left[(1 - R)^2 + 4R \sin^2 \left(\frac{\pi}{\lambda} \Delta P_{00} \right) \right]^2} \left(\frac{8\pi R}{\lambda} \right) \sin \left(\frac{\pi}{\lambda} \Delta P_{00} \right) \cos \left(\frac{\pi}{\lambda} \Delta P_{00} \right) \quad (4.12)$$

and

$$\frac{\partial I_{T_{10}}}{\partial P} = - \frac{(1 - R)^2 I_{i_{10}}}{\left[(1 - R)^2 + 4R \sin^2 \left(\frac{\pi}{\lambda} \Delta P_{10} \right) \right]^2} \left(\frac{8\pi R}{\lambda} \right) \sin \left(\frac{\pi}{\lambda} \Delta P_{10} \right) \cos \left(\frac{\pi}{\lambda} \Delta P_{10} \right) \quad (4.13)$$

Here $I_{T_{00}}$ and $I_{T_{10}}$ are respectively the transmitted intensities of the 0-0 and 1-0 modes and $I_{i_{00}}$ and $I_{i_{10}}$ are the input intensities of these modes, respectively.

For a given difference ℓ in resonance lengths between the two modes, as shown in Figure 4.13, the pulling effect may be approximated by first computing $\partial I_{10} / \partial P$ at a distance $\ell = |\Delta P_{10}|$ from the center of the 1-0 resonance. The detuning, ΔP_{00} , necessary to satisfy the relation

$$\frac{\partial I_{T_{00}}}{\partial P} - \frac{\partial I_{T_{10}}}{\partial P} = 0 \quad (4.14)$$

is thus, the magnitude of the pulling. The pulling ΔP_{00} , may then be converted to an equivalent frequency pulling Δf_p by means of the relation,

$$\frac{\Delta P}{P} = - \frac{\Delta f}{f} \quad (4.15)$$

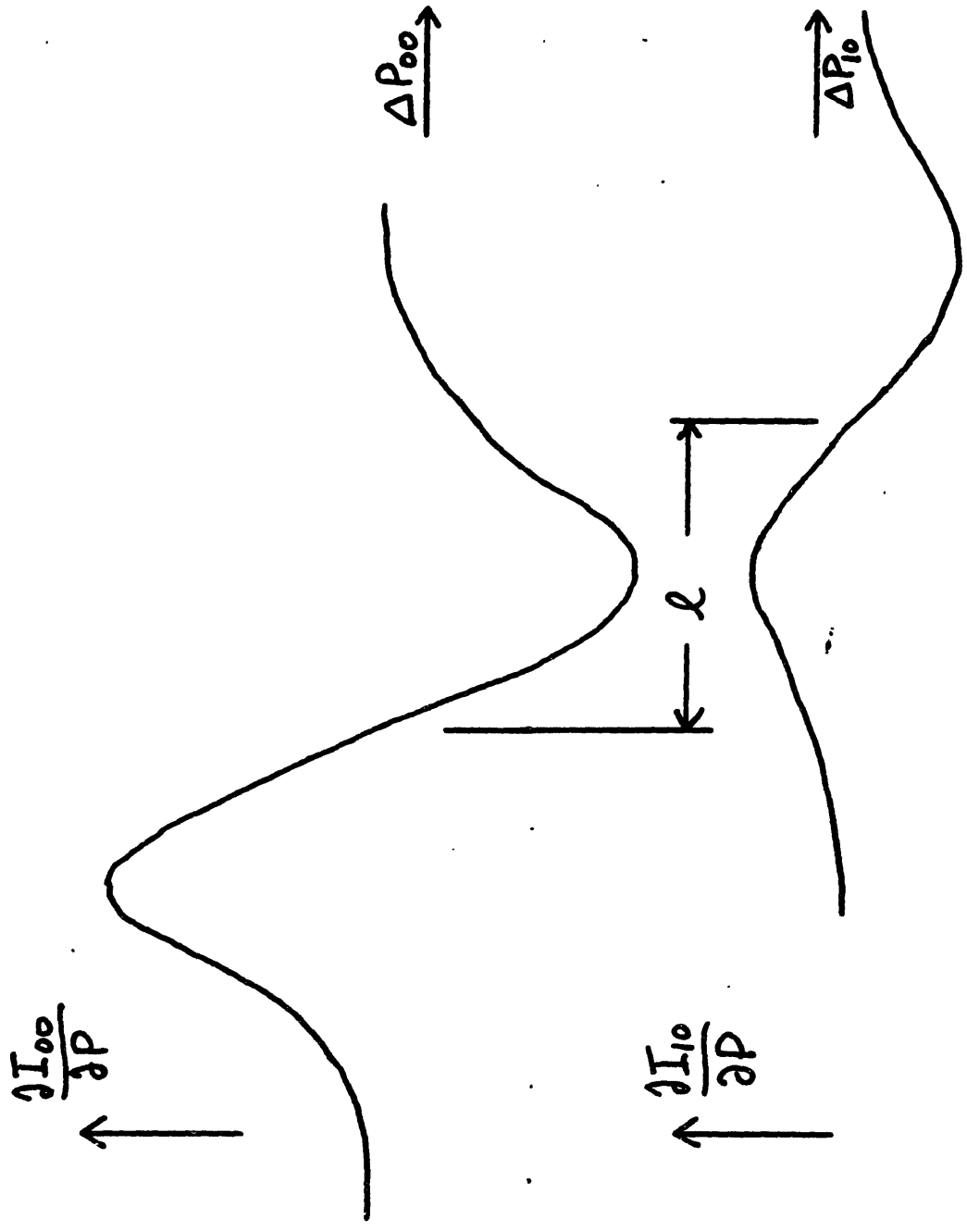


Figure 4.13

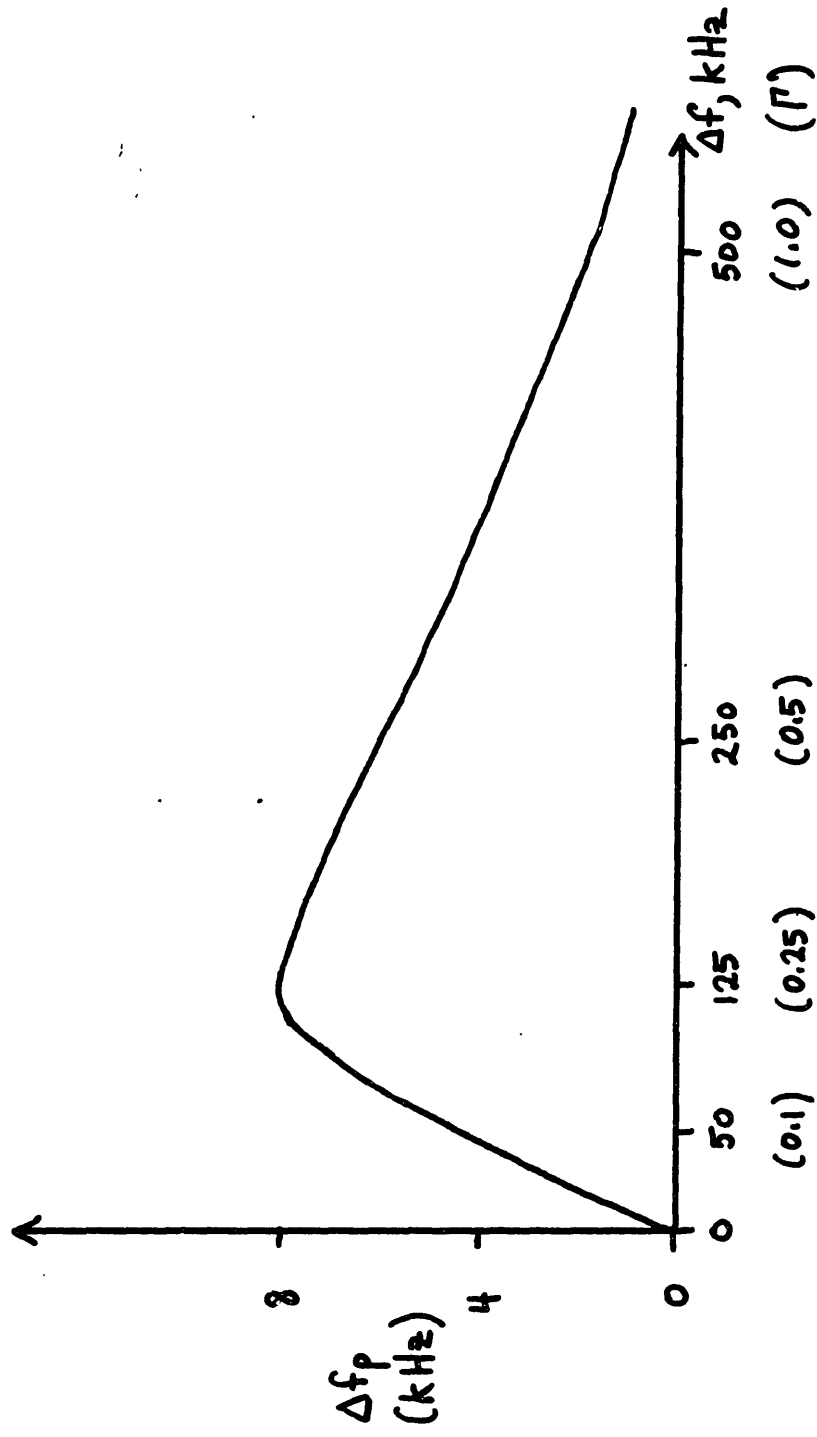


Figure 4.14

This relation is also used to convert the difference in resonance length ℓ to the resonance frequency separation of the two modes.

For the setup used in this research $f \cong 5 \times 10^{14}$, $P = 3\text{m}$ and the effective reflectivity is $\sim 98.5\%$. For a coupling into the 1-0 mode of approximately 10% of that of the 0-0 mode ($I_{i_{10}}/I_{i_{00}} = .1$) the frequency pulling Δf_p is shown in Figure 4.14 as a function of the mode separation. To compare the mode separation with the linewidth Γ (≈ 500 KHz), a separate scale is labelled in units of Γ . The pulling is thus linear for small mode separation, since both mode derivatives are linear in this case. The maximum pulling results when the maximum of the 1-0 derivative falls at the 0-0 resonance frequency. The magnitude of the pulling then falls off for mode separations larger than Γ .

In both mode pulling effects, if the coupling into the higher order modes is not identical for the cw and ccw beams, the mode pulling will result in an apparent non-reciprocal phase shift. Because of misalignment of the input beams into the cavity or because of cavity misalignment, both mode pulling effects can influence the long-term stability of the passive ring resonator setup.

To get a rough idea of the sensitivity to beam misalignments both the input beam alignment and the cavity alignment were varied. Typical curves for the change in output frequency $\Delta f = f_2 - f_1$ are shown in Figures 4.15a, 4.15b, 4.17a and 4.17b for various misalignments. Figure 4.15a and 4.15b shows the variation in Δf for vertical and horizontal angular misalignments of one of the spherical cavity mirrors.

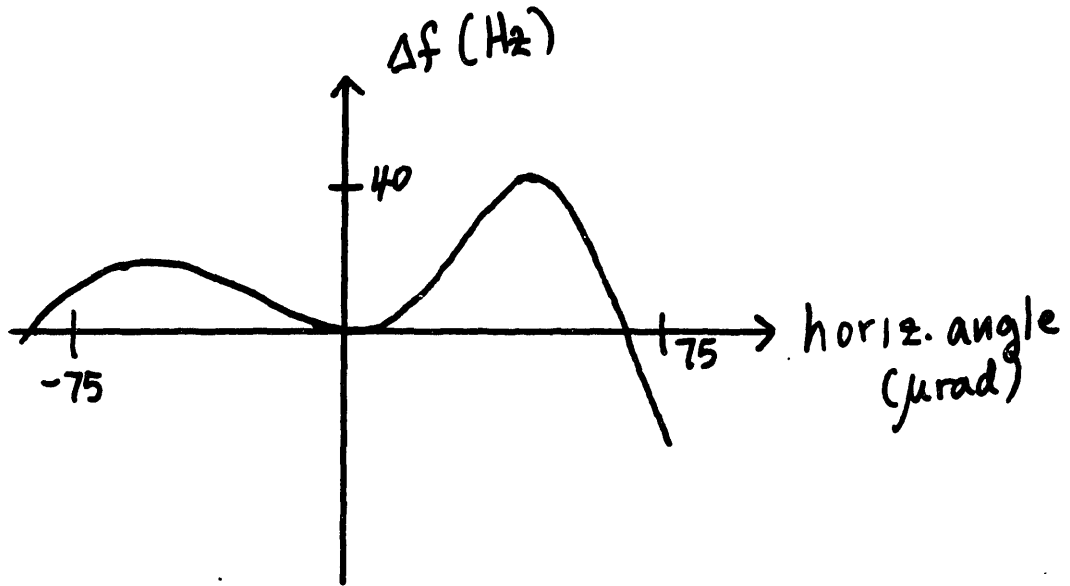


Figure 4.15a

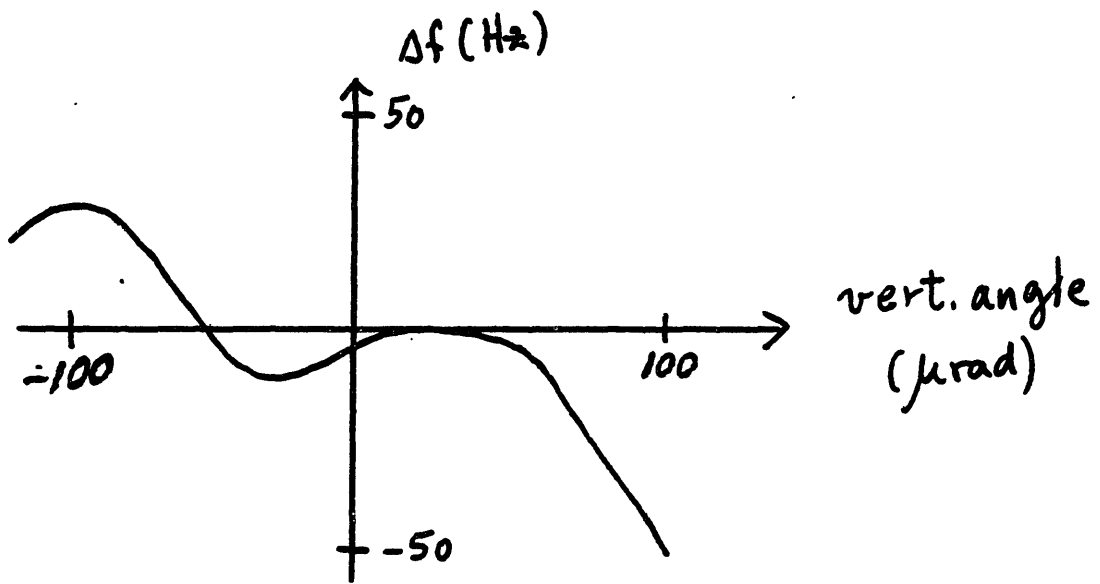


Figure 4.15b

To illustrate the effect of misalignment on these mode structures the mode structures are shown (here the modes are represented by delta functions for simplicity) for angular deviations θ'_V and θ'_H in Figure 4.16 b, and c. Figure 4.16a shows the mode structure of the aligned cavity. In the case of the vertical misalignment, shown in Figure 4.16b, the TEM_{01} mode appears, while horizontal misalignment is indicated by the appearance of the TEM_{10} mode in Figure 4.16c. As is obvious from Figures 4.16b and 4.16c, the misalignment does not effect the cw and ccw mode structures equally. Because the TEM_{10} and TEM_{01} modes separated substantially from the TEM_{00} mode, these modes probably do not produce the dominant pulling effect. In this case the pulling effect is probably due to a combination of modes, some of which are small but fall inside the linewidth of the TEM_{00} mode. The misalignments shown here for the purpose of illustration are very large compared to the actual long term stability of the cavity alignment. Similarly, curves are shown in Figures 4.17a and 4.17b for the resonance frequency shift Δf as a function of external misalignment of the input beam into the cavity. Figure 4.17a depicts Δf as a function of translational misalignment of the beam into the cavity and Figure 4.17b shows the dependence of Δf on angular misalignment of the beam into the cavity.

No attempt here was made to calculate or predict the resonance shift as a function of beam misalignment. The empirical curves shown in Figures 4.15a, b, 4.17a and b, only served as an indication of the sensitivity beam misalignments for this setup.

aligned case

at θ_V'

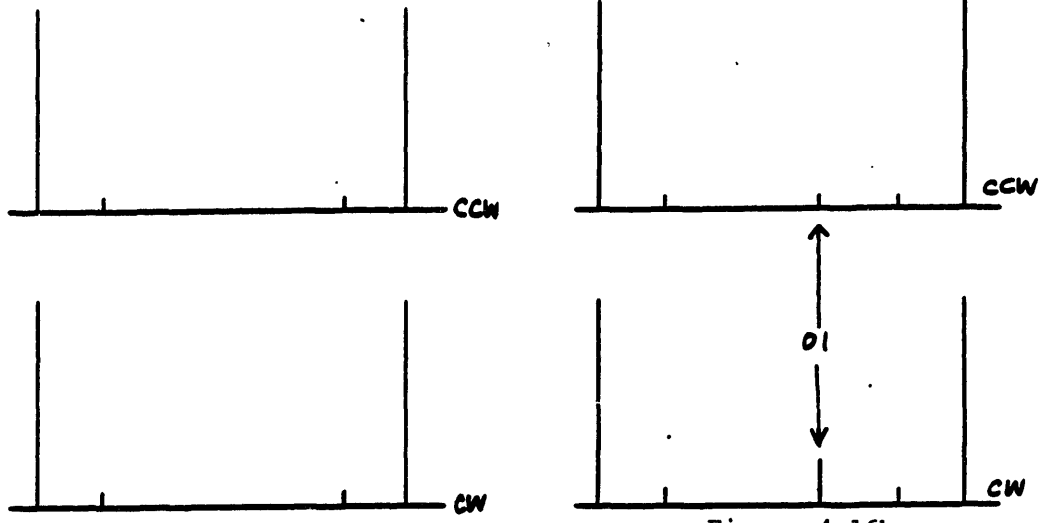


Figure 4.16a

Figure 4.16b

at θ_H'

$\rightarrow P$

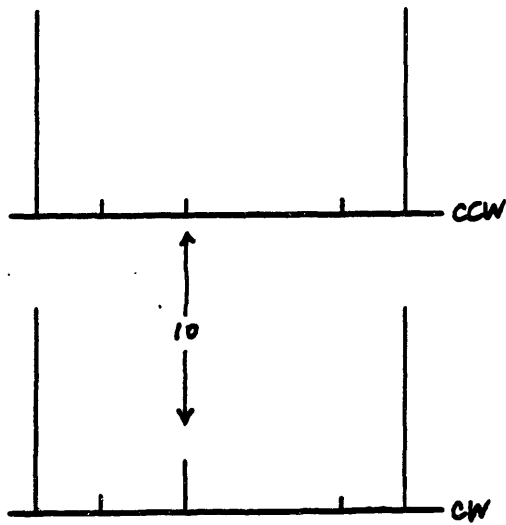


Figure 4.16c

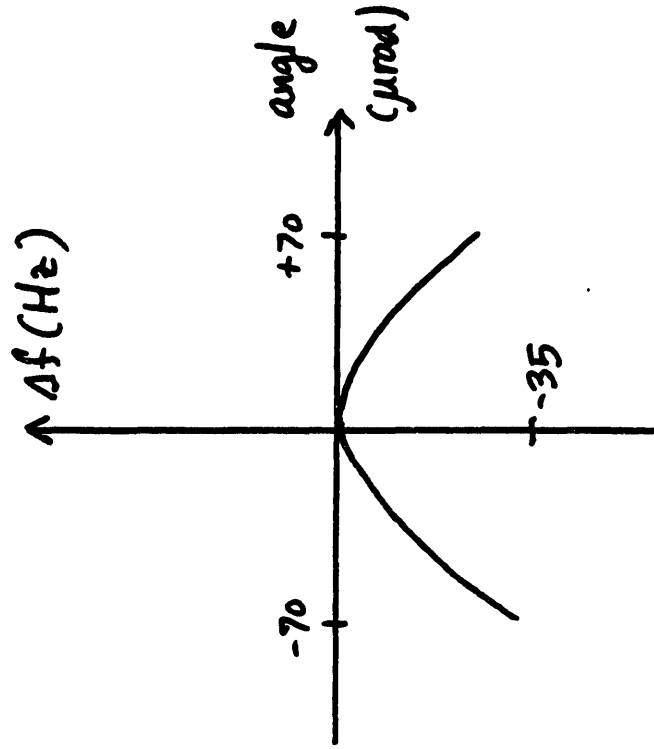


Figure 4.17b

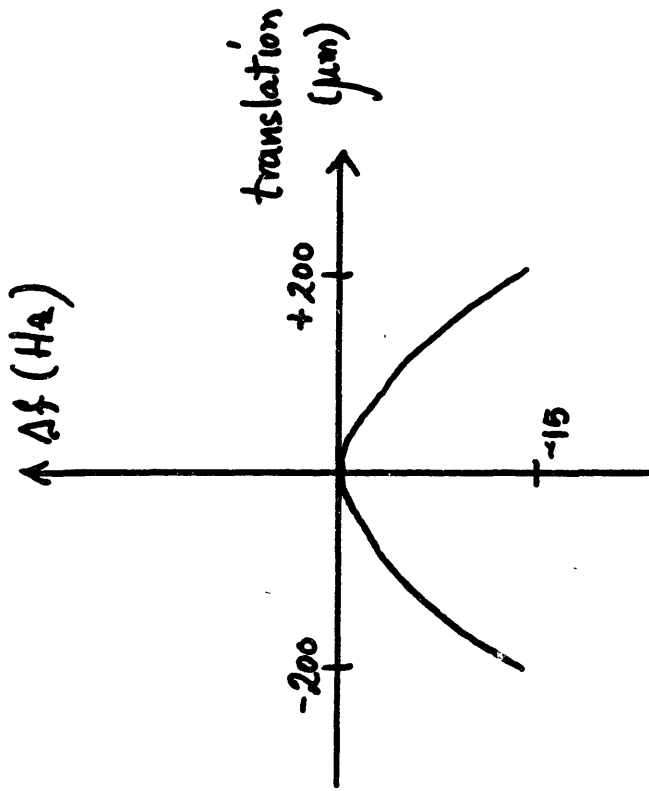


Figure 4.17a

4.6b. Electronic Error Sources

There are several electronic error sources that can influence the measurement of the cavity resonance frequencies. Many of these electronic errors are caused by the non-ideality of the servo and measurement instrumentation; for example, those errors due to higher harmonic demodulation, finite servo gain-bandwidth, and instrumentation noise and drift. In addition, the stability of the oscillator at f_1 and f_2 , as mentioned in Section 4.3, can influence the measurement of Δf .

As mentioned previously, the determination of the cavity resonances frequencies, in principle, is based upon phase sensitive demodulation (PSD) at the fundamental frequency, f_m . This demodulation process, analogous to full wave rectification, is also sensitive to higher odd harmonics. Because these harmonics on the output intensity are small, it was found that passing the signal through a bandpass filter (centered at f_m) of $Q = 2$ or $Q = 5$, adequately attenuated this potential error source. Since, in practice, the demodulator reference wave has asymmetries, the PSD is also sensitive to even harmonics. While the harmonics at frequencies greater than $2f_m$ are again small and easily eliminated, the peak to peak second harmonic content of the output intensity I_T is $\sim 1/3 I_T$ (this is for the modulation amplitude mentioned in Section 4.4). If a $Q = 2$ bandpass filter is used, the second harmonic generates an error signal of $\sim 10-100$ Hz, depending on the demodulator asymmetry as well as the $2f_m$ phase and amplitude. For illustration, where two or three PSD's demodulate the same photodetector (PD) signal, the output offsets were found to differ

by an equivalent of 10-50 Hz. In addition, these outputs drifted ~5 Hz relative to each other in a time interval of ~30 mins. Because servo bandwidth considerations preclude the use of a filter of $Q \geq 5$ in the primary feedback loop the PD signal is passed through a narrow band (Q20) notch filter at $2f_m$ prior to phase sensitive demodulation. As shown in Figure 4.9, a similar notch filter was employed at the output of PD#2. In this way, the $2f_m$ error was attenuated to a level that was found to be insignificant for the purpose of this research.

Another source of error arises from the inability of the primary servo loop to perfectly correct for large reciprocal cavity pathlength changes or large laser frequency changes. To illustrate this, suppose the laser frequency f_o jitters at a frequency f_j with amplitude Δf_j . The primary feedback loop, via the cavity length, changes the cavity resonance frequency by an amount $\Delta f_j G(f_j)/G(f_j) + 1$, where $G(f_j)$ is the gain of the servo at frequency f_j . If $G(f_j)$ is large but non-infinite, the cavity will be off resonance by a residual frequency Δf_r of magnitude

$$\Delta f_r = f_c - f_o = \Delta f_j \frac{1}{1 + G(f_j)} \quad (4.16)$$

Since the laser jitter is common to both the cw and ccw beam, both of these beams are off-resonance by the above amount, as depicted in Figure 4.18. If the cw and ccw outputs are demodulated in PSD#1 and PSD#2 respectively, the PSD#3 outputs will have offsets proportional to fundamental generated by Δf_r . To correct for this residual reciprocal

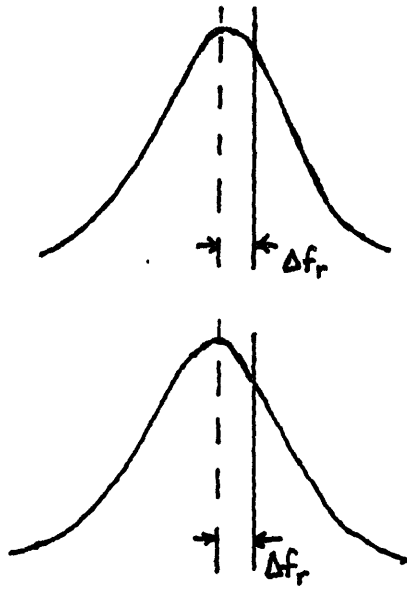


Figure 4.18

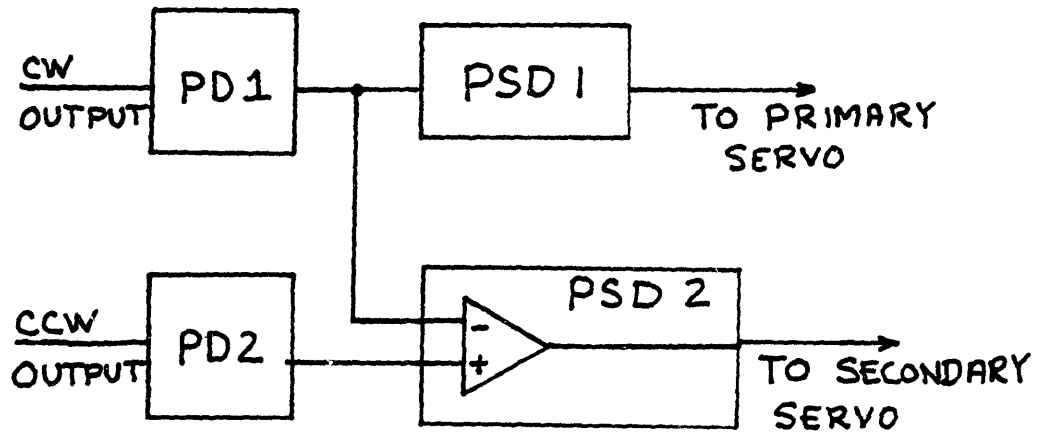


Figure 4.19

offset as shown in Figure 4.19, we subtract the output of PD#1 from PD#2. Hence, if this subtraction were perfect the output of PSD#2 will be zero, correctly indicating the absence of non-reciprocal phase shift, i.e. $\Delta f = 0$. In practice, if the photodetector responses are not perfectly matched or if the cw and ccw intensities are unequal, a fraction β of Δf_r will erroneously appear as a non-reciprocal phase shift, thus given by,

$$\Delta f = \beta \Delta f_r \quad (4.17)$$

In the setup used here, the primary servo electronics depicted in Figure 4.20, consisted of two "integrator-like" amplifiers followed by a high voltage amplifier for driving the PZT. The first two amplifiers of the transfer function shown in Figure 4.21, are integrators at low frequency and had a zero at corner frequencies of ~100 Hz. The gain of the entire servo loop is shown in Figure 4.22. The bandwidth of the loop was ~3 KHz, and was primarily restricted by the response of the PZT and its associated mount. For measurement of DC non-reciprocal phase shifts such as those due to rotation, the DC gain of the loop was very adequate ($>10^9$) and no reliance on subtraction was necessary. In an AC measurement, such as the Fresnel-drag measurement, the gain of the servo, and the subtraction quality β were an important consideration (see Section 5.2).

Other electronic sources of errors are those due to biases and drifts of the amplifiers in the servo loop. For example, if integrator

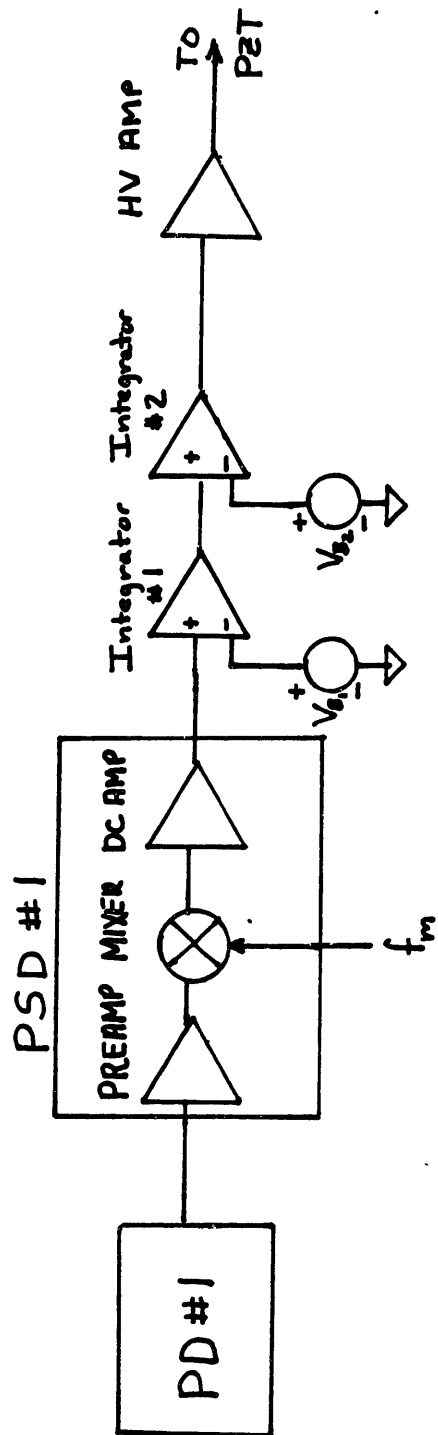


Figure 4.20

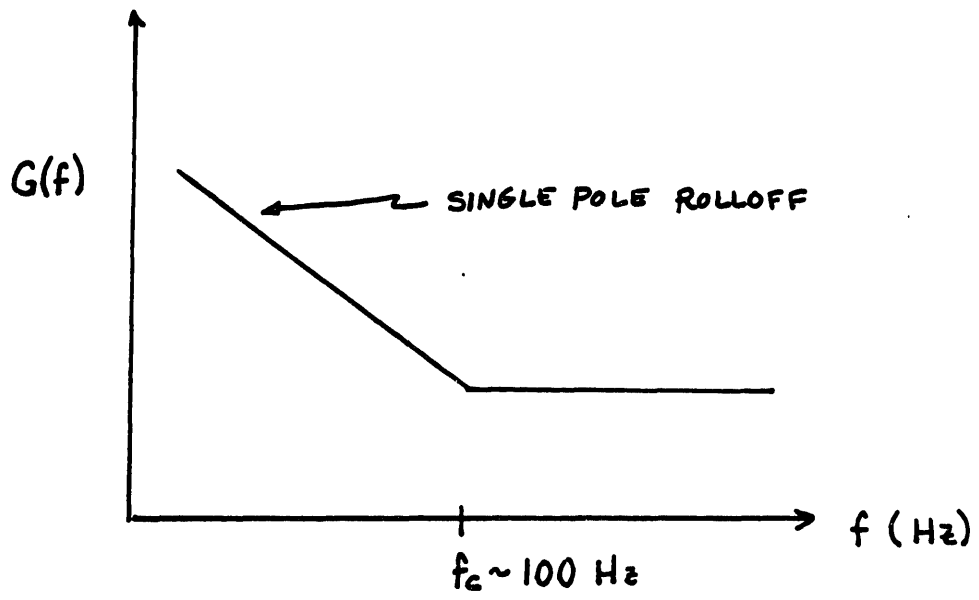


Figure 4.21

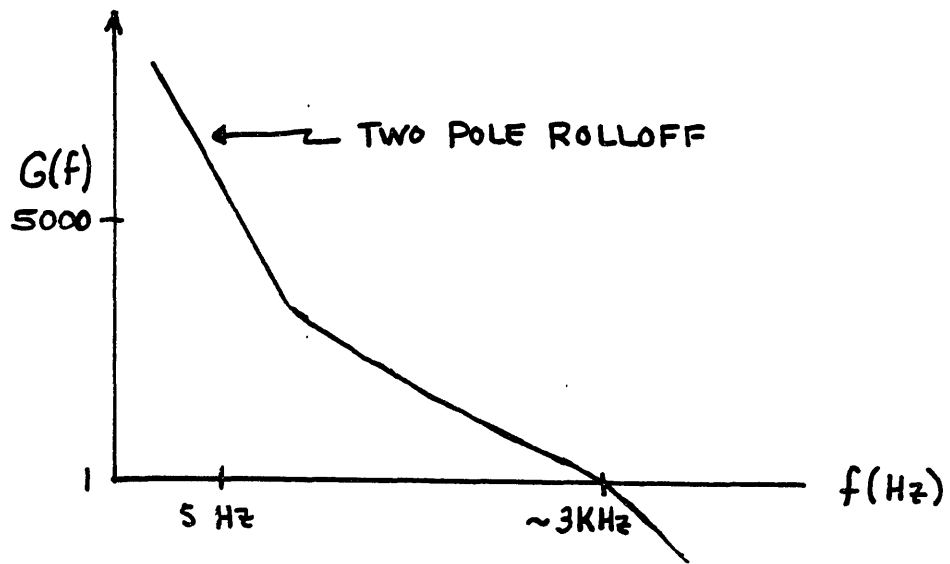


Figure 4.22

#1, as shown in Figure 4.20, has an input voltage bias V_{B_1} , the servo corrects for this bias by moving the cavity off resonance to produce a compensating output, $-V_{B_1}$, at the output of PSD#1. Both cavity resonances are thus moved off center by a frequency Δf_r proportional to V_R , divided by the gain of PSD#1. In order to minimize this error, the bias is adjusted to zero as well as possible, and the gain of the PSD is increased as much as possible. In addition, the residual error is then attenuated by the subtraction process previously described. A similar argument holds for offsets in the DC amplifier of the PSD. In practice, this error source is adequately attenuated. Other biases, such as V_{B_2} are similarly treated and are, in fact, attenuated to a greater degree by the gain of integrator 1.

4.6c. Effects of Air Currents

Another source of error is caused by air currents in the cavity. These air currents, possibly due to temperature gradients and other external disturbances, produce non-reciprocal phase shift via the Fresnel-drag. To get an idea of the magnitude of this effect, suppose a cylinder of air, 30 cm in length, is made to flow in a direction parallel to one beam and antiparallel to the other (as in the Fizeau Expt., Section 2.2). Assuming an index of air $n \approx 1.0003$ and assuming a speed $v \approx 10$ cm/sec, Eqs. (2.4) and (3.18) give $\Delta f \approx 21$ Hz.

To reduce the effects of air currents in this research, we found that simply sealing the cavity was adequate. Certainly a vacuum system was considered in order to completely eliminate this

and is suggested for future work.

4.6d. Scattering Effects

Another important source of error is due to light backscattering from cavity mirrors and scattering from the external input optical components. Each of these results in an oscillatory non-reciprocal frequency shift at the difference frequency $f_2 - f_1$. To illustrate this effect, consider the case of intra-cavity backscattering as shown in Figure 4.23. Suppose light of amplitude E_s , is back scattered from the cw beam into the ccw mode the cavity. Assuming for the moment that the fields of the cw and ccw beams differ by a constant phase, θ_s , i.e. $f_1 = f_2$, the total field of the ccw beam is given by

$$E_{ccw} = e^{i(Kz - \omega t)} [E_o + E_s e^{i\theta_s}] \hat{z} \quad (4.18)$$

where E_o is the amplitude of the ccw beam in the absence of backscattering and \hat{z} is the direction of light propagation. Assuming $E_o \gg E_s$, the total field is then given by,

$$E_{ccw} \approx E_o e^{i(Kz - \omega t)} e^{i \frac{E_s \sin \theta_s}{E_o}} \hat{z} \quad (4.19)$$

Hence, the roundtrip phase shift in the ccw direction is now incremented by $E_s/E_o \sin \theta_s$. Since a phase shift of 2π corresponds to a resonance frequency shift of 100 MHz (the cavity free spectral range) the ccw resonance frequency is changed by,

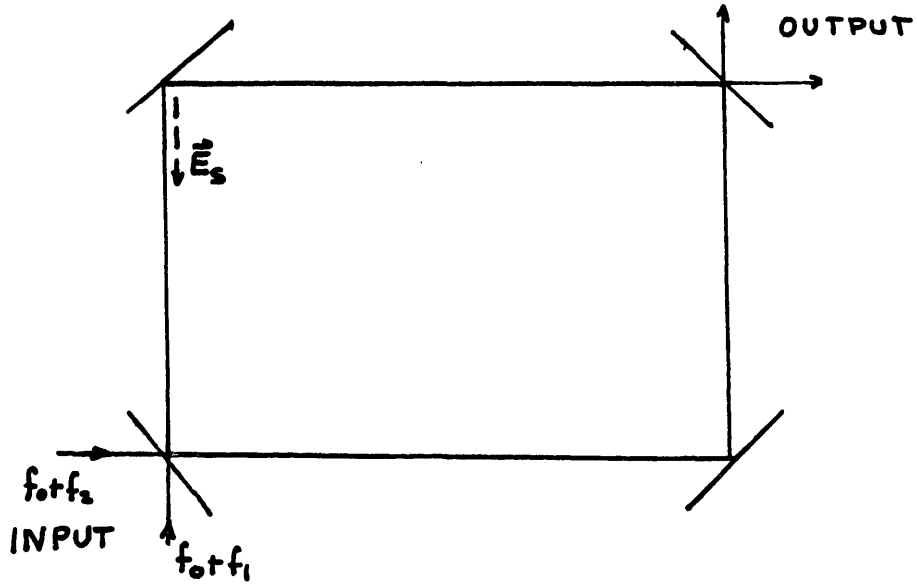


Figure 4.23

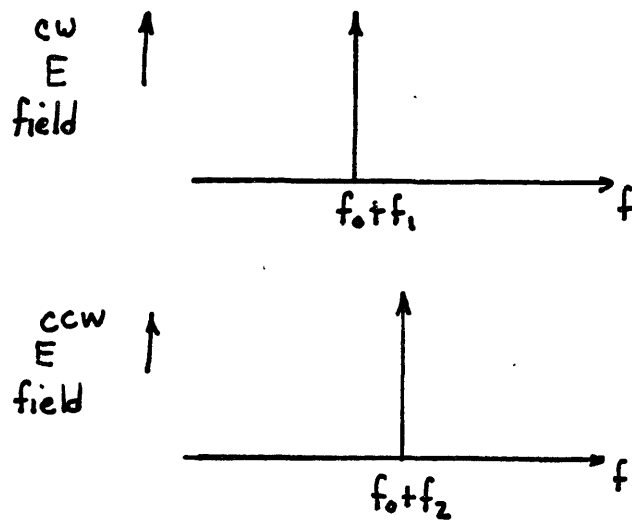


Figure 4.24

$$\Delta f_{\text{ccw}} = \frac{100 \text{ MHz}}{2\pi} \left(\frac{E_s}{E_o} \sin \theta_s \right) \quad (4.20)$$

Now if $f_1 \neq f_2$, as depicted by the power spectrum in Figure 4.24, then

$$\theta_s = 2\pi(f_1 - f_2) t \quad (4.21)$$

resulting in an oscillatory resonance frequency shift at $f_1 - f_2$.

For a typical cavity mirror the total fractional scattered intensity is approximately .1%. For scattering into a solid angle of $\sim 10^{-6} (\text{rad})^2$, based on a 1 m cavity length and a mode size of ~ 1 mm, the fraction of backscattered intensity is typically on the order of 10^{-9} . Hence, $\frac{E_s}{E_o}$ is typically 3×10^{-5} . For simplicity, if only one mirror is considered and the backscattering is in only one direction, this corresponds to an apparent oscillatory non-reciprocal phase shift of amplitude ~ 500 Hz. In this experimental setup, this amplitude was observed to vary between 100 to 500 Hz. Since this oscillatory error is at frequency $f_1 - f_2$, it is sufficiently attenuated for the filter time constants, τ , appropriate to the performance curve (see Figure) as long as

$$f_1 - f_2 \gg 1/2\pi\tau \quad (4.22)$$

The data in Figure 4.10 was taken for $f_1 - f_2 \sim 70$ Hz.

Many applications, of course, require the use of small frequency differences and it is therefore desirable to further reduce the scattering effect in the broad frequency region of interest. This may be conveniently achieved by putting a phase modulator (P/M) in either beam prior to cavity injection as shown in Figure 4.9. If the P/M is driven at a frequency f_j with a sufficient amplitude to suppress the carrier frequency, then the frequency of the oscillatory error signal will be shifted by integral multiples of $\pm f_j$ (depicted for a few sidebands in the spectrum shown in Figure 4.25), which can then be removed by appropriate filtering techniques. This technique is illustrated in Figure 4.26 for $f_2 - f_1 \sim 1$ Hz, where the scattering was enhanced for illustration. The left-hand portion of Figure 4.26 is the open loop output of PSD#2, demonstrating the oscillatory error at ~ 1 Hz. When the phase modulator was driven at $f_j = 4$ KHz, the frequency of this oscillation was shifted by integer multiples of 4 KHz, which were therefore greater attenuated (right hand portion of Figure 4.26) because they fell well outside the 5 Hz bandwidth of the employed filter.

Another, yet more extensive, way that this backscattering phenomena may introduce errors is by coupling reciprocal laser frequency noise into non-reciprocal sources of error. For instance, if the laser frequency jitters at frequency f_n , the resultant sidebands, as shown in Figure 4.27, are common to both beams. In the absence of scattering this jitter introduces no error, as discussed in Section 4.3. In the presence of scattering, the sidebands of the two beams beat, causing an oscillatory error at the corresponding beat frequency. Thus, if, for

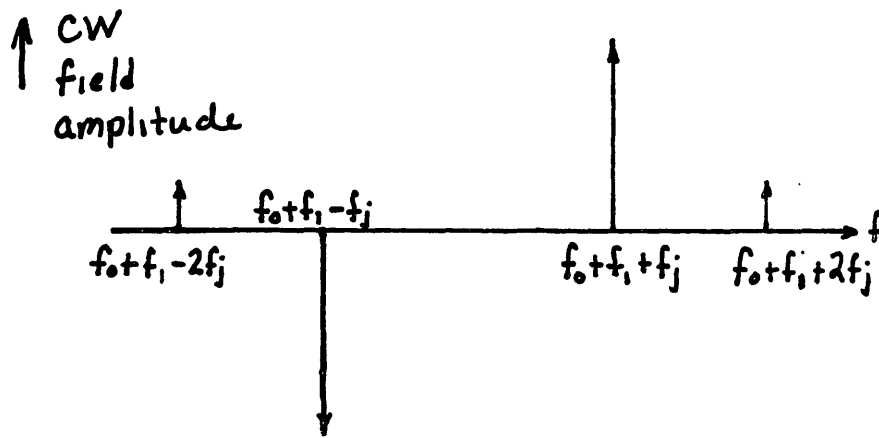
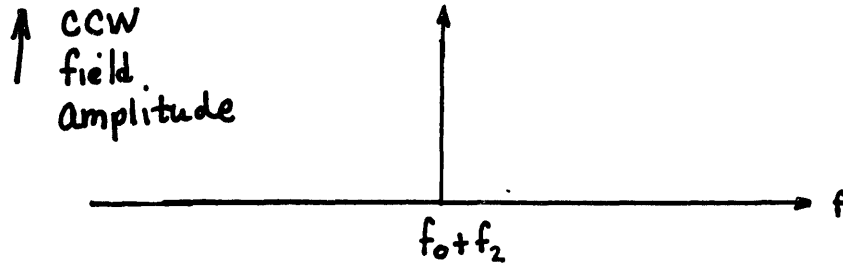


Figure 4.25

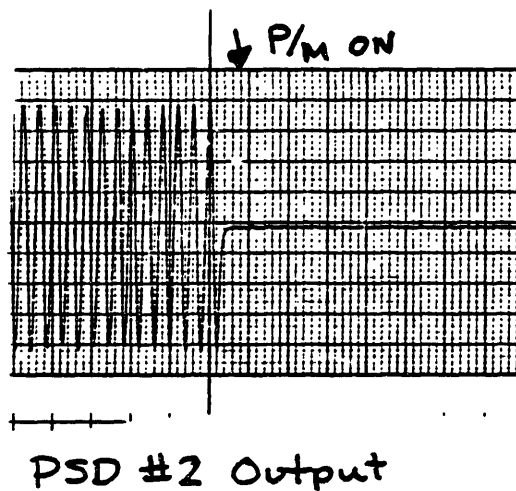


Figure 4.26

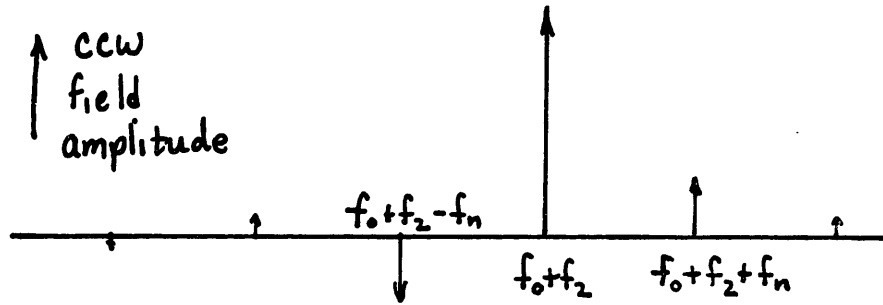
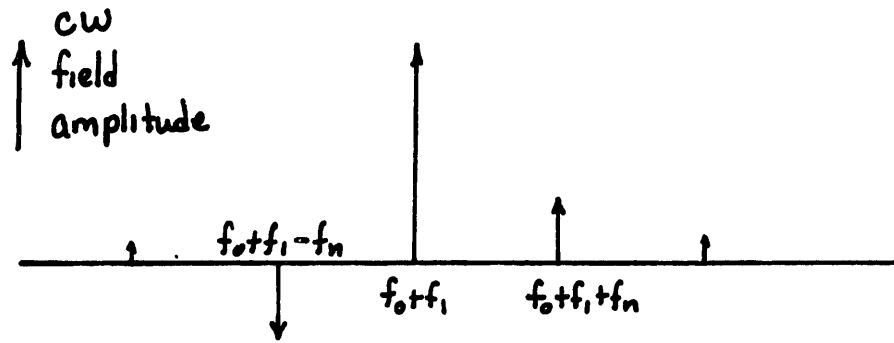


Figure 4.27

example, $f_2 - f_1 = 70$ Hz and the laser frequency jitter was at $f_n \sim 70$ Hz, a resultant oscillatory error was observed even with the low frequency filter time constants that we commonly employ. Figure 4.28 shows part of the low frequency noise spectrum of our laser. The left-hand scale indicates the laser frequency jitter amplitude at f_n . The right-hand scale indicates the corresponding output error size when $f_2 - f_1$ was tuned to approximately f_n . Because the laser jitter was found to roll off at higher frequency, this error was also greatly attenuated using the previously mentioned phase-modulation technique.

4.6e. Polarization Effects

Yet another potential source of error is due to the two polarization eigenstates of the cavity having different resonance frequencies. Consider light of vertical polarization given by \vec{E}_x and of horizontal polarization \vec{E}_y incident on a cavity mirror tilted at $\sim 45^\circ$ as shown in Figure 4.29. Because the mirror surface is not at normal incidence to the light, \vec{E}_x and \vec{E}_y will have different phase shifts and different reflected amplitudes at the dielectrically coated mirror given by the Fresnel reflection coefficients. Denoting the reflection coefficient for \vec{E}_x as unity (for simplicity) and the relative reflection coefficient of \vec{E}_y as $ne^{i\beta}$, the reflected fields are given by,

$$\begin{pmatrix} E_x \\ E_y \end{pmatrix}_r = \begin{pmatrix} 1 & 0 \\ 0 & ne^{i\beta} \end{pmatrix} \begin{pmatrix} E_x \\ E_y \end{pmatrix}_i \quad (4.23)$$

where the subscripts "i" and "r" indicate the incident and reflected

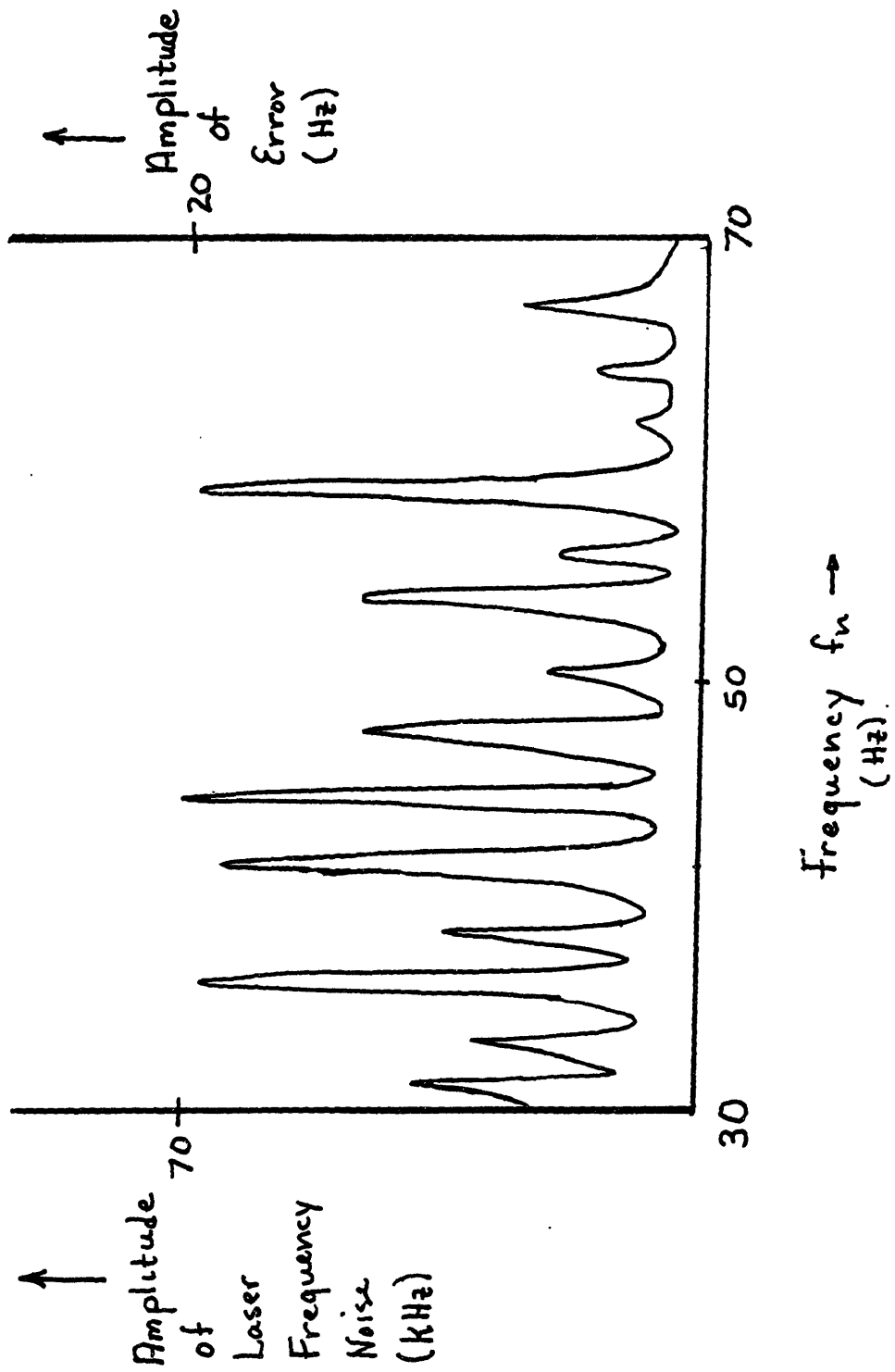


Figure 4.28

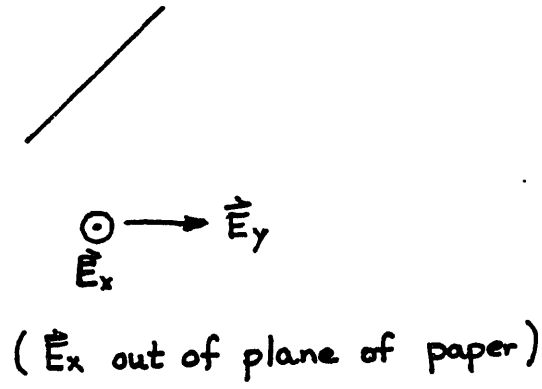


Figure 4.29

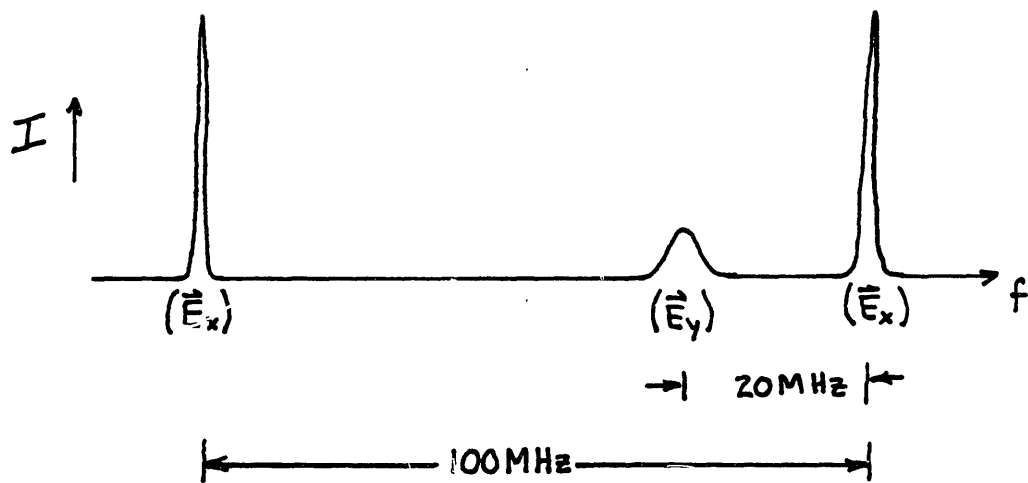


Figure 4.30

fields, respectively.

In the cavity used in this experiment, the mirrors were coated for high reflectivity for vertical polarization and tilted at $\sim 45^\circ$. The factor η in the above expression was less than unity, resulting in a larger net loss for horizontal polarization in the cavity. In addition, because of the relative phase shift β ($\sim 30^\circ$ when summed over all mirrors in the cavity), the resonance frequencies of the vertical and horizontal polarizations were different by ~ 20 MHz. This is depicted in Figure 4.30, where a free spectral range of the cavity is shown for the case of both polarizations being present in the cavity. The increased linewidth of the horizontal polarization is due to the fact that $\eta < 1$.

If vertically polarized light is used to measure the resonance frequencies of the cavity, the presence of the horizontal component of polarization appears as a higher order mode and can pull the effective resonance frequency of the vertical reference mode (see Section 4.6a). If different amplitudes of \vec{E}_y are injected in the cavity for cw and ccw beams, this results in a non-reciprocal phase shift. Hence, in the passive ring resonator setup, a polaroid was used to attenuate the component of horizontal polarization entering the cavity.

It is convenient here to briefly discuss, in a semi-analytical manner, the more complicated case of a birefringent element being present in the cavity. This case applied to the measurement of the Fresnel-drag, where a glass window with residual stress birefringence was inserted into the cavity (see Chapter 5).

Consider the case, as shown in Figure 4.31, of light incident on a birefringent transparent material. The ordinary and extraordinary axes

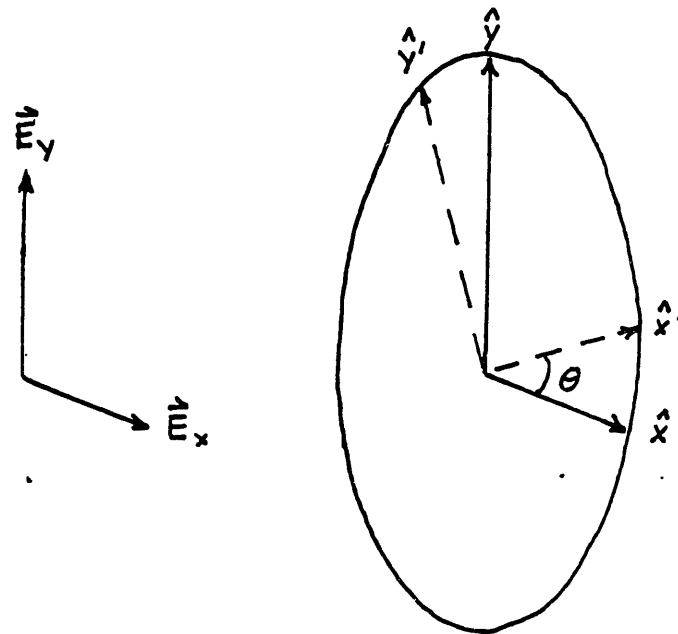


Figure 4.31

of the material are denoted as x' and y' . The relative phase shift for light propagation along the y direction with respect to x' direction is denoted as γ . If the polarization of the incident light is along the x or y direction which are inclined at an angle θ with respect to the axes x' and y' , then the transmitted fields are given by,

$$\begin{pmatrix} E_x \\ E_y \end{pmatrix}_t = \begin{pmatrix} \cos \theta & -\sin \theta \\ \sin \theta & \cos \theta \end{pmatrix} \begin{pmatrix} 1 & 0 \\ 0 & e^{i\gamma} \end{pmatrix} \begin{pmatrix} \cos \theta & \sin \theta \\ -\sin \theta & \cos \theta \end{pmatrix} \begin{pmatrix} E_x \\ E_y \end{pmatrix}_i \quad (4.24)$$

where the matrices in terms of θ are the familiar rotation matrices for transforming between the primed and unprimed coordinate systems.

Equation (4.24) reduces to

$$\begin{pmatrix} E_x \\ E_y \end{pmatrix}_t = \begin{pmatrix} \cos^2\theta + \sin^2\theta e^{i\gamma} & \cos \theta \sin \theta (1-e^{i\gamma}) \\ \sin \theta \cos \theta (1-e^{i\gamma}) & \sin^2\theta + \cos^2\theta e^{i\gamma} \end{pmatrix} \begin{pmatrix} E_x \\ E_y \end{pmatrix}_i$$

$$= \begin{pmatrix} a & c \\ c & b \end{pmatrix} \begin{pmatrix} E_x \\ E_y \end{pmatrix}_i \quad (4.25)$$

Because of the off-diagonal elements in the above equation, incident light polarized along either the x or y directions will be rotated and phase shifted such that the output is a superposition of x and y polarized light.

Briefly, to obtain an understanding of how the resonance frequencies of the cavity are altered when a birefringent element is inserted into the cavity, consider the case shown in Figure 4.32. Here, for simplicity, only of the mirror reflectivities (that of M_4) in Figure 4.32, is shown to have the polarization dependence in Eq. (4.23), where $\eta = 1$. Mirror M_2 is assumed to have a reflection coefficient of 1, while mirrors M_1 and M_3

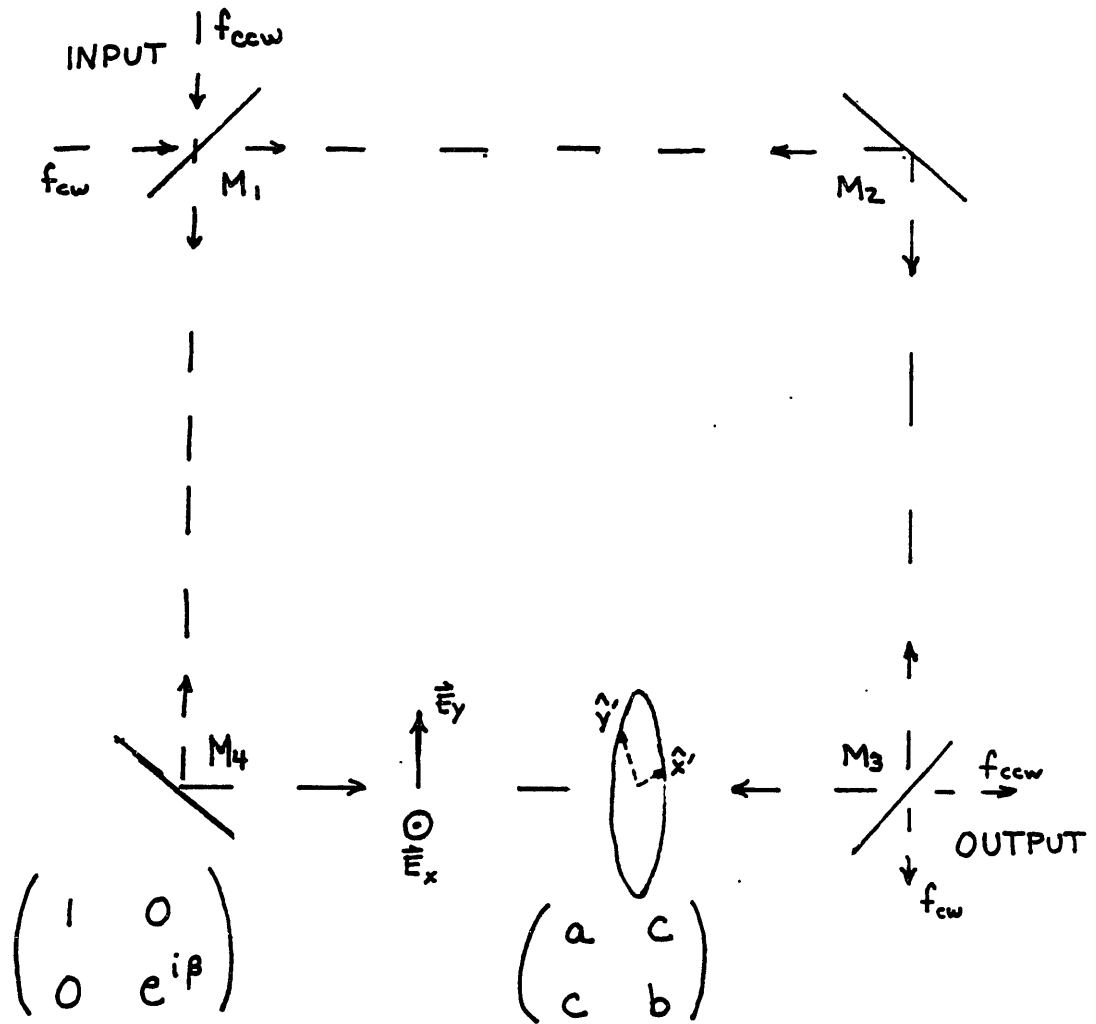


Figure 4.32

are assumed to have reflection and transmission coefficients of r and t , respectively. Consider light of polarization in either the x (vertical) or y (horizontal) directions incident on the cavity. The total ccw transmitted field, when summed over all the transmitted output fields for the multiple beam interference (analogous to the argument for a single polarization in Section 3.4) gives

$$\begin{pmatrix} E_x \\ E_y \end{pmatrix} = t^2 e^{i\delta/2} \begin{pmatrix} a & c \\ c & b \end{pmatrix} \begin{pmatrix} 1 & 0 \\ 0 & e^{i\beta} \end{pmatrix} \left[1 + r^2 e^{i\delta} \begin{pmatrix} a & c \\ c & b \end{pmatrix} \begin{pmatrix} 1 & 0 \\ 0 & e^{i\beta} \end{pmatrix} + \dots \right] \begin{pmatrix} E_x \\ E_y \end{pmatrix}_i \quad (4.27)$$

where δ consists of all the phase shifts in the cavity other than those in the birefringent element and M_4 . The ccw transmitted field is thus given by

$$\begin{pmatrix} E_x \\ E_y \end{pmatrix} = t^2 e^{i\delta/2} \begin{pmatrix} a & c \\ c & b \end{pmatrix} \begin{pmatrix} 1 & 0 \\ 0 & e^{i\beta} \end{pmatrix} \sum_{n=0}^{\infty} \left[\begin{pmatrix} a & c \\ c & b \end{pmatrix} \begin{pmatrix} 1 & 0 \\ 0 & e^{i\beta} \end{pmatrix} r^2 e^{i\delta} \right]^n \begin{pmatrix} E_x \\ E_y \end{pmatrix}_i \quad (4.28)$$

Likewise, a similar expression may be obtained for the cw propagating beam,

$$\begin{pmatrix} E_x \\ E_y \end{pmatrix} = t^2 e^{i\delta/2} \sum_{n=0}^{\infty} \left[\begin{pmatrix} 1 & 0 \\ 0 & e^{i\beta} \end{pmatrix} \begin{pmatrix} a & c \\ c & b \end{pmatrix} r^2 e^{i\delta} \right]^n \begin{pmatrix} E_x \\ E_y \end{pmatrix}_i \quad (4.29)$$

The summation in terms in Eqs. (4.28) and (4.29) contain the roundtrip phase shift inside the cavity for the two polarizations of light. In both the cw and ccw cases, as shown in Eqs. (4.28) and (4.29), the polarizations E_x and E_y are not polarization eigenstates of the cavity because the birefringent material rotates the polarization of the light inside the cavity (as represented by the off diagonal element c). The new eigenstates of the cavity are thus superpositions of E_x and E_y . The phase of the eigenvalues for these new eigenstates is then a measure of the resonance frequencies of the cavity.

As one step further, because the matrices in the summations in Eqs. (4.28) and (4.29) do not commute the polarization eigenstates and eigenvalues are different for cw and ccw beam propagation. Hence, the resonance frequencies of the cavity are different for cw and ccw propagation.

For demonstration of this effect, a glass window was stressed to enhance the birefringence and placed inside the cavity. The cw and ccw resonances are shown in Figures 4.33a and 4.33b for the case of vertically polarized input light. (These figures are traced from actual data.) The TEM_{00} modes in the figures exhibit asymmetries as a result of the enhanced birefringence in the glass. Here, the incident light was rotated inside the cavity and split into the two polarization eigenstates. The lineshapes in Figures 4.33a and 4.33b are superpositions of these two eigenstates of different resonance frequencies, thus giving the asymmetries shown in the figures. In addition, it must be noted that the asymmetries are different for

CW BEAM

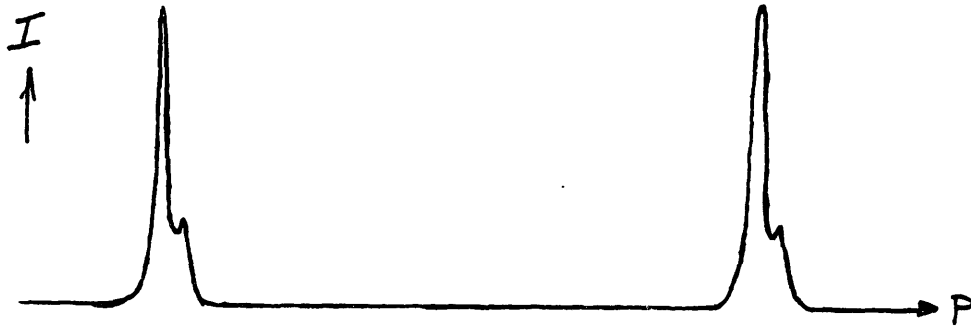


Figure 4.33a

CCW BEAM



Figure 4.33b

cw and ccw propagation, which resulted in a non-reciprocal phase shift ($\sim \Delta f = 5 \text{ KHz}$).

Because of inhomogeneities in the stress birefringence in the glass the line asymmetries and thus the non-reciprocal phase shift was found to be a function of the transverse position of the beam inside the glass. In this case, as the glass window was moved (over its entire diameter) with respect to the beam, the resonance frequency difference $\Delta f = f_{\text{cw}} - f_{\text{ccw}}$ was found to vary by a few KHz.

For the case where care was taken to minimize the stress in the glass, the resonance frequency difference Δf is plotted as a function of the transverse position x of the beam inside the glass, as shown in Figure 4.34. Due to residual stress birefringence in the glass (from the manufacturing process) there was still a non-reciprocal phase shift of up to 50 Hz depending on the position of the beam inside the glass. Here, because the effect was relatively small, no asymmetries were directly visible on the cavity lineshape.

The conclusion from these studies of birefringence effect was that care should be taken to minimize the stress in the glass when conducting the Fresnel-drag experiment. In addition, it was also necessary, as discussed in Section 5.2, to minimize transverse motion of the glass when the glass was moved back and forth along the cavity axis in the drag measurement.

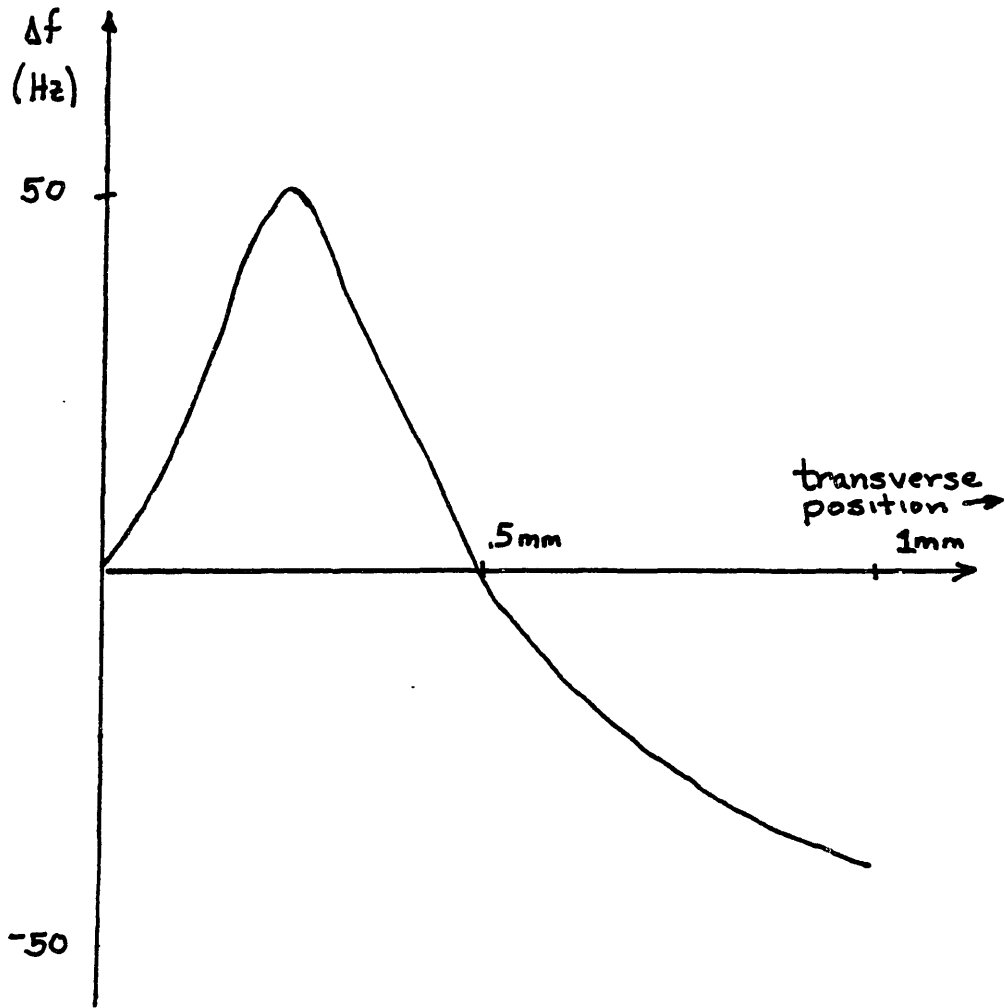


Figure 4.34

CHAPTER 5

MEASUREMENT OF FRESNEL-DRAG IN THE
PASSIVE RING RESONATOR

5.1. Introduction and Overview of Experimental Arrangement

This chapter describes the application of the passive ring resonator setup to the Fresnel-drag measurement, as well as the measurement itself. For reasons discussed in Section 4.2, and because of the error sources presented in Chapter 4, the Fresnel-drag measurement presented here is an AC form of the "shuttling rod" configuration used by Zeeman.¹⁶

A simplified diagram of the arrangement used for measurement of the drag is shown in Figure 5.1. As was mentioned in Section 4.2, a glass window was moved with sinusoidal displacement $|\vec{z}| = z_0 \sin 2\pi f_f t$ along the direction of the propagation of light inside the cavity. The sinusoidal velocity of the medium was thus given by $|\vec{v}| = 2\pi f_f z_0 \cos 2\pi f_f t$. The displacement of the medium ($z_0 \approx 1$ cm) was measured by means of an interferometer in which a mirror was mounted on the same mount as that of the glass window to form one arm of the interferometer. The displacement amplitude was servo stabilized. The driving frequency, f_f (~ 5 Hz), was measured by means of an electronic counter. The oscillatory resonance frequency shift at frequency f_f due to the drag was then measured. The predicted resonance frequency shift for glass at normal incidence was given by Eq. (4.3). For reasons

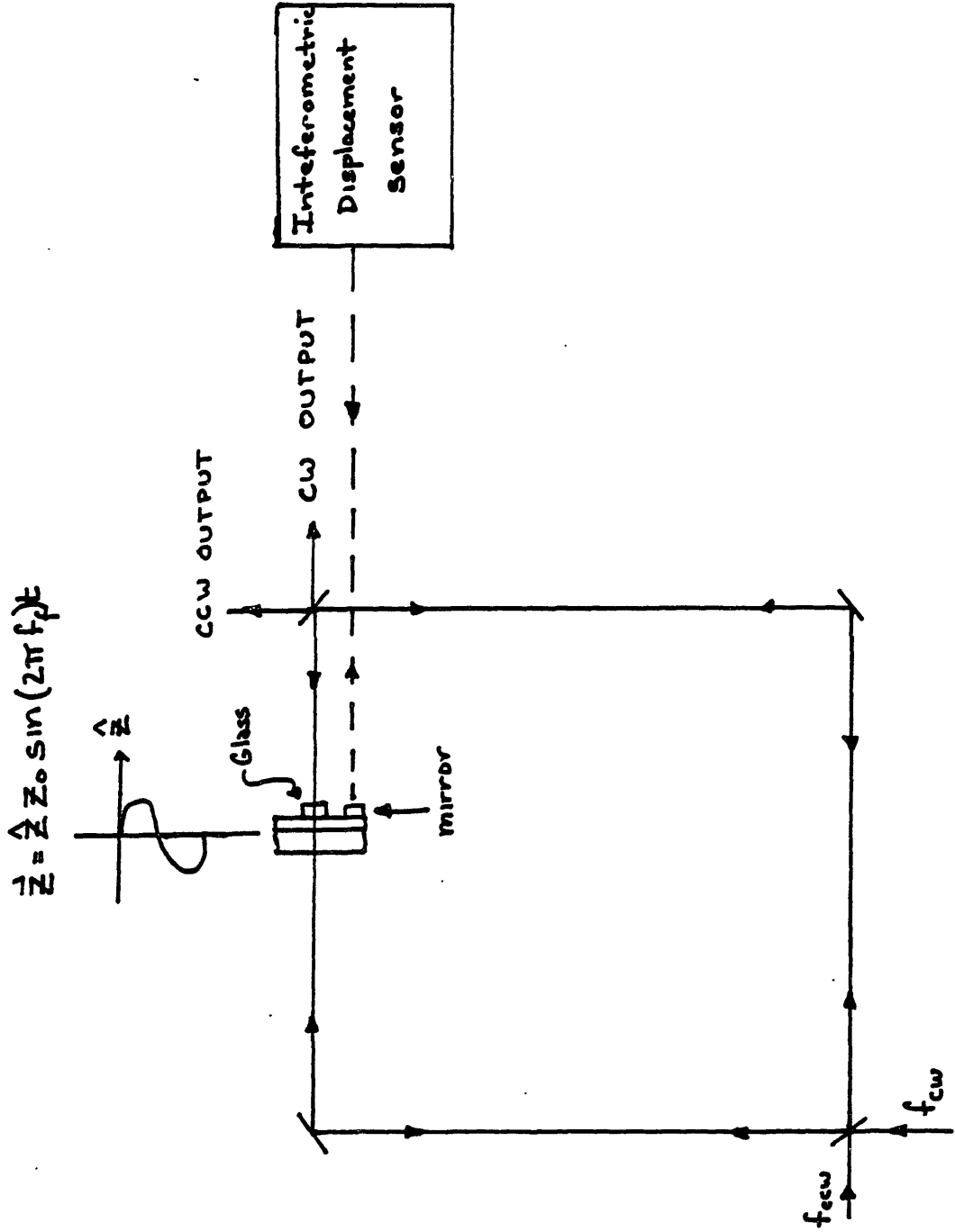


Figure 5.1

discussed in Section 5.2, however, it was necessary to tilt the glass at an angle of incidence θ ($\sim 5^\circ - 10^\circ$) and the correction to Eq. (4.3) for this configuration is presented in Section 5.6.

It is convenient here to mention that the feasibility of doing a precision measurement of the Fresnel-drag was first determined based on fundamental signal to noise considerations. For a typical arrangement used in this experiment where glass of index $n \sim 1.5$ and length $l \sim 1$ cm was moved at a velocity $v \sim 25$ cm/s the expected resonance frequency shift Δf was ~ 1 KHz. By detecting the resonance frequency shift at the driving frequency f_f and averaging over a reasonable integration time of $\tau = 100$ s, it was considered possible to measure the resonance frequency shift to $\sim .02$ Hz based on shot-noise statistics. Since our intention was to measure the drag to ~ 1 part in 10^4 as a first attempt, the experiment was thus considered feasible.

This chapter begins with a discussion of the various considerations involved with the placement of the glass window inside the cavity as well as a discussion of the considerations for moving the glass window inside the cavity. The apparatus used for constraining the motion of the glass is also described. In Section 5.3, the details of the alignment, measurement and stabilization of the velocity are presented. The technique employed for measurement of the resonance frequency shift due to the drag is discussed in detail in Section 5.4. The calibration of the measurement, discussed in Section 5.5 is broken into two separate sections, the first (Section 5.5.1) of which discusses various checks performed on the measurement system. The latter section,

Section 5.52, describes the measurement of the various parameters which appear in the drag calculation. Here, a typical data run where the resonance frequency shift and velocity were measured is also presented for illustration. The chapter concludes with a discussion of the correction to the drag calculation for the configuration used in this experiment where the glass was tilted at an angle of incidence θ relative to the direction of light propagation.

5.2. Considerations and Apparatus for Moving Glass in Cavity

One of the first considerations when introducing a glass window into the cavity was that cavity finesse should not be severely compromised. Hence, the glass windows were anti-reflection (AR) coated on both sides. Typically, this lowered the finesse by a factor of approximately 1.5. Another potential problem source, which was attenuated by the AR coatings, was that due to multiple reflections in the glass. For a typical AR coated glass window, the change in reflected intensity (due to etalon effects) as a function of small angular displacement is depicted in Figures 5.2a and 5.2b. In Figure 5.2a the maximum change in intensity for angles near 1° was approximately 0.6%. Due to the increased spatial separation between reflections, the corresponding intensity changes at $\sim 4^\circ$ were less than 0.15%. It was considered desirable to attenuate any possible effects due to multiple reflections, and therefore the glass windows in this experiment were tilted by a minimum angle of incidence of $\sim 5.1^\circ$ with respect to the direction of light propagation. In addition, data was

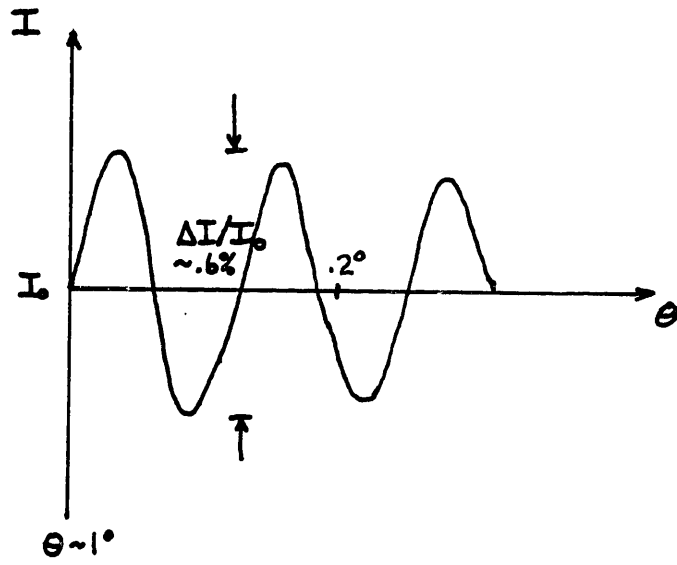


Figure 5.2a

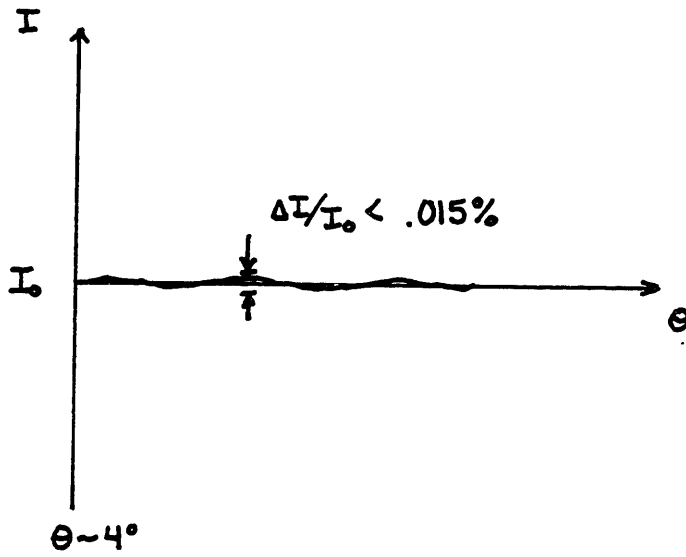


Figure 5.2b

taken to check the angular dependence (see calculation of angular dependence of drag, Section 5.6) of the Fresnel drag for angles of incidence up to $\sim 13^\circ$.

There were many other considerations, based on the measurement problems presented in Chapter 4, that necessitated tight control of the glass motion in the cavity. Even though the effects of birefringence and cavity misalignment are DC effects, it was certainly important to minimize the modulation of these effects when moving the glass back and forth inside the cavity. The birefringence studies discussed in Section 4.6e, showed that one of the most important considerations, was that the glass should be restricted from moving transverse to the beam. As shown in Figure 4.34, glass translation of ~ 0.1 mm with respect to the beam was found to cause an error Δf of approximately 30 Hz. Hence, to assure that the beam did not translate across the glass throughout its motion, it was necessary to align the velocity vector of the glass as closely as possible to the propagation vector of the light (see Section 5.3).

It was also necessary to restrict angular wobble of the glass throughout its motion, so as to avoid translational misalignment of the cavity mode (see misalignment, discussion in Section 4.6a). In addition, angular wobble of the glass was undesirable because slight angle changes greatly increase the optical pathlength inside the glass and thus the resonance frequency of the cavity. For instance, for an angle of incidence $\theta \approx 6.6^\circ$, using glass of $n \sim 1.5$ and thickness 6 mm, an angular wobble of ~ 0.1 mrad was found to produce a reciprocal

resonance frequency shift of ~11 MHz. Based on the error mechanism discussed in Section 4.6b, this was potentially a large source of error.

With the above considerations in mind, a few available linear bearing-mounts, of the type depicted in Figure 5.3a, were investigated. Here, the glass was mounted on a mirror mount, which was then attached to a cylindrical shaft (brass tubing). The shaft was constrained to move in the z direction by two nylon bearings (see also velocity alignment, Section 5.3). The nylon bearings ~1/8" thick were tightly press-fitted into a hollow aluminum block of length ~6". The mirror mount allowed for adjustment of the angle of incidence in both the horizontal and vertical directions. The glass was snugly pressed against the mirror mount by means of an aluminum retaining ring, as shown in the Figure 5.3a. Rubber "O" rings were placed on both sides of the glass in order to minimize stress birefringence.

As shown in Figure 5.3a, another similar bearing-shaft system was attached via an aluminum crossbar to the main bearing-shaft system to constrain the latter shaft from rotating about its axis. Small adjustments of the crossbar length also allowed for fine tuning of the bearing-shaft tolerance, and thus, the angular wobble as well. Both bearing shafts were then moved in the z-direction by means of an electro-mechanical driver, which was connected to the crossbar via an aluminum rod. To eliminate coupling vibrations to the cavity the whole assembly was attached to a structure which was anchored to the ceiling and floor, but mechanically isolated from the cavity. This isolation structure is shown in the photograph of the setup in Figure 5.3b.

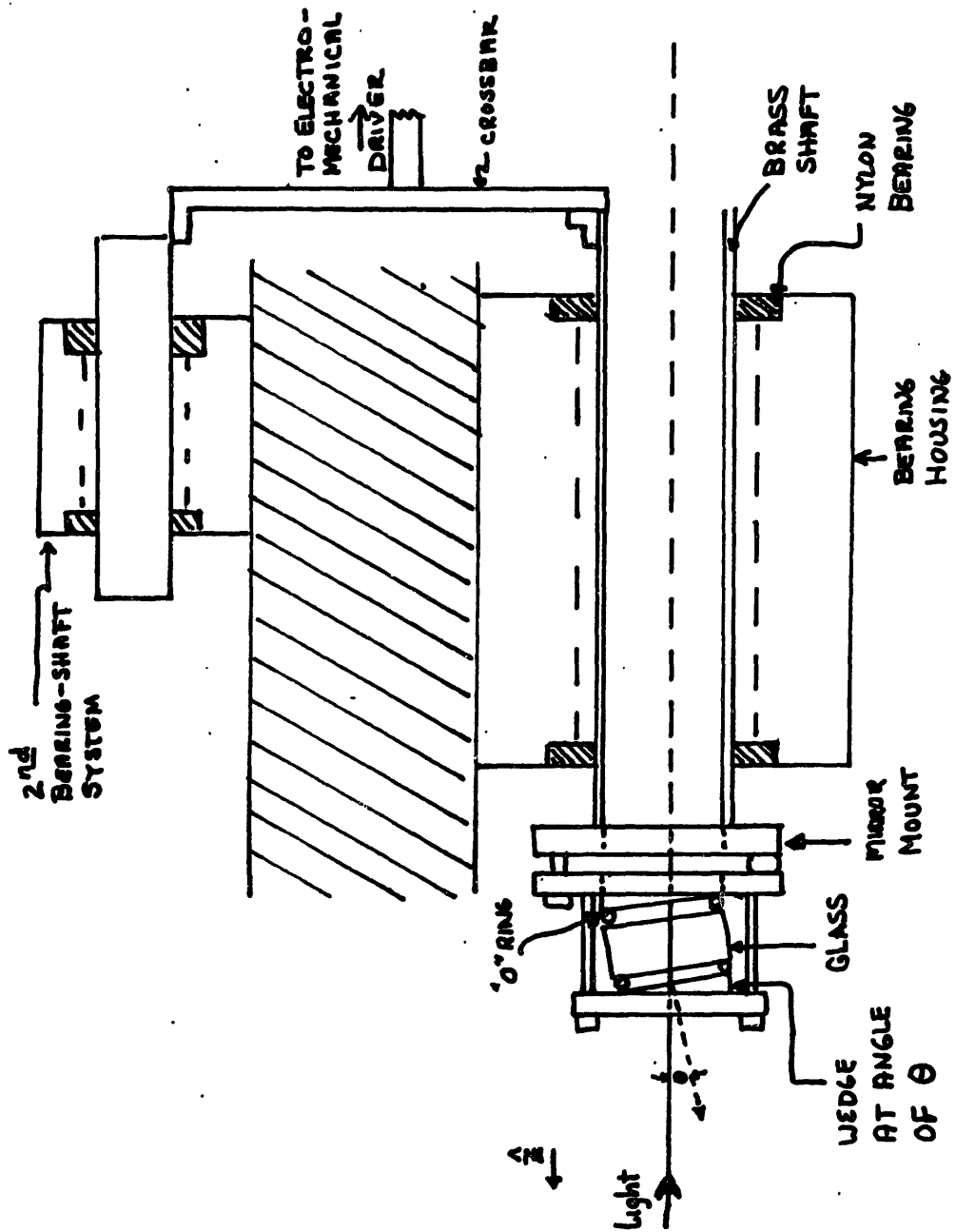


Figure 5.3a

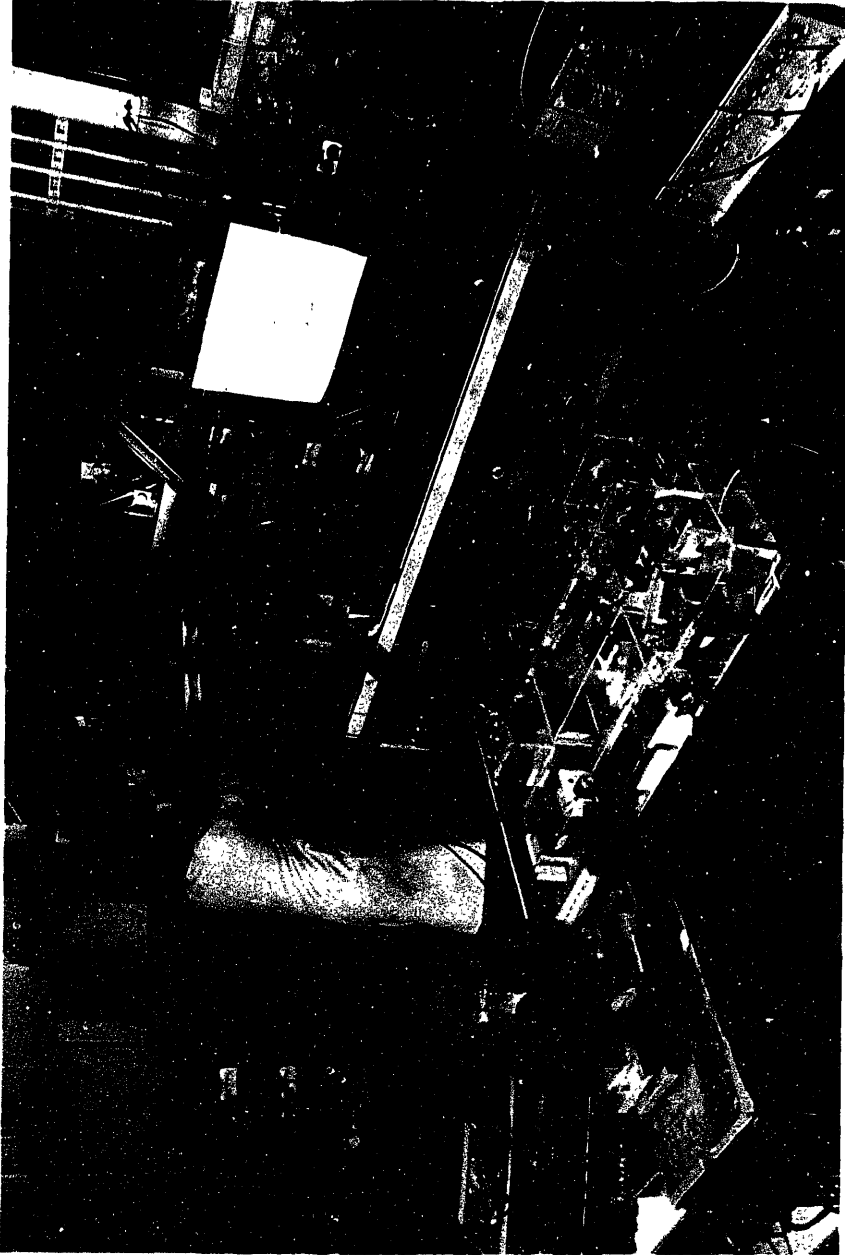


Figure 5.3b

A few similar bearing systems, with different tolerances between the shaft and bearing, were tested to find a reasonable compromise between ease of driving and low wobble. The sag and wobble of the bearing-shaft system was then checked by mounting a mirror in place of the glass and monitoring the angular deviation of a reflected laser beam off the mirror surface. The shaft was moved slowly (\sim DC) to record the angular deviation as a function of z . This deviation was found to match the deviation at faster sinusoidal rates (\sim 5 Hz). Thus, the slow sag of the bearing-shaft system was the same as the angular wobble when driven sinusoidally over the same range of z (\sim 1 cm).

The non-reciprocal phase shift due to bearing-shaft angular sag was then evaluated for the case of the glass window moving in the resonator. For the bearing-shaft system used in this experiment, a typical curve for the non-reciprocal phase shift Δf , as a function of the position, z , is shown in Figure 5.4. Here, z is varied very slowly ($v = 0$) to avoid Fresnel-dragging of the light. This curve thus was a measure of the sum of the effects of glass misalignment in the cavity, including those effects due to birefringence in glass. For the case of the glass moving at sinusoidal velocity at frequency f_f , this position dependence was thus modulated at f_f (see system checks, Section 5.5.1).

As previously mentioned, another source of error at the sinusoidal dragging frequency, f_f , was due to large reciprocal pathlength changes resulting from angular wobble of the glass (see Section 4.6b).

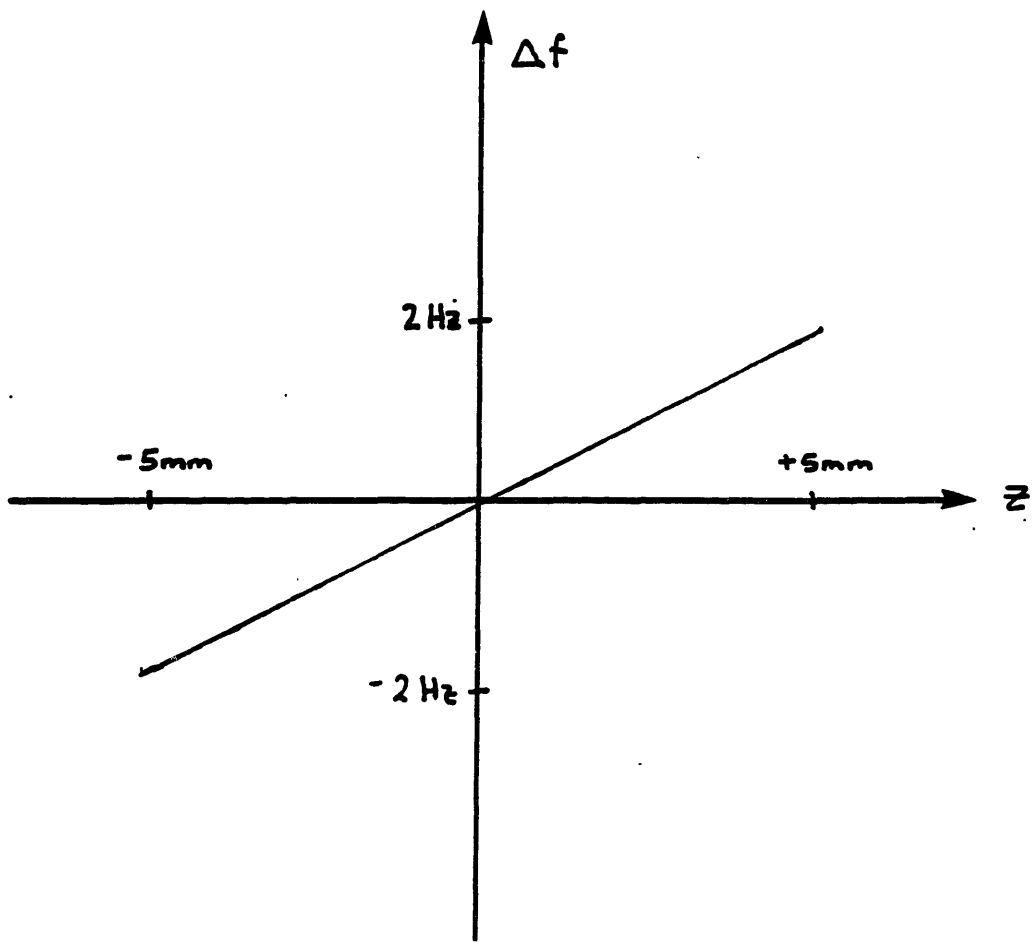


Figure 5.4

For the bearing-shaft system actually used, with a 6 mm piece of glass of $n \sim 1.5$ and angle of incidence $\theta \sim 6.6^\circ$, the reciprocal resonance frequency shift was ~ 2.2 MHz. Since the resultant non-reciprocal error was determined by the gain of the primary feedback loop at f_f , it was not considered feasible to move the glass at a higher frequency, where the gain was low. On the other hand, knowing that the magnitude of the Fresnel-drag was proportional to f_f , it was desirable to increase the gain of feedback loop and seek a reasonable compromise for f_f . Thus, another integrator-type amplifier of transfer function similar to those depicted in Figure 4.21, was added to the servo electronics. The resultant loop gain, as shown in Figure 5.5, had the transfer function characteristics of a triple integrator at low frequency. For $f_f \sim 5$ Hz, the loop gain was $\sim 5 \times 10^4$, resulting in a residual reciprocal phase shift, of ~ 45 Hz for the previous example. With a subtraction (discussed in Section 4.6b) factor, β , stable to approximately 2%, this gave a net error of ~ 0.9 Hz. In this example, the magnitude of the Fresnel-drag was ~ 1 KHz.

The transfer function of the bearing-driver system provided yet another consideration for the selection of f_f . Because of the friction in the tight-tolerance bearing, the range of driving frequencies was fairly limited. Due to the effects of static friction there was significant cross-over distortion on the sinusoidal velocity (as shown in Figure 5.6a) for driving frequencies of 2 Hz and below. This output velocity, due to the bearing load, rolled off rapidly for $f_f \gtrsim 7$ Hz. As shown in Figure 5.6b, the output waveform for $f_f \sim 5$ Hz was reasonably undistorted (see Section 5.6a for a discussion of the effects of higher harmonics on the motion). Hence, for this setup, which was by no means optimized, a reasonable and

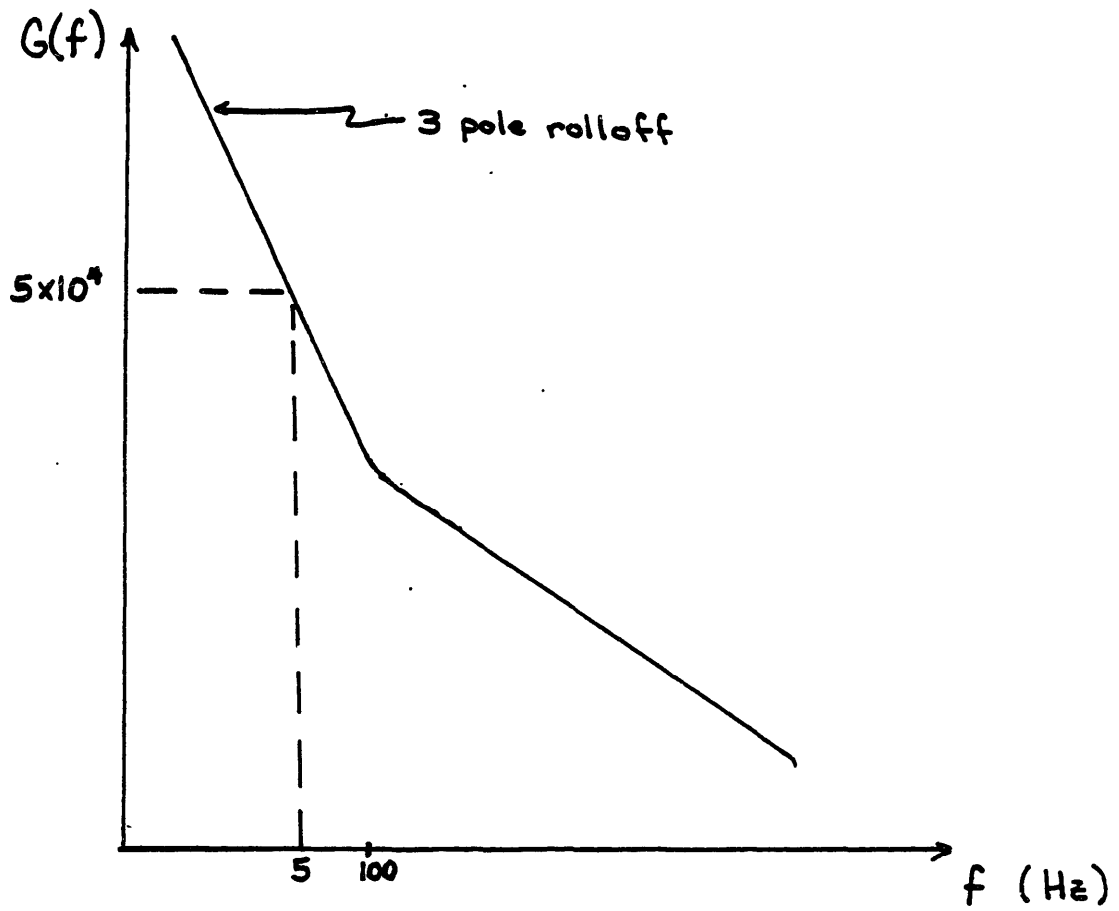


Figure 5.5

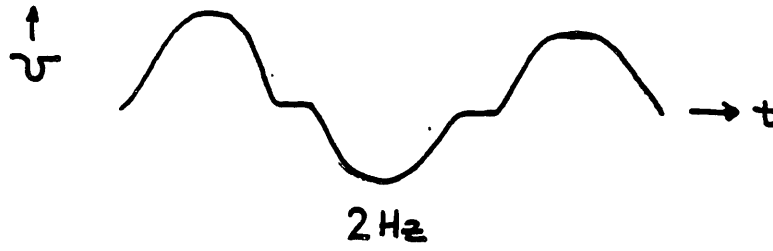


Figure 5.6a

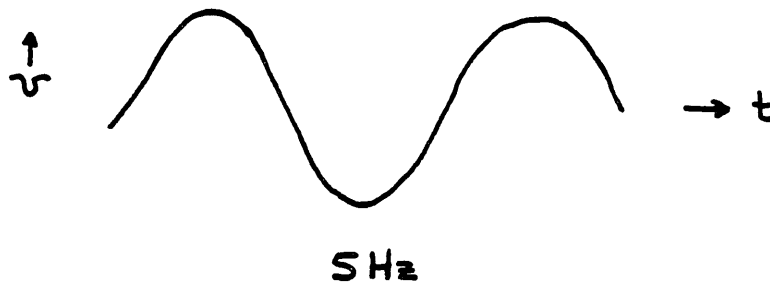


Figure 5.6b

convenient value of $f_f \sim 5$ Hz was used.

5.3. Details of Alignment, Measurement and Stabilization of the Velocity

The apparatus used during the experiment to align the velocity direction of the glass is shown in Figure 5.7a. The bearing housing was mounted directly to a large screw-adjusted mount that allowed for adjustment of the vertical angle of the bearing, θ_v . The mount, which also had a variable pivot for vertical translation, was attached to a milling-machine-type horizontal slide to provide for horizontal translation, x . The horizontal slide was then attached to a rotary table that allowed for adjustment of the horizontal angle of the bearing, θ_H .

To establish the direction and position of the cavity beam (without the bearing assembly in the cavity), the cavity mode was tightly apertured ($\lesssim .4$ mm) as shown in Figure 5.7b. An external laser beam was then brought into the cavity and aligned through the apertures, as shown in Figure 5.7c. A quadrant detector, shown in greater detail in Figure 5.7d, was mounted on the shaft of the bearing assembly in place of the glass mount. Using the x and y translations the shaft position was centered with respect to the beam as indicated by a null in the quadrant detector x and y outputs. The shaft was then driven back and forth over its ~ 1 cm range and the z dependence of the detector output was monitored. The velocity direction was thus aligned by changing θ_H and θ_v such that the detector outputs were zero for all z . Since the detector was sensitive to displacements of less than

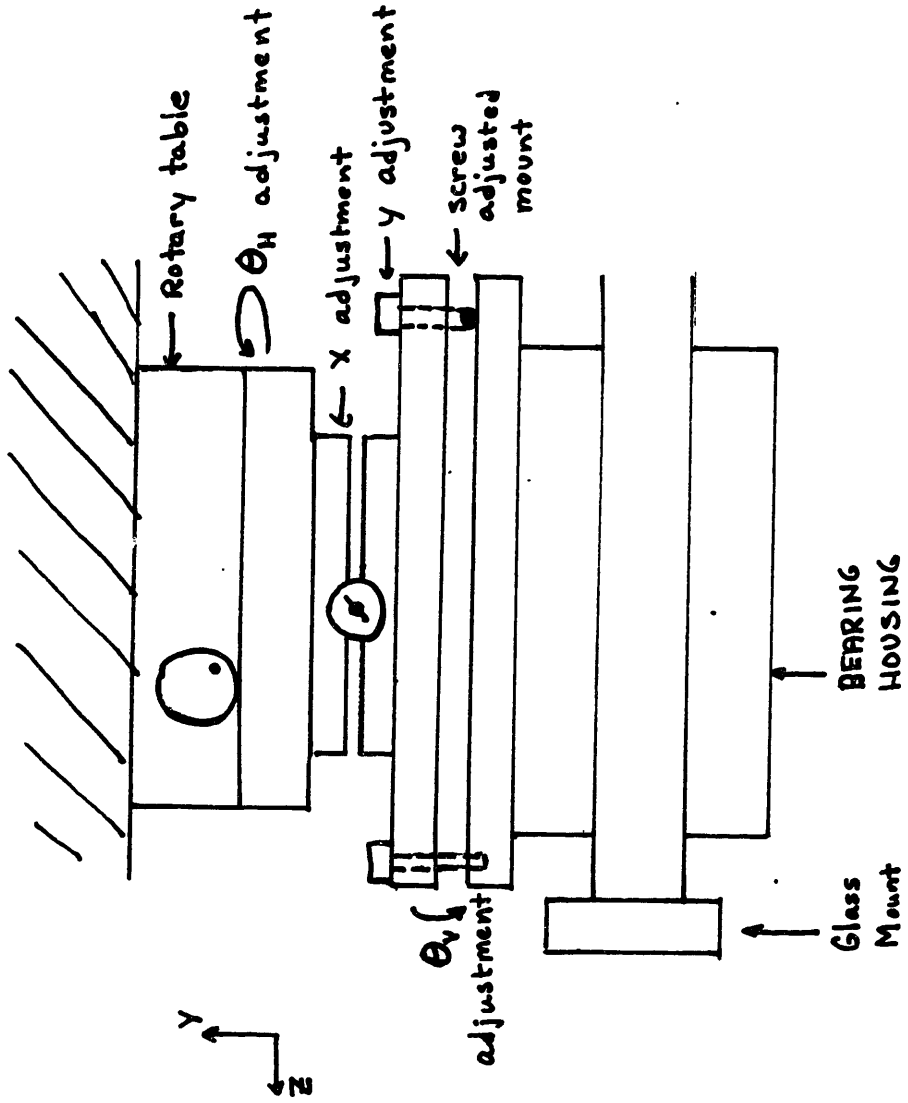


Figure 5.7a

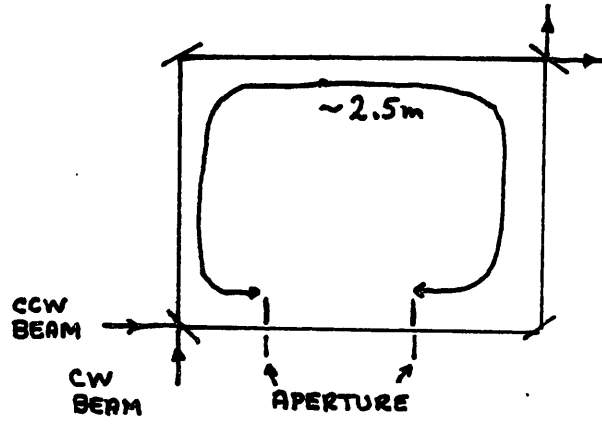


Figure 5.7b

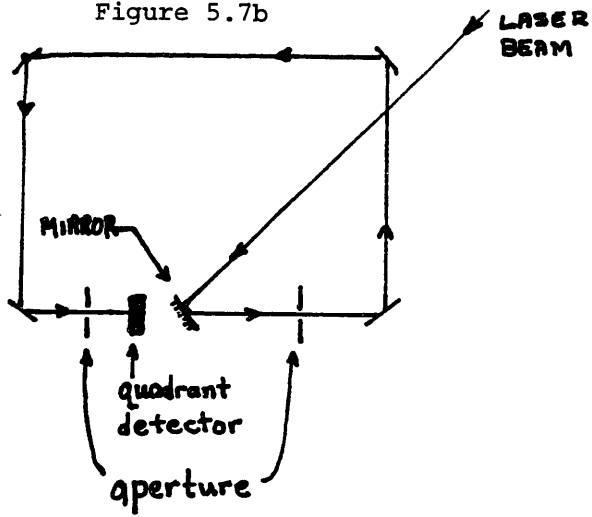


Figure 5.7c

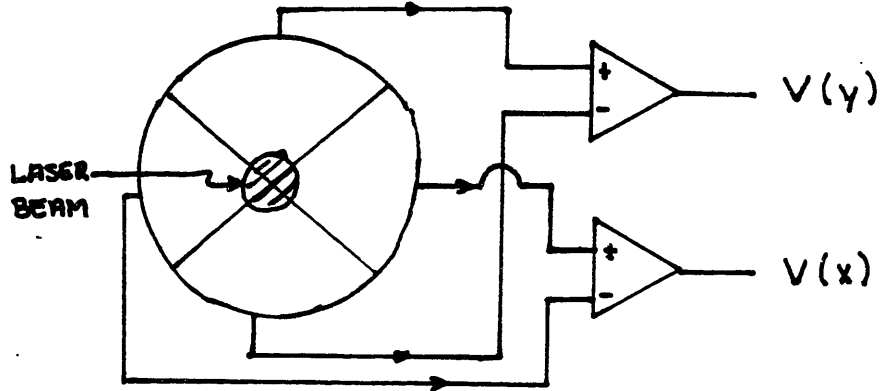


Figure 5.7d

$\sim 1 \mu\text{m}$, this alignment uncertainty was negligible compared to the uncertainty due matching the external alignment laser to the cavity mode reference. An upper bound on the magnitude of this error was roughly given by $\sqrt{2}$ times the aperture diameter, divided by the distance between apertures ($2\frac{1}{2}$ m), or about $\Delta\theta \approx 250 \mu\text{rad}$ ($\sim .8$ mm of arc). For the Fresnel-drag experiment, since the drag was known to be proportional to the cosine of the angle (see Section 5.6), this error was also considered negligible.

Because of the dependence of the glass birefringence effect on velocity misalignment, as discussed in Section 5.2, the position dependence of the non-reciprocal phase shift was very sensitive to this alignment. While the above error in the initial velocity alignment only caused an error $\Delta f \sim 1$ Hz over the 1 cm travel of the shaft, the isolation structure on which the bearing was mounted was found to bend by \sim a few minutes of arc throughout the long-term duration of the experiment. Hence, it was necessary to "tweak" θ_v and θ_H for each sample of glass to minimize the positional dependence of the non-reciprocal phase shift. The errors in the velocity direction resulting from this fine adjustment also resulted in uncertainties that were insignificant for the purpose of this experiment.

With the direction of the velocity determined, an apparatus was constructed for measuring the amplitude of the sinusoidal velocity at frequency f_f . Since the displacement of the glass was to be varied sinusoidally at f_f , i.e. $z = z_0(f_f) \sin(2\pi f_f t)$, it followed of course that the velocity was given by,

$$|\vec{v}(f_f)| = 2\pi f_f z_o(f_f) \cos[2\pi f_f t] \quad (5.1)$$

where $z_o(f_f)$ was the amplitude of the displacement at the driving frequency f_f .* The frequency f_f was measured with a counter which was both accurate and stable enough for the purposes of this experiment (see Section 5.5.2b). Forgetting the AC detection for the moment, it was convenient to measure the displacement z by interferometric means. For a peak to peak displacement of .8 cm at $f_f = 5$ Hz (again using $n = 1,5$, and glass thickness 6 mm) the Fresnel drag was expected to result in a peak to peak frequency shift of ~1 KHz. Since, in principle, a simple interferometer was known to be sensitive to length changes of less than one fringe, it was considered achievable to measure z to 1 part in 10^4 or better, if necessary. In addition, averaging over many periods of the motion was also expected to provide for increased measurement sensitivity.

The displacement sensing setup used in this experiment employed an interferometer and a HeNe laser source as depicted in Figure 5.8. Here, a mirror was placed on the same mount as that of the glass window (see Figure 5.3a) to form one arm of the interferometer. Light from this arm was then interfered with that of a reference arm which was attached to the same table on which the cavity is formed.

* Since only the component of the resonance frequency shift at f_f was to be measured in the AC detection scheme, only that corresponding component of the velocity was also to be measured.

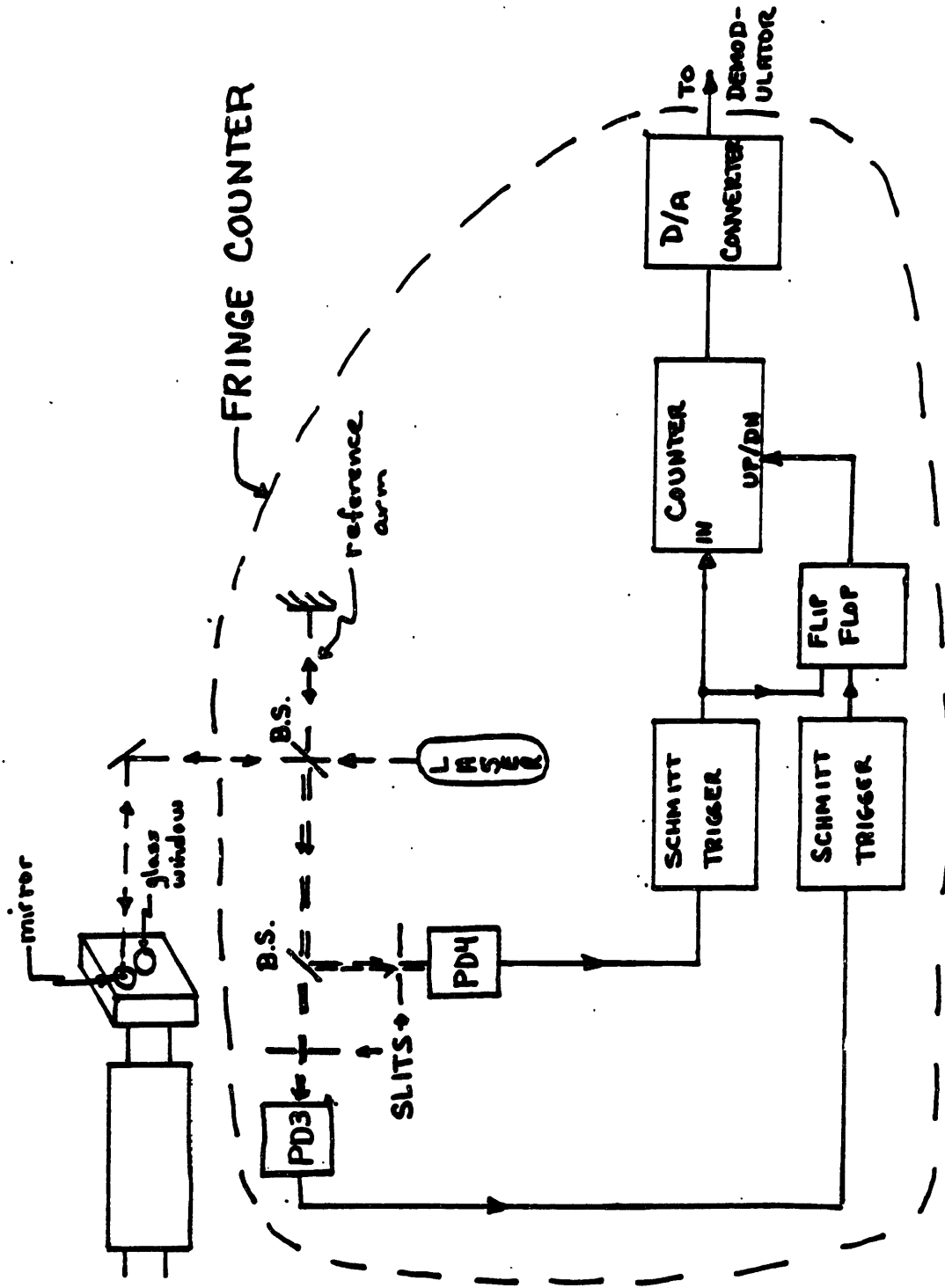


Figure 5.8

In this way, the displacement (hence velocity) of the mechanically isolated glass mount was measured with respect to the cavity. [This was of course necessary since any movement of the isolation structure with respect to the table was also expected to contribute to the Fresnel drag as measured by the cavity.]

The interference pattern was observed, via a beam splitter, by two photodetectors (PD3 and PD4) as shown in the figure. The reference arm of the interferometer was slightly tilted to achieve a set of horizontal fringes as shown in Figure 5.9a. By means of adjustable horizontal slits the detectors were made to observe points in the fringe pattern that were spatially separated by roughly 90° in the vertical direction, y (shown in Figure 5.9a). As the glass mount was moved forward or backward the fringe pattern shown in Figure 5.9a moved correspondingly to the right or to the left. Hence the resultant output of PD3 as shown in Figure 5.9b, either led or lagged (by $\sim 90^\circ$) that of PD4, depending on direction of motion. After these outputs were converted to square waves (via Schmitt trigger gates), this phase difference was used to generate a logic state, via a flip flop, corresponding to the direction of motion. An up/down counter was then employed to count the number of fringes observed by PD4. The flip flop signal indicated whether the fringe count was to be incremented or decremented. The digital output of the counter, thus varied sinusoidally, as did the motion. The counter output was then converted to an analog signal using a digital to analog converter (D/A).

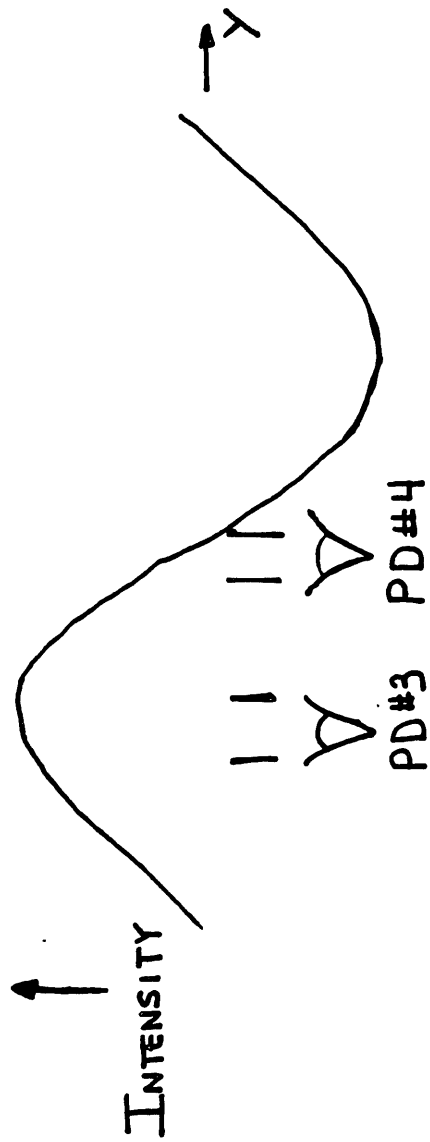


Figure 5.9a

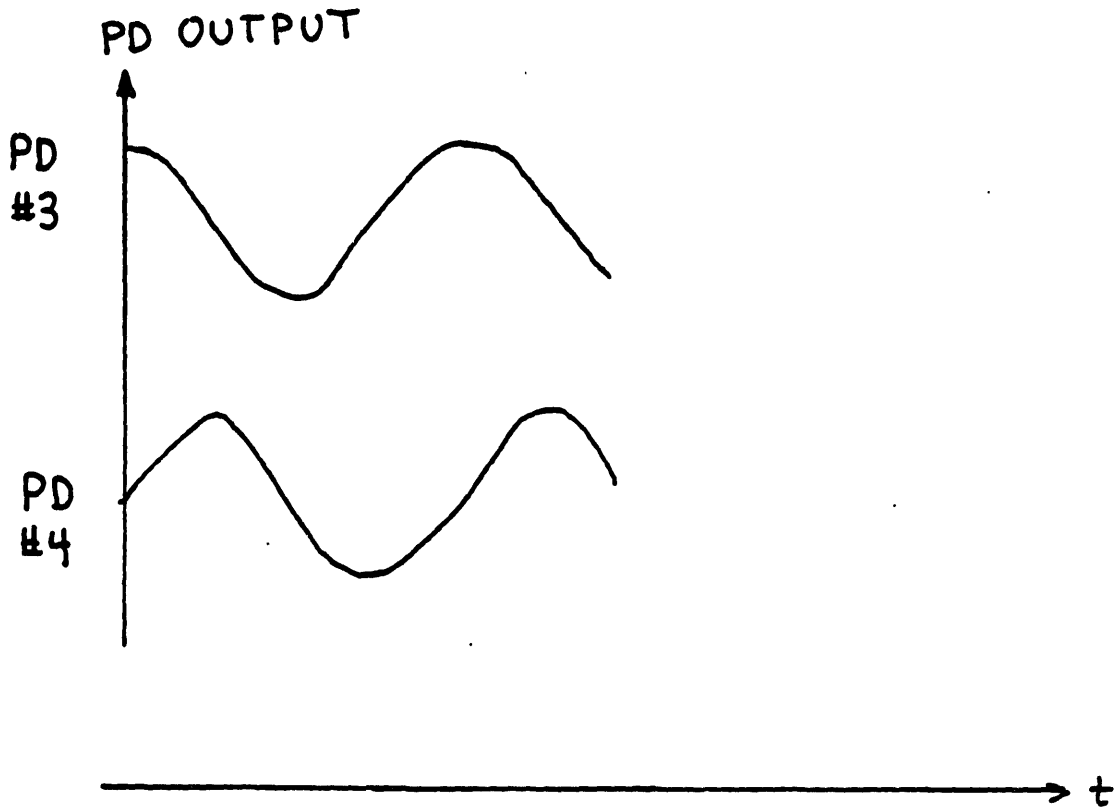


Figure 5.9b

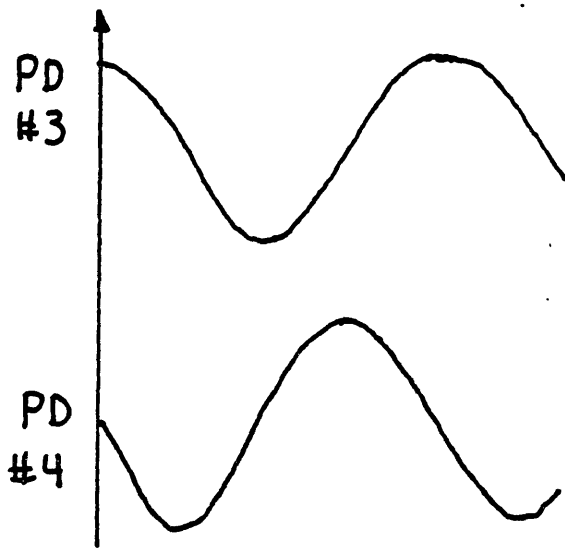


Figure 5.9c

The D/A converted after each increment (or decrement) of the counter. Hence, the sinusoidal output of the D/A, corresponding to a peak to peak number of fringes $\sim 26,000/\text{period}$, was a smooth sine wave.

Since, however, the motion itself was expected to have some higher harmonic distortion, the output of the D/A was demodulated (in PSD#3) at the fundamental frequency, f_f . In the case of the fringe counter output, a filtered signal from the A/D itself was used as the demodulator reference as shown in Figure 5.10. In this way, the output of PSD#3 was constructed to be a measure only of the desired amplitude of the motion at f_f , and did not require phase adjustment.

Primarily because of slow increases in bearing friction, the amplitude of the motion was found to decrease at a rate of typically .25% per minute. This was of course undesirable since the data was intended to be averaged over several observation periods ~ 2 min. Hence, the servo, depicted in Figure 5.10, was employed for the necessary long-term stabilization of the motion amplitude. Here, the output of the fringe counter (V_{FC}) was bandpass filtered ($Q = 5$) at f_f , in PSD#3, prior to demodulation in the mixer. The output of the mixer was then subtracted from a stable DC reference voltage, V_{DC} , prior to amplification and low pass filtering. The output of PSD#3, via an integrator (of the same type as in Figure 4.21), was then used to adjust the amplitude of the signal generator at f_f , as shown in the figure. Hence, by varying the drive to the electromechanical transducer, the amplitude of the motion was adjusted. The servo thus stabilized the motion amplitude such that the output of the mixer was equal to V_{DC} , giving a null in the PSD

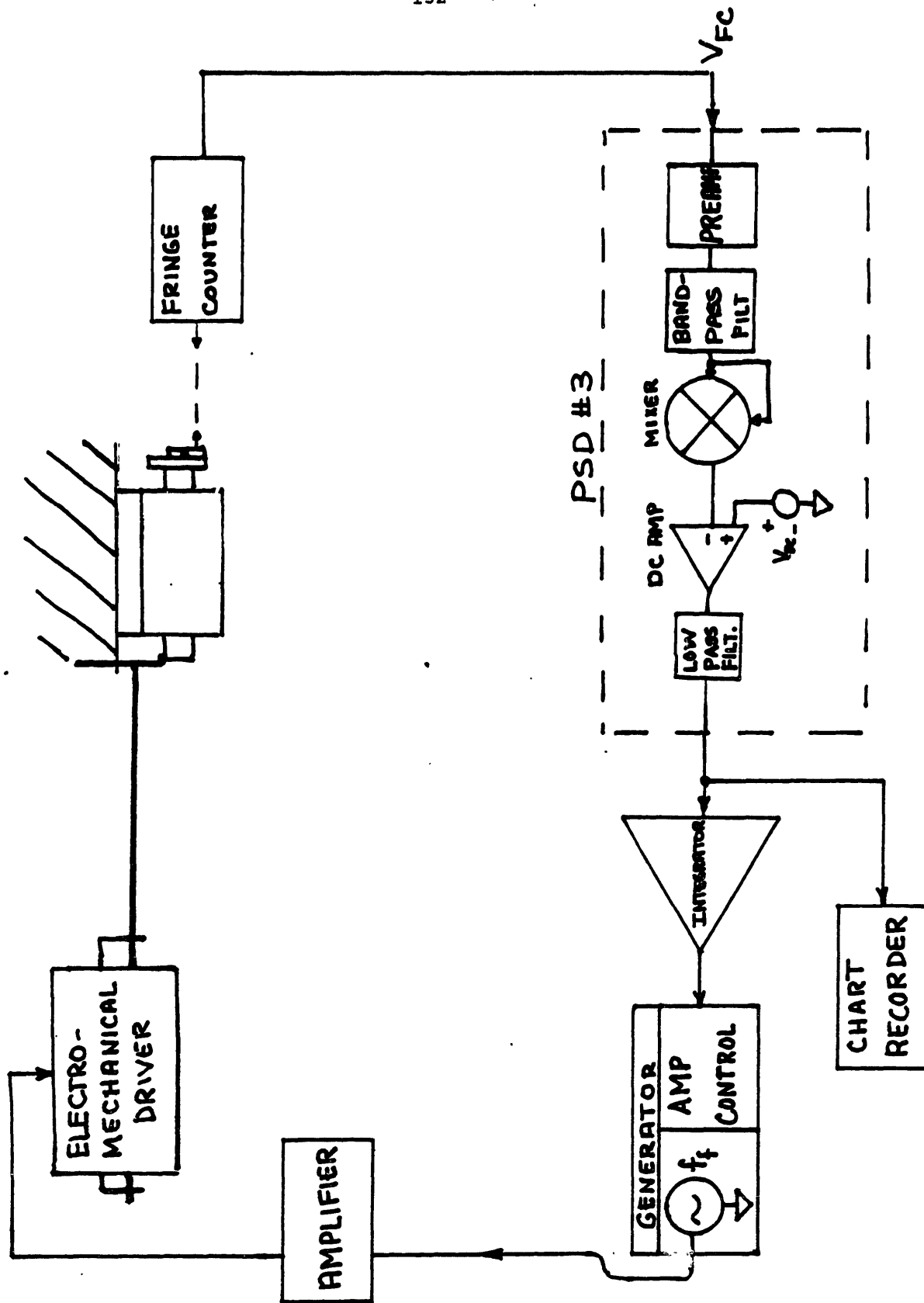


Figure 5.10

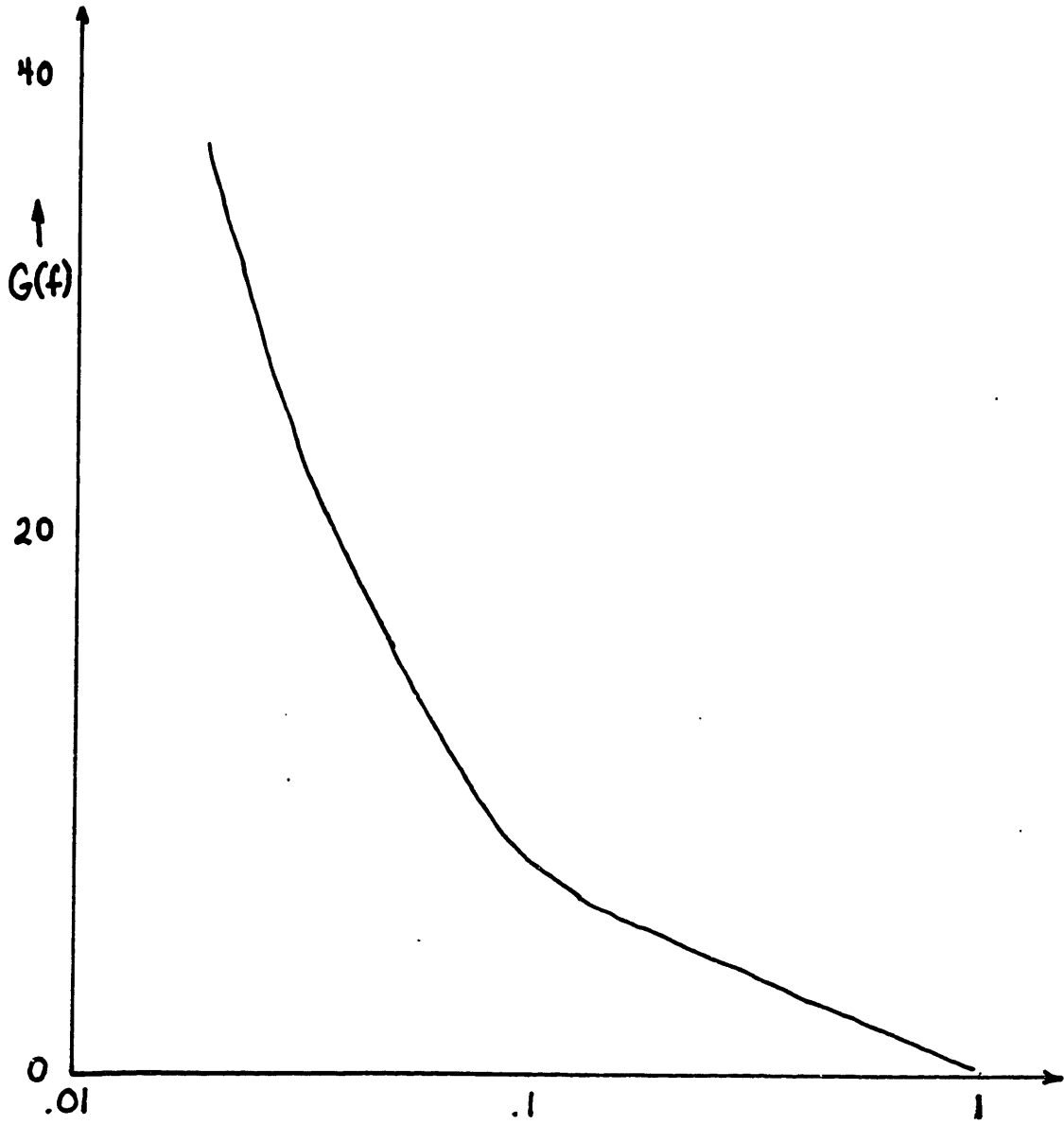


Figure 5.11

output. Choosing a value for V_{DC} allowed for selection of the amplitude of the motion at f_f . The servo gain as a function of frequency is shown in Figure 5.11.

A typical PSD output monitored by a chart recorder throughout the data run, is shown in the left hand portion of Figure 5.12. [The high frequency noise is due to residual $2f_f$ from the mixer. The servo bandwidth was small compared to $2f_f$, and thus, the jitter on the motion due to this noise was negligible.] The DC output of PSD#3 was thus stabilized to better than .01% for time periods, although not shown here, of up to 1 hour or more.

The component of the fringe counter output, V_{FC} , at f_f was measured by using a variable amplitude reference as shown in Figure 5.13. The reference generator was phase locked to the driving frequency f_f . Its output amplitude was simultaneously put into PSD#3 and into a calibrated (see Section 5.5.2a) AC voltmeter (ACVM). The reference amplitude V_R was adjusted such that the output of PSD#3, shown in the right hand portion of Figure 5.12, was equal to that output level (-null) as during the data run. In this way, by using a reference of low harmonic distortion, the equivalent output voltage $V_{FC}(f_f)$ of the fringe counter was determined. In addition, $V_{FC}(f_f)$ was thus determined independent of the PSD gain and V_{DC} , assuming that these parameters did not change in the time interval between the data run and calibration (see Section 5.5.2a). The value of V_R for which $V_R(f_f) = V_{FC}(f_f)$ was then measured by the ACVM. The numbers in Figure 5.12 represent the digital output of the ACVM (corresponding to V_R)

PSD #3 OUTPUT

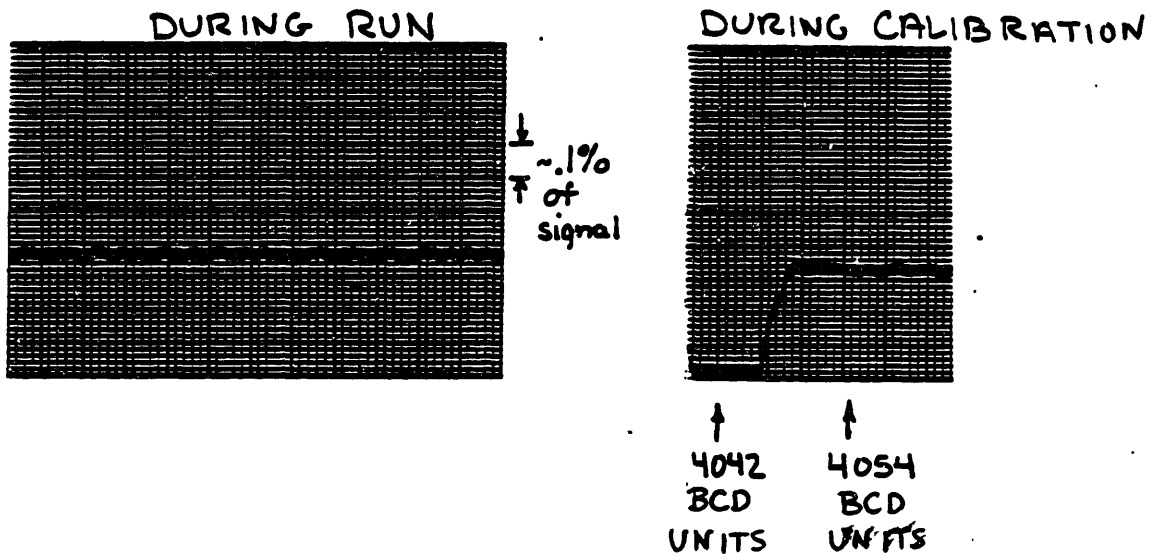


Figure 5.12

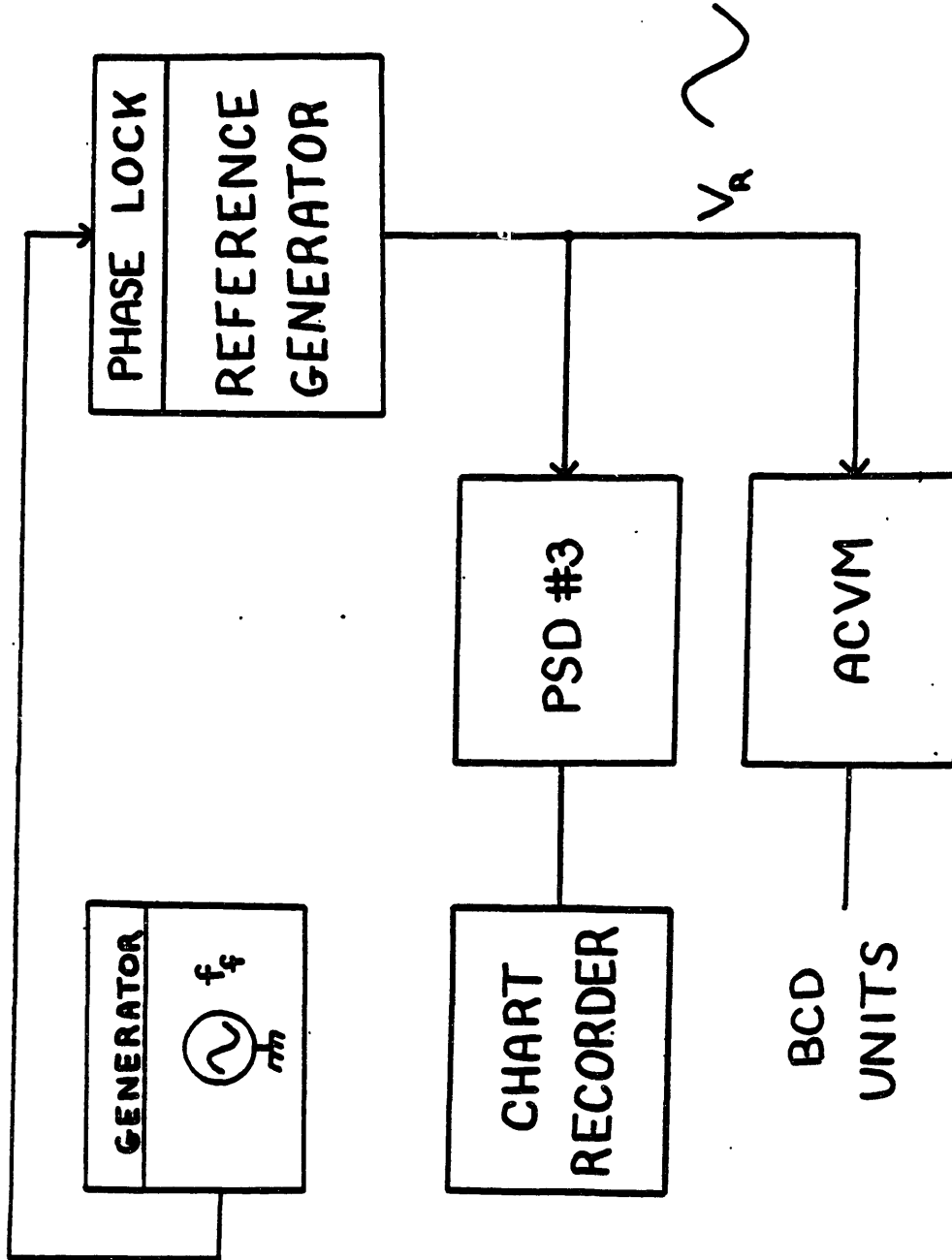


Figure 5.13

in binary coded decimal (BCD) units. The peak to peak value of V_R was related to the BCD output V_{BCD} (Section 5.5.2a) by,

$$V_{BCD} = \frac{1638.4}{\pi} (\text{Volt}^{-1}) (V_{R_{pp}}) \quad (5.2)$$

For the case of the fringe counter output it was convenient to define the corresponding BCD output as $Z(\text{BCD})$. Hence,

$$Z(\text{BCD}) = \frac{1638.4}{\pi} (\text{Volt}^{-1}) V_{FC(f_f)_{pp}} \quad (5.3)$$

where the "pp" subscripts denote the peak to peak value.

The fringe counter output $V_{FC}(f_f)$ [pk to pk] was then related to the peak to peak amplitude of the motion $Z_{o_{pp}}(f_f)$ via the gain of the fringe counter, as depicted in Figure 5.14. The gain of the fringe counter was comprised of the interferometer-counter gain and of the D/A converter gain, as shown in the figure.

The gain of the interferometer-counter system was then determined to be the following. Due to practical considerations, the interferometer laser beam was inclined at a vertical angle ψ ($\sim 1^\circ$), as depicted in Figure 5.15, with respect to the velocity of the mirror M (and hence, of the glass as well). Thus, to achieve proper interferometric alignment the mirror also had to be tilted by the angle ψ . For a displacement of Δz in the direction of \vec{v} , the total pathlength change in the arm of the interferometer was $2\Delta z \cos \psi$. Hence the number of fringes observed by the interferometer and counted by the counter was

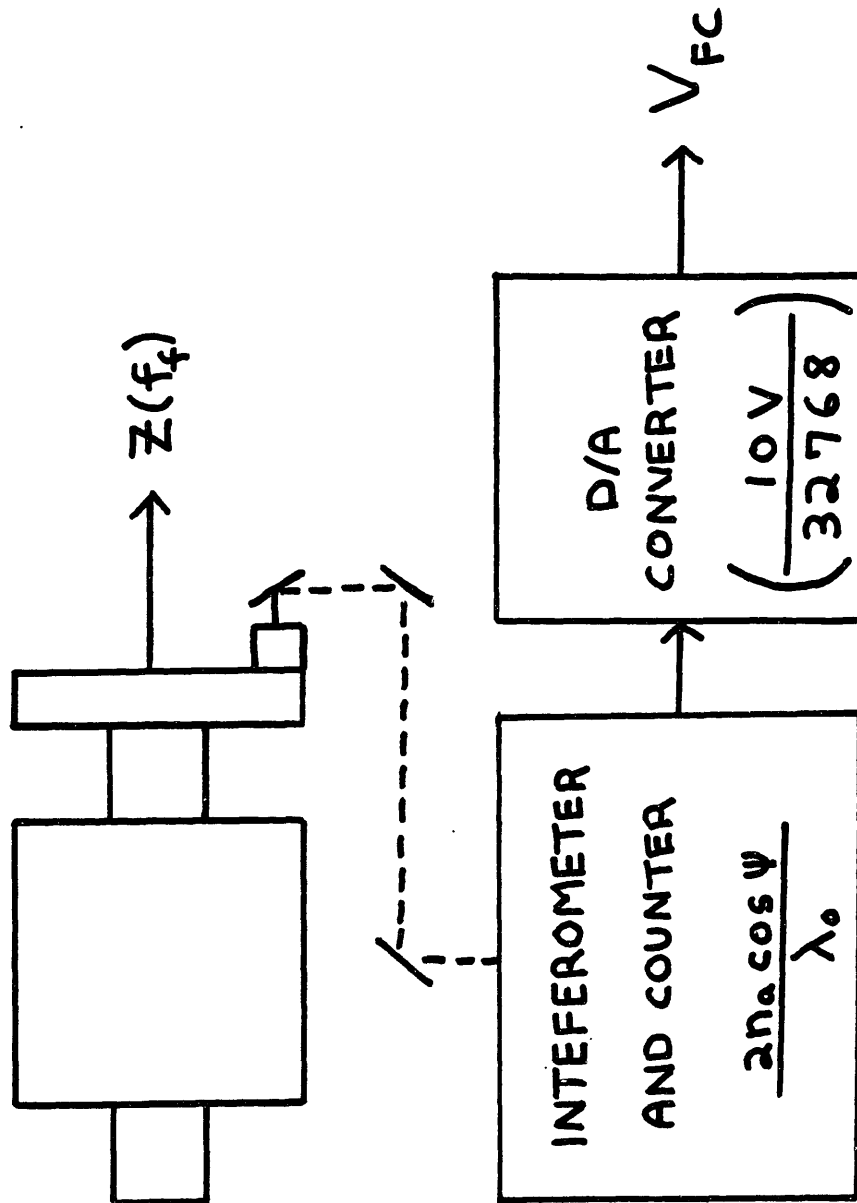


Figure 5.14

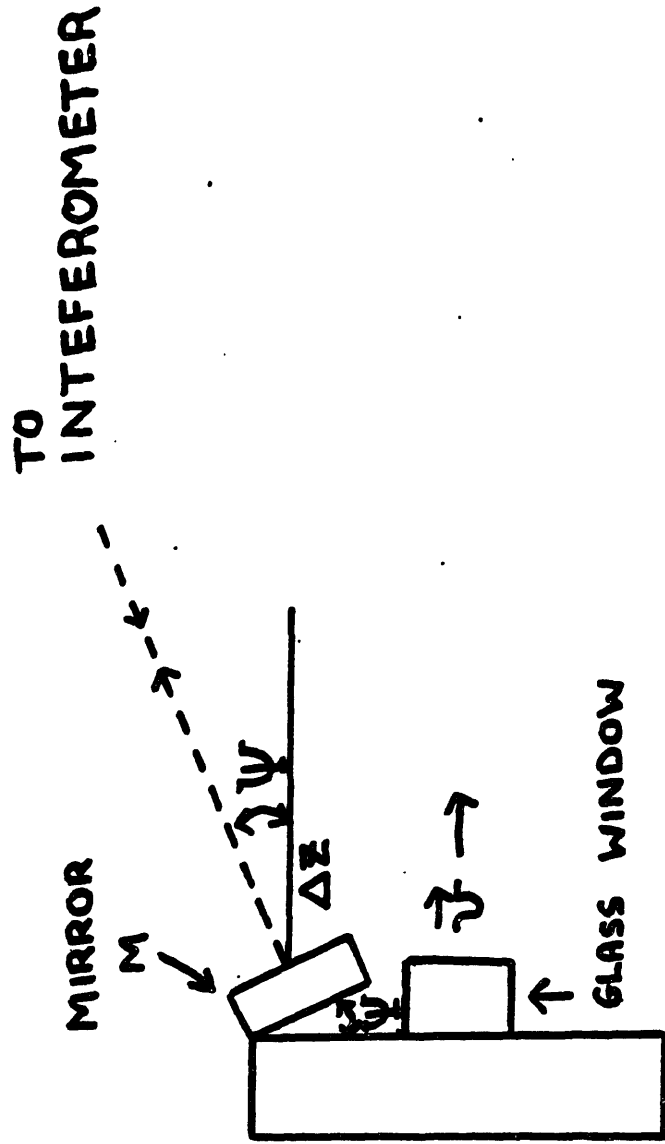


Figure 5.15

given by,

$$\# \text{ fringes} = \frac{2\Delta z \cos \psi}{\lambda} \quad (5.4)$$

where λ was the wavelength of the light utilized. Since the experiment was conducted in air of index η_a ,

$$\lambda = \frac{\lambda_o}{\eta_a} \quad (5.5)$$

where λ_o is the vacuum wavelength of the HeNe laser source. Hence, the gain of the interferometer-counter system was given by

$$\frac{\# \text{ fringes}}{\Delta z} = \frac{2\eta_a \cos \psi}{\lambda_o} \quad (5.6)$$

For the given digital input, corresponding to the number of fringes counted, the analog voltage output of the 16-bit D/A converter was given by,

$$V_{FC} = \frac{10 \text{ Volts}}{32768} (\# \text{ fringes}) \quad (5.7)$$

Combining Eqs. (5.6) and (5.7) and using the peak to peak values for the motion displacement $Z(f_f)$ and $V_{FC}(f_f)$,

$$V_{FC}(f_f)_{pp} = \frac{2\eta_a \cos \psi}{\lambda_o} \left(\frac{10 \text{ Volts}}{32768} \right) Z_o(f_f)_{pp} \quad (5.8)$$

Since the measurement of $Z_o(f_f)_{pp}$ was read out during the experiment in terms of the quantity $Z(\text{BCD})$ (as explained earlier), Eqs. (5.3) and (5.8) were combined to give

$$Z_o(f_f)_{pp} = \left(\frac{\pi \text{ Volts}}{1638.4} \right) \left(\frac{32768}{10 \text{ Volts}} \right) \left(\frac{\lambda_o}{2\eta_a \cos \psi} \right) Z(\text{BCD}) \quad (5.9)$$

$$= \frac{\lambda_o \pi}{\eta_a \cos \psi} Z(\text{BCD}) \quad (5.10)$$

Hence, the corresponding peak to peak velocity of the glass motion in the z-direction of the cavity was given by

$$v(f_f)_{pp} = 2f_f \frac{\lambda_o \pi^2}{\eta_a \cos \psi} Z(\text{BCD}) \quad (5.11)$$

A typical value for $|\vec{v}(f_f)_{pp}|$ in this experiment was approximately 25 cm/sec where $f_f \approx 5$ Hz.

5.4. Details of the Measurement of Resonance Frequency Shift Due to Light Drag

The basic scheme for detection of non-reciprocal phase shift (discussed in Sections 4.3 and 4.4) was also employed, with a few modifications, for the detection of the oscillatory Fresnel-drag effect. As described in Sections 4.3 and 4.4, the open loop output of PSD#2 is a measure of the non-reciprocal phase shift. In the case of the AC Fresnel-drag effect, this output was an oscillatory voltage at f_f proportional to the drag, given by Eq. (4.3) (for glass of normal

incidence). Since the output of PSD#2 contains the entire spectrum (depending on its bandwidth) of non-reciprocal phase shifts it was first important to separate the drag effect from the other effects. Hence, as shown in Figure 5.16, the output of PSD#2 was demodulated at f_f in PSD#4. In this configuration, it would have been necessary to calibrate the DC output of PSD#4 in terms of the resonance frequency shift at f_f , namely $\Delta f(f_f)$. This calibration would have depended on gain of PSD#4 as well as all the factors that determine the size of the discriminant at f_m (~30 KHz); such as, the beam intensities, the cavity modulation excursion, the photodetector gains, and the gain and phase of PSD#2. Since this calibration was subject to change during the course of the data run, it was considered necessary to construct a null system in which the frequency readout was independent of the gain factors mentioned above.

One way of providing for a null readout would have been to use the closed loop configuration described in Section 4.4. In this case, the output of PSD#2 would have been used to correct the frequency of the ccw beam (for all low frequency non-reciprocal phase shifts) and the correction signal at f_f would have been due to the drag signal. Since however, only that non-reciprocal phase shift at f_f was of interest for this measurement, it was more convenient to construct a null system for this signal component alone. In this way, the need for a wideband servo loop was eliminated. The basis of this scheme, was to sinusoidally modulate (via a voltage controlled oscillator) the frequency f_2 , of A/O #2, 180° out of phase with the drag signal,

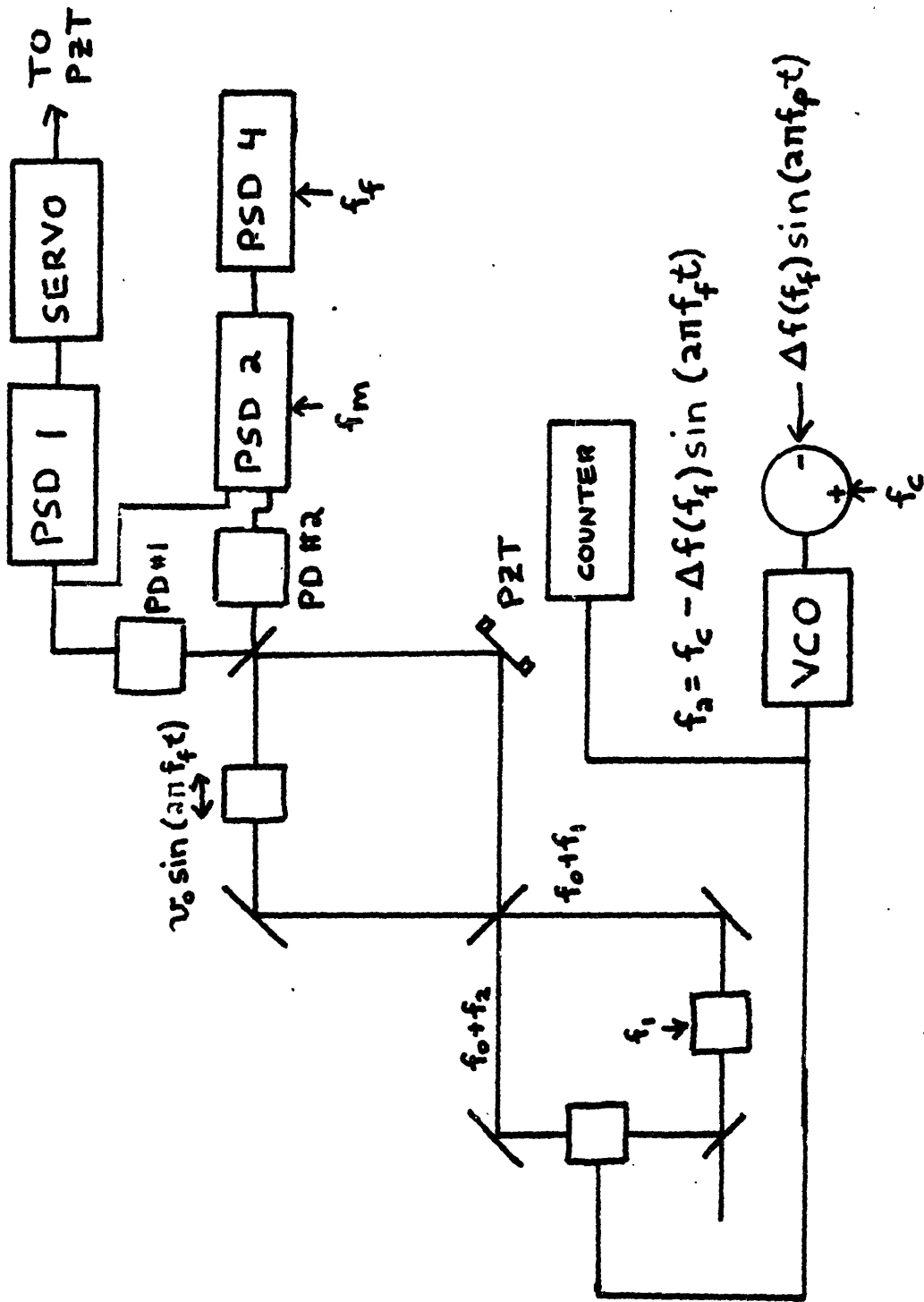


Figure 5.16

as shown in Figure 5.16. The output of PSD#4 resulting from this frequency modulation was equally sensitive to the gain factors mentioned above. Hence, the modulation amplitude necessary to null the output of PSD#4 was equal to the resonance frequency shift $\Delta f(f_f)$ resulting from the drag. This modulation amplitudes was measured and provided a convenient and calibrated readout of $\Delta f(f_f)$.

It must be noted here, that changing the frequency of A/O #2 also slightly changed the angular direction of the ccw beam prior to cavity injection. Typically, for a frequency change of 1 KHz, the angular deviation was $\sim .16$ μ rad. From the misalignment curve shown in Figure 4.17b, this angle change was expected to result in a maximum error in Δf of $\sim .1$ Hz. Here, this represented an error in Δf which was small compared to other errors in the measurement of Δf .

The frequency compensation and measurement setup used in this experiment is depicted in Figure 5.17. The VCO, driven at constant carrier frequency f_c (~ 40 MHz) was modulated at the rate f_f by a generator of variable amplitude. In order to keep the phase of the frequency modulated wave from drifting with respect to that of the drag signal, the generator was phase locked to the output of the fringe counter (see Section 5.3). Since the fringe counter output was a measure of the displacement of the dragging medium, a variable phase shifter of $\sim 90^\circ$ was employed to synchronize the frequency modulation to the velocity (and hence, the drag) of the medium. The frequency modulation was then converted to a voltage modulation by means of a calibrated (Section 5.5.2a) frequency-to-voltage (F/V) converter. Since the F/V

operating range was only 100 KHz, the output of the VCO was first biased to a low center frequency by means of a passive mixer. To eliminate errors from small harmonic distortion in the generator or nonlinearities in the VCO or F/V, the output of the F/V was demodulated at f_f in PSD#5. As in the displacement measurement (Section 5.3) the signal itself served as the PSD reference to measure the amplitude of the signal independent of its phase.

The procedure to establish the proper output null of PSD#4 was as follows. The phase of the reference in PSD#4 was adjusted to maximize the "in phase" drag signal output by nulling the quadrature component of the demodulated output. The frequency modulation was then applied to the A/O and the phase shifter ($\sim 90^\circ$) was adjusted to preserve the quadrature null of PSD#4. The amplitude of the frequency modulation was then adjusted to null the output of PSD#4 (when the reference was in phase with the signal). In this way, the frequency modulation was adjusted to be of the same amplitude as the drag signal but 180° out of phase. Typically, for a measurement error of .01%, the phase of the frequency modulation only had to be matched to that of the drag signal by $\sim .8^\circ$, which was done throughout the measurement. A typical output null of PSD#4 is shown in the left-hand portion of Figure 5.19, as well as the associated frequency modulation at the output of PSD#5. As shown in the figure, the noise on the null, primarily due to noise in the cavity, was typically .1 % of the signal size. The dc value of the output, over an observation time of ~ 2 mins however, was measurable to $\sim .03\%$ of the signal size. Each data run consisted of

several such observation times.

The equivalent output of the F/V was calibrated in the same manner as was used for the displacement measurement (described in Section 5.3). Briefly, a reference wave at f_f , of amplitude measured by a calibrated AC voltmeter (ACVM), was injected into PSD#5. The amplitude of the reference was then adjusted to obtain the same output of PSD#5 as during the data run, as in the right hand portion of Figure 5.19. The amplitude of the reference wave was then recorded in the binary-coded decimal units of the ACVM. The output of the ACVM denoted as $f(\text{BCD})$, was then related to the peak to peak frequency modulation by,

$$f(\text{BCD}) = [5.1041 \times 10^{-3} \text{ Volts/Hz}] \left(\frac{1638.4}{\pi \text{ Volts}} \right) \Delta f(f_f)_{\text{pp}} \quad (5.12)$$

$$= (2.6619/\text{Hz}) \Delta f(f_f)_{\text{pp}} \quad (5.13)$$

where the bracketed term is the gain of the F/V converter (see Section 5.5.2a). The numbers written on the upper right hand portion of Fig. 5.19, represent the measured size of $\Delta f(\text{BCD})$ corresponding to a given frequency excursion.

5.5. Calibration: System Checks and Parameter Measurements

5.5.1. System Checks

In order to calibrate the measurement system many checks of the system were performed during the course of the data runs. Most of these checks were first conducted during data runs with an arbitrarily chosen glass window of BK-7 ($n \approx 1.5$) of thickness 6 mm. Subsequent checks were also conducted in other data runs employing different glass samples.

One of the first concerns in this measurement was to make sure that the position-dependent non-reciprocal phase shifts mentioned in Section 5.2, were not affecting the drag measurement. Briefly, as mentioned before, this non-reciprocal phase shift was caused by cavity misalignment and glass birefringence effects which would vary (with z) as a result of the sag in the bearing-shaft system on which the glass was mounted. Prior to each run, this position dependence was observed by moving the glass slowly back and forth along z . By tightening the bearing or by finely adjusting the direction of motion to coincide with direction of the light (\hat{z}) it was possible to insure the variation of non-reciprocal phase shift was always less than ~ 8 Hz over the entire 1 cm range of z . This dependence on z , was found to fit into three basic smooth shapes of typical amplitudes shown in Figure 5.18. As shown in the figures, Δf was found to be either constant, or linearly,

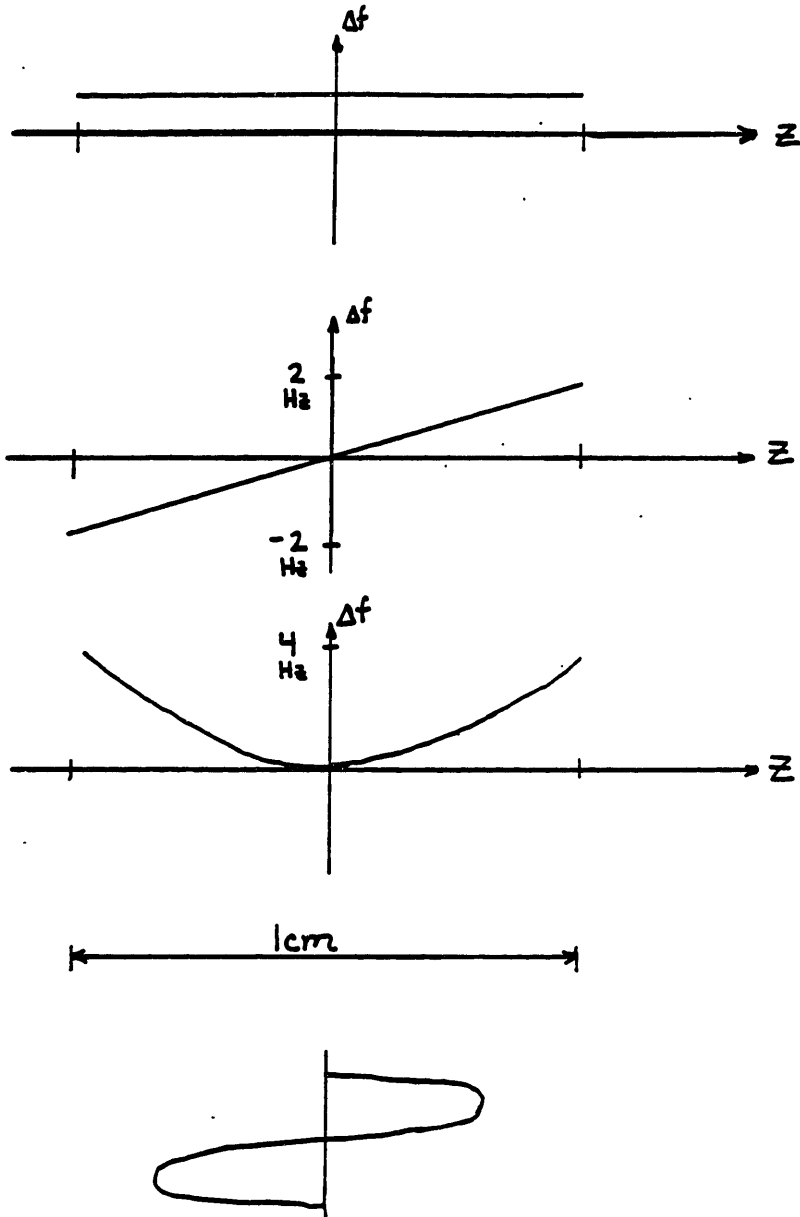


Figure 5.18

or quadratically dependent on z . If the glass position was modulated over typically 70% of this range (as shown in Figure 5.18) of z the latter two position dependences were expected to be modulated at f_f .

Many data runs were conducted for different position dependences in the amplitude range mentioned above. For instance, drag data was taken for various cases of the linear position dependence, that is, linear dependence of different slope magnitudes (and sign). Similarly this was done for the quadratic dependence. There was no observed correlation (at least within the stated error bars) between the output $\Delta f(f_f)$ and the various position dependences. This was of course, explained by the following. In the linear case, the modulated Δf is 90° out of phase with the drag signal, since the latter signal is proportional to the velocity. In the quadratic case, the resultant modulation of Δf is primarily at frequency $2f_f$, or at the second harmonic. In summary, for the sizes of the position-dependent non-reciprocal phase shifts observed in this experiment, there was no measurable effect on the drag measurement.

As another check for possible error sources, the effects of cavity misalignment and external beam misalignment on the measured drag were investigated. The cavity was misaligned by $\sim \frac{1}{4}$ of the range presented in Figure 4.15, and there was no observed change (to within the error bars) in the measured drag signal, $\Delta f(f_f)$. Similarly, although the external misalignment was comparable to that presented in Chapter 4, there was no observable dependence of the data on external alignment.

The electronic instrumentation was also checked for possible error contributions to the measurement. For instance, the system used for measurement of $\Delta f(f_f)$ (described in the previous section) was verified to be truly a null system by perturbing the appropriate gains and phases of PSD#2 and PSD#4. In addition, to check that effects of $2 f_m$ were sufficiently filtered, the center frequencies and Q's of the notch filters, shown in Figure 4.9, were varied in a small region about the quiescent operating point. To verify that the effects of higher harmonics in f_f (due to distortion in the motion of the glass) were adequately attenuated, the Q's of the bandpass filters in PSD's #3, #4 and #5 were varied. In PSD#4 and #5 where a Q of 20 was employed the effects of higher harmonics in f_f were found to be sufficiently attenuated. In PSD#3, where a Q = 5 filter was used (due to bandwidth considerations in the displacement stabilization servo) it was found that there was a small residual effect (~1 part in 2200) due to insufficient filtering of the harmonics of the motion. Hence, a correction to the displacement measurement given by Eq. (5.10), was added.

Another electronic source of error that was investigated was that due to large reciprocal pathlength changes in the glass as mentioned in Section 5.2. The gain of the primary feedback loop and the subtraction coefficient, β , defined in Section 4.6b, were perturbed to verify this effect. During each data run, the residual reciprocal effect Δf_r (see Section 4.6b), due to insufficient servo gain, was recorded. In addition, β was kept to less than 2%, during the measurements.

This still gave an uncertainty in $\Delta f(f_f)$ of $\beta \Delta f_r$. These "subtraction" errors are recorded in the error bars of the measurement of $\Delta f(f_f)$ (see data, Section 5.5.2a). This error (typically 1 Hz), due to reciprocal pathlength changes in the glass varied depending on the angle of incidence, and the glass thickness and index. It is convenient to note here that the gain of the primary servo loop at f_f (~50,000) was sufficient to properly detect the non-reciprocal drag effect to within negligible error. For a peak-to-peak resonance frequency shift of 1 KHz, this error would have been ~.02 Hz.

The scattering effects, illustrated in Section 4.6d, were also investigated as possible sources of error. In this experiment, the phase modulation technique, described in the same section, was employed. The modulation amplitude was varied to increase the carrier frequency component and the effect on the drag measurement was studied. In this way, the magnitude of the carrier suppression, employed during the experiment, was found to be sufficiently high to attenuate the effects due to scattering.

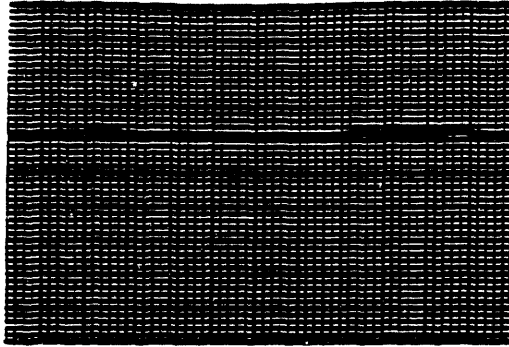
5.5.2 Parameter Measurements

5.5.2a Measurement of $\Delta f(f_f)$: Data Readout and Scale Factor Calibration

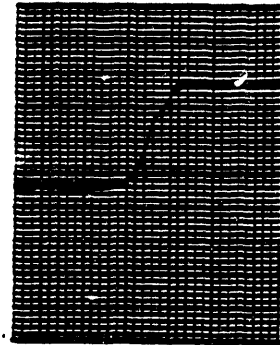
The setup and readout procedure for measuring the resonance frequency shift $\Delta f(f_f)$ due to the light drag were discussed in Section 5.4. Here, the readout is illustrated for a particular data run. In this data run, a glass window of BK-7 of index $n \sim 5.15$ and length $l \sim 6$ mm, was tilted at angle of incidence $\theta \sim 10^\circ$. The peak-to-peak sinusoidal ($f_f \sim 5$ Hz) velocity was ~ 25 cm/sec. The data output, recorded on the chart recorder for one observation time (~ 2 min), is shown in Figure 5.19. The output of PSD#4, employing a low pass filter time constant of 3s, is shown in the bottom chart recorder channel. The null point of PSD#4, i.e. that output level corresponding to no input, is indicated in the figure. The corresponding output of PSD#5, indicating the frequency modulation amplitude necessary to null the output of PSD#4 (as described in Section 5.4 this level was equivalent to the amplitude of the drag signal, $\Delta f(f_f)$) is shown on the top chart recorder channel. The servo stabilized amplitude of the motion, i.e. the output of PSD#3 (see Section 5.3 and also Section 5.5.2b), is shown on the middle chart recorder channel.

The amplitudes of the frequency modulation was adjusted so as to provide a null output of PSD#4. Using this adjustment the scale of the output of PSD#4 was calibrated to be .125% of the total output per large box (or 3.2 BCD Units/Box or 1.2 Hz/Box). Thus, if the output of PSD#4 was not at null, a correction was made. The average output

PSD #5 Output



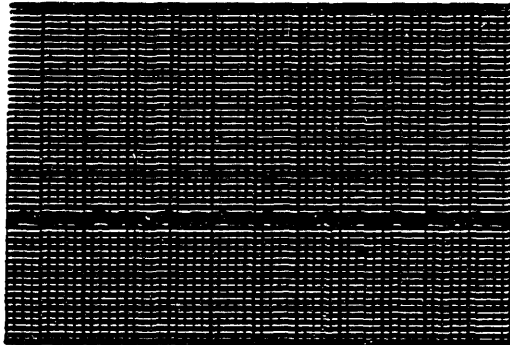
↓
~ .12%
↑
of freq
mod.
signal



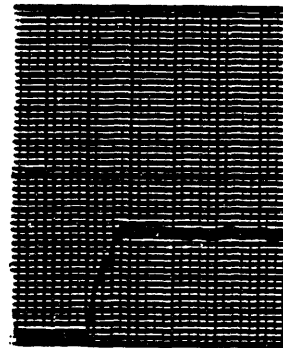
↑
2585
BCD
UNITS

↑
2567
BCD
UNITS

PSD #3 Output



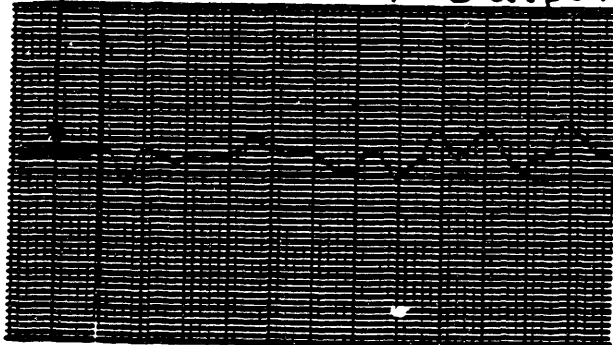
↓
~ .1%
↑
of
velocity
signal



↑
4042
BCD
UNITS

↑
4054
BCD
UNITS

PSD #4 Output



↓
~ .12%
↑
of drag
signal

↓
1.2 Hz
↑
or

↑
CALIBRATION

Figure 5.19

level of PSD#4, for the observation time shown here, was measured to be zero, with an uncertainty in the average level of approximately $\pm \frac{3}{10}$ of a large box (or $\pm .037\%$ of the total signal). The frequency modulation amplitude $f(\text{BCD})$ measured by PSD#5 was then calibrated, as shown in Figure 5.19, using a reference input measured by an AC voltmeter (ACVM) in BCD units (this procedure was outlined in Sections 5.3 and 5.4). The output scale of PSD#5 was calibrated for input reference amplitudes of $2555 \pm .5$ BCD Units and $2567 \pm .5$ BCD Units. The scale here, as indicated in the figure, was thus measured to be $3.9 \pm .3$ BCD Units/Box. By interpolation the output of PSD#5, shown in Figure 5.19, was measured to be

$$\begin{aligned} f(\text{BCD}) &= (2555 \pm .5 \text{ BCD Units}) + \left(3.9 \pm .3 \frac{\text{BCD Units}}{\text{Box}} \right) (1.7 \text{ Boxes} \pm .14 \text{ Boxes}) \\ &= 2561.6 \pm .9 \text{ BCD Units} \end{aligned}$$

As mentioned previously, there was also an error in the readout of the PSD#4 output of $\sim 3/10$ box, corresponding to ~ 1 BCD units. The measurement of $f(\text{BCD})$ is shown in the first row of Table 2, as well as the two readout errors. The total readout error, shown in the table, was obtained by adding the two readout errors in the quadrature. As shown in the table, several similar measurements were performed during the same data run.

Another error encountered throughout the course of the run, was that error due to large residual reciprocal phase shifts in the

cavity, as discussed in Section 5.2. Here this residual shift was ~40 Hz (106 BCD Units). With a subtraction factor $\beta < \frac{1}{50}$ this uncertainty was estimated to be ± 1.8 Hz (2.1 BCD Units).

Table 2

Observation	f(BCD) (BCD Units)	Readout Error (BCD Units)		
		PSD#4	PSD#5	Total
1	2561.6	1	.9	1.3
2	2561.5	1.3	.9	1.6
3	2560.5	1	.9	1.3
4	2560.8	1	.9	1.3
5	2559.7	1	.9	1.3
6	2561.1	.8	.9	1.2

Another error in the readout of PSD#5 was due to the instability of the PSD gain over the time duration between the run (in Figure 5.19) and the calibration (in Figure 5.19). In separate tests, this gain was found to vary randomly on the order of 1.5 parts in 10^4 per hr. Knowing this, the calibration was done within ~20 mins of each observation. Thus, the readout error due to PSD drift (~0.5 parts in 10^4 or .1 BCD Units) was small compared to those listed in Table 2.

Given the measurements of f(BCD) and associated readout errors, the resonance frequency shift $\Delta f(f_f)_{pp}$ was obtained (see Section 5.4) via the expression,

$$\Delta f(f_f)_{pp} = \frac{f(\text{BCD})}{[5.1041 \times 10^{-3} \frac{\text{Volts}}{\text{Hz}}] [\frac{1638.4}{\pi \text{ Volts}}]} \quad (5.14)$$

$$= \frac{f(\text{BCD})}{2.6619/\text{Hz}} \quad (5.15)$$

The uncertainty in the above scale factor also contributed to the measurement uncertainty in $\Delta f(f_f)_{pp}$. The first term in the denominator was due to the gain of the frequency to voltage converter (F/V). The F/V conversion ratio was calibrated periodically for fixed idnput frequencies and found to be stable to ~ 2 parts in 10^4 . In addition, the frequency response of the F/V was measured, and no rolloff (at $f_f \sim 5$ Hz) was observed within the measurement uncertainty of less than 1 part in 10^4 . With these error bars the gain of the F/V converter at f_f was given by

$$(5.1041 \pm .004) \times 10^{-3} \text{ Volts/Hz}$$

The other component of the scale factor in Eq. (5.14) was given by the gain of the ACVM. The ACVM gain appears in both the measurement of $\Delta f(f_f)_{pp}$ and $z(f_f)_{pp}$ (Eq. (5.9)). Since the drag factor α was proportional to $\Delta f(f_f)_{pp}/z(f_f)_{pp}$, the measurement of α was independent of this gain factor. It was known however, that this would not be the case if the ACVM had nonlinearities or an offset. While no such nonlinearities were found, the ACVM had a small offset. For an input sinusoid of peak-to-peak amplitude $V_{R_{pp}}$ the output of the ACVM was

given by,

$$V(\text{BCD}) = \frac{1638.4}{\pi} \left(\frac{\text{BCD Units}}{\text{Volt}} \right) V_{R_{pp}} + 1.75 \text{ BCD Units} \quad (5.16)$$

Hence, a correction of 1.75 BCD units was added to both the readout measurements of the frequency $f(\text{BCD})$ and the displacement $z(\text{BCD})$ to obtain $\Delta f(f_f)_{pp}$ and $z(f_f)_{pp}$. In this way, the gain of the ACVM divided out in the measurement of α , and did not contribute to the uncertainty of the measurement. Thus, $\Delta f(f_f)$ was given by,

$$\Delta f(f_f)_{pp} = \frac{f(\text{BCD}) + 1.75 \text{ BCD Units}}{(2.6619 \pm .0006)/\text{Hz}} \quad (5.17)$$

Using Eq. (5.17), the measurements of $f(\text{BCD})$ were converted into the corresponding measurements of $\Delta f(f_f)_{pp}$, as shown in Table 3. The average resonance frequency shift for the run was 962.7 Hz with a standard deviation for the run $\sigma_r \sim .2$ Hz. The errors for the run are summarized in Table 4, including the previously mentioned scale factor and the "subtraction" uncertainty. The total uncertainty obtained by adding the various uncertainties in quadrature.

Several data runs, similar to the one described here, were taken for the same configuration (same angle of incidence same f_f , same glass window and approximately the same velocity). For the most part, these data runs were conducted on separate days, and each time the setting-up procedure was repeated; for instance, prior to each run, the angle of incidence (see Section 5.2g) of the glass was adjusted as

Table 3

Observation	$f(f_{pp})$ (Hz)	Total (Hz) Readout Error
1	962.9	.49
2	962.9	.60
3	962.6	.49
4	962.7	.49
5	962.3	.49
6	962.8	.45

Table 4

Ave $\Delta f(f_{pp})$	Typical Readout Error	Subtraction Error	σ_r	Scale Factor Error	Total Run Uncertainty
962.7 Hz	.5 Hz	.8 Hz	.2 Hz	.2 Hz	1 Hz

well as the cavity alignment. The results of these data runs, normalized for the same velocity, are shown in table 5. The average of these drag measurements was 960.3 Hz with a standard deviation of ~.5 Hz. The measurement and configuration parameters are shown in Table 6. The uncertainty in $\Delta f(f_{pp})$ was obtained by adding the standard deviation in quadrature with the average error/run. The measurements and uncertainties in the other parameters are discussed in the following sections.

Table 5

run	$f(f_{pp})$ (Hz)	run uncertainty (Hz)
1	960	1.1
2	960.9	1.2
3	960.8	1.2
4	960.5	1.2
5	959.5	1
6	960.2	1.1

Table 6

Glass	Index	$v(f_{pp})$ (cm/s)	$\Delta f(f_{pp})$	θ	l
BK-7	1.51537	25.587	960.3 ± 1.2	10°	.64050 cm

5.52b. Measurement of $V(f_f)_{pp}$: Data Readout and Calibration

The setup and readout procedure for the determination of the glass velocity $V(f_f)_{pp}$ were described in Section 5.3. The displacement readout is illustrated here for the same sample of data used for the purpose of illustration in the last section. As mentioned previously, the middle chart recorder channel, shown in Figure 5.19, was the output of PSD#3 during the data run. This output was a measure of the displacement of the glass $z_o(f_f)_{pp}$ given by Eq. (5.10). The displacement readout $Z(\text{BCD})$ was obtained by the same method as was described in Section 5.4 for the frequency excursion, $f(\text{BCD})$. Briefly, the output of PSD#3 (hence $Z(\text{BCD})$) was calibrated after the run, by using a reference wave input measured in BCD units by the ACVM. As shown in Figure 5.19, the output scale of PSD#3 was calibrated for reference amplitudes of 4042 ± 5 BCD Units and $4054 \pm .5$ BCD Units. Hence, the output scale for PSD#3 in Figure 5.19 was $3.9 \pm .35$ BCD Units/Box. The output of PSD#3 during the run, obtained by comparison to the calibrated output in Figure 5.19, was $Z(\text{BCD}) = 4055.6 \pm .7$ BCD Units. The displacement was stabilized to this value throughout the data run.

There were a few corrections added to the readout measurement $Z(\text{BCD})$. As mentioned in Section 5.5.1, because of higher harmonics on the motion, it was necessary to add a correction of -1.8 BCD Units (or ~ 1 part in 2200) to $Z(\text{BCD})$. In addition, due to the ACVM offset described in the previous section, a correction of 1.75 BCD units was added. Incorporating these corrections, as well as an error of $\sim .3$ BCD

Units due to the PSD gain drift (described in the last section) gave,

$$Z(\text{BCD}) = 4059.2 \pm .8 \text{ BCD Units}$$

The peak-to-peak displacement of the glass $z(f_f)_{pp}$ was obtained from the readout $Z(\text{BCD})$ via Eq. (5.10). To determine possible scale factor errors, the uncertainty in each term of Eq. (5.9) was investigated. The first term in Eq. (5.9), was due to the ACVM gain and the corresponding correction was already added above (see Section 5.5.2a). The second term was due to the gain of the D/A converter discussed in Section 5.3. The gain of this 16-bit convertor was found to be both stable and linear to better than 3 parts in 10^5 . This error was thus negligible. Hence, $z(f_f)_{pp}$ was given by Eq. (5.10) and $v(f_f)_{pp}$ was given by Eq. (5.11). It is instructive to recall the latter relation for the present discussion:

$$v(f_f)_{pp} = 2f_f \frac{\lambda_o \pi^2}{\eta_a \cos \psi} z(\text{BCD}) \quad (5.11)$$

Here, the freespace wavelength λ_o and the index of air η_a were determined to be 6329.9 \AA and 1.00027 , respectively. As discussed in Sections 5.5.2h and 5.5.2e the errors in these two terms were negligible for this experiment. The angle of tilt of the interferometer mirror, ψ , was measured to be $1^\circ \pm .3^\circ$ (while the angle was unchanged during a given data run, it was varied within this range from run to run). The frequency of the motion f_f , was monitored throughout the data run by a stable

frequency counter. For this data run, as well as the other runs,

$$f_f = (5.0454 \pm .0005) \text{ Hz}$$

where the error bar indicates the maximum random drift of the oscillator during the measurement. Thus from Eq. (5.11), the velocity was measured to be,

$$v(f_f)_{pp} = (25.587 \pm .006) \text{ cm/s}$$

where the relative uncertainties in the velocity measurement for this data run are summarized in Table 7. The uncertainties shown here were very similar for all data runs. Since the velocity itself was slightly different ($\pm .3\%$) for the various data runs shown in Table 5, the output frequencies were normalized (for comparison) for a velocity, $v(f_f)_{pp} = 25.525 \pm .006 \text{ cm/s}$.

Table 7

$\frac{\Delta v(f_f)_{pp}}{v(f_f)_{pp}}$	$\frac{\Delta f_f}{f_f}$	$\frac{\Delta(\cos \psi)}{\cos \psi}$	$\frac{\Delta[z(\text{BCD})]}{z(\text{BCD})}$ (readout error)
2.5×10^{-4}	1×10^{-4}	1.05×10^{-4}	2×10^{-4}

5.5.2c. Determination of Index of Refraction and Dispersion

The indices of refraction of the glass types used in the experiment were measured by the manufacturers. The indices n of BK-7, SF-1 and SF-57, shown in Table 8, were measured by Schott Optical Glass Inc.²⁹ In each case, the index of glass was determined to an absolute uncertainty of $\Delta n = 3 \times 10^{-5}$ for a sample taken from amongst the same melt as the glass pieces used in this experiment. The measurements were conducted with a HeNe laser at 22°C and 1 atm pressure. Because, however, these measurements were not conducted on the glass samples used here, it was necessary to allow for the uncertainty in n due to inhomogeneity of the melt. The maximum error due to this inhomogeneity, supplied by Schott, was $\Delta n = 1 \times 10^{-4}$. This uncertainty, shown in table 8, was then the dominant uncertainty in n .

Table 8

Glass Type	n	Δn	$dn/d\lambda$ (μm^{-1})
BK-7	1.51537	.0001	-3.4221×10^{-2}
SF-1	1.71275	.0001	-9.6252×10^{-2}
SF-57	1.83980	.0001	-1.3829×10^{-1}
Fused Silica	1.45704	.00006	-2.9036×10^{-2}

The fused silica (supracil) windows were supplied by Amersil³⁰ Inc. with index $1.45701 \pm .00003$ at $\lambda_0 = 6329.9 \text{ \AA}$ and at 20°C and one atm pressure. The index value shown in the table has been corrected for the mean temperature (23°C) used in this experiment (the temperature dependence is discussed later). Additional verification of the index was provided by I.H. Malitson²⁸ at the National Bureau of Standards. According to Malitson the maximum variation in the index (at 6328) of fused silica was found to be less than $\Delta n = 3 \times 10^{-5}$ regardless of manufacturer or melt (Malitson measured the indices of 12 different specimens, each at 60 different wavelengths. The manufacturer's quoted index was in good agreement with Malitson's measurements).

It must be noted here that corrections in the average index due to the various indices of the AR coatings on the glass windows were considered. These corrections were at most on the order of $\Delta n = 3 \times 10^{-5}$ or less, and were thus neglected for purposes of this experiment (except for fused silica).

While the above measurements were based on the temperature and pressures quoted above, there were very few significant index corrections necessary for the temperature and pressure range used in this experiment. For the glass types shown in Table , the temperature coefficient of the index was typically specified to be $\frac{dn}{dT} \sim 10^{-5}/^\circ\text{C}$ or less. For the temperature range used here $23^\circ\text{C} \pm 4^\circ\text{C}$, both the correction (for 23°C) the error in the index were negligible compared to the uncertainty quoted for BK-7, SF-1 and SF-57 a correction of $\Delta n = 3 \times 10^{-5}$, based on the thermal coefficient of $10^{-5}/^\circ\text{C}$, was added to adjust the index of fused silica for the mean temperature of the experiment. An

uncertainty of 4×10^{-5} , to account for the temperature range of the experiment, was added in quadrature to the previously quoted uncertainty in the index of fused silica. The total uncertainty is shown in Table 8. For the glasses used here, the pressure dependence of the index, dn/dp , was typically 6×10^{-7} /torr. Assuming a maximum pressure variation of 25 torr (~1 part in 30) during the experiment, the maximum index change was $\sim \pm 1.5 \times 10^{-5}$, and was thus considered negligible.

The dispersion, $\partial n/\partial \lambda$, was computed at $\sim 6328 \text{ \AA}$ from the appropriate dispersion relations provided by Schott Optical Glass and Malitson. Typically, the measurement uncertainty in the slope $\partial n/\partial \lambda$ for a particular sample was quoted as $\pm 2 \times 10^{-5}$. In addition, the variation in $\partial n/\partial \lambda$ from sample to sample was ~ 2 parts in 10^4 or less. Melt data was supplied for the specific glass samples used in this experiment that substantiated this error bar. Since the fractional contribution of the dispersion term, $\lambda \partial n/\partial \lambda$, to the drag (Eq. (5.3)) was less than 10% for all glasses used here, the error due to this term was thus insignificant compared to the error in n .

5.22d. Determination of Length of Glass Windows

The lengths of the glass windows were measured by Special Optics Inc.³¹ Here, a device was employed that was sensitive to mechanical contact of the glass piece. This device is generally used for measuring optical surface flatness and radii of curvature of mirrors and lenses. The maximum device sensitivity is typically on the order of $\lambda/20$, or

approximately 2×10^{-6} cm. The device was calibrated for length standards traceable to the National Bureau of Standards.

The length measurements for the glass windows used in this experiment are shown in Table 9. These measurements were conducted with the accuracy necessary for this experiment, typically $\pm 4 \times 10^{-5}$ cm in the cases of BK-7, SF-1 and SF-57 and $\pm 5 \times 10^{-4}$ cm for the fused silica windows. The length measurements were also checked, with an uncertainty of $\sim 10^{-4}$ cm, by the calibrations laboratory at Draper Laboratories.³²

The measurements were done at 22°C, and while the correction to the mean temperature of this experiment (23°C) was considered negligible, an error bar was assigned for the $\pm 4^\circ\text{C}$ range of the experiment. This error bar was based on the expansion coefficients provided by the glass manufacturers.^{29,30,28} For the BK-7, SF-1 and SF-57 windows of ~ 6 mm length, this error was typically $\pm 2 \times 10^{-5}$ cm. In the case of fused silica where the maximum length used in the experiment was ~ 15 mm this uncertainty was 3×10^{-6} cm. The total errors in the length measurements were computed by adding the temperature error in quadrature with the original measurement uncertainty, are shown in Table 9. In the cases where two windows of either BK-7 or SF-57 were used in the experiment, the lengths and uncertainties are doubled.

Table 9

Glass Material	Length (cm)	Length Uncertainty (cm)
BK-7	0.64050	4.5×10^{-5}
BK-7	1.28100	9×10^{-5}
SF-1	0.62378	4.5×10^{-5}
SF-57	0.59854	5×10^{-5}
SF-57	1.19708	1×10^{-4}
Fused Silica	0.1991	5×10^{-5}
Fused Silica	0.4952	5×10^{-5}
Fused Silica	1.0429	5×10^{-5}
Fused Silica	1.4937	5×10^{-5}

5.5.2e. Index of Air

The index of air n_a , was evaluated at $\lambda = 6328$ using the dispersion relation found in the CRC tables.³³ This index was computed at the mean temperature in which the experiment was conducted, $23^\circ\text{C} \pm 4^\circ\text{C}$. The error in temperature provided an uncertainty of ± 4 parts in 10^6 . Assuming also, pressure variations of up to 1 part in 30, the maximum error due to the pressure dependence of the index was ~ 1 part in 10^5 . Hence, the value of n_a was

$$n_a = 1.00027 \pm .00001$$

5.5.2f. Determination of Optical Perimeter of Cavity

The perimeter of the cavity was determined by measuring the cavity free spectral range, $c/P_o n_a$. Here, c is the speed of light in a vacuum, P_o is the physical perimeter of the cavity and n_a is the index of air. The measurement configuration is depicted in Figure 5.20. As shown by the solid lines in the figure, the frequency f_2 was adjusted such that the ccw beam was "on resonance" as described in Section 4.3 (here the cavity was locked to the cw beam frequency). After this was done, mirrors M_1 and M_2 were placed into the ccw beam path to divert the beam, as shown by the dashed line, prior to cavity injection. The ccw beam was frequency shifted by f_p in A/O #3 and then aligned into the cavity. The frequency f_p was adjusted such that the ccw beam was "on resonance" but shifted by one free spectral range. For this condition, f_p , was then measured on a frequency counter to be

$$f_p = c/P_o n_a = [101.8484 \pm .0002] \text{ MHz} \quad (5.18)$$

Here, the alignment of the ccw beam into the cavity was varied to check the sensitivity of the measurement to external alignment. An upper bound for these variations due to misalignment was $\sim \pm 200$ Hz, as shown in the above error bar. Using $c = 2.997925 \times 10^{10}$ cm/s gave,

$$P = P_o n_a = [294.3494 \pm .0006] \text{ cm} \quad (5.19)$$

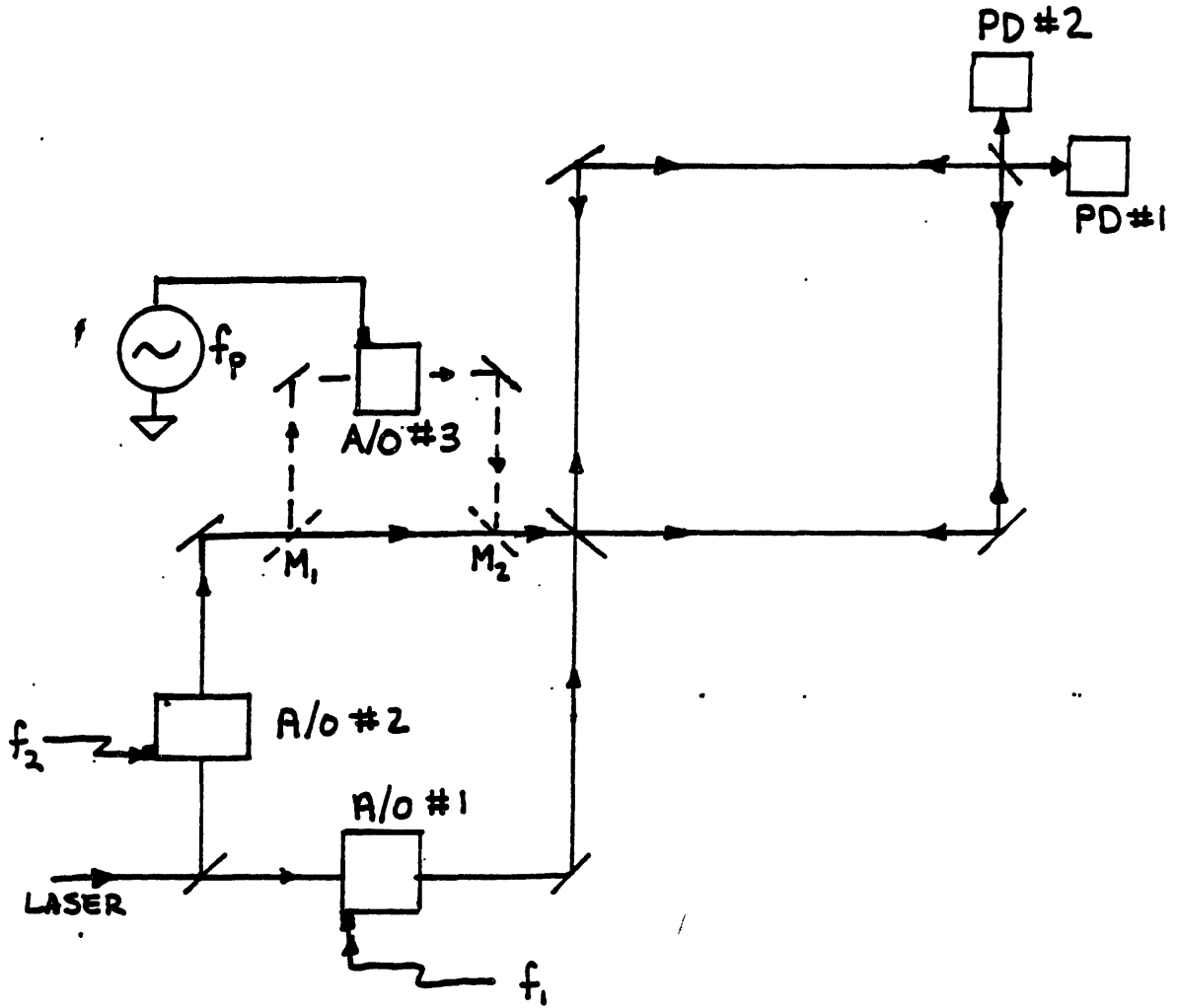


Figure 5.20

The optical pathlength used in the experiment was then computed taking into account the change in optical pathlength, $\ell n/\cos \phi$, due to insertion of the glass (of index n , length ℓ , at an angle of refraction ϕ) in the cavity. Hence, in the experiment, the total optical perimeter was given by,

$$P = \left(P_o - \frac{\ell}{\cos \phi} \right) n_a + \frac{n\ell}{\cos \phi} \quad (5.20)$$

$$= P_o n_a + (n - n_a) \ell / \cos \phi \quad (5.21)$$

For the purpose of this experiment, it was only necessary to know the perimeter to approximately 1 part in 4×10^5 . Hence, the perimeters shown in table 10 were rounded off to the fifth significant digit. In fact, since the fractional contribution of the second term in Eq. (5.21), was at most 1/150, the many uncertainties in this term were negligible. The uncertainties in the lengths and indices in the glass, shown in tables 8 and 9, were negligible for the perimeter accuracy necessary here. In addition, the fractional contribution of the angular term $1/\cos \phi$ was at most 1.3×10^{-5} , and hence, was neglected as well as the uncertainty in ϕ . The maximum error in P_o due to expansion of the cavity over the $\pm 4^\circ\text{C}$ temperature range was on the order of $\Delta P_o/P_o \approx 2 \times 10^{-6}$, and was thus neglected. Likewise, the fractional error due to changes in n_a over the temperature range was $\sim 10^{-5}$. Hence, the perimeter measurements, accurate to within the round-off error of the values stated in table 10, contributed negligible

uncertainties to the drag measurement.

Table 10

Glass Type	Length (cm)	P (cm)
Fused Silica	.1991	294.44
Fused Silica	.4952	294.58
Fused Silica	1.0429	294.83
Fused Silica	1.4937	295.03
BK-7	.64050	294.68
BK-7	1.28100	295.01
SF-1	.62378	294.79
SF-57	.59854	294.85
SF-57	1.19707	295.35

5.5.2g. Determination of the Angle of Incidence

The angle of incidence, θ , of the glass normal n with respect to the cavity beam was adjusted by means of the following procedure. Prior to the experiment, the reflection from the surface of the glass was aligned parallel ($\pm 1^\circ$) to the beam inside the cavity, as shown in Figure 5.21a. As discussed in Section 5.3, another laser beam, used for the interferometric fringe counter, was directed onto a mirror mounted on the same mount as the glass window. The reflection from this mirror was recorded as a fiducial reference for the case of the glass being at normal incidence to the cavity beam. When the window

was mounted on a horizontal wedge of angle θ , as shown in Figure 5.3a. the reflection from the mirror was aligned to the previously mentioned fiducial reference point ($\pm .2^\circ$). This ensured that the angle θ was aligned properly with respect to the cavity beam.

The wedge angle θ was measured by means of two laser beams, parallel to $.05^\circ$, as shown in Figure 5.21b. One beam was aligned normal to the mirror and the reflection of the second beam from the window was measured. The horizontal deflection x of the reflection from the glass was then measured at a distance y away from the glass. The accuracy of this measurement ranged from $\pm .1^\circ$ to $\pm .18^\circ$ for the various values of θ .

The total uncertainty in θ was obtained by adding the individual uncertainties, mentioned above, in quadrature. These total uncertainties for each value of θ pertinent to the experiment are shown in table 11.

Table 11

θ	$\Delta\theta$
5.15°	$.25^\circ$
6.45°	$.25^\circ$
$6.6^\circ, 6.7^\circ$	$.25^\circ$
10°	$.27^\circ$
10.15°	$.27^\circ$
12.7°	$.29^\circ$
15.65°	$.29^\circ$

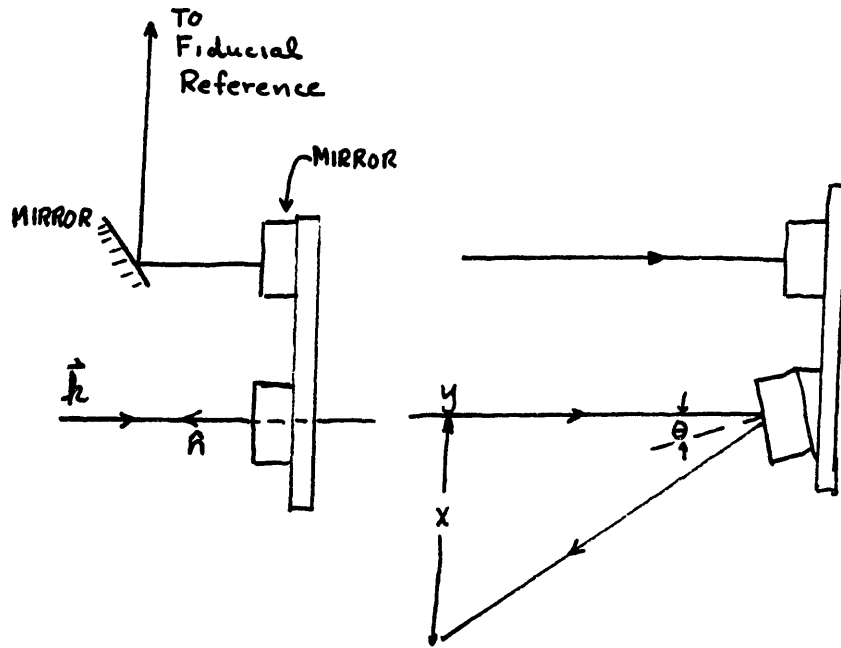


Figure 5.21a

Figure 5.21b

5.5.2h. Determination of the Wavelength of the Laser

In this experiment, one HeNe laser was employed for the measurements of the cavity resonances, and another HeNe laser was used for the interferometric fringe counter discussed in Section 5.3. The vacuum wavelength of the neon transition was measured by Hanes and Baird at the National Research Council³⁴ (Ottawa, Canada) to be,

$$\lambda_{\circ} \approx 0.63299139 \text{ } \mu\text{m}$$

where the uncertainty was about 2 parts in 10^8 . Since our laser operated on the gain curve of this transition, the maximum error in λ_{\circ} was ~ 1 pt in 10^6 and (due to the ~ 1 GHz width of the gain curve) was thus neglected.

5.6. Correction for Angular Dependence in Drag Calculation

In this experiment, the glass was tilted at an angle of incidence θ with respect to both \vec{v} and the incident light. Hence, it was necessary to correct the expression (Eq. (4.3)) derived for glass at normal incidence, to account for this angle dependence. In addition, since the experiment was conducted in air instead of in a vacuum, this correction is also added in this section.

In order to derive the angular dependence of the drag, it is necessary to first derive an expression for the ray velocity for light travelling at an angle γ' in a moving medium. Since this can be found elsewhere in textbooks³⁵ it shall only be discussed briefly here. Consider light travelling at velocity \vec{u}' in a medium of index n' as shown in Figure 5.22. In addition, suppose that \vec{u}' is in the $x'y'$ plane of the rest frame of the medium S' , and that the angle between \vec{u}' and the x' axis is γ' . If the medium is moving at velocity \vec{v} with respect to an observer in the S frame of reference, then the x and y velocity components in S are given by,

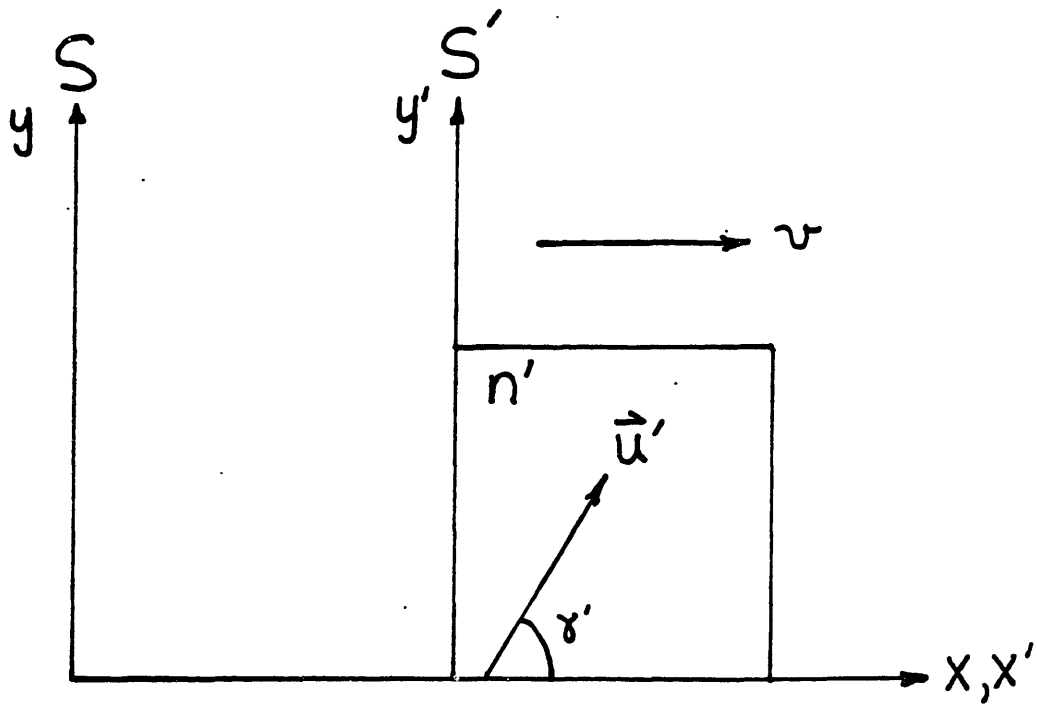


Figure 5.22

$$u_x = \frac{u'_x + v}{1 + vu'_x/c^2} \quad u_y = \frac{u'_y (1 - v^2/c^2)^{1/2}}{1 + vu'_x/c^2} \quad (5.22)$$

Denoting the angle between the velocity in the S frame and the x axis as γ , the above equations can be expressed as

$$u \cos \gamma = \frac{u' \cos \gamma' + v}{1 + \frac{vu' \cos \gamma'}{c^2}} \quad (5.23)$$

and

$$u \sin \gamma = \frac{u' \sin \gamma' (1 - v^2/c^2)^{1/2}}{1 + \frac{vu' \cos \gamma'}{c^2}} \quad (5.24)$$

By combining the two equations above (as shown by Moller³⁵), the magnitude of the velocity in the S frame is given by,

$$n = \frac{n' \left[1 + \frac{v^2}{u'^2} + \frac{2v}{u'} \cos \gamma' - \frac{v^2}{c^2} \sin^2 \gamma' \right]^{1/2}}{1 + \frac{vu'}{c^2} \cos \gamma'} \quad (5.25)$$

Approximation of u to first order in v/c gives,

$$u \approx \frac{c}{n'} + v(1 - 1/n'^2) \cos \gamma' \quad (5.26)$$

where $u' = c/n'$ was used to obtain the above expression.

In the configuration used in this experiment the glass velocity is parallel (or antiparallel) to the direction of incident light. Hence, expansion of $n' (\equiv n(\lambda'))$ in terms of the doppler shifted wavelength λ' gives the identical result for the dispersion term as that given by Eq. (2.11) (i.e. there is no transverse doppler shift here). Carrying out this expansion for n' in terms of λ' in Eq. (5.26) gives,

$$u \approx \frac{c}{n} + v \left[\left(1 - \frac{1}{n^2} \right) \cos \gamma' - \frac{\lambda_0}{n^2} \frac{\partial n}{\partial \lambda} \right] \quad (5.27)$$

where $n \equiv n(\lambda_0)$. (The correction to the dispersion term due to the fact that the experiment was conducted in air, is small and shall be neglected here.)

The experimental configuration used in this experiment is shown in Figure 5.23. Here, the incident light was parallel to the velocity vector \vec{v} . The glass of length l and index $n(\lambda') \equiv n'$ (where λ' is measured in the rest frame of the glass) was tilted at an angle of incidence θ . The angle of refraction ϕ' was thus given by Snell's law,

$$\sin \phi' = \sin \theta \frac{n_a}{n'} \quad (5.28)$$

where n_a is the index of the surrounding air.

The derivation of the optical pathlength change due to the drag for this configuration, is analogous to the discussion in Section 2.4 for normal incidence. The pathlength QQ'' of the light inside the glass is the sum of the QQ' and the length $Q'Q''$, the latter being the

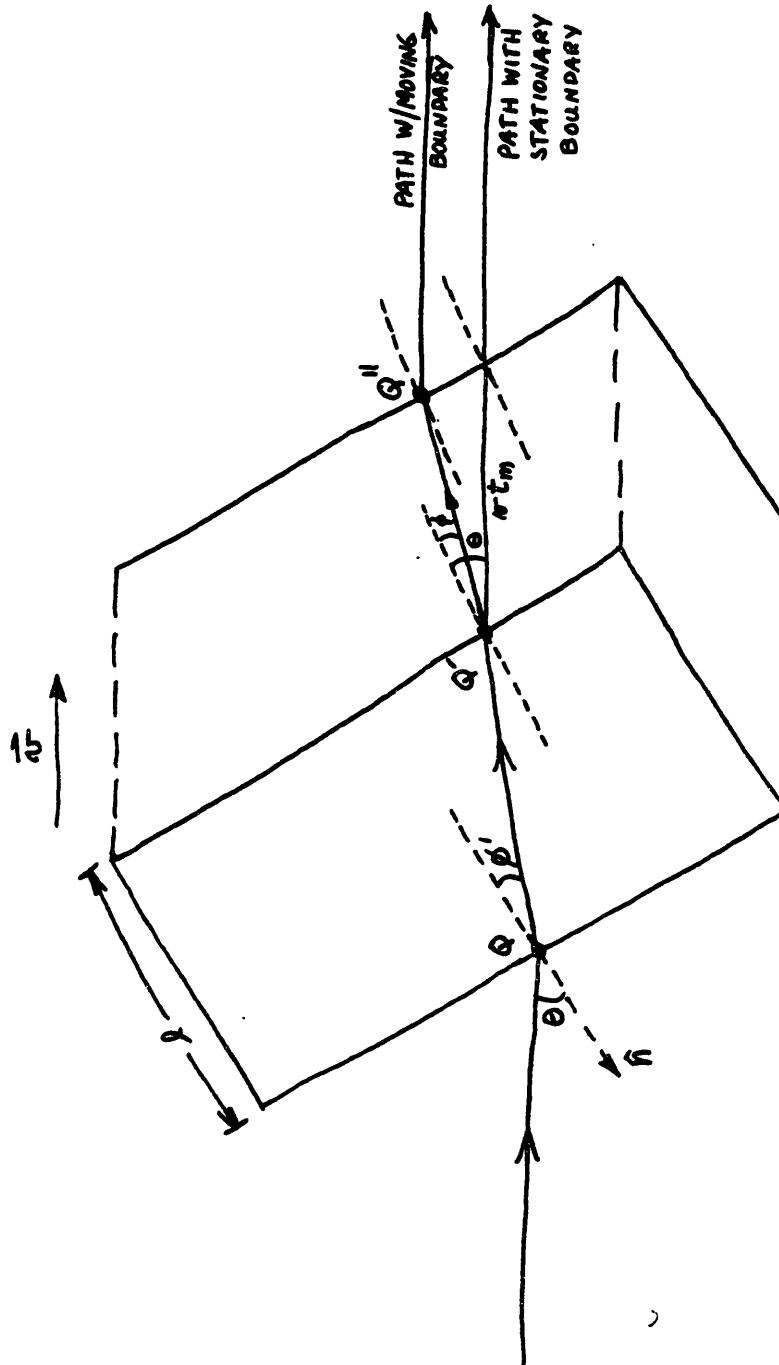


Figure 5.23

extra pathlength due to the motion of the boundary. To first order in v/c , both pathlengths observed in the lab frame are identical to those observed in the rest frame of the glass (a Lorentz contraction is of the order v^2/c^2). The length QQ' is given by,

$$QQ' = \ell / \cos \phi' \quad (5.29)$$

It is useful at this point to define the time interval, as observed in the lab frame, for which the light traverses the pathlength QQ'' , as t_m . During this time, the boundary of the glass moves a distance vt_m , as shown in the figure. By geometry, the distance $Q'Q''$ is given by,

$$Q'Q'' = vt_m \frac{\cos \theta}{\cos \phi'} \quad (5.30)$$

Adding QQ' and $Q'Q''$ and dividing by the velocity along the direction of the light ray, u (given by Eq. (5.27), where γ' is now $\theta - \phi'$)

$$t_m = \frac{\ell / \cos \phi' + vt_m \cos \theta / \cos \phi'}{\frac{c}{n} + \cos(\theta - \phi') v \left[1 - \frac{1}{n^2} \right] - \frac{v\lambda_0}{n^2} \left[\frac{\partial n}{\partial \lambda} \right]} \quad (5.31)$$

where ϕ' is still in terms of the index n' and is yet uncorrected for the doppler effect. Solving for t_m to first order in v/c gives,

$$t_m = \frac{\ell n}{c \cos \phi'} - \frac{\ell v n^2}{c^2 \cos \phi} \left[\cos(\theta - \phi') (1 - 1/n^2) - \frac{\cos \theta}{\cos \phi'} - \frac{\lambda_0}{n^2} \frac{\partial n}{\partial \lambda} \right] \quad (5.32)$$

To derive the total change in time of propagation due to the glass motion, it is necessary to account for the decrease in light propagation time through the air, Δt_a . For the case where the glass is stationary the light would exit the glass at Q' , in a direction parallel to the incident light. With the glass motion, the beam is translated* by a distance b , as shown in the expanded view in Figure 5.24, before exiting the glass at Q'' . The pathlength difference in air is thus given by $Q''a' - Q'a$ as shown in the figure. Labelling $Q''a'$ as d , and recalling $Q'a$ as vt_m , the pathlength difference in air, $-(vt_m - d)$, is given by,

$$d - vt_m = -vt_m \frac{\cos \theta}{\cos \phi'} \cos(\theta - \phi') \quad (5.33)$$

Hence,

$$\Delta t_a = \frac{-vt_m \frac{\cos \theta}{\cos \phi'} \cos(\theta - \phi')}{c/n_a} \quad (5.34)$$

where n_a is the index of air and c is the speed of light in a vacuum.

To arrive at the total time change t^+ , for the beam propagating in the direction of \vec{v} , Δt_a is added to t_m giving,

* The effect due to beam translation in the cavity was investigated as a separate side experiment. By rotating the glass in the cavity, it was found that the resonance frequency shift was in good agreement with the pathlength increase due to rotation of the glass and was unaffected by the translation of the beam inside the cavity (at least for the magnitude of translation in this experiment).

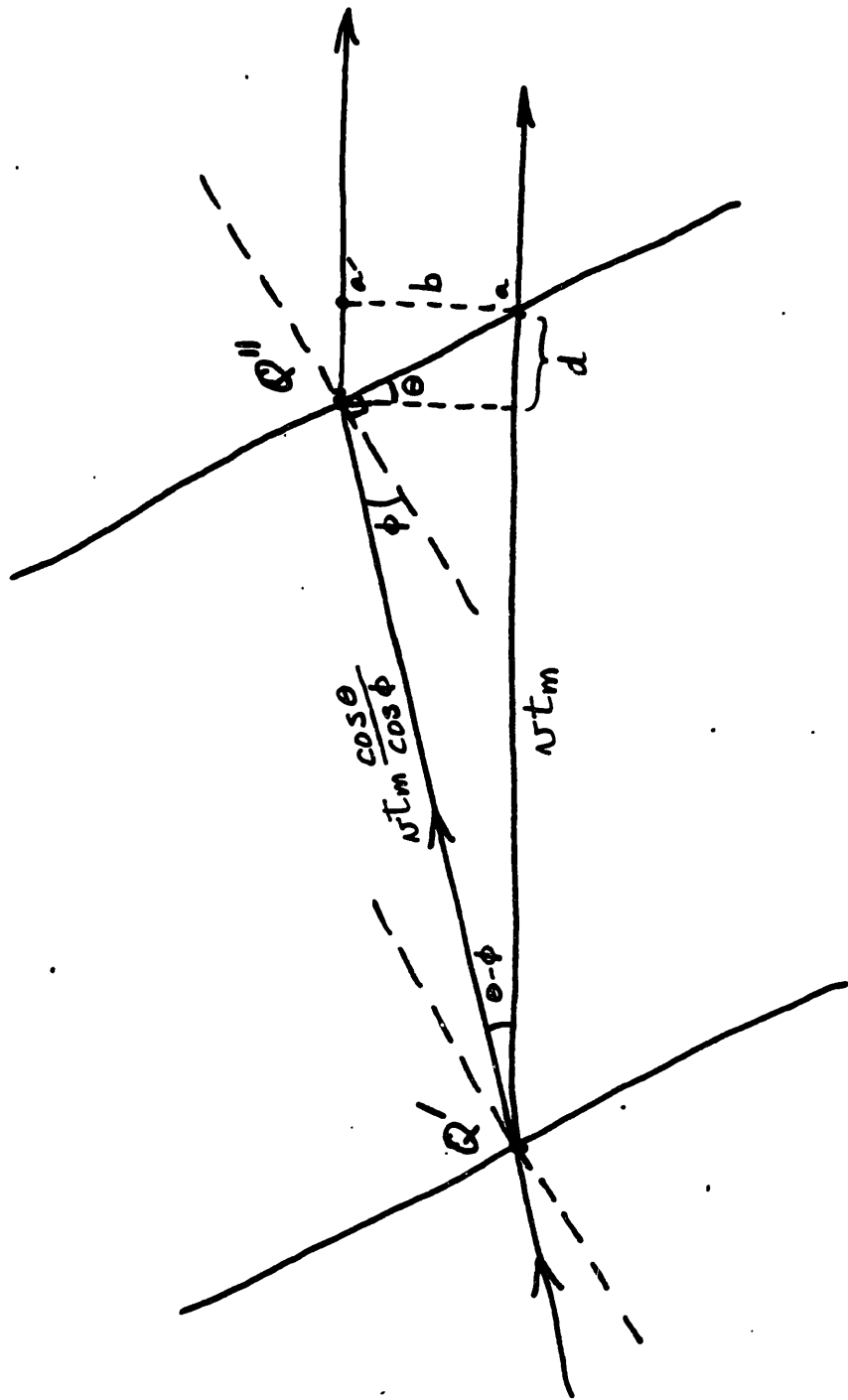


Figure 5.24

$$t^+ = t_m \left[1 - \frac{v}{c} n_a \cos(\theta - \phi') \frac{\cos \theta}{\cos \phi'} \right] \quad (5.35)$$

Combining Eqs. (5.31) and (5.35), and dropping terms of order v^2/c^2 gives,

$$t^+ = \frac{1}{c} \left\{ \frac{ln}{\cos \phi'} - \frac{l}{\cos \phi'} \frac{v}{c} \left[nn_a \frac{\cos \theta}{\cos \phi'} - \lambda_o \frac{\partial n}{\partial \lambda} + n^2 \cos(\theta - \phi') - n^2 \frac{\cos \theta}{\cos \phi'} \right] \right\} \quad (5.36)$$

Rearranging this equation to obtain a convenient form gives

$$t^+ = \frac{1}{c} \left\{ \frac{ln}{\cos \phi'} - \frac{l}{\cos \phi'} \frac{v}{c} \left[nn_a - \cos(\theta - \phi') - \lambda_o \frac{\partial n}{\partial \lambda} + n^2 \left(\cos(\theta - \phi') - \frac{n_a}{n'} \frac{\sin \theta \sin(\theta - \phi')}{\cos \phi'} - \frac{\cos \theta}{\cos \phi'} \right) \right] \right\} \quad (5.37)$$

Ignoring, for the moment, the dispersion correction in ϕ' , the time t^- , for a beam propagating antiparallel to \vec{v} , is given by letting $\vec{v} \rightarrow -\vec{v}$. The difference in time of propagation in the cavity Δt , between the two beams is thus given by,

$$\Delta t = t^- - t^+ = \frac{2l}{c \cos \phi'} \left\{ \frac{v}{c} \left[nn_a - \cos(\theta - \phi') - \lambda_o \frac{\partial n}{\partial \lambda} + n^2 \left(\cos(\theta - \phi') - \frac{n_a}{n} \frac{\sin \theta \sin(\theta - \phi')}{\cos \phi'} - \frac{\cos \theta}{\cos \phi'} \right) \right] \right\} \quad (5.39)$$

The optical pathlength difference ΔP is obtained by multiplying Δt by the vacuum speed of light c , i.e.

$$\Delta P = P - P^+ = c\Delta t \quad (5.40)$$

Before substituting for Δt , it is now convenient to account for the differences in optical pathlength due to the dispersive dependence of $\cos \phi'$. (Because this correction results in the two counter propagating beams traversing different paths inside the glass, it is convenient to discuss this correction separately). Since a correction to ϕ , as shown from Eqs. (5.28) and (2.9), is of order v/c , the correction to those terms proportional to v/c in Eq. (5.37) is negligible (order v^2/c^2). Only that pathlength change associated with the term $ln/c \cos \phi'$ is thus considered here. Letting $\phi' = \phi + d\phi$, the change in pathlength for small $d\phi$ may be obtained by the expansion,

$$\frac{ln}{c \cos(\phi + d\phi)} = \frac{ln}{c \cos \phi} + \frac{ln}{c \cos \phi} \tan \phi d\phi \quad (5.41)$$

where the second term is due to the change in ϕ . To get an expression for $d\phi$ due to the doppler shift, Eq. (2.9) is then substituted into Eq. (5.28) (Snell's Law) to give

$$\frac{\sin \theta}{n(\lambda_o) + \lambda_o \frac{v}{c} \frac{\partial n}{\partial \lambda}} \cong \sin(\phi + d\phi) \quad (5.42)$$

Again, the correction for the index of air is small here and is thus neglected. By expansion of this equation, and by noting that $\frac{\sin \theta}{n(\lambda_0)} = \sin \phi$, the following expression for $d\phi$ may be obtained for the beam incident in the \vec{v} direction:

$$d\phi \approx - \frac{\tan \theta}{n} \frac{v}{c} \lambda_0 \frac{\partial n}{\partial \lambda} \quad (5.43)$$

Hence, by substituting the above equation into Eq. (5.41), the pathlength change $\Delta P(d\phi)$ due to $d\phi$ is given by,

$$\Delta P(d\phi) \approx - \frac{l}{c \cos \phi} \tan^2 \phi \left(\frac{v}{c} \right) \lambda_0 \frac{\partial n}{\partial \lambda} \quad (5.44)$$

The corresponding pathlength change for the oppositely directed beam is again obtained by letting $v \rightarrow -v$. Equation (5.39) may thus be put in terms of ϕ instead of ϕ' by adding the above correction. Doing this, as well as substituting Δt into Eq. (5.40) the total optical pathlength difference between the two beams is given by,

$$\Delta P \approx \frac{2l}{\cos} \frac{v}{c} \left\{ n n_a - \cos(\theta - \phi) - \lambda_0 \frac{\partial n}{\partial \lambda} (1 - \tan^2 \phi) + n^2 \left[\cos(\theta - \phi) - \frac{n_a}{n} \frac{\sin \phi \sin(\theta - \phi)}{\cos \phi} - \frac{\cos \theta}{\cos \phi'} \right] \right\} \quad (5.45)$$

Recalling that $\Delta f/f = -\Delta P/P$, the resonance frequency shift resulting from this pathlength difference is given by

$$\Delta f \approx - \frac{2\ell}{P \lambda_o \cos \phi} v \left\{ n n_a - \cos(\theta - \phi) - \lambda_o \frac{\partial n}{\partial \lambda} (1 - \tan^2 \theta) \right. \\ \left. + n^2 \left[\cos(\theta - \phi) - \frac{n_a}{n} \frac{\sin \theta \sin(\theta - \phi)}{\cos \phi} - \frac{\cos \theta}{\cos \phi'} \right] \right\} \quad (5.46)$$

For the range of n and θ used in this experiment, the fractional contribution of the bracketed term, in the equation above, ranged from -10^{-6} to -10^{-5} . Hence, this term was insignificant for the purpose of this experiment, that is,

$$\Delta f \approx - \frac{2\ell}{P \lambda_o \cos \phi} v \left[n n_a - \cos(\theta - \phi) - \lambda_o \frac{\partial n}{\partial \lambda} (1 - \tan^2 \phi) \right] \quad (5.47)$$

or

$$\Delta f \approx - \frac{2\ell v}{P \lambda_o \cos \phi} \alpha^{SR} \left(n, \frac{\partial n}{\partial \lambda}, \theta \right) \quad (5.48)$$

where α^{SR} is defined here as the effective drag coefficient for the "shuttling rod" configuration given by,

$$\alpha^{SR} \equiv \alpha^{SR} \left(n, \frac{\partial n}{\partial \lambda}, \theta \right) \equiv n n_a - \cos(\theta - \phi) - \lambda_o \frac{\partial n}{\partial \lambda} (1 - \tan^2 \phi) \quad (5.49)$$

CHAPTER 6

DATA ANALYSIS, SUMMARY AND CONCLUSION

6.1. Introduction

This chapter is concerned with the analysis of the data. In Section 6.2 the data for the various drag measurements is summarized and analyzed. Here, plots are presented to show the dependence of the resonance frequency shift on the various parameters in Eq. (5.47). In Section 6.3, the measurements of the effective "shuttling rod" drag coefficient α^{SR} are then summarized and compared with the theoretical prediction for α^{SR} as given by Eq. (5.49). Finally, some concluding remarks are included in Section 6.4.

6.2. Data Analysis

The resonance frequency shift Δf due to the light drag was measured for many different values of the index n , the length of glass l , the angle of incidence θ and the velocity \vec{v} . The results for the particular combinations of the above variables used in this experiment are presented in Tables 11 and 12.

As shown in Table 11, there were 15 different configurations, that is, combinations of n , l and θ , for which data was taken at the same velocity \vec{v} . Only approximate values for l , n and the dispersion of the glass $\frac{\partial n}{\partial \lambda}$ are shown here in Table 11, whereas more accurate values

Table 11

Configuration	Glass Type	n	$\frac{\partial n}{\partial \lambda}$ (μm^{-1})	l (cm)	$\alpha_{\text{th}}^{\text{SR}}$	θ (deg)	$\Delta f(f)_e$	$\Delta f(f)_{\text{th}}$ (Hz)	$\Delta f(f)_e - \Delta f(f)_{\text{th}}$ (Hz)
1	BK-7	1.515	-0.034	0.64	.53783	5.15	954.3 ± 0.8	944.4 ± 0.4	9.9 ± 0.9
2	BK-7	1.515	-0.034	0.64	.53806	6.45	955.0 ± 0.8	945.8 ± 0.4	9.2 ± 0.9
3	BK-7	1.515	-0.034	0.64	.53893	10	960.4 ± 1.0	951.0 ± 0.6	9.4 ± 1.2
4	BK-7	1.515	-0.034	0.64	.53987	12.7	966.4 ± 1.3	956.5 ± 0.7	9.9 ± 1.5
5	BK-7	1.515	-0.034	1.28	.53783	5.15	1895.8 ± 2.1	1887.2 ± 0.8	8.6 ± 2.2
6	SF-1	1.713	-0.096	0.62	.77465	5.15	1333.2 ± 0.7	1323.8 ± 0.5	9.4 ± 0.9
7	SF-1	1.713	-0.096	0.62	.77500	6.6	1335.5 ± 0.7	1325.6 ± 0.5	9.9 ± 0.9
8	SF-1	1.713	-0.096	0.62	.77621	10.15	1342.2 ± 1.1	1331.7 ± 0.7	10.5 ± 1.3
9	SF-57	1.840	-0.138	0.60	.92885	6.6	1533.8 ± 1.1	1523.7 ± 0.6	10.1 ± 1.3
10	SF-57	1.840	-0.138	0.60	.93022	10	1539.9 ± 1.7	1529.7 ± 0.7	10.2 ± 1.8
11	SF-57	1.840	-0.138	1.20	.92888	6.7	3052.4 ± 2.0	3042.9 ± 1.0	9.5 ± 2.2
12	F.S.*	1.457	-0.029	0.20	.47893	15.65	275.4 ± 0.8	265.8 ± 0.3	9.6 ± 0.9
13	F.S.	1.457	-0.029	0.50	.47711	10.2	662.0 ± 0.9	651.7 ± 0.4	10.3 ± 1.0
14	F.S.	1.457	-0.029	1.04	.47614	5.15	1369.8 ± 1.2	1360.9 ± 0.6	8.9 ± 1.3
15	F.S.	1.457	-0.029	1.49	.47614	5.15	1958.8 ± 2	1947.8 ± 0.8	11 ± 2.2

*F.S. represents fused silica

are shown Tables 9 and 8. In the data shown in Table 11, several data runs, for each configuration listed, were averaged to form the data point shown in Table 11. This was done in a manner similar to the data point listed as "configuration #3" which was illustrated in Section 5.5.2a. Although the velocity varied slightly ($\sim\pm 0.3\%$) from run to run, each of these runs, and hence the average results in Table 11, were normalized for a peak to peak velocity of

$$|\vec{v}(f_f)| = 25.525 \pm .006 \text{ cm/s} \quad (6.1)$$

The measured resonance frequency shift $\Delta f(f_f)_e$ at the driving frequency f_f ($f_f \sim 5$ Hz, see Section 5.5.2b) is shown in Table 11 where the error bars were obtained in a manner similar to that illustrated in Section 5.5.2a.

The theoretical, or expected, resonance frequency shift $\Delta f(f_f)_{th}$ was computed from Eq. (5.48), where the theoretical value of the "shuttling rod" drag coefficient α_{th}^{SR} was computed from Eq. (5.49). The uncertainty in α_{th}^{SR} is discussed in Section 6.3 and the various uncertainties in the variables appearing in Eq. (5.48), which were propagated into $\Delta f(f_f)_{th}$, are listed in Sections 5.5.2b through 5.5.2h.

The difference between the measured resonance frequency shift and the predicted resonance frequency shift is shown in the last column of Table 11, where the error bar was obtained by adding the uncertainties in $\Delta f(f_f)_e$ and $\Delta f(f_f)_{th}$ in quadrature. As shown in Table 11, the average difference between the expected and measured resonance frequency shifts

was approximately 10 Hz. This difference was fairly consistent throughout the various measurements where, as shown in Table 11, the resonance frequency shift was varied from ~275 Hz to ~3 KHz.

The measured and predicted resonance frequency shifts are shown in Table 12 as a function of the velocity for glass type BK-7 of length $l = .6405$ cm and angle of incidence $\theta = 6.45^\circ$ (configuration #2 in Table 11). Here, the velocity $v(f_f)$ was varied over a range of approximately 20 cm/s to 29 cm/s, or a fractional variation of approximately 40%. (This range was limited by the displacement range and frequency response of the bearing-electromechanical driver system.)

A plot of the resonance frequency shift $\Delta f(f_f)$ vs. $v(f_f)$ is shown in Figure 6.1. The measured values $\Delta f(f)_e$ are depicted as points and the theoretical values $\Delta f(f)_{th}$ are shown as x's. Because of the large range of Δf in Figure 6.1, the difference between $\Delta f(f)_e$ and $\Delta f(f)_{th}$ is difficult to see; thus, an expanded scale is shown in Figure 6.2, where the same labeling convention is used for the plot.

As shown in Figure 6.2 and Table 12, the difference between $\Delta f(f_f)_e$ and $\Delta f(f_f)_{th}$ varied linearly with $v(f_f)$, which effectively gave a different slope (by ~1 part in 10^2) for the measured curve in Figure 6.2 than that for the theoretical curve. As one additional note, the linearity of the curve in Figure 6.2 was investigated. Here the ratio $\Delta f(f_f)_e/v(f_f)$ for each point was compared to the average value of $\Delta f(f_f)_e/v(f_f)$, or the slope of the measured curve Figure 6.2. The maximum deviation of $\Delta f(f_f)_e/v(f_f)$ from the average slope was found to be less than ~1 part in 1600, which was well within the typical

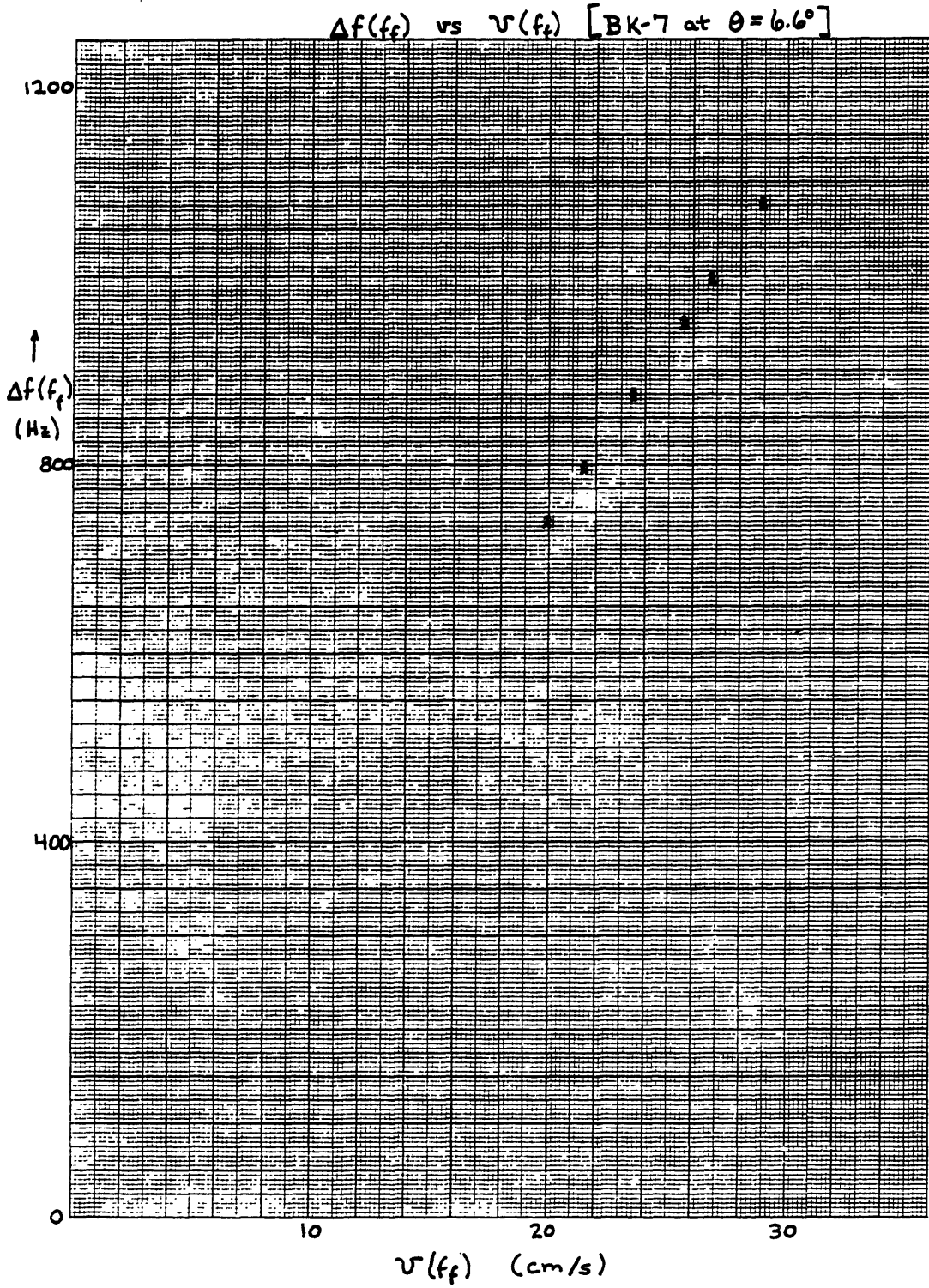


Figure 6.1

$\Delta f(f_f)$ vs $v(f_f)$ [BK-7 at $\theta = 6.6^\circ$]

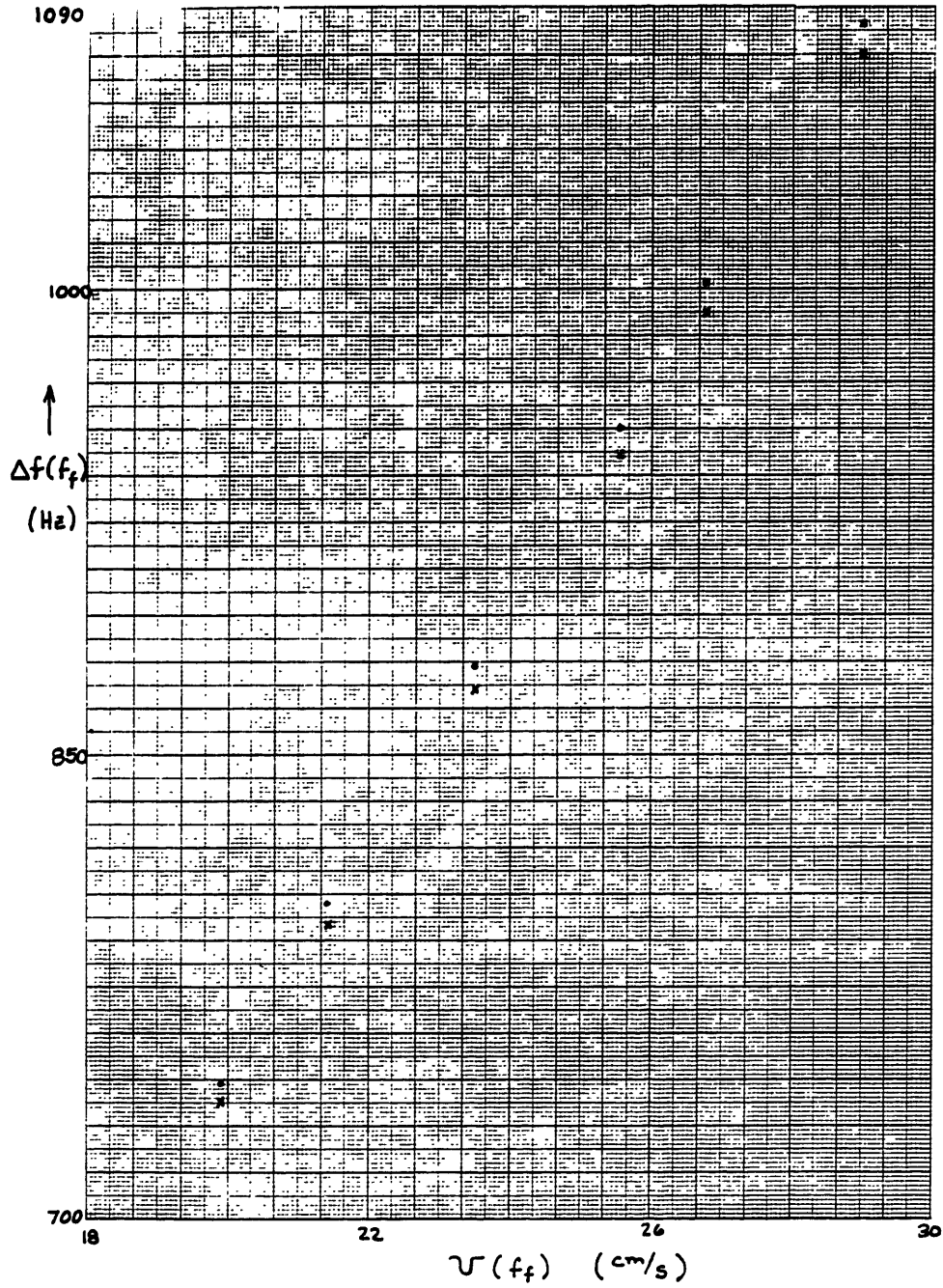


Figure 6.2

Table 12

$\vec{v}(f_f)$ (cm/s)	$\Delta f(f_f)_e$ (Hz)	$\Delta f(f_f)_{th}$ (Hz)	$\Delta f(f_f)_e - \Delta f(f_f)_{th}$
19.899	744.0 ± 0.9	737.3 ± 0.3	6.7 ± 0.9
21.438	802.1 ± 0.9	794.3 ± 0.3	7.8 ± 0.9
23.492	878.9 ± 0.9	870.5 ± 0.4	8.4 ± 1.0
25.525	955.0 ± 1.0	945.8 ± 0.4	9.2 ± 1.1
26.770	1001.8 ± 1.0	991.9 ± 0.4	9.9 ± 1.1
28.985	1084.5 ± 1.0	1074.0 ± 0.5	10.5 ± 1.1

error bar (~1 part in 1000) for a given point on the curve.

To further investigate the difference between $\Delta f(f_f)_e$ and $\Delta f(f_f)_{th}$, shown in Table 11, the resonance frequency shift $\Delta f(f_f)_e$ was plotted as a function of the length of glass l for the fixed velocity given by Eq. (6.1). This was done for three different glass types as shown in Figures 6.3, 6.4, and 6.5. In each of these figures, the points represent the measured values, while the x's represent the theoretical values. (Because of the large range of $\Delta f(f_f)$ depicted in these figures, and because of the small difference between $\Delta f(f_f)_e$ and $\Delta f(f_f)_{th}$, it is difficult to see the difference between $\Delta f(f_f)_e$ and $\Delta f(f_f)_{th}$.)

In Figure 6.3, the resonance frequency shift vs. l is shown for fused silica, where l was varied by approximately an order of magnitude. Since the data points for the various lengths were taken at different angles of incidence θ , as shown in Table 11, the data was normalized for $\theta = 5.15^\circ$ (the θ dependence of the drag was checked and is shown later in Figures 6.6, 6.7 and 6.8). As shown in the inset of Figure 6.3, an offset (for $l = 0$) was observed of $\approx 9.8 \text{ Hz} \pm .5 \text{ Hz}$ which was obtained by fitting a straight line through the data points.

Likewise, similar offsets of $\approx 9.8 \text{ Hz} \pm .8 \text{ Hz}$ and $10.1 \text{ Hz} \pm 1 \text{ Hz}$, were obtained from the plots of $\Delta f(f_f)$ vs. l for the cases of BK-7 and SF-57 shown in Figures 6.4 and 6.5, respectively. The dashed line in Figure 6.5 represents, for the purpose of illustration, the theoretical resonance frequency shift for SF-57, without including the dispersion term in α^{SR} given by Eq. (5.49). The fractional contribution of this term was -9.4% for SF-57, which was the most dispersive glass type

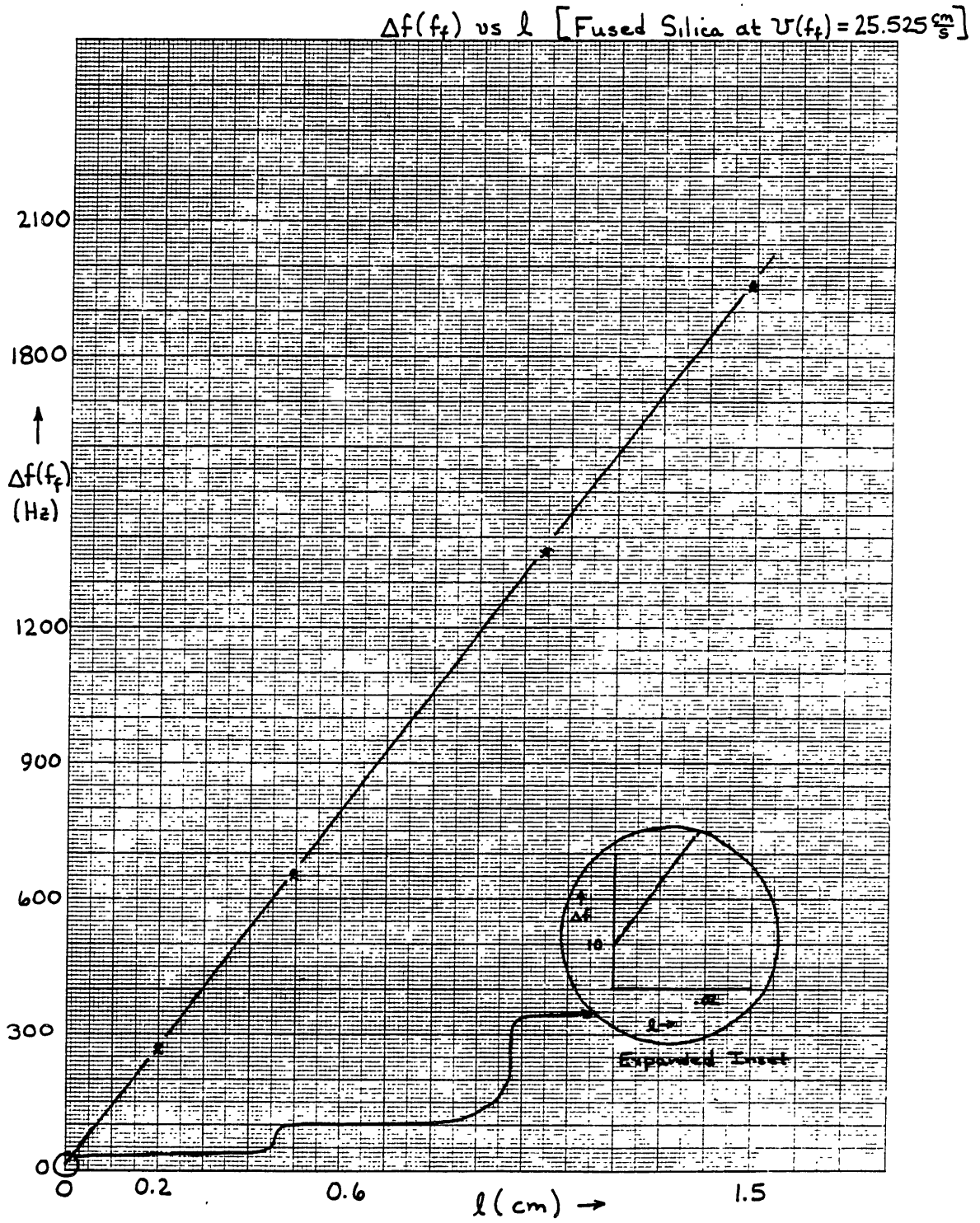


Figure 6.3

$\Delta f(f_f)$ vs. l [BK-7 at $v(f_f) = 25.525 \text{ cm/s}$]

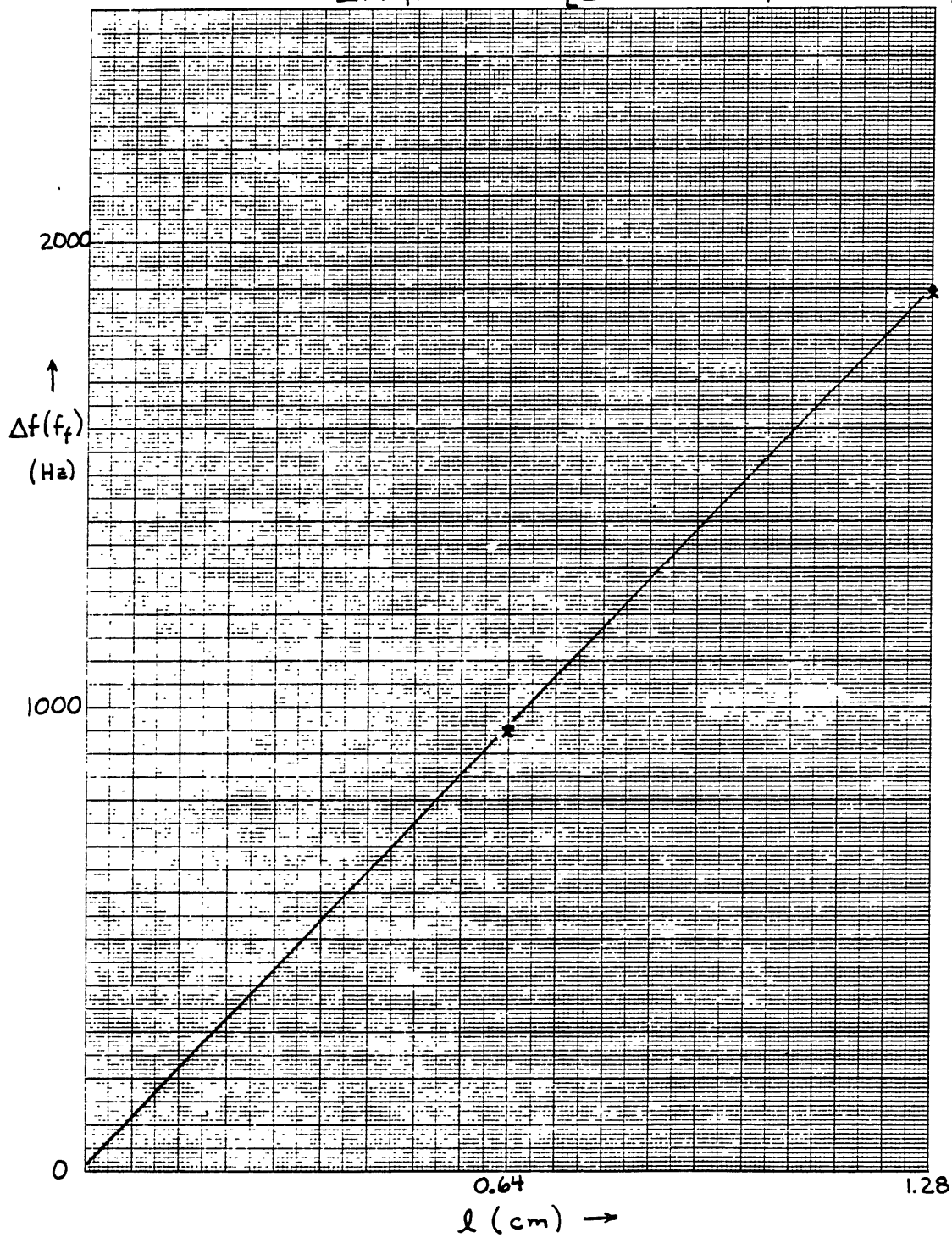


Figure 6.4

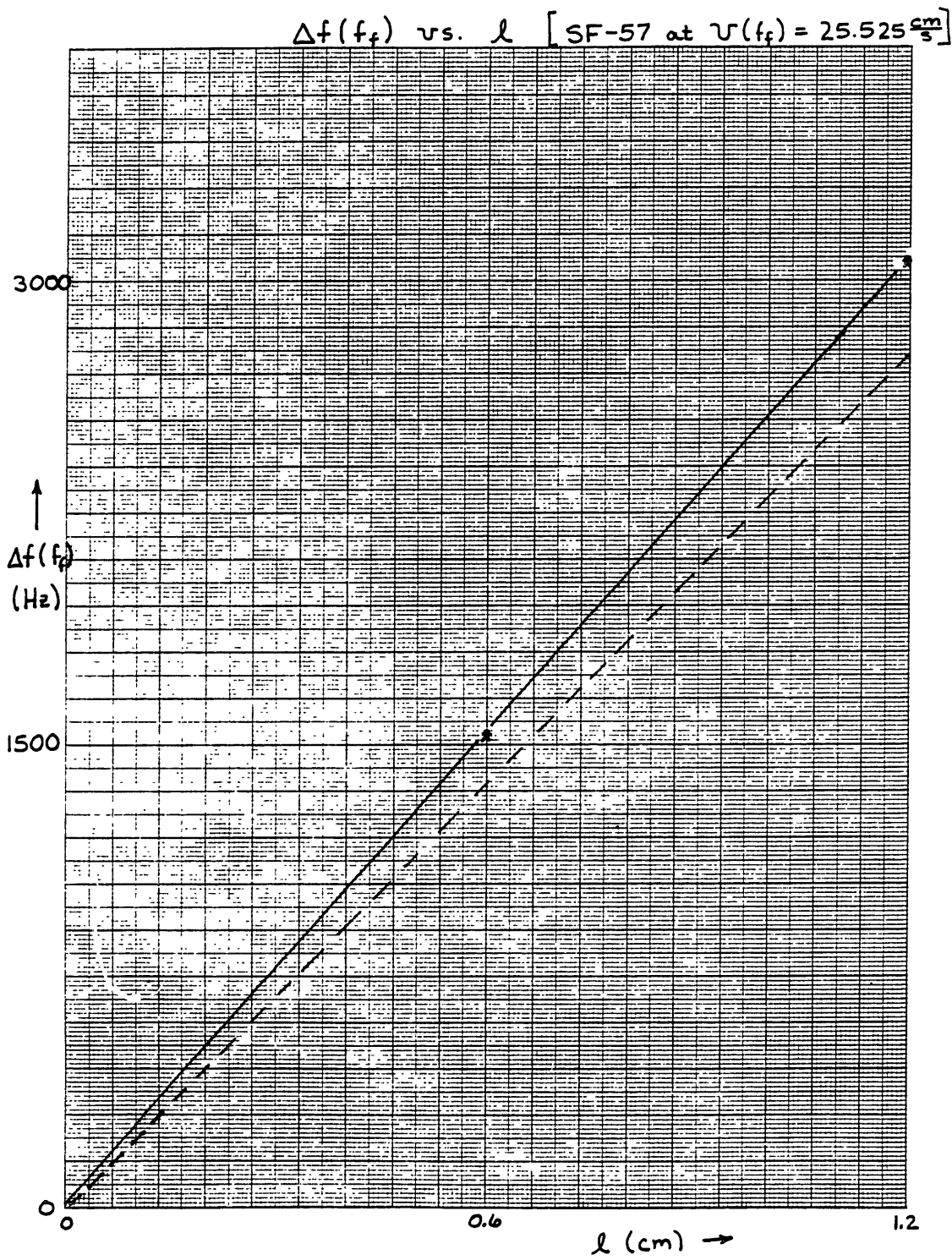


Figure 6.5

used in this experiment.

In the cases of BK-7 and SF-57, two pieces of glass, each of length ~ 0.6 cm were used to obtain the total length of glass represented by the points for $l \approx 1.2$ cm in Figures 6.4 and 6.5. (In this case, an air gap of ~ 0.5 cm was placed between the two pieces of glass to avoid multiple reflections between surfaces. A correction was made to the expected resonance frequency shift of ~ 0.5 Hz based on the drag due to this "shuttling rod of air"). As was again demonstrated by these plots, the offset was independent of n to within the stated error bars. The linearity of the various length plots was checked via a χ^2 fit to the data, and the various values of χ^2 and the offsets are shown in Table 13.

The angular dependence of the drag is depicted in Figures 6.6, 6.7, and 6.8 where $\Delta f(f_f)$ is plotted as a function of the angle of incidence θ for BK-7, SF-1 and SF-57, respectively. The points in each curve represent the measured values taken from Table 11, while the circled points represent the theoretical values. As shown in these plots, the offset of 9.8 Hz was independent of θ . To verify this, and to check the angular dependence of the drag, the various plots of $\Delta f(f_f)$ vs. θ were fitted to the angular dependence of the drag given by Eq. (5.47). The values of χ^2 as well as the offset are shown in Table 13.

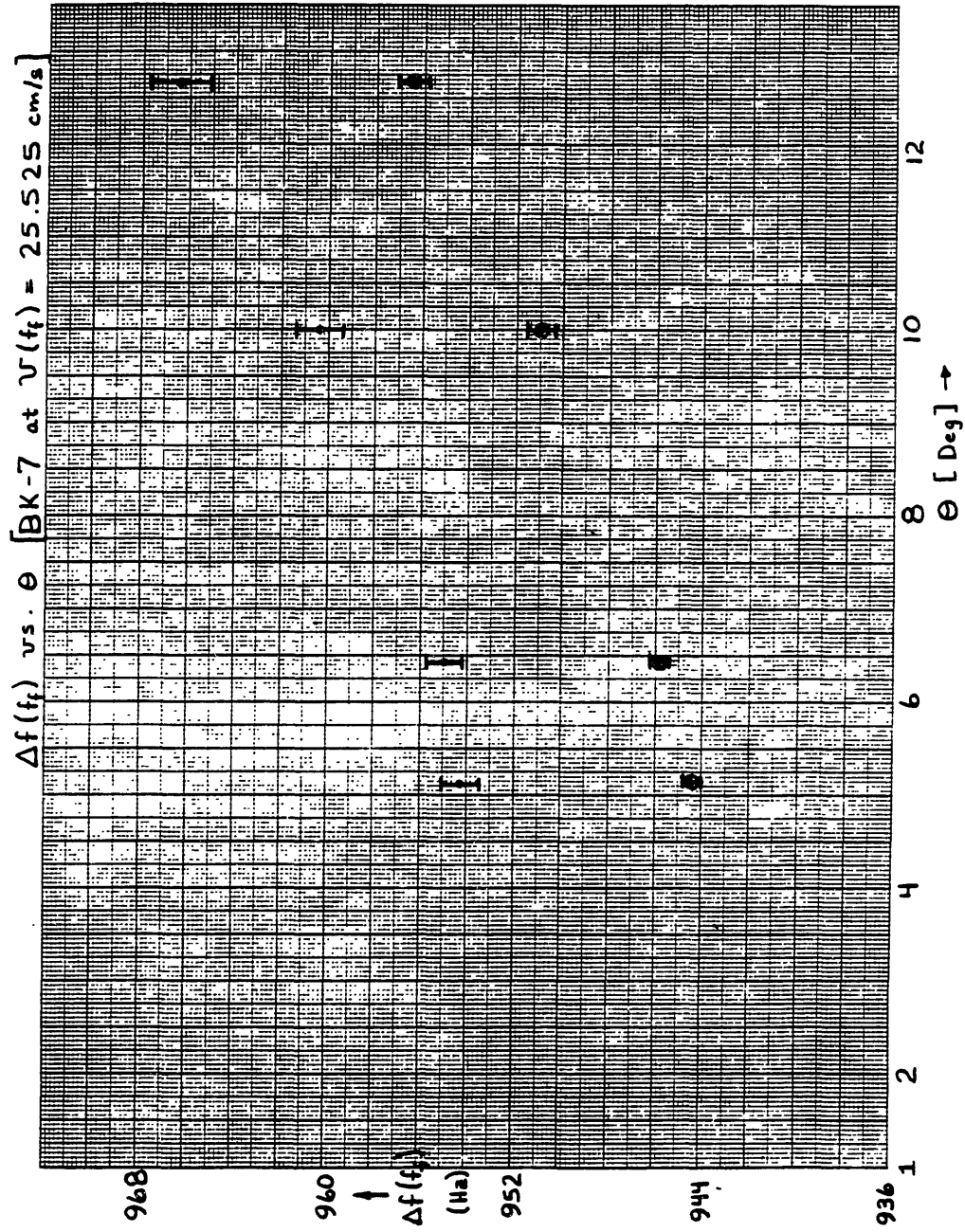


Figure 6.6

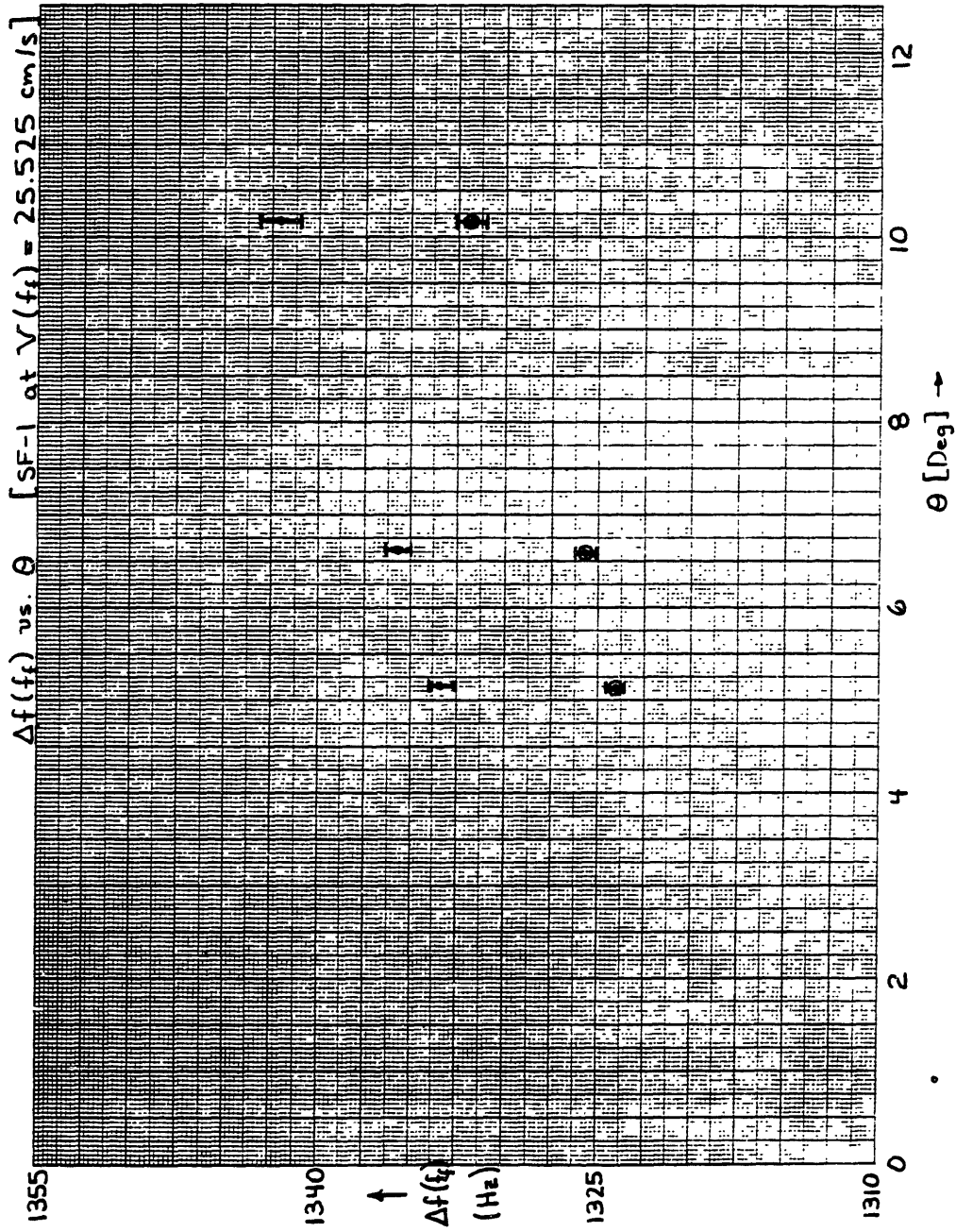


Figure 6.7

$\Delta f(f_f)$ vs. θ [SF-57 at $v(f_f) = 25.525$ cm/s]

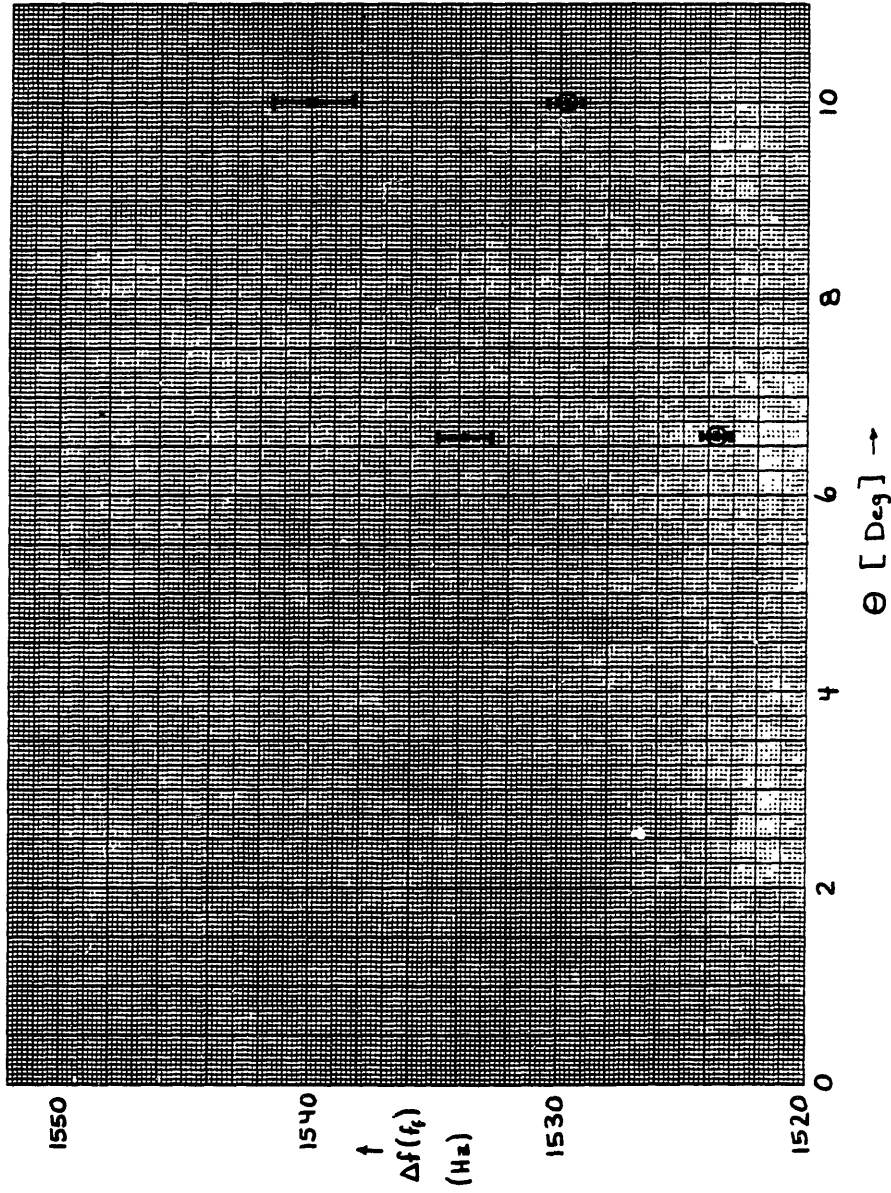


Figure 6.8

Table 13

Glass Type	Plot	χ^2	Offset (Hz)
BK-7	$\Delta f(f_f)$ vs l	0.2	9.8 ± 0.8
SF-57	$\Delta f(f_f)$ vs l	0.01	10.1 ± 1.0
Fused Silica	$\Delta f(f_f)$ vs l	1.3	9.8 ± 0.5
BK-7	$\Delta f(f_f)$ vs θ	0.6	9.6 ± 0.5
SF-1	$\Delta f(f_f)$ vs θ	0.6	9.9 ± 0.6
SF-57	$\Delta f(f_f)$ vs θ	.004	10.1 ± 0.9

For the velocity given by Eq. (6.1), the average offset for the length plots was obtained by taking a weighted average (according to the error bars on the offsets) of the offsets in Table 13 with the result that,

$$\overline{\text{offset}} = 9.8 \pm .4 \text{ Hz} \quad (6.2)$$

The same average offset was also obtained from the plots of $\Delta f(f_f)$ vs θ .

In addition, the resonance frequency shift was plotted in Figure 6.9 as a function of α_{th}^{SR} (from Table 11) for the velocity in Eq. (6.1). In Figure 6.9, the measured values $\Delta f(f_f)_e$ are shown as points and the theoretical values $\Delta f(f_f)_{th}$ are shown as x's (here again, it is difficult to see the difference between $\Delta f(f_f)_e$ and $\Delta f(f_f)_{th}$ on this scale). The data points from Table 11 for which $l \approx 0.6$ cm

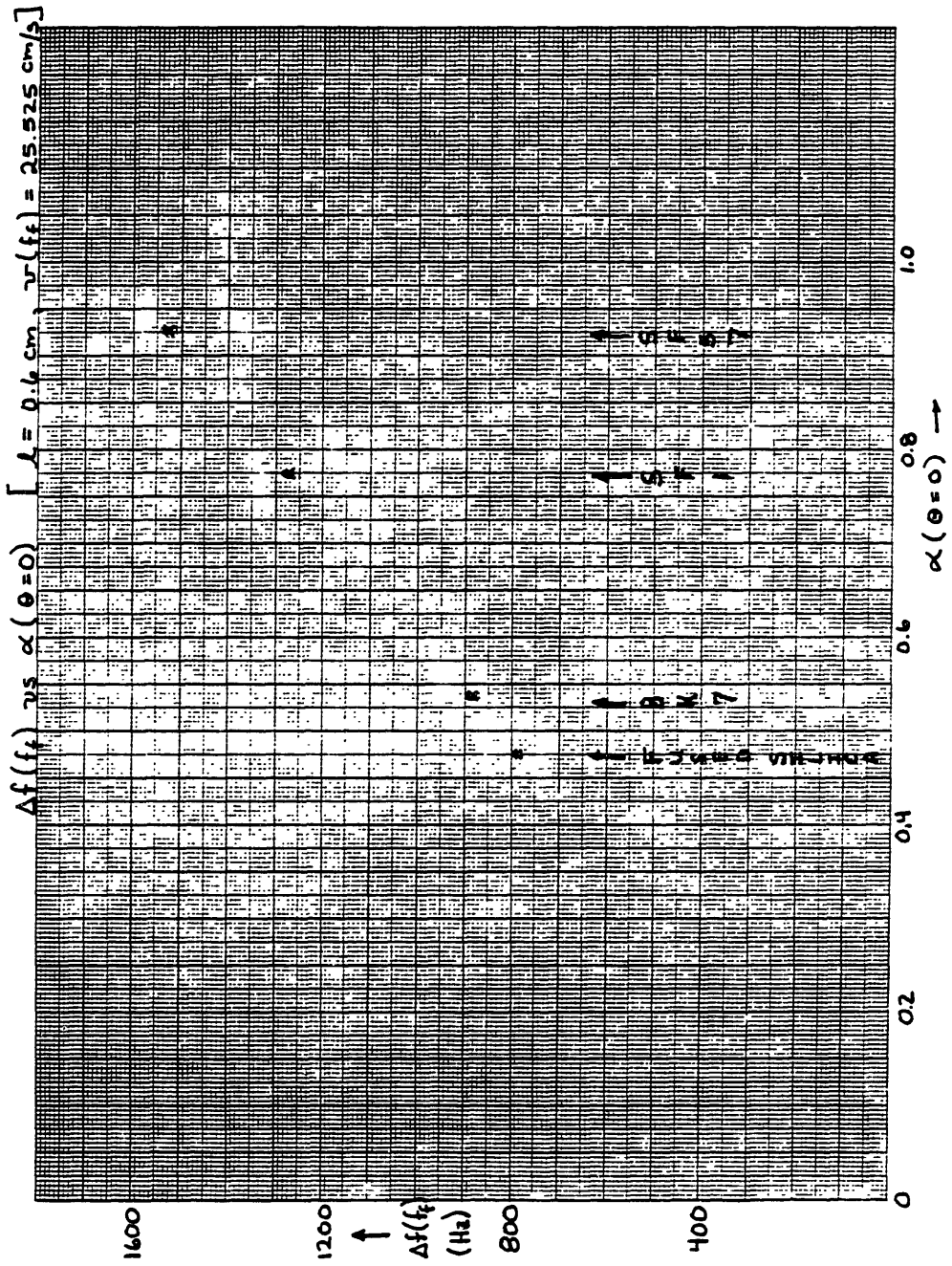


Figure 6.9

for BK-7, SF-1 and SF-57 and $l \approx .5$ cm for fused silica were used for this plot. The various data were then normalized for $l = .6$ and $\theta = 0$ for the purpose of this graph. A similar offset to those presented in Table 13 was obtained here.

To summarize the data regarding this offset thus far, the offset was found to be independent (to ± 4 Hz) of the index n , the length of glass l , and the angle of incidence θ . Since there was a residual $\Delta f(f_f)_e$ when f was extrapolated to zero in the length curves (Figures 6.3, 6.4 and 6.5), this suggested that the offset was not due to the drag effect in the glass. In addition, possible causes of the offset due to surface effects were ruled out by the fact that the same effect was observed when the number of surfaces (of glass) were doubled in the cases of BK-7 and SF-57 as discussed earlier. As stated earlier, the offset, as shown in Tables 11 and 13, was found to be constant when the velocity was held constant, and varied linearly (as shown in Table 12) for changes in the velocity of the medium.

The above evidence suggested that the offset was due to the drag produced by moving air back and forth inside the cavity as the glass was moved to and fro. This was also supported by the fact that, in all the measurements, we used glass windows of identical cross-sectional area (~1 inch diameter). Hence, for a given velocity (corresponding to a given displacement) the volume of air being moved was the same for all the measurements.

The above hypothesis was also consistent with a rough calculation for the drag due to the air. Using an argument similar

to that found in Section 4.6e, for an effective length of air of ~2.5 cm (on each side of the glass) and a velocity of ~25 cm/s the expected resonance frequency shift is ~9 Hz.

Since the offset was found to be reproducible (to ± 0.4 Hz), for the data taken at $v(f_f) = 25.525$ cm/s, shown in Table 11, the offset stated in Eq. (6.2) was subtracted from the measured values of $\Delta f(f_f)_e$ in Table 11. The corrected resonance frequency shift, for each of the 15 configurations in Table 11 was then compared to the theoretical value, as shown in Table 14. Here the uncertainty in the offset was propagated into the uncertainty in $\Delta f(f_f)_e$. As shown in the last column of Table 14, the difference between measured and theoretical values of $\Delta f(f_f)$ varied randomly for the various measurements, and in addition, was always within the stated uncertainties in $\Delta f(f_f)_e - \Delta f(f_f)_{th}$.

6.3. Determination of the Drag Coefficient

The drag coefficient for the "shuttling rod" experimental arrangement was determined by means of Eq. (5.48) for the 15 configurations listed in Tables 11 and 14. Solving Eq. (5.48) for α^{SR} , the measured value of α^{SR} was given by,

$$\alpha_e^{SR} = \Delta f(f_f)_e \frac{P \lambda_o \cos \phi}{2l v(f_f)} \quad (6.3)$$

where the peak to peak amplitudes of the measured resonance frequency shift $\Delta f(f_f)_e$ and the velocity $v(f_f)$ were used in Eq. (6.3). The values for the angle of refraction ϕ were obtained by Snell's law and the

Table 14

Configuration	Glass Type	n	$\frac{\partial n}{\partial \lambda}$ (μm^{-1})	λ (cm)	$\alpha_{\text{th}}^{\text{SR}}$	θ (deg)	$\Delta f(f_e)$	$\Delta f(f_{\text{th}})$ (Hz)	$\Delta f(f_e) - \Delta f(f_{\text{th}})$ (Hz)
1	BK-7	1.515	-0.034	0.64	.53783	5.15	944.5 ± 0.9	944.4 ± 0.4	0.1 ± 1.0
2	BK-7	1.515	-0.034	0.64	.53806	6.45	945.2 ± 0.9	945.8 ± 0.4	-0.6 ± 1.0
3	BK-7	1.515	-0.034	0.64	.53893	10	950.6 ± 1.1	951.0 ± 0.6	-0.4 ± 1.3
4	BK-7	1.515	-0.034	0.64	.53987	12.7	956.6 ± 1.3	956.5 ± 0.7	0.1 ± 1.5
5	BK-7	1.515	-0.034	1.28	.53783	5.15	1886.0 ± 2.1	1887.2 ± 0.8	-1.2 ± 2.3
6	SF-1	1.713	-0.096	0.62	.77465	5.15	1323.4 ± 0.8	1323.8 ± 0.5	-0.4 ± 0.9
7	SF-1	1.713	-0.096	0.62	.77500	6.6	1325.7 ± 0.8	1325.6 ± 0.5	0.1 ± 0.9
8	SF-1	1.713	-0.096	0.62	.77621	10.15	1332.4 ± 1.2	1331.7 ± 0.7	0.7 ± 1.4
9	SF-57	1.840	-0.138	0.60	.92885	6.6	1524.0 ± 1.2	1523.7 ± 0.6	0.3 ± 1.3
10	SF-57	1.840	-0.138	0.60	.93022	10	1530.1 ± 1.7	1529.7 ± 0.7	0.4 ± 1.8
11	SF-57	1.840	-0.138	1.20	.92888	6.7	3042.6 ± 2	3042.9 ± 1.0	-0.3 ± 2.2
12	F.S.*	1.457	-0.029	0.20	.47893	15.65	265.6 ± .9	265.8 ± 0.3	-0.2 ± 1.0
13	F.S.	1.457	-0.029	0.50	.47711	10.2	652.2 ± 1	651.7 ± 0.4	0.5 ± 1.1
14	F.S.	1.457	-0.029	1.04	.47614	5.15	1360.0 ± 1.2	1360.9 ± 0.6	-0.9 ± 1.3
15	F.S.	1.457	-0.029	1.49	.47614	5.15	1949.0 ± 2	1947.8 ± 0.8	1.2 ± 2.2

*F.S. represents fused silica

angles of incidence θ , stated in Table 14. The values of the optical perimeter P and the wavelength λ_o are shown in Sections 5.5.2f and 5.5.2h, respectively. Based on the values of $\Delta f(f_f)_e$ in Table 14 (that is, after the offset was subtracted from $\Delta f(f_f)_e$), α_e^{SR} was computed for each of the configurations in Table 14 and the results for α_e^{SR} are shown in Table 15.

The fractional contribution to the uncertainty in α_e^{SR} for each term in Eq. (6.3) is shown in Table 16 for a typical measurement; in this case, configuration #3 for BK-7 at an angle of incidence $\theta = 10^\circ$. As shown in Table 16, the dominant source of uncertainty in α_e^{SR} was due to the uncertainty in the measurement of $\Delta f(f_f)_e$. A discussion of the uncertainty in $\Delta f(f_f)_e$ is included in Section 5.5.2a. Likewise, discussions of the uncertainties in the other parameters in Table 16 are included in Sections 5.5.2b,d,f,g and h.

Table 16

$\frac{\Delta \alpha_e^{SR}}{\alpha_e^{SR}}$	$\Delta l/l$	$[\Delta f(f_f)_e]/\Delta f(f_f)_e$	$\frac{\Delta P}{P}$	$\frac{\Delta \lambda_o}{\lambda_o}$	$\frac{\Delta \cos \phi}{\cos \phi}$	$\frac{\Delta v(f_f)}{v(f_f)}$
1×10^{-3}	1×10^{-4}	1×10^{-3}	$<3 \times 10^{-5}$	$<10^{-5}$	3×10^{-4}	2×10^{-4}

Table 15

Configuration	Glass Type	n	$\frac{\partial n}{\partial \lambda}$ (μm^{-1})	λ (cm)	θ (deg)	α_e SR	α_{th} SR	$\alpha_e - \alpha_{th}$ SR
1	BK-7	1.515	-0.034	0.64	5.15	$.5379 \pm 5 \times 10^{-4}$	$.53783 \pm 1.1 \times 10^{-4}$	$6 \times 10^{-5} \pm 1 \times 10^{-3}$
2	BK-7	1.515	-0.034	0.64	6.45	$.5377 \pm 5 \times 10^{-4}$	$.53806 \pm 1.1 \times 10^{-4}$	$-6 \times 10^{-4} \pm 1 \times 10^{-3}$
3	BK-7	1.515	-0.034	0.64	10	$.5387 \pm 6 \times 10^{-4}$	$.53893 \pm 1.3 \times 10^{-4}$	$-4 \times 10^{-4} \pm 1 \times 10^{-3}$
4	BK-7	1.515	-0.034	0.64	12.7	$.5399 \pm 8 \times 10^{-4}$	$.53887 \pm 1.5 \times 10^{-4}$	$1 \times 10^{-4} \pm 1 \times 10^{-3}$
5	BK-7	1.515	-0.034	1.28	5.15	$.5375 \pm 6 \times 10^{-4}$	$.53783 \pm 1.1 \times 10^{-4}$	$-6 \times 10^{-4} \pm 1 \times 10^{-3}$
6	SF-1	1.713	-0.096	0.62	5.15	$.7744 \pm 5 \times 10^{-4}$	$.77465 \pm 1.2 \times 10^{-4}$	$-3 \times 10^{-4} \pm 7 \times 10^{-4}$
7	SF-1	1.713	-0.096	0.62	6.6	$.7751 \pm 5 \times 10^{-4}$	$.77500 \pm 1.2 \times 10^{-4}$	$1 \times 10^{-4} \pm 7 \times 10^{-4}$
8	SF-1	1.713	-0.096	0.62	10.15	$.7766 \pm 7 \times 10^{-4}$	$.77621 \pm 1.5 \times 10^{-4}$	$5 \times 10^{-4} \pm 9 \times 10^{-4}$
9	SF-57	1.840	-0.138	0.60	6.6	$.9291 \pm 7 \times 10^{-4}$	$.92885 \pm 1.3 \times 10^{-4}$	$2 \times 10^{-4} \pm 8 \times 10^{-4}$
10	SF-57	1.840	-0.138	0.60	10	$.9304 \pm 1 \times 10^{-3}$	$.93022 \pm 1.6 \times 10^{-4}$	$2 \times 10^{-4} \pm 1 \times 10^{-3}$
11	SF-57	1.840	-0.138	1.20	6.7	$.9288 \pm 6 \times 10^{-4}$	$.92888 \pm 1.3 \times 10^{-4}$	$-1 \times 10^{-4} \pm 7 \times 10^{-4}$
12	F.S.*	1.457	-0.029	0.20	15.65	$.4786 \pm 2 \times 10^{-3}$	$.47893 \pm 1.3 \times 10^{-4}$	$-7 \times 10^{-4} \pm 3 \times 10^{-3}$
13	F.S.	1.457	-0.029	0.50	10.2	$.4775 \pm 7 \times 10^{-4}$	$.47111 \pm 6 \times 10^{-5}$	$8 \times 10^{-4} \pm 1 \times 10^{-3}$
14	F.S.	1.457	-0.029	1.04	5.15	$.4758 \pm 5 \times 10^{-4}$	$.47614 \pm 6 \times 10^{-5}$	$-7 \times 10^{-4} \pm 9 \times 10^{-4}$
15	F.S.	1.457	-0.029	1.49	5.15	$.4764 \pm 5 \times 10^{-4}$	$.47614 \pm 6 \times 10^{-5}$	$6 \times 10^{-4} \pm 9 \times 10^{-4}$

*F.S. represents fused silica

The theoretical value of the drag coefficient α_{th}^{SR} , shown in Table 15 for the various measurements, was obtained from Eq. (5.49). The uncertainties in α_{th}^{SR} , stated in Table 15, were primarily due to the uncertainties in n (see Section 5.5.2c) and θ (see Section 5.5.2b). The fractional contributions of the uncertainties in n and θ to the uncertainty in α_{th}^{SR} ($\Delta\alpha_{th}^{SR}/\alpha_{th}^{SR} \sim 2 \times 10^{-4}$) for configuration #3 were $\sim 1.8 \times 10^{-4}$ and 1.5×10^{-4} , respectively.

The measured drag coefficient α_e^{SR} is compared to the theoretical drag coefficient α_{th}^{SR} in the last column of Table 15. Since the values for α^{SR} are different for the various measurements, it was convenient to compare the measured values to the theoretical values on a fractional basis, i.e., $(\alpha_e^{SR} - \alpha_{th}^{SR})/\alpha_{th}^{SR}$. The error bar stated in the last column of Table 15, a typical error bar for $(\alpha_e^{SR} - \alpha_{th}^{SR})/\alpha_{th}^{SR}$ was 1×10^{-3} and each of the measurements of α_e^{SR} were in agreement with α_{th}^{SR} to within the uncertainties stated in Table 15.

To illustrate the results in the last column of Table 15, a histogram is presented in Figure 6.10. In Figure 6.10, each of the values $(\alpha_e^{SR} - \alpha_{th}^{SR})/\alpha_{th}^{SR}$ from Table 15 were rounded off to the first significant digit and were represented as one observation ($N = 1$). The total number N of observations for each possible value of $(\alpha_e^{th} - \alpha_{th}^{SR})/\alpha_{th}^{SR}$ is shown in Figure 6.10; for instance, there were three measurements for which $(\alpha_e^{SR} - \alpha_{th}^{SR})/\alpha_{th}^{SR}$ was 1×10^{-4} . The solid vertical line in Figure 6.10 represents perfect agreement with theory, that is, $\alpha_e^{SR} - \alpha_{th}^{SR} = 0$. As shown in the histogram the measurements are distributed randomly about the vertical line in the center.

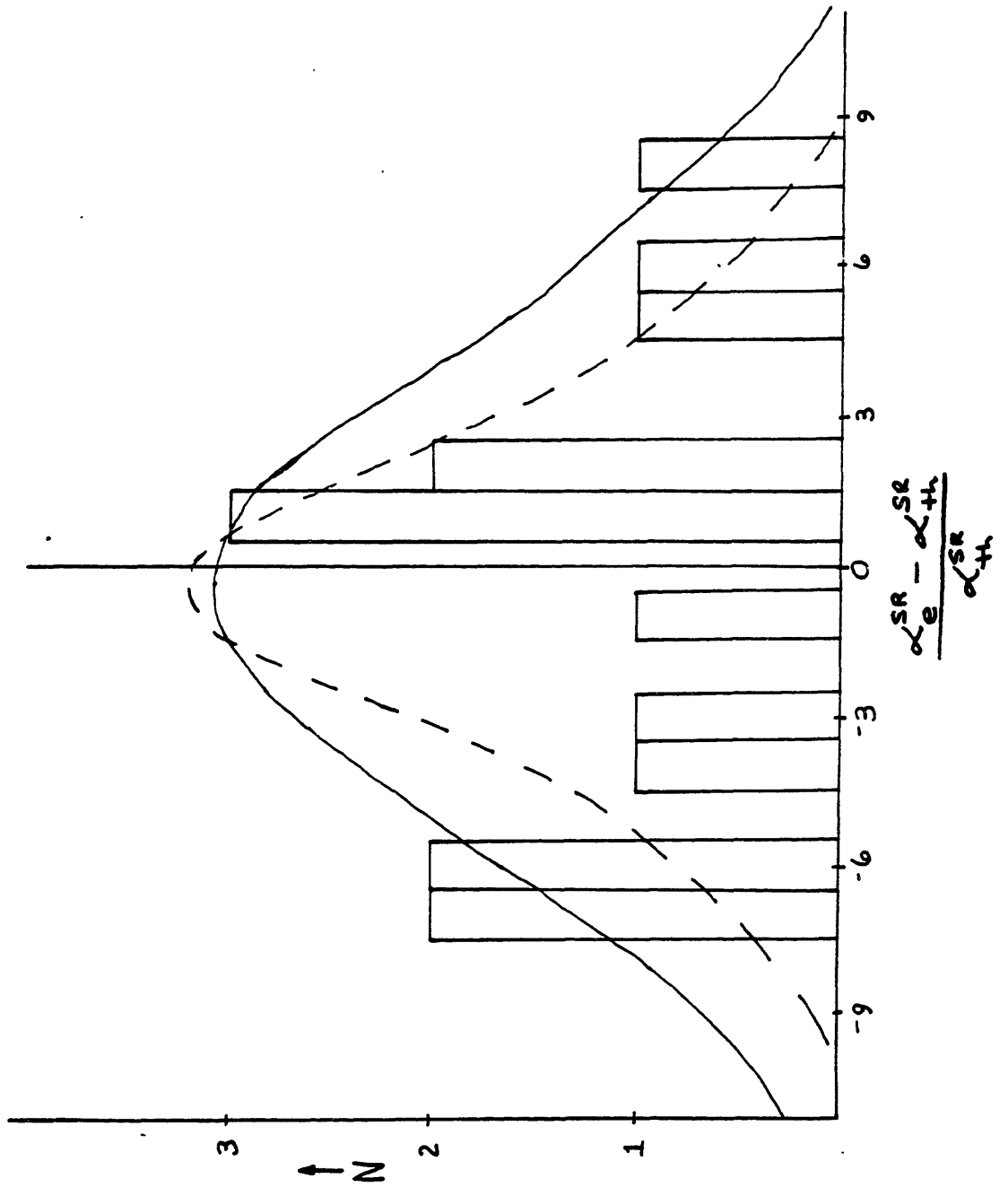


Figure 6.10

If $(\alpha_e^{SR} - \alpha_{th}^{SR})/\alpha_{th}^{SR}$ is averaged over all the measurements, the average agreement with theory is given by,

$$\frac{(\alpha_e^{SR} - \alpha_{th}^{SR})}{\alpha_{th}^{SR}} \approx -5 \times 10^{-5} \pm 5 \times 10^{-4} \quad (6.4)$$

where the uncertainty quoted in Eq. (6.4) is the standard deviation, or spread, of the results in the last column of Table 15. The above result is represented, for illustration, by the solid gaussian curve of width 5×10^{-4} shown in Figure 6.10, where the curve is centered at $\alpha_e^{SR} - \alpha_{th}^{SR}/\alpha_{th}^{SR} = -5 \times 10^{-5}$.

If the results in the last column of table 15 are averaged by means of a weighted average (according to the error bars for each result), the average agreement with theory is given by,

$$\frac{\alpha_e^{SR} - \alpha_{th}^{SR}}{\alpha_{th}^{SR}} \approx -4 \times 10^{-5} \pm 2.4 \times 10^{-4} \quad (6.5)$$

The result in Eq. (6.5) is represented in the histogram (Figure 6.10) by the dashed gaussian curve of width 2.4×10^{-4} centered at $\alpha_e^{SR} - \alpha_{th}^{SR}/\alpha_{th}^{SR} = -4 \times 10^{-5}$.

As an additional note, the confidence for the inclusion of the dispersion term in α^{SR} (see Eq. (5.49)) was evaluated. For illustration, in the case of SF-57, which was the most dispersive glass type used in this experiment, the fractional contribution of the dispersion

term was ~10%. In the case of $l = 1.2$ cm for SF-57 (configuration #11), the agreement with theory for the inclusion of the dispersion term was ~1 pt in 730 with an uncertainty of ~1 pt in 130.

6.4. Conclusion

In summary, the drag coefficient α^{SR} was measured for 15 different configurations (as shown in Table 15) where the index n was varied from ~1.46 to ~1.84 and the dispersion was varied from $-0.029 \mu\text{m}^{-1}$ to $-0.138 \mu\text{m}^{-1}$. In addition, the angular dependence of the drag coefficient (as shown in Eq. (5.49)) was measured (as shown in Figures 6.5, 6.6, and 6.7) by varying the angle of incidence θ from approximate 5° to 13° . To check the scale factor in Eq. (5.48), the length of the glass l , was varied by approximately an order of magnitude (see Figures 6.3, 6.4 and 6.5) and the velocity was varied by approximately 40% (see Figures 6.1 and 6.2).

The various drag measurements were in good agreement with the theoretical predictions of special relativity, as evidenced by Eqs. (6.4) and (6.5), to within the stated uncertainties of the experiment. We conclude that if a solid glass medium of index n , dispersion $\partial n/\partial\lambda$, and length l is moved at velocity v , the resultant drag is indeed given by the predictions of special relativity as applied to the "shuttling glass rod" configuration.

CHAPTER 7

SUMMARY AND SUGGESTIONS FOR FUTURE WORK

7.1. Summary

The Fresnel-drag effect was measured using a passive ring resonator technique. The Fresnel-drag effect describes the change in the velocity of light in a moving medium when observed in an inertial frame other than that of the medium.

A first attempt at explaining this effect was made by Fresnel in the early 19th century, who explained the effect in terms of a partial dragging of the ether.¹¹ Fizeau, in 1859, directly measured the Fresnel-drag in flowing water using an interferometric arrangement.¹² Later, after the ether theory was shown to be incorrect by Michelson and Morley¹⁴ the drag effect was explained by Einstein's theory of special relativity. In his more accurate measurements, Zeeman (in the early 1900's) measured the drag effect in "shuttling glass rods" using an interferometric arrangement.¹⁶ Due to the motion of the boundaries in the "shuttling rod" configuration, the effective drag, as measured in the lab frame, has a slightly different form than that of the flowing water experiments in which the boundaries of the medium are stationary. In his experiments, Zeeman verified the predicted drag to within ~1%. In addition, Zeeman verified to ~1 part in 6, the existence of the dispersion term in the drag coefficient. This term is due to the fact that the effective wavelength in the rest

frame of the medium is doppler-shifted from that of the source.

Recently, the Fresnel-drag was measured by several different researchers using a ring laser arrangement.^{19,20} In the more accurate of these experiments, a rotating disc was placed inside the cavity as a means of producing the drag.^{13,21} In most of these experiments, there was very little improvement of the quantitative determination of the drag coefficient over those measurements performed by Zeeman. In the ring laser experiment conducted by Bilger and Stowell²¹ using the rotating glass disc, their stated uncertainty was $\sim .04\%$ (one standard deviation of the measurement). While this uncertainty was an improvement over the measurement uncertainties of Zeeman's experiment, the result obtained by Bilger and Stowell actually differed from the calculated value by ~ 3 standard deviations. Hence, one was left to wonder whether their result agreed or disagreed with theory.

The Fresnel-drag measurements performed in this thesis utilized, for the first time, the passive ring resonator approach. The passive ring resonator setup used here was by no means optimized for precision measurement of the Fresnel-drag. The very fact that this technique was being developed and studied in our lab as a result of its rotation sensor applications, suggested a convenient method for measuring the Fresnel-drag.

The passive ring resonator technique may be used to measure, in general, non-reciprocal phase shifts experienced in the propagation of light. In this technique, two counterpropagating beams sharing a common optical cavity, are used to measure the difference in

optical pathlength for clockwise (cw) traversal of the cavity versus counterclockwise (ccw) traversal of the cavity. The difference in optical pathlength $\Delta P = P_{cw} - P_{ccw}$ is then observed in terms of the difference in resonance frequencies of the cavity, $\Delta f = f_{cw} - f_{ccw}$.

In the setup used here, a common laser source was used for both cw and ccw beams, each of which was shifted in frequency (to f_{cw} and f_{ccw} , respectively) prior to entering the cavity. In this way, the measurement of Δf was independent of common laser frequency jitter and drift. The cw resonance of the cavity was automatically locked to f_{cw} by means of a primary feedback loop that adjusted a piezo-electrically controlled cavity mirror. The operation of this feedback loop was based on a 32 KHz cavity length modulation rate as a means of detecting the center of the cavity resonance. The frequency f_{ccw} was then adjusted, either using an open loop configuration or by means of a secondary feedback loop, such that the ccw beam was "on resonance." The frequency $f_1 - f_2$ was then measured and related to the difference in optical pathlength, ΔP .

The performance of the passive ring resonator sensor was studied and compared to the fundamental (shot noise) limit for this setup. The short term stability of the setup was found to be consistent with the fundamental limit, that is, for integration times τ of up to 10s. The longer term random drift of the setup, that is for $\tau \gtrsim 10s$, showed a departure from the $\tau^{-1/2}$ dependence of the fundamental limit indicating the DC drift of the setup.

Many sources of error were investigated as possible courses for the long term drift. These included the pulling effects of higher order transverse modes and misalignment as well as electronic sources of error, backscattering effects, polarization effects, and air currents.

Because of the DC drift of the setup, we used an AC technique for measuring the Fresnel-drag effect. Here, a glass window was employed as the dragging medium, since a solid medium lent itself to convenient and precise measurements of the velocity and index profile. The experiment was thus an AC form of Zeeman's "shuttling glass rod" arrangement, where the glass was moved back and forth sinusoidally inside the cavity at $f_f \sim 5$ Hz.

To eliminate possible errors due to multiple reflections in the glass, the glass window was tilted at an angle of incidence θ (typically 5° to 10°) to the direction of beam propagation. The drag calculation was then corrected for this angular dependence.

In order to prevent the glass from wobbling in its motion and thus modulating DC effects of non-reciprocal phase shift (such as those due to birefringence in the glass and cavity misalignment) the glass was mounted on a shift which was tightly constrained to move in the direction of light propagation by means of a bearing. To measure the velocity $v(f_f)$ of the medium a mirror was placed on the same mount as that of the glass window. This mirror was then used to form one arm of an interferometer. The displacement of the glass was thus detected interferometrically and the driving frequency, f_f , was measured to obtain the velocity.

The sinusoidal non-reciprocal variation in the resonance frequency $\Delta f(f_f)$ due to the drag was then detected. In order to measure Δf independent of the gain of the cavity and instrumentation a null system was employed. Here, the ccw beam frequency f_{ccw} was modulated 180° out of phase with the drag signal. The amplitude $\Delta f(f_f)$ of the frequency modulation necessary to null the drag signal was then measured as the resonance frequency shift due to the drag.

The optical perimeter of the cavity was measured by measuring the free spectral range of the cavity. The indices^{28,29,30} of refraction n as well as the lengths³¹ l of the glass windows used in the experiment were measured by the suppliers of the windows. The angle of incidence θ , was basically measured by means of measuring the angle of reflection of the beam from the glass surface.

The resonance frequency shift $\Delta f(f_f)$ was measured for fifteen different combinations of n , l , and θ at a velocity $v(f_f) \sim 25$ cm/s. By using four different types of glass, n was varied from ~ 1.46 to ~ 1.84 and the dispersion $\partial n/\partial \lambda$ was varied from $\sim -0.03 \mu\text{m}^{-1}$ to $\sim -0.14 \mu\text{m}^{-1}$. The length was varied from 0.2 cm to 1.5 cm for fused silica and from 0.6 cm to 1.2 cm for BK-7 and SF-57 glass types. The angular dependence of the drag was checked by varying θ from $\sim 5^\circ$ to $\sim 13^\circ$. In all of these measurements where $\Delta f(f_f)$ varied from ~ 275 Hz to ~ 3 KHz there was a residual offset in $\Delta f(f_f)$ of 9.8 ± 0.4 Hz regardless of n , l and θ . This offset was found to be due to the Fresnel-drag of the air, which was being pushed back and forth by the glass.

The velocity dependence of the drag was checked for BK-7 (of $l = 0.6$ cm and $\theta = 6.6^\circ$) by varying $v(f_f)$ from ~ 20 cm/s to 29 cm/s. Because the offset varied linearly with $v(f_f)$, this provided additional evidence that the drag was due to the air currents.

After subtracting the same offset for all fifteen measurements performed at $v = 25$ cm/s the measured drag coefficients α_e^{SR} were determined and compared to the theoretical values α_{th}^{SR} . In each comparison, $(\alpha_e^{SR} - \alpha_{th}^{SR})/\alpha_{th}^{SR}$, the measured value was in good agreement (to within the uncertainty of each measurement of typically 1×10^{-3}) with the theoretical value. Taking an average over all the measurements, the spread in $\alpha_e^{th} - \alpha_{th}^{SR}/\alpha_{th}^{SR}$ was $\sim 5 \times 10^{-4}$ with a mean agreement with theory of $\sim 5 \times 10^{-5}$. If the measurements were averaged according to a weighted average (based on the individual error bar/measurement) the spread in $\alpha_e^{SR} - \alpha_{th}^{SR}/\alpha_{th}^{SR}$ was $\sim 2.4 \times 10^{-4}$ with a mean agreement with theory of $\sim 4 \times 10^{-5}$. In addition, the confidence in the inclusion of the dispersion term was ~ 1 part in 130, with an agreement with theory of ~ 1 part in 730. These results led us to the conclusion that the drag experienced in light propagation for the "shuttling glass rod" configuration is indeed given by the predictions of special relativity.

The above result represents a quantitative improvement in the determination of the drag coefficient of approximately two orders of magnitude over Zeeman's experiment. In addition, the confidence in the inclusion of the dispersion term was increased by a factor of ~ 30 .

In the ring laser-rotating disc measurement of Bilger and Stowell,²¹ as stated earlier, the rms standard deviation of the measurement

was quoted as $\pm 0.04\%$. The theoretical value of the drag coefficient fell almost three standard deviations away from the measured value. In their experiment, the drag was measured by only varying the velocity (they varied the velocity by approximately an order of magnitude). The drag coefficient was obtained by measuring the scale factor between the beat frequency and the velocity. Since the drag coefficient α was not varied, any errors in their scale factor would have introduced errors in α . One of the difficulties in measuring the scale factor was due to the fact that the drag, in their configuration, depended on the distance of the refracted beam from the axis of rotation of the disc. Hence, they had to know the precise trajectory of the beam inside the glass. Another possible problem was that their experiment was a dc measurement and depended on the DC stability of the ring laser.

7.2. Suggestions for Future Work

There are several experimental improvements that can be made for future measurements of the Fresnel-drag using the passive resonator technique. The first of these would be the use of a vacuum system for either entire cavity, or for a region around the moving glass alone, to eliminate the effects of air currents.

In addition, it would be helpful to increase the signal by increasing the velocity. This could be achieved by either increasing the frequency of the AC drive to the glass or by increasing the displacement. To do this, better means of constraining the motion

of the glass with greater dynamic range and frequency response should be investigated. After tight control of the glass motion is achieved the length of glass should also be increased (with, of course, more accurate length measurements) to obtain a larger signal. It is also possible to obtain glass substrates from Schott Glass Inc.²⁹ with lower stress birefringence (by a factor of ~100) than the glass samples used here in order that such tight control of the glass motion is not as crucial.

The dominant source of uncertainty for a given measurement of α_e^{SR} was due to readout errors in $\Delta f(f_f)$. Cumulatively, these errors resulted in a fractional uncertainty of $\sim 10^{-3}$ in α_e^{SR} . Among these, the uncertainty due to imperfect common mode rejection of large reciprocal pathlength changes in the glass could be eliminated. To do this, the gain of the primary servo loop could be increased using a PZT of higher frequency response. In addition, the subtraction factor β could be improved by better matching of the detectors and by active stabilization of the beam intensities.

Another contribution to the readout uncertainty in $\Delta f(f_f)$ was due to the readout uncertainties of the frequency-modulation of the A/O necessary to null the drag signal (typically on the order of one part in 2500). This uncertainty could be eliminated by an on-line computer readout of the frequency modulation amplitude. In the same way, an on-line computer readout of the displacement fringe count would eliminate readout errors in the velocity. In addition, it would be useful to stabilize the displacement to small fractions of a fringe.

Finally, as a means of reducing the uncertainties in α_{th} , the index of the glass must be determined more accurately. This could be done by sending the samples to NBS.³⁶ In this experiment, the index was only known to within a maximum uncertainty of ~1 part in 20,000 resulting in an uncertainty in α_{th}^{SR} of ~1 part in 5000. In addition, greater care should be taken to measure the angle of incidence, θ , more accurately.

REFERENCES

1. Barut et al., *Laser Focus* 49, Oct. 1982.
2. E.J. Post, *Rev. Mod. Phys.* 39, 475 (1967).
3. M.O. Scully, in *Proceedings of the Fifth International Conference on Laser Spectroscopy*, H. Walther and K. Rothe, eds. (Springer-Verlag, Berlin, 1979); M.P. Hangan, M.O. Scully, and K. Just, *Phys. Lett.* 77A, 88 (1980).
4. G.A. Sanders, M.G. Prentiss, and S. Ezekiel, *Opt. Lett.* 6, 569 (1981).
5. A.H. Rosenthal, *J. Opt. Soc. Am.* 52, 1143 (1962).
6. M.E. Ash, Charles Stark Draper Laboratory, Inc., Cambridge, Massachusetts (personal communication, December 1976); D.H. Eckhardt, *Proc. Soc. Photo-Opt. Instrum. Eng.* 157, 172 (1978).
7. For example, the Boeing 757 and 767 aircraft employ ring laser gyroscopes made by Honeywell Inc.
8. V. Vali and R.W. Shorthill, *Appl. Opt.* 15, 1099 (1976).
9. S. Ezekiel and S.R. Balsamo, *Appl. Phys. Lett.* 30, 478 (1977).
10. D. Newman et al., *Phys. Rev. Lett.* 40, 1355 (1978).
11. A.P. French, *Special Relativity* (W.W. Norton & Co., New York, New York) 1968.
12. H. Fizeau, *Ann. de. Chim. et de Phys.*, (3), 57, 385, 1859.
13. H.R. Bilger and A.T. Zavodny, *Phys. Rev.* A5, 591 (1972).
14. A.A. Michelson and E.W. Morley, *Am. J. Sci.* 34, 333 (1887).
15. P. Zeeman, *Arch. Neerl. Sci. Exactes Nat.* 3A 10, 131 (1927).
16. P. Zeeman, *Proc. Roy. Acad. Amsterdam* 22, 469 (1920); *Proc. Roy. Acad. Amsterdam* 22, 512 (1920); P. Zeeman et al., *Proc. Roy. Acad. Amsterdam* 23, 1402 (1922).
17. H.A. Lorentz, *Versuch einer Theorie der elektischen und optischen Erscheinungen in bewegten korpern* (Brill, Leiden, 1895), p. 101.
18. W.F. Parks and J.T. Dowell, *Phys. Rev.* A9, 565 (1974).

19. W.M. Macek, J.R. Schneider, and R.M. Salamon, J. Appl. Phys. 35, 2556 (1964).
20. G.A. Massey and A.E. Siegman, IEEE J. Quantum Electron. QE-6, 500 (1970).
21. H.R. Bilger and W.K. Stowell, Phys. Rev. A 16, 313 (1977).
22. F. Aronowitz, Laser Applications, edited by Monte Ross (Academic, New York, 1971), pp. 134-200.
23. W.M. Macek and D.T.M. Davis, Jr., Appl. Phys. Lett. 2, 67 (1963).
24. A. Yariv, Introduction to Optical Electronics (Holt, Rinehart and Winston, Inc., New York, 1971), Chapter 4.
25. T.A. Dorschner et al., IEEE J.Q. Elect. QE16, 1176 (1980).
26. A. Yariv, Introduction to Optical Electronics (Holt, Rinehart and Winston, Inc., New York, 1971), Chapter 10.
27. Observation of Special Variations in the Resonance Frequency of an Optical Resonator, R.E. Meyer, G.A. Sanders and S. Ezekiel, submitted to Journal Opt. Soc. Am.
28. I.H. Malitson, J. Opt. Soc. Am. 55, 1205 (1965).
29. Schott Optical Glass, Duryea P.A.
30. Hereaus Amersil Inc., Sayreville, N.J.
31. Special Optics, Little Falls, N.J.
32. Draper Laboratory, Cambridge, MA.
33. Handbook of Chemistry and Physics, 58th ed. (CRC Press, Cleveland, Ohio) 1977.
34. G.R. Hanes and K.M. Baird, Metrologia 5, 32 (1969).
35. The Theory of Relativity (Oxford University Press, Delhi) 2nd ed., 1972.
36. National Bureau of Standards, Washington, D.C.

BIOGRAPHICAL NOTE

Glen Sanders was born in Chicago, Illinois on August 11, 1955. He graduated at the top of his high school class before attending the University of Colorado at Boulder, where he received his Bachelor of Science in Engineering Physics in 1977. In addition at CU, he received the Frank H. Prouty Scholarship for highest academic performance in the School of Engineering. In the summer of 1977, he worked as an Engineer at Honeywell (Minneapolis, MN) designing microprocessor hardware for automatic test equipment. In September 1977, he began his graduate work at the Massachusetts Institute of Technology. His doctoral research was conducted under the supervision of Prof. Shaoul Ezekiel as a research assistant in the Research Laboratory of Electronics. In May of 1983, he received his Ph.D. in Physics from the Massachusetts Institute of Technology.



Room 14-0551
77 Massachusetts Avenue
Cambridge, MA 02139
Ph: 617.253.5668 Fax: 617.253.1690
Email: docs@mit.edu
<http://libraries.mit.edu/docs>

DISCLAIMER OF QUALITY

Due to the condition of the original material, there are unavoidable flaws in this reproduction. We have made every effort possible to provide you with the best copy available. If you are dissatisfied with this product and find it unusable, please contact Document Services as soon as possible.

Thank you.

PAGE 98 occurs twice in this document

There is a page 162b